Experimental and Numerical Investigation of the Flow Structures at the Rear of Three-Dimensional Bluff Bodies

by

Naseeb A. Siddiqui

A thesis submitted to the
School of Graduate and Postdoctoral Studies in partial
fulfillment of the requirements for the degree of

Doctor of Philosophy in Mechanical Engineering

Department of Mechanical and Manufacturing Engineering/Faculty of Engineering and Applied Science

University of Ontario Institute of Technology (Ontario Tech University)

Oshawa, Ontario, Canada

May 2023

THESIS EXAMINATION INFORMATION

Submitted by: **Naseeb Ahmed Siddiqui**

Doctor of Philosophy in Mechanical Engineering

Thesis title: **Experimental and Numerical Investigation of the Flow Structures at the Rear of Three-Dimensional Bluff Bodies**

An oral defense of this thesis took place on May 26, 2023, in front of the following examining committee:

Examining Committee:

Chair of Examining Committee	Dr. Bale Reddy
Research Supervisor	Dr. Martin Agelin-Chaab
Examining Committee Member	Dr. Brendan MacDonald
Examining Committee Member	Dr. Yuping He
University Examiner	Dr. Ahmed Barari
External Examiner	Dr. Hachimi Fellouah, University of Sherbrooke

The above committee determined that the thesis is acceptable in form and content and that a satisfactory knowledge of the field covered by the thesis was demonstrated by the candidate during an oral examination. A signed copy of the Certificate of Approval is available from the School of Graduate and Postdoctoral Studies.

ABSTRACT

Flows around bluff bodies have complex structures, which create drag, surface contamination and stability issues for transportation systems. The standard Ahmed body (SAB) is a simplified representative three-dimensional (3D) bluff body that is known to produce the essential features of complex bluff bodies. This thesis studies the flow structures at the rear end of 3D bluff bodies to aid the development of flow control strategies. In the first method, a modified SAB with a 25° slant angle is proposed that uses elliptical curvature at the rear end and is denoted as the elliptical Ahmed body (EAB). The particle image velocimetry (PIV) technique is used to provide the detailed flow structure. The PIV study is conducted at a Reynolds number of 4.31×10^4 based on the model height. This experimental study is complemented by detached eddy simulations at Reynolds numbers of 1.47×10^4, 4.31×10^4 and 1.90×10^5. In the second method, the effect of a hydrophobic coating on the flow structure of the SAB and EAB is investigated experimentally using the PIV technique and for the same Reynolds numbers stated above. For both methods, the coherent structures are evaluated using advanced analysis techniques, such as frequency analysis, proper orthogonal decomposition, dynamic mode decomposition, Q-criterion and λ_2-criterion. For the Reynolds numbers and specific conditions investigated, the results show that the elliptical curvature creates significant reorganization of the flow structures, where the slant separation bubble, longitudinal C-vortices and lower recirculation bubble are eliminated, whereas the upper recirculation bubble shifts toward the slant surface. This flow restructuring provides ~10.4% drag reduction and reduces surface contamination. In addition, the hydrophobic coating increases the slant separation bubble and the Strouhal number at the slant surface of the SAB, while the wake recirculation length is not significantly affected. However, the shear stress, turbulent kinetic energy, and Strouhal numbers are reduced over the EAB with the coating. Overall, the results show that elliptical curvature and hydrophobic coating have the potential for drag reduction and the mitigation of surface contamination. However, further investigation is required before generalized conclusions can be drawn.

Keywords: Bluff body; Ahmed body, flow control; hydrophobic coating; coherent structure, Q-criterion, λ_2-criterion, proper orthogonal decomposition, dynamic mode decomposition.

AUTHOR'S DECLARATION

I hereby declare that this thesis consists of original work which I have authored. This is a true copy of the thesis, including any required final revisions, as accepted by my examiners.

I authorize the University of Ontario Institute of Technology (Ontario Tech University) to lend this thesis to other institutions or individuals for the purpose of scholarly research. I further authorize the University of Ontario Institute of Technology (Ontario Tech University) to reproduce this thesis by photocopying or by other means, in total or in part, at the request of other institutions or individuals for the purpose of scholarly research. I understand that my thesis will be made electronically available to the public.

_____ Naseeb Ahmed Siddiqui

STATEMENT OF CONTRIBUTIONS

The majority of the results reported in Chapter 4 are published as follows:

Publications in Journals

N. A. Siddiqui, M. Agelin-Chaab, "Investigation of the wake flow of the elliptical Ahmed body using detached eddy simulation," ***International Journal of Heat and Fluid Flow*** 101, 109125, 2023. [Impact factor: 2.6]

N. A. Siddiqui, M. Agelin-Chaab, "Experimental investigation of the flow features around an elliptical Ahmed body," ***Physics of Fluids*** 34, 105119, 2022. [Impact factor: 4.9]

N. A. Siddiqui, M. Agelin-Chaab, "Flow features of the Ahmed body at a low Reynolds number,'' ***International Journal of Heat and Fluid Flow*** 98, 109052, 2022. [Impact factor: 2.6]

N. A. Siddiqui and M. Agelin-Chaab, "A simple passive device for the drag reduction of an Ahmed body," ***Journal of Applied Fluid Mechanics*** 14, 147–164, 2021. [Impact factor: 1.3]

N. A. Siddiqui, M. Agelin-Chaab, "Effects of hydrophobic coatings on the flow structure at the rear of 3D bluff bodies," ***Experimental in Fluids*** *(Under Review)* [Impact factor: 3.3]

Publications in Conference Proceedings

N. A. Siddiqui and M. Agelin-Chaab, "Detached Eddy Simulation of the 28° Ahmed Body at a Low Reynolds Number." *Proceedings of the* ***ASME 2022 Fluids Engineering Division Summer Meeting***. *Volume 1: Fluid Applications and Systems (FASTC); Fluid Measurement and Instrumentation (FMITC); Fluid Mechanics (FMTC)*. Toronto, Ontario, Canada. August 3–5, 2022. V001T03A028.

T. Harley, N. A. Siddiqui and M. Agelin-Chaab, "Effect of the Rear Geometry on the Flow Structure and Drag of the Ahmed Body," ***Proceedings of the ASME 2022 Fluids Engineering Division Summer Meeting***. *Volume 1: Fluid Applications and Systems (FASTC); Fluid Measurement and Instrumentation (FMITC); Fluid Mechanics (FMTC)*. Toronto, Ontario, Canada. August 3–5, 2022. V001T03A028.

I performed the majority of the testing, analysis, and writing of the manuscript.

ACKNOWLEDGEMENTS

At first, I express my humility to the Lord, who helped me throughout the Ph.D. journey by embellishing and enlightening me with devotion to be a seeker of knowledge.

I express wholehearted gratitude to my academic advisor Dr. Martin Agelin-Chaab for his invaluable guidance, feedback, and patience that tremendously bestowed a fruitful Ph.D. research. I am also indebted to his support in presenting and publishing my research work at conferences and high-impact journals. It would have been impossible to complete the research work without his consistent encouragement and motivation.

I also want to acknowledge and thank my committee members, Dr. Brendan MacDonald and Dr. Yuping He, for providing valuable suggestions. It greatly helped to revitalize the research work.

I want to thank Sedam Kumahor and Amir Sagharichi for their help with the data acquisition, and especially Dr. Mark F. Tachie for the permission to use his research facilities.

Finally, I express my deepest gratitude to my adorable wife, Waresa Azizi, for her love, patience, calmness, and support. To my mother, Nikhat Tara Siddiqui, Father, C.L. Siddiqui, brother Tashneem Siddiqui, and sister, Shajima Siddiqui, for their prayers and moral encouragement that kept me going.

TABLE OF CONTENTS

LIST OF FIGURES

LIST OF TABLES

LIST OF ABBREVIATIONS AND SYMBOLS

DF-PIV	Double frame particle image velocimetry
DMD	Dynamic mode decomposition
DES	Detached Eddy Simulation
DNS	Direct Numerical Simulation
DDES	Delayed Detached Eddy simulation.
IDDES	Improved Delayed Detached Eddy simulation.
EAB	Elliptical Ahmed body
EAB_9	Elliptical Ahmed body at 9 m/s
EAB_9_Exp.	Elliptical Ahmed body at 9 m/s. Experimental
EAB_40	Elliptical Ahmed body at 40 m/s
ESS	Elliptical slant surface
E_{uu}	Energy spectrum
FOV	Field of view
FRB	Front roof bubble
HSAB	Hydrophobic standard Ahmed body
HEAB	Hydrophobic elliptical Ahmed body
IA	Interrogation area
LRB	Lower recirculation region
LSV	Large-scale separated vortex
LES	Large Eddy Simulation
LRB	Lower recirculation region
LSV	Large-scale separated vortex
NBL	Negative bifurcation line
OSL	Opposite shear layer
POD	Proper orthogonal decomposition
PIV	Particle image velocimetry
PBL	Positive bifurcation line
QAS	Quasi axi-symmetric structure

RSS	Rectangular slant surface
RANS	Reynolds averaged Navier-Stoked simulation
R_{uu}	Streamwise auto-correlation
SSB	Slant separation bubble
SAB	Standard Ahmed body
SAB_3.1	Standard Ahmed body at 3.1 m/s
SAB_9	Standard Ahmed body at 9 m/s
SAB_9-Exp.	Standard Ahmed body at 9 m/s experiment
SAB_40	Standard Ahmed body at 40 m/s
SBL	Slant bubble length
SCV	Secondary C vortices
SGLOF	Subgrid global luminescent oil-film
SRE	Slant rear edge.
SSB	Slant separation bubble
SSE	Slant side edge
SUE	Slant upper edge
SVD	Singular value decomposition
S-PIV	Standard particle image velocimetry
SWB	Symmetric wake bubble
S_t	Strouhal number
S_k	Stokes number
S.L	Slant length
TDS	Three-dimensional structure
TKE	Turbulent kinetic energy
TR-PIV	Time resolved particle image velocimetry
URB	Upper recirculation region
U	Normalized time-averaged streamwise velocity
U_∞	Freestream velocity
UU	Normalized normal stress
UW	Normalized shear stress

VLES	Very large eddy simulation
h	Test model height
H_r	Wake recirculation height
L_r	Recirculation length
S_t	Strouhal number
S.L.	Slant length
U	Normalized time-averaged streamwise velocity
U_∞	Freestream velocity
UW,UV,VW	Normalized shear stress
V	Normalized time-averaged spanwise velocity
W_r	Wake recirculation width
W	Test model width
X	Normalized streamwise coordinates
Y	Normalized spanwise coordinates
Z	Normalized wall-normal coordinates
ν	Viscosity
ρ	Density
W	Normalized time-averaged wall-normal velocity
α	Slant angle
t_p	Particle response time
t_f	Characteristic temporal scale

Chapter 1: Introduction

The chapter provides background information related to bluff bodies focusing on the effect of the rear end on the flow features. It also discusses the motivation and objectives of the thesis. Finally, the structure of the thesis is outlined.

1.1 Background

A bluff body is defined as a body that causes flow separation over a substantial part of its surface because of the nature of its shape [1]. They show a premature boundary layer separation from the surface and create a wake with unsteady velocities. The region occupied by the separated wake is generally denoted by the recirculation region having significant low pressures, which is a feature of drag creation [2], [3]. When the Reynolds number is low, the flow over a bluff body is strongly affected by viscosity, and the body experiences drag forces primarily due to skin friction. As the Reynolds number surpasses a certain threshold, the wake undergoes vortex shedding, which leads to a substantial decrease in pressure at the rear surface. This pressure reduction becomes the dominant contributor to the overall drag experienced by the bluff body [4].

The most common examples of three-dimensional (3D) bluff bodies are trains, buses, cars, and some submersible vehicles [5], [6]. The flow around 3D bluff bodies is inherently three-dimensional and exhibits complex characteristics, such as turbulent boundary layers, flow separation and reattachment, longitudinal C-vortices and a large turbulent wake at the rear end. Understanding the effects of these flow characteristics has considerable practical significance because they are closely associated with drag, surface contamination and stability issues, etc. [4], [6].

Figure 1.1(a) shows the difference between the high-pressure at the front and the low-pressure region at the rear of a vehicle. This pressure disparity, resulting from flow separation at the rear end, gives rise to the dominant form of drag known as pressure drag, which constitutes a significant portion of the total drag experienced by 3D bluff bodies [7]–[9]. Subsequently, the rear end is the main contributor to the drag and depends on the slant angle, as shown in Figure 1.1(b), which dramatically alters the flow features [10]–[12]. At high speeds, such complex 3D bluff body shapes can account for more than 60% of the total fuel consumption [13]. Thus, given a reduction in the aerodynamic drag by 10%, fuel

consumption in real-world driving may go down by 2.5–4% [13]. Similarly, the recent trend shows an interest towards bluff shape submersible vehicles such as squat submarines. The flow around this type of vessel also encounters the problem of pressure drag and surface contamination [5]. Furthermore, there are other underwater vehicles that show flow features similar to the 3D bluff bodies, for example, the shallow-running flat submerged bodies [14] and multi-state submersible vehicles [15]. Other underwater applications of 3D bluff bodies which are not transportation related include large structures, such as caisson structures or oscillating water columns (OWC), wave energy converters (WECs) [16], and underwater energy storage systems [17].

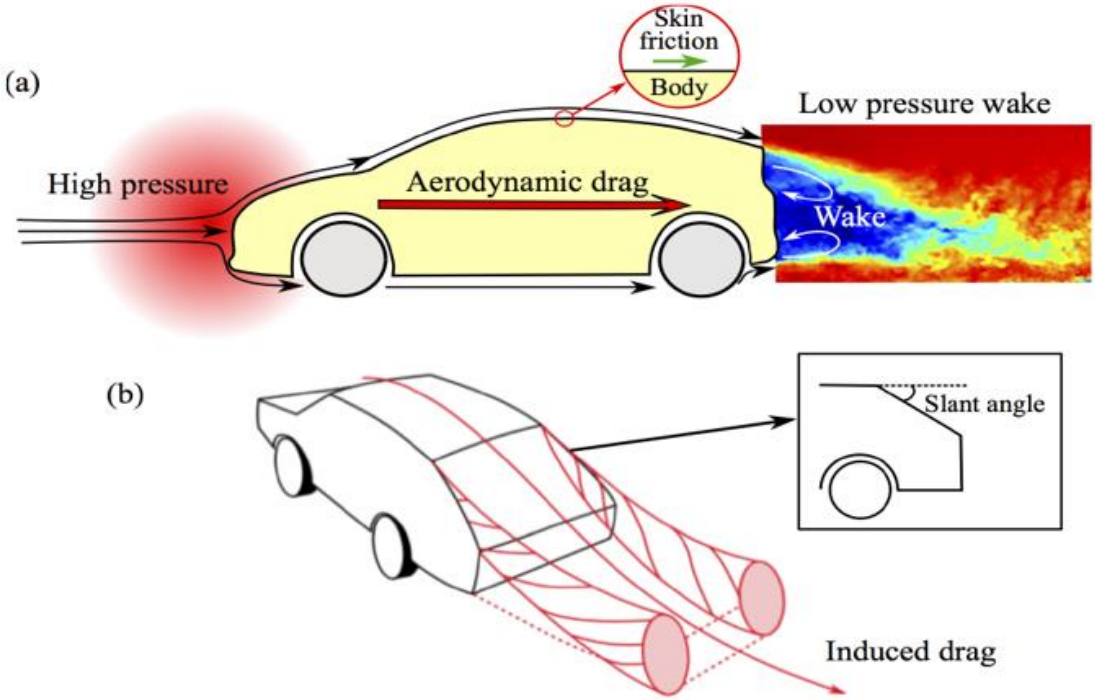

Figure 1.1: Conceptual description of the drag origin [6], [18]. (a) Schematic of drag around the vehicle (b) C-vortices from the side edges and the effect of slant angle.

Subsequently, the control of complex flow characteristics at the rear of 3D bluff bodies relies on fundamental comprehension of the sources of the drag and surface contamination mechanisms which must first be studied on basic bluff bodies for a refined understanding of the flow physics. There are different simplified 3D bluff geometries, especially in the ground transportation sector, such as the Ahmed body [19], [20].

The Ahmed body provides unique opportunities to analyze the flow behavior in great detail by focusing on the rear end [10]. The standard Ahmed body (SAB) produces complex three-dimensional structures (TDS) and unsteady turbulent structures at the rear end, depending on the slant angle. Since the Ahmed body represents several vehicle models, it is the most studied simplified geometry, and it has become a benchmark model [21]. Similarly, the flow around some submersible vehicles produces similar flow features to the SAB at the rear end, which are found to encounter significant resistance in terms of drag and surface contamination [5], [22], [23]. Accordingly, the SAB reserves a special position among the simplified 3D bluff bodies that have a flow structure common to both ground and underwater vehicles. Also, the Ahmed body is a member of larger critical geometries showing relevant flow features due to specific geometric parameters [22]. Therefore, this thesis employs the Ahmed body as the representative 3D bluff body to understand the flow features focusing on the rear end and relate it to drag and surface contamination.

In the SAB with the rectangular slant surface, the slant angle remains the main factor that distinguishes the model into high and low drag regimes [24], [25]. In the high-drag regime between slant angles 12.5° and 30°, the slant separation bubble (SSB), a pair of counter-rotating longitudinal C-vortices, and wake recirculation region behind the body, including the upper recirculation bubble (URB) and lower recirculation bubble (LRB) are the primary flow features. In this high-drag region, the flow has a three-dimensional structure (TDS) dominated by turbulent eddies of various orders. On the contrary, in the low-drag regime, the flow becomes massively separated, and the C-vortices lose energy, which generates the quasi-axisymmetric separated (QAS) flow at the rear [10], [26]. It should be noted that the three-dimensional and unsteady behavior of the SAB between the $25°<\alpha<30°$ slant angle is not well understood, especially at a 25° slant angle, having a complex flow structure [27], [28]. In fact, the flow structure at the rear of the 25° SAB is so complex that low order turbulence models such as the Reynolds-averaged Navier-stokes (RANS) cannot capture it [29]. Additionally, there is currently limited understanding of the unsteady flow physics associated with the rear-end flow structure of the 25° SAB, and the existing knowledge is fragmented across experimental studies and numerical simulations. It was shown by Ahmed et al. [10] that the wake of the Ahmed body contributes up to 70% pressure drag of the total drag. Specifically, at 25° SAB, almost 64%

of pressure drag is from the slant surface, 30% from the vertical base, and only 6% from the forebody [10], [30], [31].

The subject of shape modification using rounding of the rear edge and its effect on the wake flow features has hardly been discussed in the open literature until recently [32]. For example, Thacker et al. [33] rounded the sharp edge of the slant surface on the 25° SAB. This modification successfully suppressed flow separation and provided 10% drag reduction. Nevertheless, another investigation conducted examined the effects of rounding both the top and side edges of the slant surface on the 25° SAB in [34], [35]. Interestingly, while rounding the top edge resulted in a notable 16% reduction in drag, no improvement in drag was observed when rounding the side edges. The primary factor contributing to this reduction was the suppression of flow separation and the elongation of the recirculation region [34], [35]. These studies found compelling benefits in terms of drag reduction due to the modification in the complex TDS found at the rear of the 25º SAB. Nonetheless, the idea of shape modification by implementing an elliptical curvature at the rear end of the SAB has not been attempted so far. Therefore, the flow structure of the modified SAB with elliptical curvature, which is denoted as the elliptical Ahmed body (EAB), will provide physical insight into the rear end flow features and its impact on the drag and surface contamination.

Similarly, in recent times, there has been a notable surge of interest in surface modification methods aimed at altering the characteristics of the boundary layer, particularly with regard to the application of hydrophobic coatings. These coatings, possessing a water contact angle exceeding 90º, generate a shear-free air-water interface [36]–[38]. Consequently, hydrophobic coatings have gained recognition as a viable technique for achieving diverse objectives, including the reduction of viscous drag [39] anti-icing capabilities [40] and self-cleaning properties [41]. The concept of employing hydrophobic coatings to manipulate the flow dynamics around simple 2D bluff bodies has garnered attention, specifically in terms of delaying flow separation and regulating subsequent vortex behavior in the wake [42]–[44].

1.2 Motivation

In Canada, the transportation industry consumes around 23% of the total energy produced [45]. Furthermore, the transportation sector is heavily dependent on fossil fuels and contributes up to 22% of the greenhouse gases in Canada [46]. Addressing these pressing global concerns of greenhouse gas emissions and fuel consumption requires innovative approaches to enhance the efficiency of vehicles. Despite their prevalence in the transportation industry, there remains some knowledge gap regarding complex flow phenomena occurring at the rear of some 3D bluff bodies. For example, the flow around the 25º slant angle of the SAB is so complex that low fidelity simulations such as RANS cannot capture the flow dynamics. Thus, high fidelity investigation of flow separation, vortex shedding, and wake dynamics at the rear end provides fundamental insights. Moreover, fundamental studies of turbulent flow around the EAB is not reported in the open literature. Such physical understanding can pave the way for the development of innovative flow control strategies and drag reduction techniques resulting in a more efficient transportation sector and low greenhouse gas emissions. Moreover, studying the wake flow characteristics offers valuable insights into the rear window surface contamination observed in the context of the LRB. The presence of the LRB at the rear end close to the ground leads to the entrainment of contaminants, propelling them toward the rear window. This phenomenon poses significant challenges, particularly for autonomous vehicles relying on cameras and sensors. Understanding and addressing this issue is crucial for mitigating the adverse effects of surface contamination on the performance and reliability of autonomous vehicle systems. Furthermore, it has been observed that the application of hydrophobic coatings in close proximity to the separation point manifests significant effects, thereby suggesting a direct influence on the boundary layer at this critical location [37]. Nonetheless, previous investigations have predominantly concentrated on scrutinizing the consequences of hydrophobic coatings on simpler geometries of bluff bodies, notably cylinders and spheres [42]–[44]. However, the flow structure at the rear end of a three-dimensional (3D) bluff body, exemplified by the complex flow structures encountered in the 25º SAB, remains a subject that has not yet been explored. The intricate flow patterns observed in the rear end of the 25º SAB present challenges in terms of comprehension. Consequently, an in-depth examination of the

implications of applying hydrophobic coatings to the rear end of the SAB, as well as its modified version, the EAB, provides a compelling avenue to unravel novel physical insights.

1.3 Objective

Based on the above discussion, the main objective of the thesis is outlined as follows:

- Conduct detailed velocity measurements of the flow around the 25^o SAB and EAB.
- Perform high-fidelity numerical analysis of the flow around the 25^o SAB and EAB.
- Experimentally investigate the effects of hydrophobic coatings on the wake flow characteristics of the 25^o SAB and EAB.
- Extract and analyze the turbulent quantities, such as the Reynolds stresses and turbulence kinetic energy, as well as the frequency spectra.
- Apply multiple point advanced analysis techniques such as two-point correlation, proper orthogonal decomposition (POD) and dynamic mode decomposition (DMD) to identify the unsteady flow features in the wake of the 25^o SAB and EAB.

1.4 Thesis Structure

The thesis is organized into five chapters as follows. The literature review of previous studies on the flow structure of the Ahmed body and flow control methods is presented in Chapter 2. Detailed experimental setup, including test facilities, measurement procedures, and the description of the setup for the numerical investigation, is reported in Chapter 3. Chapter 4 reports the results and discussion in detail, including the vortex identification and model decomposition methods used to document the flow features. Finally, Chapter 5 presents the summary and conclusions of the thesis and recommendations for future work.

Chapter 2: Literature Review

This chapter discusses the flow features of bluff bodies, specifically focusing on the three-dimensional bluff bodies represented by the generic vehicle model of the Ahmed body. The survey of the relevant literature highlights the important development in understanding the turbulent flow behavior and areas of immediate concern in the development of flow control to improve the aerodynamic performance of road vehicles. Finally, a summary of the literature is provided, and the relevant research gaps are stated.

2.1 Bluff Body Flow

A bluff body is defined as a body that, as a result of its shape, causes flow separation over a substantial part of its surface and undergoes a massive flow separation at the rear end [1]. The region defined by the separated wake is generally denoted by the base having significant low pressures, which is a strong factor of high drag creation. The base pressure is a direct function of the near-wake flow topology and boundary layers at separation. Hence, when a body moves in a still fluid, it increases the total energy of the fluid. This increased energy is directed to the wake, which is a function of an organization of continuously generating vortices due to the body's surface. However, such a base region, despite having a great scientific value, which depends on geometrical and fluid dynamics parameters, is complex and still an open problem [31], [47].

For two-dimensional bluff bodies, this phenomenon is documented where the alternate shedding of two-counter rotating vortices creates huge perturbation energy contributing to aerodynamic drag. Hence, reducing the concentrated vortices or even reducing their strength provides encouraging results [4], [48]. Bearman [47] highlighted this physical phenomenon by stressing that vortex formation distance influences the base pressure devoid of the method used. It is confirmed by Parezanović and Cadot [31] and Thiria et al. [32] that placing a small cylinder at the back of a 2-D blunt-body extends the recirculation length and increases the global pressure in the base region. Figure 2.1(a) & (b) denote these phenomena where bluffness (Dr/D) is related to the wake width, and at a given bluffness, increased recirculation length provides greater base pressure, hence reduced drag. It also shows the equilibrium between the entrainment and reversed flow which will be different for the turbulent flow [51]. The significance of these studies establishes that the base drag

can be reduced by modifying the wake recirculation region, and hence, methods should be developed to control it.

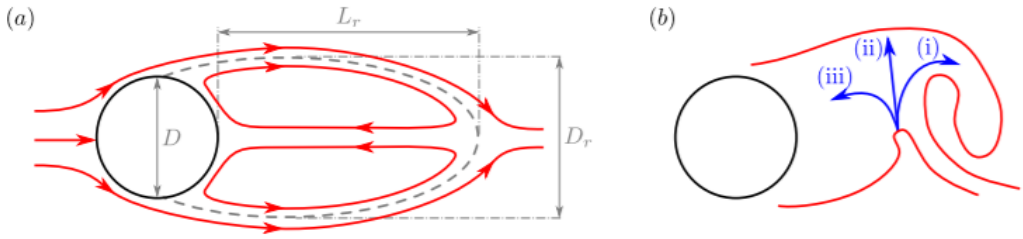

Figure 2.1: (a) Mean flow (b) instantaneous flow dynamics around a circular cylinder. In (b) (i) and (ii), entrainment flows; (iii), reverse flow[51].

The flow around complex 3D bluff bodies is more complicated than the 2D bluff bodies. Since the complex 3D bluff bodies produce high TDS that are responsible for drag, surface contamination and stability according to the application. In this context, many industrial flows are produced by the motion of 3D bluff bodies [3], [52]. The most common examples of bluff bodies are encountered in the transportation industry, such as trains, buses, and cars. The design constraint requires body bluffness which inevitably brings complex three-dimensional flow to the rear end of the body [13], [53], [54]. Thus, these vehicle models represent a 3D bluff body having a blunt rear edge. The growing desire for energy efficiency and safety related to stability and soiling mitigation provides the impetus to understand wake dynamics and force intensities around basic 3D simplified vehicle bodies. The aim is to develop mechanisms capable of reducing undesired effects using geometric optimization or flow control devices [28], [31]. Furthermore, several optimization tools such as geometric optimization [6], [55], genetic algorithm [56], [57], and explorative gradient method [58] are being used to develop unique vehicle shapes and devices to reduce adverse aerodynamic effects. In addition, the optimum shapes of the vehicles are similar in detail and, as such, do not provide significant brand differences. Thence, stylists began to search for non-conventional shapes to provide a brand signature [35]. However, geometric customization requires a great deal of attention to systematically study the parameters that can initiate a framework of a paradigm shift in the conception of the solid-fluid interface. Hence studying and controlling the external flow over the rear end became crucial, which led to the creation of several generic vehicle models [59]. The idea

of the current research is to focus on specific vehicle models that can provide opportunities to investigate rear end effects.

Likewise, the design of a submarine seeks to identify the optimal shape for the vessel to enhance its hydrodynamic performance, while also reducing the amount of energy required for propulsion. This approach can help increase the range and duration of the submarine's operations. There is also the emergence of lightweight mini-submarine designs for amateur underwater explorers. There has been recent attention given to this particular type of submarine. One notable characteristic of this submarine is its length-to-depth ratio (L/D) of less than four, which alters the type of drag force experienced from skin friction to pressure drag [60]. Such underwater transportation system also encounters the problem of surface contamination along with drag [15], [23]. Even the classical streamlined submarines experience around 80-90% of the skin friction drag, and pressure drag amounts to 10-20% of the total drag. In fact, the flow around submarines such as the squat and Chalmers ship model produces similar flow features to that of the Ahmed body at the rear end [5], [14], [61]. Hence, the trend in underwater transportation provides new avenues to develop flow control methods to reduce pressure drag, taking inspiration from ground transportation systems. There are other underwater applications of 3D bluff bodies as well, including large structures, such as caisson structures or oscillating water columns (OWC), wave energy converters (WECs) [16], and underwater energy storage systems [17]. Therefore, the Ahmed body as a representative 3D bluff body creates a unique opportunity to study the effect of flow features due to flow control methods relevant to the ground and underwater transportation. The work of Ahmed et al. [10] significantly improved the comprehension of the flow around different shapes of road vehicles: it characterizes the critical influence of the rear end configuration. It also represents several vehicle models. Significant work has been carried out on this, and it has become a benchmark model [21].

2.2 Simplified Road Vehicle Geometry

The movement of a bluff body in close proximity to the ground affects the flow around it, resulting in highly turbulent separation and reattachment. Studying the interaction between the body and the ground, as well as investigating the unsteady flow, require a significant amount of experimental effort due to their complex nature. Reproducing the

relative movement between the vehicle and the ground in experiments is also a challenging task. Notwithstanding, the optimization of road vehicles requires a complete understanding of these complex phenomena. Therefore, several generic vehicle models have been developed, which can be divided as follows: simple bodies and basic car shapes [59], [62].

Simplified bodies, including the SAE body, Ahmed body, and Rover, are frequently utilized in time-accurate investigations. The main advantage of these models is that they require less computational and experimental resources than actual production vehicles while still allowing researchers to analyze the flow characteristics of different vehicle components without interference. Furthermore, these models provide a diverse set of numerical and experimental validation data, which is crucial for validating simulations. Although simplified vehicles are commonly used for research purposes, the shapes of these models do not precisely match the geometries of real cars. Consequently, insights obtained from these simplified models may not be easily transferable to the development of production vehicles, particularly in complex areas of the car geometry such as the A- and C-pillars, the highly curved rear end, and the wheelhouse region. As a result, actual production car geometries are typically utilized in the actual optimization process. However, these geometries are not widely accessible and, as a result, are not typically featured in the open literature for validation purposes [59], [62]. Therefore, a compromise between the simplified geometries, such as the Ahmed body, and production cars, such as MIRA and DrivAer, is required.

Furthermore, previous studies have shown that a significant contribution to the aerodynamic drag is from the rear end of the body, as shown in Figure 1.1, which dramatically affects the flow features of a vehicle [53]. Therefore, greater focus is put on facilitating an apprehension of the rear end flow behavior to provide a physical understanding of the flow field [10], [11], [54], [61]. The focus of current research is on specific vehicle models that can provide opportunities to investigate rear end effects. In the framework of road vehicle aerodynamics, the work of Ahmed et al. [10] significantly improved the comprehension of the flow around different shapes of road vehicles: it characterizes the critical influence of the rectangular rear end configuration. Since it

represents several vehicle models, significant work has been carried out on this, and become a benchmark model [21].

The Ahmed body [10] is perhaps the most studied generic vehicle model in the literature. Morel [22] classified the Ahmed body, along with the slanted cylinder [63] as one of a group of "critical geometries," showing exclusive flow behavior with some specific geometric parameters such as the slant angle. Thus, the slant angle remains the dominant factor distinguishing the Ahmed model between high and low drag regimes in its current rectangular rear end shape [24], [25]. Figure 2.2 by Choi et al.[53] provides a conceptual representation of the flow structure with slant angles. It possesses a large wake recirculation region characterized by a slant angle of less than 10°. The majority of the studies in this range are conducted at a 0° angle which is known as the square back Ahmed body [57], [64]–[68]. Whereas a slant separation bubble (SSB), counter-rotating longitudinal C-vortices, and wake recirculation region are the significant causes of drag increases between the slant angle of 12.5°-30°. Within this range, the flow has a three-dimensional structure (TDS) that contributes to increased drag (Figure 2.2(b))) and is hence called a high-drag regime. Compared to the 0° (square back) model, the counter-rotating C-vortices increase pressure drag by 50% around a critical angle of 30° [21]. Notably, at 30°, the wake can be first in the high-drag regime and then switch to the low-drag regime, but the duration of the low-drag regime decreases with increasing Reynolds number [69]. Several studies have explored the high-drag regime of the Ahmed body [25], [34], [58], [70]–[77]. A slant angle greater than the critical angle (30°) results in weakened C-vortices that lose energy, and the flow becomes massively separated at a 35° angle. Such separation generates quasi-axisymmetric separated (QAS) flow, which substantially reduces the drag and is considered a low-drag regime [25], [78], [79]. The TDS transforms into QAS flow when enlarged vortices occasionally merge with the base flow, creating a large-scale separated vortex (LSV) [80], [81]. According to the review by Yu and Bingfu [11], most experimental and numerical studies on the Ahmed body are concentrated on the slant angle of 0°, 25°, and 35° only to grasp time-averaged and time-dependent flow structures. Such an approach restricts a comprehensive study of fastback vehicles and the lack of control of drag forces, especially in high-drag slant angles.

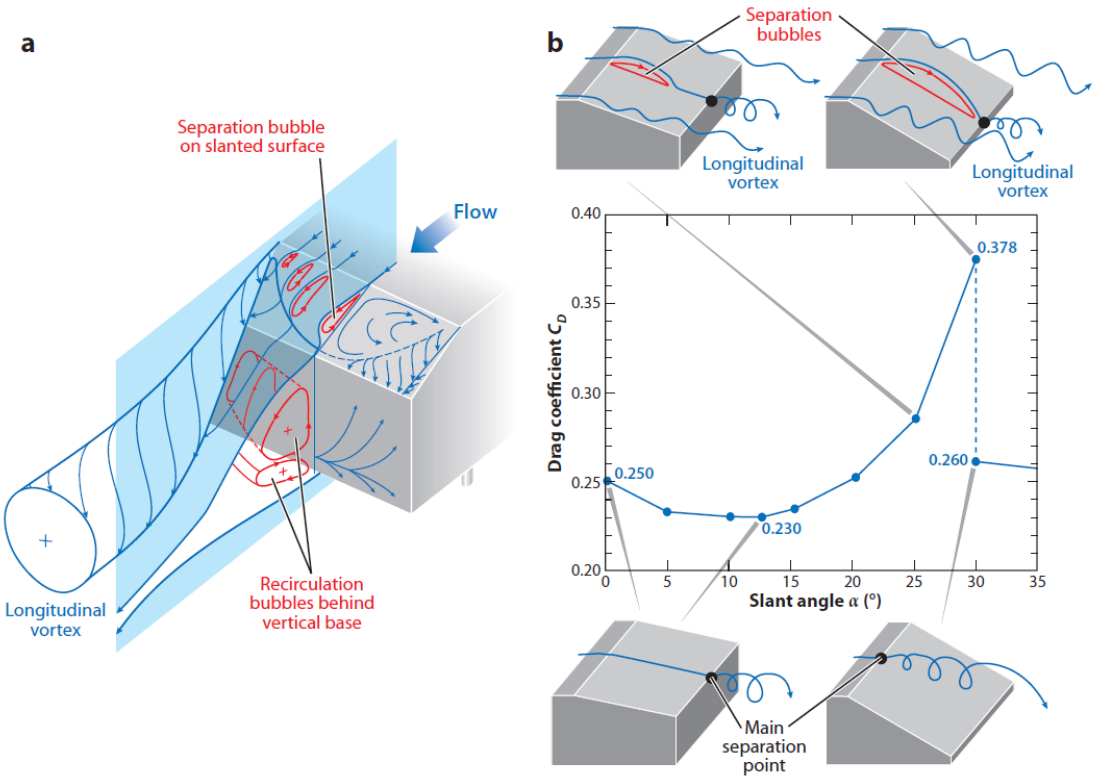

Figure 2.2: (a) Time-averaged three-dimensional flow structures of the Ahmed body in the wake (b) the variation in drag coefficient for different slant angles [53] **(**Reproduced with permission from Annu. Rev. Fluid Mech. 46, 441-468 (2014). Copyright 2014, Annual Reviews.).

However, Sims-Williams [82] studied the slant angles 27.5°and 30° and pointed out that the proximity of the slant angle with the critical angle is more crucial than the absolute angle since the wake structure characteristic frequency is sensitive to the slant angle. Still, they did not discuss the transition mechanism from high to low drag, which was later carried out in [26], [80], [81], [83], [84]. In those studies, a variety of slant angles, ranging from 0^o to 25^o, as well as 27.5°, 29°, 29.5°, 30°, 32.5°, and 35° were studied. In their study, they found that the transition from the TDS to QAS happened due to the occasionally enlarged vortices in the unsteady phenomena that create a large-scale separated vortex (LSV). Another related study [85] performed the IDDES simulations of 25°, 30°, 32°, 33°, and 35° slant angles at a high Reynolds number of 7.68×10^5. Guilmineau [85] characterized the flow features and studied the effect of the slant angle. Thus, in the high-drag region, the slant angle range, $25° < \alpha \leq 30°$, has not been explored in great detail at low Reynolds numbers, such as examining the parameters responsible for the transition from TDS to QAS for the time-averaged flow and the detailed flow structure at low

Reynolds numbers. These high-drag angles will be referred to as the transition angle range (TAR): $25° \leq \alpha \leq 30°$. Therefore, a systematic study of the flow development in the TAR is needed.

In several studies, the Ahmed body is also used as a notchback vehicle [86]–[89]. Furthermore, under crosswind conditions, both the slanted rear surface and the near wake region downstream of the rear vertical base play an important role in the flow dynamics [78]. The development of turbulence flow parameters shows that turbulence rate and velocity fluctuations are significantly high on both the windward and the leeward model side [70]. The effect of crosswind is also studied [90], [91]. There is a significant influence on C-vortices during crosswind conditions. The importance of C-vortices projects serious concerns for the vehicle aerodynamic performance. The creation of SSB over the slant surface is ascribed to the entrainment of the counter-rotating C-vortices [48], which finally coalesce into the wake flow and influence the formation of the URB [73], [77], [79]. It should be noted that such counter-rotating C-vortices are also found in the delta wing [48], [58], and aircraft fuselage [59], influencing drag and stability. In fact, both the Ahmed body and aircraft fuselage are part of much larger critical geometries studied by Morel [22]. Zigunov et al. [94] found two stable flows on the critical Reynolds number of 25,000, a vortex flow pattern, and a fully separated flow at a 45° angle. Furthermore, the existence of LRB in the SAB is responsible for self-soiling at the rear window, which is detrimental to driver vision and electronic equipment such as sensors and cameras [95]–[97].

Although the time-averaged flow structures of the Ahmed body are understood, the instantaneous dynamics are scattered. Various coherent frequencies have been found around the front [98], at the slant [99], [100], at the roof [72], and in the wake [31], [98], [100], [101]. The Strouhal numbers (S_t) over the slant surface of the 25 ° Ahmed body at the symmetry plane have been associated with the K-H instability [98] with an S_t=0.27-0.35 and flapping of the SSB [102] at an S_t=0.11 near the upper edge of slant surface. Whereas S_t=0.18 and S_t=0.33 are also reported [100], [103]. However, a small SSB over the slant surface was found [72] and a predominant frequency of S_t=0.2 throughout the slant surface. A periodical spanwise vortex was created by the roll-up of the shear layer behind the bubble, resulting in S_t=0.2. In addition, these vortices correlate with the

predominant frequency in the middle of the model roof [72]. Based on this, it was concluded that S_t=0.2 emanated from the hairpin vortices at the front-end recirculation bubble at the roof. On the other hand, in the wake of the 25° Ahmed body at the symmetry plane, a range of predominant frequencies S_t=0.48-0.52 was found by different studies [70], [72]. These findings are supported by PIV and flow visualization data [72], which showed a growth-and-burst process of the two recirculation bubbles behind the base. However, it was argued that the hot-wire measurements used in previous studies [72] are not spatially dependent, so such dynamics are implied [71]. Subsequently, the time-resolved PIV data found a dominant frequency of S_t=0.23 in the wake of the 25° Ahmed body [71]. This frequency is ascribed to the alternating contraction and expansion of the C-vortices. In addition, at the rear end of the body, boundary layers separate and form shear layers with a dominant frequency of S_t=2.30. The periodic movement of the C-vortices was not found [72], but a similar bluff body, such as a high-speed train, shows a cyclic process in the C-vortex, as reported in [71], [104].

In addition, flow control methods are also being investigated in the literature to modify the TDS flow structure for better aerodynamic performance, as recently reviewed [13], [105]. Therefore, the high-drag regime of the Ahmed body is still not fully understood, and a better understanding of the TDS flow field is required, which is also recently highlighted in [73], [77]. Specifically, at a 25° slant angle, TDS contributes 64% of pressure drag from the rear end, 30% from the vertical base, and 6% from the forebody [10], [30], [31]. The presence of TDS and unsteady behavior further complicates the study of the 25° slant angle and makes it difficult to understand and control. As a result, the 25° Ahmed body got a lot of attention in the literature. According to the recent review by Yu and Bingfu [106], at low Reynolds numbers, the relevance of the 25° Ahmed body is not fully explored, despite the fact that more than 50 research articles have been published on the topic at medium to high Reynolds numbers. Some of the important experimental and numerical investigations are documented in Table 2.1 and Table 2.2. Several simulation methods have been used in the existing literature [29], [34], [107]–[113]. Table 2.2 provides a summary of the literature on the numerical investigation of the Ahmed body. The investigations were conducted either above 2×10^5 (Range I) or below 0.33×10^5 (Range II) apart from only Kobayashi et al. [80].

Table 2.1: Experimental studies of the Ahmed body.

	Method	Re_h (10^5)	Literature	Slant angle	Model scale
1	Wind tunnel	13.60	Ahmed et al.[10]	0°, 5°,10°,12.5°,15°,20°,25°,30°,35° 40°	1:1
2	Wind tunnel	2.0	Sims-Williams and Dominy [82]	30°	1:1
3	Wind tunnel	2.0	Duell and George [114]	0°	1:0.44
4	Wind tunnel	4.20	Khalighi et al. [115]	0°	1:1
5	Water tunnel	0.30	Spohn and Gillieron [116]	25°	1:0.288
6	Wind tunnel	9.10	Lienhart and Becker [117]	25° and 35°	1:1
7	Wind tunnel	5.90	Sims-Williams and Duncan [118]	25°	1:1
8	Wind tunnel	4.50-7.70	Vino et al. [119]	30°	1:1
9	Wind tunnel	2.30-12.20	Thacker et al. [33], [102], [120]	25°	1:1
10	Wind tunnel	2.90-13.6	Conan et al. [9]	10°,20°,25°,30°,40°	1:1
11	Wind tunnel	8.50	Heft et al. [121]	25°	1:1
12	Water tunnel	0.003–0.40	Grandemange et al. [122]	0°	1:0.25
13	Wind tunnel	1.10	Grandemange et al. [31], [123]	0°	1:0.25
14	Wind tunnel	0.60	Wang et al. [124]	25° and 35°	1:0.33
15	Wind tunnel	0.70	Kohri et al. [26], [83]	0°,12.5°,25°,27.5°,29°,30°,32.5° 35°	1:0.287
16	Wind tunnel	1.60-7.90	Lahaye et al. [125]	0°	1: 0.7
17	Water tunnel	0.14	Tunay et al. [126]	25°	1:0.25
18	Water tunnel	0.14	Tunay et al. [127]	25°, 30°, 35°	1:0.25
19	Water tunnel	0.17	Cadot et al. [128]	0°	1:0.25
20	Water tunnel	0.17	Essel et al. [65]	0°,25°,35°	1:0.18
21	Water tunnel	0.26	Venning et al. [71]	25°	1:0.25
22	Water tunnel	0.30	Venning et al. [129]	25°	1:0.25

23	Wind tunnel	5.90-9.0	Volpe et al. [130]	0°	1:1
24	Wind tunnel	0.50-2.40	Zhang et al. [72]	25°	1:1
25	Wind tunnel	2.20-6.50	Barros et al. [131]	0°	1:1.03
26	Wind tunnel	3.50	Sellappan et al. [77]	25°	1:0.4
27	Wind tunnel	0.30-2.70	Liu et al. [79]	35°	1:1
28	Water tunnel	1.47, 4.31 & 1.90	Present study	25°	1:0.25

The 25° SAB is investigated in 13 studies in Range I, considered to be a high Reynolds number, but only six studies are in Range II, which is considered low Reynolds number studies. Furthermore, the difference between Range I and Range II also lies in the model length scale, where almost all the Range I study used the full-scale model similar to the Ahmed body [10]. However, at a low Reynolds number in Range II, the model used is as small as 1:0.1875 of the square back model (0°) while 1:0.25 for 25° SAB. At first, initial simulations focused on the Ahmed body by Han [132] and when combined with incompressible turbulence models, the $k-\in$ of the turbulence model underestimated the base pressure. Later, using the Reynolds-Averaged Navier-Stoked (RANS) equations, Makowski et al. [133] conducted a detailed analysis of the flow structure over the Ahmed body. More recently, due to the completely separated flow of the 35° Ahmed body, it was observed that the RANS turbulence models successfully anticipated the flow behavior around the body [29]. However, the model was unable to represent the three-dimensional structure associated with the 25° Ahmed body. This problem is often caused by an under-prediction of the turbulent stresses due to an under-accounting of the turbulence produced by non-local, inertial range turbulent structures. Furthermore, an interesting study by Fares [110] used the Lattice Boltzmann method (LBM) to calculate the SAB angle for 25° and 35° and demonstrated that this increasingly popular method could achieve similar results. Thus, overcoming the standard uniform mesh limitation of the LBM by combining regions of embedded refinement and a novel interpolation scheme at a wall, a Very Large Eddy Simulation (VLES) scheme is proposed to model turbulent transport and solve the discretized equations using finite differences.

Table 2.2: Numerical studies of the Ahmed body.

Sr. No.	Method*	Re_h (10^5)	Literature	Slant angle	Model scale
1	LES	42.90	Howard and Pourquie [134]	28°	1:1
2	LBM	9.10	Fares [110]	25° and 35°	1:1
3	URANS	8.90	Guilmineau [29]	25° and 35°	1:1
4	DDES	8.90	Ashton and Revell [109]	25°	1:1
5	LES	8.90	Keogh et al. [108]	25°	1:1
6	LES	7.60	Minguez et al. [98]	25°	1:1
7	IDDES	7.60	Guilmineau [85]	25°,30°,32°,33°,35°	1:1
8	LBM	7.60	Cai et al. [135]	35°	1:1
9	SAS, RANS, DDES, SBES	7.60	Delassaux et al. [34]	25°	1:1
10	LES	7.60	Aljure et al. [136]	25°	1:1
11	LES and DES	7.60	Serre et al. [137]	25°	1:1
12	PANS	6.40	Rao et al. [25]	25° and 35°	1:1
13	LBM	4.60	Lucas et al. [138]	0°	1:1.03
14	URANS	4.10	Khalighi [115]	0°	1:0.347
15	LES	3.50	Osth et al. [139]	0°	1:1.03
16	LES	3.0	Mirzaei et al. [140]	0°	1:1.03
17	LES	2.10	Krajnovic and Davidson [141]	0°	1: 0.43
18	LES	2.10	Krajnovic and Davidson [142]	25°	1:1
19	LES	2.10	Krajnovic and Davidson [143]	25°	1:1
20	LES	2.0	Hinterberger et al. [144]	25°	1:1
21	LBM	0.63	Kobayashi et al. [80]	27.5°	1:0.277
22	LES	0.33	Hesse and Mrgans [145]	0°	1:0.25
23	LES	0.30	Longa et al. [64]	0°	1:0.08
24	PANS	0.30	Mirzaei et al. [140]	25° and 0°	1:1.03
25	RANS	0.27	Corallo et al. [107]	0°,5°,10°,15°,20°,25°,30°	1:1
26	LES	0.14	Tunay et al. [126]	25°	1:0.25

27	LES	0.14	Tunay et al. [146]	25°	1:0.25
28	IDDES	0.14	Kang et al. [147]	0°	1:0.1875
29	SOFV	0.10	Podvin et al. [112]	0°	1:1
30	DNS	0.10	Podvin et al. [113]	0°	1:1
31	LES	0.08	Minguez et al. [148]	25°	1:1
32	PNSE	0.08	Bruneau et al. [149]	0°	1:1
33	PNSE	0.08	Bruneau et al. [150]	0°	1:1

*PNSE: Penalized Navier-Stokes equation, IDDES: Improved delayed detached eddy simulation, LBM: Lattice Boltzmann model, LES: Large eddy simulation, SOFV: Second-order finite volume, PANS: Partial averaged Navir-stokes, URANS: Unsteady Reynolds averaged Navier-stokes, SAS: Scale-adaptive simulation, SBES: Stress-Blended Eddy Simulation, DDES: Delayed detached eddy simulation

There have also been LES studies, again mostly focusing on the 25° case, such as in [98], [108], [136], [137], [142]–[144], [151], [152]. The LES has shown results for front-end and afterbody separation that are on par with studies [108], [145], [162]. Several subgrid-scale models and wall treatments were used in these studies, but many failed to achieve the level of accuracy that one would expect at such a level of closure, despite some being more successful than others. The high-Reynolds number (7.68×10^5) necessitated meshes of up to 48 million cells, although even this falls short of the ideal resolution for a wall-resolved LES [137]. Indeed, in summarising their comprehensive study, Serre et al. [137] indicated the hybrid RANS–LES approaches that are appealing, although mesh generation requires special attention in the RANS–LES interface. It is noteworthy that the TDS of industrial flows at high Reynolds numbers incurs a high numerical cost [34]. It is imperative that LES be used to enable reliable flow simulations. However, LES can become prohibitively expensive computationally, especially for wall-bounded turbulent flows, which exist in the majority of the applications (almost as expensive as DNS) [153]–[156]. Therefore, for wall-bounded flows, in particular, there must be a compromise between the precision of physical modeling and the associated computational cost [157].

Although DNS is the best numerical method to capture the unsteady flow characteristics, it is still too expensive to use in commercial applications.

Subsequently, the Detached Eddy Simulation (DES), a hybrid model introduced by Spalart [158] that combines the RANS and LES, is becoming increasingly popular as a compromised method. Recent review papers highlight the development of such hybrid simulation methods used for both streamlines and bluff body flows [157], [159], [160]. It has been demonstrated through some foundational research that the DES is an appealing method for modeling the 25° Ahmed body, which represents a high-drag slant angle [137]. Moreover, Shur et al. [161] further developed the DES models by combining SST k-ω and Delayed Detached Eddy Simulation into the so-called Improved-Delayed Detached Eddy Simulation (IDDES). This particular model has shown superiority in capturing the flow field in both the TDS and QAS regions [29], [34], [111], [162]–[165]. Hence the IDDES method is employed for the current investigation.

2.2.1 Effect of low Reynolds number

The literature above reveals that the high drag 25° Ahmed body is studied at several high Reynolds numbers using different sizes of the test models. However, the effect of low Reynolds numbers on a scaled model has been studied by only a few. A scaled model with a Reynolds number of 0.14×10^5 was compared by Tunay et al. [70], [126], [127], [146] with a full-scale model at a Reynolds number of 7.68×10^5 by Lienhart and Becker [117]. It was concluded that the wake parameters compared well with the full-scale Ahmed body at the high Reynolds number. Similarly, investigations in [98], [116], [119], [166] also suggest that with minor differences such as velocity magnitude and recirculation size, the flow structure is close to high Reynolds numbers. Hence, the time-averaged large-scale structure [71] and transient nature [27] compare well with the full-scale high-Reynolds number. Further, Avadiar et al. [27] studied the effect of a low Reynolds number over the DrivAer model and found that although the wake structures are close to those of a high Reynolds number ($\leq 0.2 \times 10^6$), the drag coefficients are unlikely to be the same. Instead, the scaled model permits a comprehensive understanding of the time-mean and transient behavior. Despite the SSB and the time-averaged turbulence quantities fitting well with experiments, the drag coefficients differ [27], [137].

The effect of the Reynolds number on the drag coefficient is not well documented in the literature. According to Meile et al. [167], the drag coefficient shows a 13% increase from a Reynolds number 0.7×10^6 to 2.7×10^6 and then becomes almost constant. Thacker et al. [33] indicated a 5% increase in drag from 0.5×10^6 to 4×10^6. However, for the low Reynolds number at 7.31×10^4, Kohri et al. [26] experimentally found around 24% in drag variation at the 25° slant angle compared to the experiments of Ahmed et al. [10] conducted at the length-based Reynolds number of 4.29×10^6 at the same slant angle. This drag discrepancy between high and low-order Reynolds numbers is caused by increased contribution from the skin friction while the pressure drag count remains almost constant [26]. Additionally, the contribution of the skin friction at a low Reynolds number between 3.35×10^4 and 1.10×10^5 is 0.088 compared to the 0.050 reported by Kohri et al. [83], an increase of 0.04 count. Consequently, Avadiar et al. [27] concluded, based on the low Reynolds number study on the DriveAer model, that drag discrepancy at low order of Reynolds number exists for the Ahmed body also. In addition, the LES simulation by Minguez et al. [148] and Tunay et al.[146] over the 25° Ahmed body confirmed that the Reynolds number has no significant effect on the flow topology; nonetheless, it affects the magnitude of the flow parameters [127].

Table 2.3 summarizes existing studies on the Ahmed body at low Reynolds numbers. As shown, the studies by Cadot et al. [128], Essel et al. [65], Kang et al. [147] and Tunay et al. [126] have comparable Reynolds numbers. On the other hand, the studies by Grandemange et al. [122] have much lower Reynolds numbers.

Table 2.3: Summary of low Reynolds number studies over the Ahmed body.

Sr. No.	Method	Re_h	Title	Slant angle	Model scale
1	Exp.	8300	Spohn & Gillieron [116]	25°	1/3.5.
2	Num.	8275	Bruneau et al.[149]	0°	1/0.288
3	Num.	8275	Bruneau et al. [150]	0°	1/0.288
4	Num.	8322	Minguez et al. [148]	25°	1
5	Exp.	340, 410	Grandemange et al. [122]	0°	1/11.0.
6	Exp.+ Num.	14800	Tunay et al. [126]	25°	1/4
7	Exp.	14800	Tunay et al. [127]	25°,30°, 35°	1/4
8	Num.	10000	Podvin et al. [112]	0	1
9	Exp.	14000	Tunay et al. [70]	25°, 35°	1/4
10	Num.	14000	Kang et al. [147]	0°	1/5.33
11	Exp.+ Num.	14800	Tunay et al.[146]	25°	1/4
12	Exp.	17000	Cadot et al. [128]	0°	1/4.
13	Exp.	17000	Essel et al. [65]	0°,25°,35°	1/5.3
14	Exp.	26000	Venning et al. [71]	25°	1/4
15	Exp.	30000	Venning et al. [129]	25°	1/4

Num. – numerical; Exp. – experimental

Therefore, low Reynolds numbers reproduce the flow topology of the high Reynolds number at a significantly low cost and time. On the other hand, the flow features found at low Reynolds numbers over the Ahmed body have been reported on the real cars with significantly higher Reynolds numbers. Recent efforts have focused on identifying and analyzing the wake bistability of more realistic cars [8]. Bonnavion et al. [8] investigated bistability in two full-scale vehicles and reported that both showed bistability. According to them, one of the vehicles was characterized by an inversion of its vertical gradient during formation. As a result of its large height-to-width ratio, the authors believed that the mechanism was likely similar to the one found in square-backed Ahmed bodies [168]. These bistabilities are found at really low Reynolds numbers [31], [122]. Therefore, it

encourages further investigation to provide a better understanding of the flow structure at low Reynolds numbers.

However, with few studies at the low Reynolds number, time-averaged and unsteady flow features of the Ahmed body are still not completely understood. For example, Minguez et al. and Serre et al. [98], [137] performed accurate LES simulations capturing all the major flow features. Nonetheless, the drag coefficient is overestimated by 40% compared to the experiment. Although they found that the flow topology, including separation-reattachment at the slant surface and time-averaged and turbulence quantities, fit well with the experiment, the drag coefficient deviates. Contrary to what the experiment predicted, the behavior of this coefficient does not reflect whether the flow over the slant matches the experiment. Serre et al. [137] argued that it is related to the big recirculation region at the front-end separation, specifically the low Reynolds number. This front-end recirculation is also reported by Spohn & Gillieron [116]. Furthermore, the existence of the slant separation bubble was not captured at the Reynolds number of 2×10^6 using the unsteady simulation by Rao et al. [25]. They found the QAS without the SSB. Nonetheless, the non-existence was attributed to the low Reynolds number effect referencing studies conducted by others [83], [107], [127], [169]. In all these studies, the SSB did not appear, contrary to the experiments [10], [33], [170]. However, as stated earlier, the existence of an SSB has been proved in Minguez et al. and Serre et al. [98], [137] at a low Reynolds number in line with a full-body experiment at a high Reynolds number. Furthermore, there are only two studies [126], [146] which investigated the spectral analysis and documented the Strouhal number at the low Reynolds number. Similarly, model decomposition methods like proper orthogonal decomposition (POD) and dynamic mode decomposition (DMD) are not used to investigate the wake flow features at the low Reynolds numbers, which provide important flow information. Consequently, there is a need to document the Ahmed body flow features at the low Reynolds number.

2.2.2 Rear surface contamination and recirculation bubble

Vehicle rear surface contamination (RSC) has been documented to be affected by recirculation bubbles in a few studies [171]. The extraction and dispersion of particles, aerosols, mineral dust, and soot particles towards the rear surface and windows have been

shown by some existing studies to be affected by unsteadiness and wake structures at the rear of vehicles [172], [173]. The scope of such surface contamination can be seen in Figure 2.3. The wake ring vortex is a part of the recirculation region which is shown by the dashed white line. Given the significance of autonomous vehicle and their heavy dependence on sensors for navigation, clear optical vision is critical and so controlling soiling and surface contamination is a necessity. Nonetheless, with few studies in this direction, the relation between the recirculation region and surface contamination is the current research focus that is expected to dominate the road vehicles of the future.

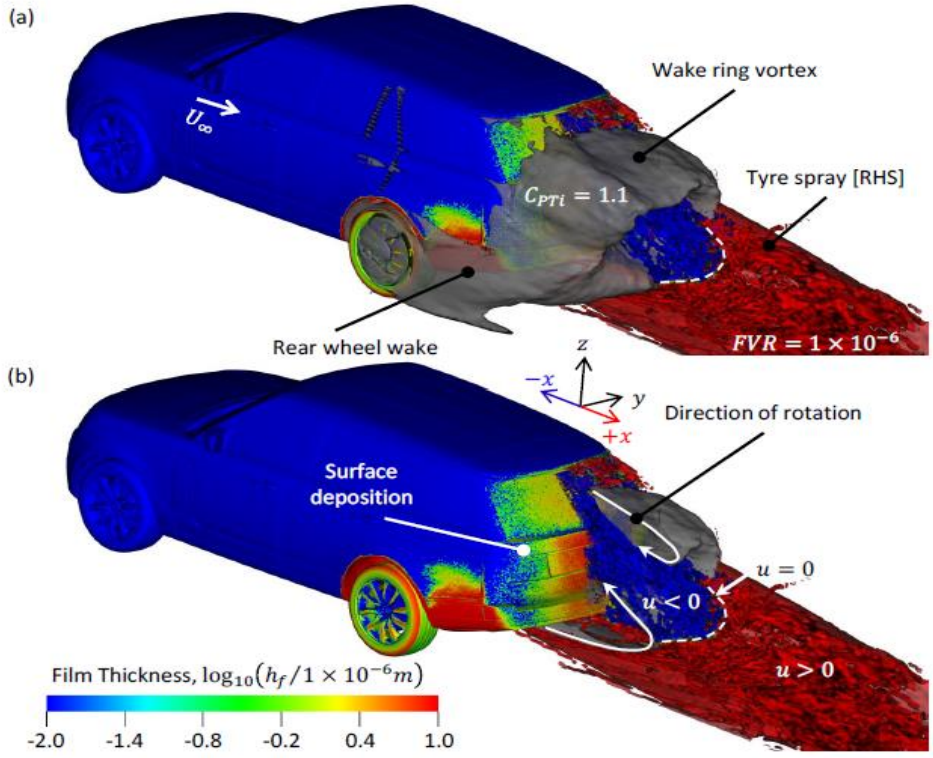

Figure 2.3: Rear surface contamination Rear Surface Deposition Process: (a) Wheel Wake and Ring Vortex Interaction, (b) Spray Capture by the Ring Vortex and its Effect on the Spray in the [95].

2.3 Flow Control

Flow control methods are divided into four important categories. This section discusses previous important studies related to them in the subsequent subsections.

2.3.1 Aerodynamic devices

Aerodynamic devices are broadly categorized into active and passive. Several active devices have been used in the literature, including movable underbody diffusers, steady blowing, steady suction, plasma actuators, and synthetic jets, as shown in Table 2.4. However, active devices require external energy and electronics to function. On the other hand, passive devices provide comparable drag reduction, are easy to implement without any extra energy, and work as an add-on component, making them simple.

Table 2.4, indicates that, in comparison to other passive devices, flaps offer superior drag reduction. For instance, using small rectangular flaps at the slant surface edges, Beaudoin & Aider [21] were able to achieve a 25% reduction in drag on a modified Ahmed body with a 30° slant angle. Such a mechanism made the flow fully separate at the slant and reduced the C-vortex emanating from the side edges. Similarly, Fourrie et al. [174] used a small bent plate as a deflector over the 25° slant Ahmed body and achieved a 9% drag reduction by modifying the C-vortex. Tian et al. [175] conducted a study on the 25° and 35° slant Ahmed body to analyze the impact of flaps. The findings demonstrated that the use of flaps resulted in a significant drag reduction of 21.2% for the 25° Ahmed model, while the 35° Ahmed model only experienced a 6% reduction in drag. Based on the works of Beaudoin et al. [21] and Fourrié et al. [174], another study [176] focused on implementing the flap at the side edges and the top edge of the slant surface over the 25° Ahmed body. However, this investigation found the best flap installed at the top edge of slanted surfaces achieving 11.8%. Similarly, vortex generators are the other alternative for the passive flow control applied to the Ahmed body. Aider et al. [177] installed vortex generators over a modified Ahmed body providing a curve at the slanted surface. Usually, vortex generators are used to delay flow separation; nonetheless, in this case, it creates an early separation that leads to massive flow separation. It established a rather extensive recirculation bubble by preventing the longitudinal vortices of the side edges. Such a mechanism had given a 12% of drag reduction. Furthermore, it was mentioned that the

relative parameters of the vortex influence the flow field. Similarly, another vortex-type mechanism was applied to the 25° Ahmed body in the form of small circular cylinders [177], [178].

Table 2.4: Active and passive aerodynamic devices. Here Exp.= Experiment and Num.= Numerical.

Flow control Method	Investigation method	Device	Drag reduction	References
Active device	Num.	Movable underbody diffuser	4%	Kang et al. [179]
	Exp.	Steady blowing	1%	Einemann et al. [180]
	Exp.		6 to 10.4%	Mestiri et al. [181]
	Num.		20%	Rouméas et al. [182]
	Exp.		6.4%	Wassen & Thiele [183]
	Exp.		5.7%	Krentel et al. [184]
	Num.		11.1%	Wassen et al. [185]
	Exp.		9-14%	Aubrun et al. [186]
	Exp. and Sim.		2.6%	McNally et al. [187]
	Exp.		29%	Zhang et al. [28]
	Exp.	Synthetic Jets	4.29%	Park et al. [188]
			8.5%	Kourta & Leclerc [189]
			10%	Tounsi et al. [190]
	Exp.	Pulsed Jet	6 to 8%	Joseph et al. [100]
			20%	Gilliéron et al. [191]
			20%	Gillieron & Kourta [192]
	Exp.	Steady suction	17%	Kourta & Gilliéron [193]
			6%	Lehugeur et al. [194]
			9.5%	Wassen & Thiele [195]

			10%	Whiteman & Zhuang [196]
	Exp.	Plasma Actuator	8%	Boucinha et al. [103]
			3.65%	Shadmani et al. [197]
			20%	Khalighi et al. [198]
Passive Flow Control	Exp.	Vortex Generator	12%	Aider et al. [177]
	Num.		2.2%	Kim & Chen [199]
	Exp.		10%	Pujals et al. [200]
	Num.		10%	Filip et al. [178]
	Num.		11.7%	Krajnović [99]
	Num.		10%	Mazyan [201]
	Exp. and Num.		4.53%	Shankar & Devaradjane [202]
	Num.	Spoiler	5%	Kim et al. [203]
	Exp.	Flaps	25%	Beaudoin & Aider [21]
	Exp.		19%	Kim et al. [204]
	Exp.		21.2%	Tian et al. [175]
	Num.	Body modification	10%	Marklund et al. [205]
	Num.		8.4 %	Cho et al. [206]
	Num.		5.639%	Song et al. [207]
	Exp. and Num.		13.23%	Hu et al. [208]
	Num.		5.20%	Wang et al. [209]
Combined Active and Passive	Num.	Blowing jets with a porous layer	30%	Bruneau et al. [150]

This cylinder creates coherent streamwise vortices and throws a high-momentum flow that precludes the formation of the separation bubble at the slant surface. It also shows a 10% drag reduction. The attached flow was also achieved by rounding the top edge of the slant surface by Thacker et al. [33] which provided a 10% drag reduction. Some of these devices are shown in Figure 2.4.

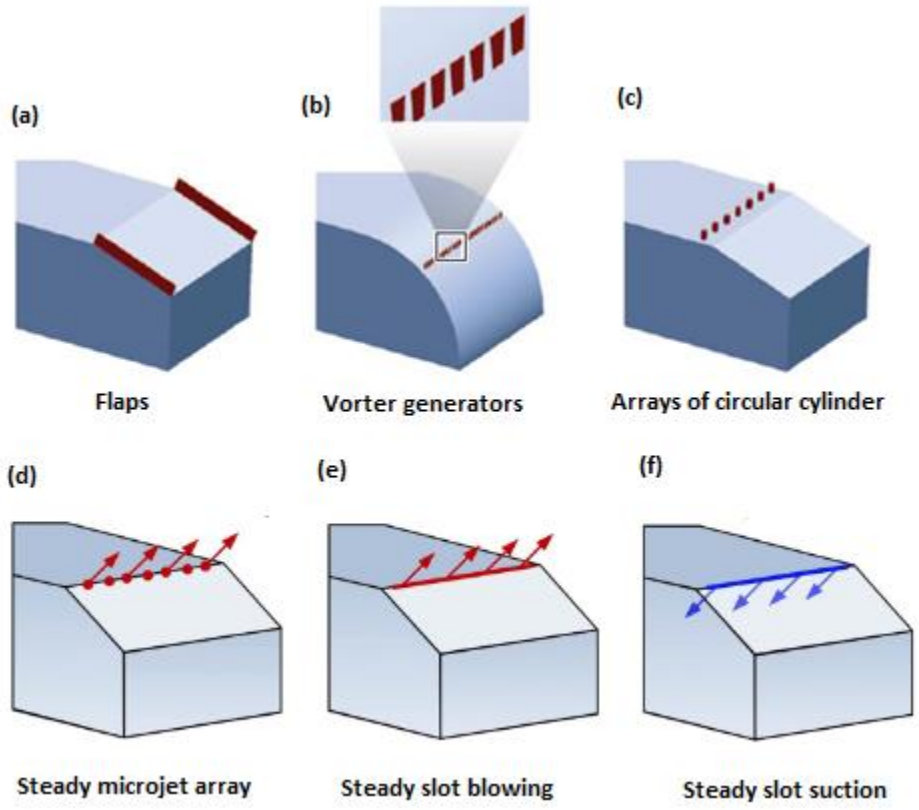

Figure 2.4: Aerodynamic devices attached to the Ahmed body. Here (a), (b), and (c) are the example of passive devices[53] while (d), (e), and (f) are the example of active devices[13].

The aerodynamics of vehicles, especially race cars, do not focus only on aerodynamic drag reduction but should also improve downforce. It is known that downforce on a road vehicle can be created through the use of the underbody shape of a vehicle, and hence, the application of underbody diffusers [210]. Ehirim et al. [211] reviewed the recent development of diffusers and the physical understanding of drag and downforce. Several recent studies have proposed new solutions for drag reduction with diffusers, including Huminic et al. [212] and Rossitto et al. [35]. Taiming et al. [213] studied the effect of a single-channel rear diffuser on the aerodynamic drag and reported a 5.3% drag reduction with a vertical diffuser at 10.46°. Similarly, non-flat underbody diffusers were studied by Huminic and Huminic [214]. While using circular and elliptical surfaces, they reported a 20% of downforce increment. In addition, a parametric study was performed on the effect of the diffuser angle on a square back and slanted Ahmed body by Buscariolo et al. [215]. They found that the slanted Ahmed body provides peak downforce at 20°, and for drag, it

is 30°. Similarly, Saleh and Ali [216] achieved a 2.47% drag reduction by modifying underbody-diffuser slice modification.

However, only flaps have high drag reductions, but the implementation of flaps is questionable since they add extra weight, add-on devices need fixing, and are aesthetically not attractive. Secondly, the study of Beaudoin & Aider [21] used the SAB at a much higher slant angle of 30°. Thirdly, the expected drag reduction of ~25% can only be accomplished by a collection of flaps around each side of the slant surface and the vertical base. Thus, the total number of flaps is up to 8, which is tedious to implement. According to the literature [13], the only method that has achieved a drag reduction of around 29% is using the active flow control steady blowing by Zhang et al. [28]. Nonetheless, the use of energy still did not completely avoid the longitudinal C-vortices, and the LRB still remains.

2.3.2 Shape modification

As a result of traveling at high speeds, vehicles create complex external flow patterns that include eddies, pressure gradients, and suction effects. Automobiles generate significantly different external flow patterns from aircraft wings, in part because they have different shapes, particularly at the rear. By manipulating the shape of an automobile, it is possible to control the external flow pattern, increasing its aerodynamic performance significantly [59]. Aerodynamics is influenced by two main factors. The first factor is geometric, as the area subject to aerodynamic force increases with the size of the outer surface of the car. Another is concerned with flow detachments and vortices [217]. Moreover, the exterior structure of the car and the components added to it impact drag, force, and moment. Throughout the vehicle, it is essential that surfaces intersect smoothly. When the styling direction has been established, the aerodynamic characteristics will roughly follow. Therefore, it is only through detailed shape optimization and the development of add-on parts that aerodynamic performance can be improved [218]. The trunk lid level and rear diffusers of high-performance cars are optimized, and the rear end flows properly [218]. Howell [219] investigates the aspect ratio of the slanted rear surface on the aerodynamic forces in detail. Gilhaus and Renn [220], Buchheim et al. [221] and Howell [219] examined how automotive shapes affect aerodynamic forces. Although these

studies did not make a serious inquiry into the physical mechanism of changes in the aerodynamic forces, they stress the importance of shape modification.

The external flow can be controlled by modifying the vehicle shape using curvature at the rear end. Depending on the radius at the transition between the windshield and roof and the roof to the rear window, the curvature at the rear end has a favorable effect [218]. The focus on reducing drag through shape optimization is growing. Despite this, most aerodynamic analyses of cars have been conducted on simplified models with sharp rear edges [10], [219], [222]. There has not been much discussion regarding rear edge curvature and aerodynamic performance until recently [32].

Morel [22] argued that the Ahmed body is a part of larger specific geometries called `critical geometries,' which show exclusive flow behavior at some specific geometric parameters. There is no monotonic relation between the drag force and some specific parameters, and the slant angle is one of those critical parameters. The slant angle is the primary characteristic distinguishing between the high and low drag modes in basic sharp edge rectangular afterbody design [24], [25]. Recent developments, however, modify the sharp rear-edge by rounding it. The idea of rounding the edges was first highlighted by Gilhaus & Renn [220] while studying the effect of geometric shapes on drag and driving stability. In contrast to the sharp rear edge, a rounded trailing edge provides up to 8.2% drag reduction over a fastback model. This study did not investigate the physical mechanism of drag reduction. It was emphasized that drag reduction should not compromise vehicle stability, and hence, the flow control mechanism needs to consider stability. Gohlke et al. [217] carried the rounded-edge theme again by rounding the A-pillar of a mini-van model. It shows local effects but, at the same time, contributes to the side forces. The side forces increased since the A-pillar vortex shifted towards the model side surface compared to the sharp edges. Thacker et al. [33] implemented the same idea over the 25° Ahmed body by rounding the sharp edge of the slant surface. It led to the flow separation suppression that reduced the drag by 10%. The displacement of vortical wake toric vortices downstream is associated with reduced drag caused by the intricate interplay among separation bubbles at the slant and recirculation at the base. However, the mean location of the longitudinal vortices is not impacted and remains spatially stable. Moreover,

rounded-edge application on a rear pillar (slant side edge) is performed as well on the Davis model. It provides striking physical modifications with an 11% drag reduction [223]. The rounding edges weaken the trailing vortices that further modify the wake structure. The flow field is more unsteady than the sharp edges and is detrimental to the dynamic stability of the vehicle. Nonetheless, [34], [35] studied the rounded-edge over the 25° Ahmed body by rounding the top and side edges of the slant surface. While a 16% reduction was reported with top edge rounding, side edges did not improve drag. The suppression of the separation and extension of the recirculation region is the major cause of the reduction. This result contrasts with Fuller & Passmore [223], who reported that it was the side edge rounding that provided drag reduction. Since both the Davis and 25°Ahmed body models represent fastback models, the flow structures with small modifications are naturally different. Hence, the Ahmed body is not exclusive in symbolizing the fastback flow structures. The effect of side edge rounding was further investigated on a realistic fastback model [35]. It increased the local drag and counter-balanced the pressure recovery achieved at the slant surface. Therefore, the side edge rounding is inefficient, at least for fastback vehicles. A recent study by Delassaux et al. [34] implemented the same idea and model. They found that the top edge of the slant surface provides a 16% drag reduction, but the side edges remain detrimental. However, it is beneficial for lift increment. Also, the rounded-edge is studied on a notchback model by rounding the top edge of the slant surface [89]. The bi-stability is suppressed due to rounding the edge and is a function of the Reynolds number and radius of curvature.

Furthermore, the idea of curvature as a method of shape modification at the rear end exist in Zigunov et al. [224] studied recently over the slanted cylinder at 20°, 32°, and 45° angles. This particular model represents the aircraft fuselage with an upswept afterbody. The flow features of such a model are close to the high-drag Ahmed body with a pair of counter-rotating vortices and slant separation bubbles. Since both cylinder and Ahmed bodies are sensitive to the slant angle, they represent critical geometry [22]. However, the model used by Zigunov et al. [224] has a distinct feature of slant surface that is necessary for the aircraft fuselage- the elliptical slant surface. A horseshoe vortex resulting from a smooth transition between counter-rotating vortices and a separation bubble is said to be

the striking feature. The contribution towards drag and lift is not reported, but a flow field modification provides criteria for further analysis within critical geometry.

Therefore, the concept of curvature represents a geometric customization that affects the flow field around the slanted fuselage. In the current thesis, the same idea of elliptical curvature is used to propose a new flow control method over the Ahmed body. A few examples of shape modification are shown in Figure 2.5.

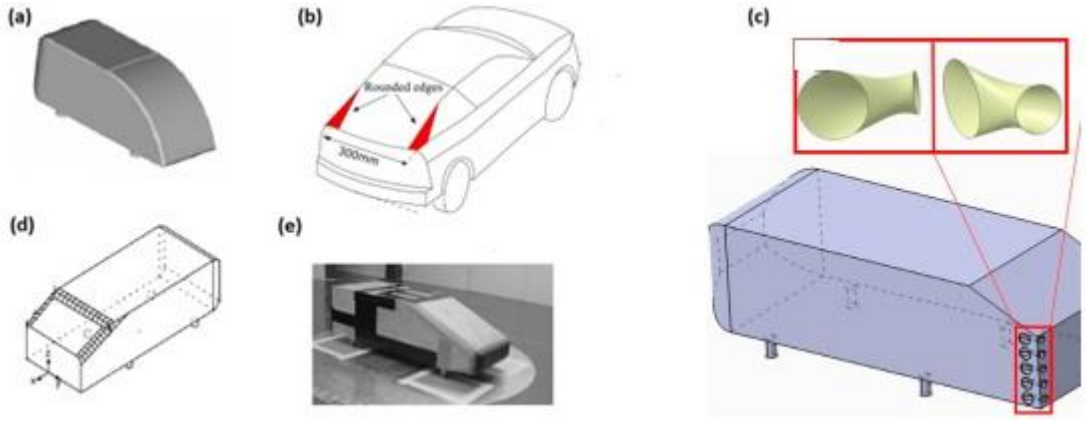

Figure 2.5: Some examples of shape modification Here (a) Aider et al. [177], (b) Rossitto et al. [35] (c) Mohammadikalakoo et al. [225], (d) Rossitto et al. [32] and € Howell & Good [7].

2.3.3 Surface modification

The surface modification here means to amend the surface morphology of the body. It can be done with several methods; however, this research was motivated by the observations made about the natural world. Reif and Dinkelacker [226] were the first to discover the complex shape of the sharkskin micro-grooved surfaces that reduce drag in turbulent conditions. The reason behind this drag reduction is the thickness of the viscous sublayer. If the thickness is greater than the roughness of the contact surface, then these rough surfaces will be immersed into it; hence the friction is transformed into viscous resistance [227]. The structure of sharkskin evolved with micro-grooved structures that consist of riblets. It was suggested that these grooved surfaces are the reason for reduced viscous drag and turbulence intensity.

Walsh [228], [229] reported a maximum of 8% drag reduction due to longitudinal grooves of shark skin riblets. They kept the dimensions of grooves in the same order as the

turbulent wall streaks and bursts. Also, the optimum rib shape is a sharp peak groove with valley curvature. The effect of riblet parameters that can affect the hydrodynamic has been developed. The viscous sub-boundary layer due to the longitudinal rib of the shark has been theoretically analyzed [230]. The theoretical calculation predicted the origin of the velocity profile from the riblets. It lies below the tips of riblets, in general, 10-20% distance of rib spacing, called the `protruding height' theory. Later, 5-8% drag reduction was improved by Becheri et al. [231] to 10% compared to smooth surfaces through oil tunnel experiments. By taking inspiration from nature, sharkskin riblet has then been modified to suit engineering problems. Nugroho et al. [232] reported the experimental results in converging-diverging riblets in the turbulent boundary layer with zero pressure. Due to large-scale periodicity in the turbulent boundary layer in the spanwise direction, the boundary layer thickness is significantly affected. Hence, the local mean velocity increase and turbulent intensity decrease making the boundary layer thin. Taking the same line of research, CUI et al. [233] recently investigated the effect of streamwise riblets in turbulent boundary layers with particle image velocimetry. They found a reduction in friction velocity, and Reynolds stresses inside the turbulent boundary layer, hence reporting drag reduction. The correlation between hairpin vortices and momentum distribution is that increase in streamwise riblet surface decreases the hairpin vortices. These are in contrast with the smooth surfaces. Similar studies have been reported in this direction, making sharkskin riblet an undisputed technique to reduce drag reduction [234]–[239].

However, the effect of riblet cannot be understood until all the factors affecting the movement of sharks are known. Lang et al. [240] investigated the existing proposals that sharkskin can bristle their scales while in motion. The experiment showed an increase in momentum close to the slip area that forms above the scales. Hence, the increase in velocity can be attributed to boundary layer control that is due to separation control. This is a separate issue to be explored. Lang and colleagues [236] brought a different perspective that deals with the angle of attack over sharkskin scales. The angle of attack is a highly influential factor in reducing drag and turbulence intensity. The scales change with swimming conditions. They also stated that the sophisticated morphology of the scales behaves as a super-hydrophobic surface with a contact angle of more than 150°. This creates boundary slipping at the interface of fluid-solid, which can reduce the velocity

gradient along with resistance due to the viscous effects. One more critical point is the working of nanochain mucus that stretches within the boundary layer creating a more stable and steady flow. They also highlighted the variation of shark riblets throughout the body and found no similar second rib on the entire surface. Domel et al. [241] designed a new kind of riblet inspired by denticles that have shown significant improvement in the aerodynamics of the wing. This inspired device can improve the drag-to-lift ratio by 323%, which outperformed the existing vortex generators at a low angle of attack.

By focusing on the shortfin mako shark, Patricia et al. [242] designed structures from the dorsal fin. The dorsal fin has somewhat different structures than the body, and the mimicked designed structure was rounded, semi-rounded, and long. They have found the best drag reduction with rounded and long denticles. The lowest drag coefficient of 0.011 was recorded for long and rounded at a 9.5º angle of attack with 5 m/s speed. Simulation and experimental studies have been undertaken by Zhang et al. [243] to see the effect of the micro-grooved surface on the blade of an air engine. They found that a micro-grooved blade has a higher drag reduction performance than the un-textured. They also optimized the position of texture on the blade surface. A bunch of application-oriented investigations have been done inspired by riblets [237], [244]–[249]. Similarly, the protrusions at the surface of sailfish were investigated for friction drag reduction [250]. They found that there was no significant improvement in the drag by the riblets of sailfish. The reported skin friction drag reduction was only 1%. This is in contrast with the improved aerodynamic performance of the shark riblets.

2.3.4 Hydrophobic coatings

On the other hand, the original inspiration for the superhydrophobic coatings came from the unique water-repellent properties of the lotus leaf [251] as well as the leaves of other plants [252]. Surfaces that are described as superhydrophobic tend to have very large contact angles and low contact angle hysteresis. It is not surface chemistry that makes coatings hydrophobic or superhydrophobic, but its surface roughness at the micro- or nanoscale [253]. Unlike most plants, lotus leaves have tiny protrusions covered with waxy crystals. The lithographically manufactured superhydrophobic surfaces use precisely patterned micron- or nanometre-sized ridges or posts [36], [38], [254]. It is reported that

water penetrates the surface corrugations in the Wenzel state [255]. Cassie's state [256] is characterized by a small-scale surface roughness that lacks hydrophobic coating, which prevents water from moving into the space between the peaks of the surface. An air-water interface is therefore formed between the peaks in the roughness of the surface.

The water-repellent characteristics of lotus leaves served as the initial inspiration for the superhydrophobic coatings. The lotus leaves [257] and other plants [258] are characterized by extraordinarily large contact angles but low contact angle hysteresis. The trapped gas also causes a partial slip by forming an air-water interface between microfeatures. In some studies, the no-slip conditions were switched to partial-slip conditions to understand the effects better. For example, a direct numerical simulation (DNS) was conducted in both slip-free and non-slip conditions [259]. The researchers discovered that the slip length largely determined the amount of drag reduction. However, despite significant efforts, surface modification has only had sporadic success in wider engineering applications, especially when applied to bluff bodies.

The impact of HPS/SHPS on internal channel flow has been the subject of many investigations [260]. The reduced drag and slip are associated with a greater amount of shear-free air-water interface. Experimental research on the hydrophobic coatings in turbulent channels has also shown that the drag is reduced by about 50% in the turbulent regime [261]. It is also claimed that the decrease in drag rises with the Reynolds number before reaching an asymptotic value. Aljallis et al. [262] demonstrated, using a super hydrophilic flat plate, that the skin friction drag reduced the turbulent boundary layer flow. Direct numerical simulation (DNS) and large eddy simulation (LES) were used to examine the exterior flow across a hydrophobic cylinder for Reynolds numbers 300 and 3900 [259]. It was discovered that the root-mean-square (r.m.s.) lift coefficient and mean drag values of a microscale circular cylinder with the hydrophobic coating decreased. The delay in separation during laminar vortex shedding decreases skin friction, but during shear layer transitions, it reduces drag. The effects of partial slip on the shedding frequency of the wake of a circular cylinder are investigated using DNS [263]. They found that the frequency of the shedding increased with the slip. Additionally, the vortex intensity, drag, and lift were reduced near the wake, while the vortex shedding was delayed with the slip.

In addition, superhydrophobic coating, for example, can delay vortex shedding and reduce drag [264], [265]. Surfaces that are superhydrophobic promote vortex shedding and early roll-up. It has been demonstrated that partial slip occurs on various superhydrophobic coatings for Reynolds numbers of up to 10000 [264]. There was a significant difference in the flow behavior depending on where the ridges were aligned in the flow direction within the superhydrophobic coatings, which means that shedding frequency occurs more frequently than on a smooth circular cylinder. A ridge aligned in the flow direction exhibits higher shedding frequencies than one aligned in the normal direction. Researchers observed diminished vortex shedding and elongated recirculation bubbles from a highly hydrophobic cylinder [264]. A circular cylinder oscillation induced by the superhydrophobic coating was measured with Reynolds numbers ranging from 1300 to 2300 [266], and it was reported that slip reduced the amplitude and lift of the oscillating cylinder. In addition, the length of the bubble and the width enlarged, but to the contrary, the intensity of the vortices was reduced, similar to the lift coefficient.

Furthermore, experimental studies were conducted on the hydrophobic circular cylinder coated with sand by Brennan et al. [267] at Reynolds numbers up to 1.4×10^4. It was found that Cassie-Baxter sand coatings significantly reduced drag compared to Wenzel coatings by 28%. As a result of the plastron's thickness and protrusion's height, there is a reduction in drag. In a study by Kim et al. [37] hydrophobic microparticles were sprayed on a cylindrical surface, while another cylinder was roughened with Teflon. The cylinder wake was studied based on the gas fraction, particle size, and direction of surface slip at Reynolds numbers of $0.7 - 23 \times 10^3$. Their observations suggest that the delay in separation and early roll-up of the vortices are due to the turbulence in the wake and shear layer. In a recent study [268], a drag reduction of 40% was found over the superhydrophobic hydrofoils at a 15° angle of attack was reported. In addition, Sooraj et al. [42] studied the effect of the superhydrophobic coating over a circular cylinder and found an increase in the TKE and Reynolds shear stresses for the superhydrophobic cylinders. The onset of vortex shedding is also delayed for the superhydrophobic surface cylinder, and they found a 15% drag reduction at a Reynolds number of 860. They highlighted that the superhydrophobic coating affects the cylinder differently while having different flow regimes. Furthermore, backward-facing steps are studied by Zeinali et al.

[44] at different Reynolds numbers. The superhydrophobic coating reduces the drag coefficient by 25% and 46% at Reynolds numbers of 400 and 2000, respectively. Additionally, the Strouhal number is augmented as a result of the modification of the recirculation region.

However, the effect of HPS on 3D bluff bodies has found limited attention. For example, using LES, a sphere was studied by Zeinali et al. [44] at different Reynolds numbers based on the HPS slip. They found that HPS reduced the drag coefficient by 25% and 46% at Reynolds numbers 400 and 2000, respectively. Additionally, the Strouhal number is augmented by 25% as a result of the prolonged recirculation region. Another study by Jetly et al. [269] implemented HPS (1-2μm air layer) on a metallic sphere in a water tank. They found that even with such a small air layer, approximately 80% drag reduction is achieved between Reynolds number 10^5 and 3×10^5. It is associated with the shifting of the separation point to the rear, which leads to decreased pressure drag. Additionally, recently a DNS study conducted by Mollicone et al. [270] investigated the effect of the HPS around a 3D bump representing a bluff body. The form drag was found to be reduced due to the HPS. The dimensions of the separation bubble decreased by up to 35% as a result of the delayed separation point. This is attributed to the significant modification of the production mechanisms of turbulent kinetic energy caused by the HPS.. However, Choi et al. [4] highlighted that 3D bluff bodies having a fixed separation point change the flow behavior from the boundary layer to wake flow which is substantially different from the moving separation point in the cylinder and sphere with Reynolds number. Therefore, depending on the nature of the flow separation in the bluff bodies, different strategies need to be developed for flow control. Although there are studies on simple bluff bodies such as cylinders [42], [43] and spheres[44], [269], the effects of the hydrophobic coating on complex 3D bluff bodies have not been attempted as far as the authors are aware.

In this regard, the extensive literature available on the standard Ahmed body (SAB) [10] is of relevance because the SAB not only shows the rich TDS but also it belongs to the same class of ‘critical’ geometries that Morel [22] described, as showing sharp flow pattern transitions depending on the rear slant angle. The flow around submarines produces

similar flow features to the SAB at the rear end, which are found to encounter significant resistance in water [14], [22]. There are other underwater applications of 3D bluff bodies, including underwater energy harvesting [271], large bluff body structures, such as caisson structures or oscillating water columns (OWC) and wave energy converters (WECs) [16] and underwater energy storage[17]. Therefore, the development and study of HPS on the flow features of the Ahmed body have tremendous significance in the bluff body flow control domain, especially in underwater applications. Furthermore, the effect of the hydrophobic coating around a complex 3D bluff body based on the nature of the flow separation at the rear end, having fully separated and attached flow, has not been attempted so far, which is significant in creating flow control methods.

2.4 Summary of the Literature

Road vehicles are bluff bodies, and understanding their flow behavior is necessary to develop flow control methods to improve their aerodynamic performance. Since the flow around road vehicles is extremely complex, simplified generic vehicle models have been developed to examine the changes in wake flow features. Within the generic vehicle models, the Ahmed body is perhaps the most studied model and has extensive data available in the open literature for verification and validation. At a 25° slant angle, the wake at the rear end of the Ahmed body is a combination of the slant separation bubble, longitudinal C-vortices, and a wake recirculation region. In terms of its contribution to aerodynamic drag, this model has a 64% contribution from pressure drag by the slant surface, 30% by the vertical base, and 6% by the forebody [10]. The synthesis of the literature suggests that understanding the time-averaged and time-dependent wake flow features at the rear end TDS is of critical importance to develop flow control methods to control drag and minimize surface contamination.

The Ahmed body as a representative 3D bluff body, provides flexibility to study the complex turbulent flow structures at the rear end. This inspired several specific studies focusing on each component of the TDS differently, namely the suppression of the SSB [34], [170], elimination of C-vortices [272] and modification of the wake recirculation region [28], [273]. In general, several flow control methods have been applied to attain drag reduction, as reviewed in the literature [13], [53], [274].

Similarly, shape modification using rounded side edges and smoothing the blunt edges have also been found to provide positive aerodynamic effects. However, as pointed out by Zhang et al. [28], most of the studies in the literature developed flow control methods by concentrating on any one out of the three important components of the TDS. Such methods not only isolate the possible influence of the interaction among the components but can also have a detrimental effect due to a lack of understanding of the flow structure interactions. For example, based on a realistic fastback model, the rounded-edge of the side edges was examined by Rossitto et al. [35] and reported that the local drag increased, and the pressure recovery was counterbalanced at the slant surface. In addition, the existence of rear window soiling is attributed to the formation of the LRB. Hence, the characterization of the interaction mechanism of the flow features should also add to the mitigation of soiling phenomena since it is detrimental to the performance of optical sensors used in the emerging area of autonomous vehicles [97], [275]. Finally, the literature revealed a few studies on the impact of the hydrophobic coating around simplified 2D bluff bodies such as cylinders and spheres, but there is no study on the complex 3D bluff body flow structures. Especially using the Ahmed body which is a simplified 3D bluff body but produces the complex TDS at the rear end.

2.5 Research Gaps

Based on the above literature review, several research gaps have been identified as follows:

- The flow around the 25º SAB is complex due to three-dimensional and unsteady flow structures which makes understanding and control challenging.
- Recent studies used the rounded edge instead of the sharp edges at the rear end of the SAB. However, the idea of elliptical curvature has not been used to influence drag reduction and soiling by modifying the rear end shape.
- Recent trend shows an interest towards bluff shape submarines where the dominant drag is the pressure drag. Such 3D bluff shape submarines provide new avenues to develop flow control methods to reduce pressure drag, taking inspiration from ground transportation systems.

- The emerging area of autonomous vehicles depends on optical sensors for navigation. Therefore, the mitigation of sensor soiling is a relevant area of research. Hence, the development of flow control devices that can provide benefits in both drag reduction and soiling mitigation is needed.
- Prior research has shown that hydrophobic coatings exhibit pronounced effects when applied in proximity to the separation point, directly influencing the boundary layer. However, existing studies have primarily concentrated on investigating the impact of hydrophobic coatings on simpler bluff bodies like cylinders and spheres. However, examination of the effect of hydrophobic coatings on the rear-end flow structure of more intricate 3D bluff bodies, such as the specific case of the SAB and modified EAB, remains unexplored in the literature.
- Application of multiple point advanced analysis techniques such as two-point correlation, proper orthogonal decomposition (POD) and dynamic mode decomposition (DMD) has not been applied to examine the unsteady wake flow structures originating from the application of elliptical curvature and the hydrophobic coating on the SAB.

Chapter 3: Methodology

This chapter discusses the experimental setup, test conditions, measurement procedures, and freestream flow characteristics. The chapter also discusses the numerical simulation procedures, including the hybrid simulation methods, governing equations, boundary conditions, mesh independence, and validation. Finally, the data analysis techniques employed in this study are discussed.

3.1 Experimental Study

The experimental facilities used for this study consist of a water tunnel and particle image velocity (PIV) system. The water tunnel is used to carry out the measurement since it offers some advantages over wind tunnels. It is excellent for flow-visualization studies, providing insight into the physics of the flow, and is more suitable for modern, laser-based methods of flow field diagnosis, such as the PIV [276]. The experimental systems are described in detail in the following sections.

3.1.1 Water tunnel and test section

The experiments were conducted in a test channel inserted into a main recirculating water tunnel. Figure 3.1 shows a schematic diagram of the water tunnel used for this study. The test section was made of a clear acrylic plate to facilitate optical access. The main water channel, as shown in Figure 3.1, consists of a flow conditioning unit (items 1-2), a test section (item 3), a tank (item 4), a centrifugal pump (item 5), a variable speed drive (item 6), piping and valves, supporting framework and a filtering system. In terms of dimensions, the main test section measures 6000 mm in length, 600 mm in width, and 450 mm in depth. In addition, the test section walls are made of 31.8-thick acrylic sheets, providing an optically transparent view. A 30-kW variable-speed drive water pump drives the flow through conditioning units before entering the test channel. The flow conditioning unit has a contraction ratio of 4.88:1.

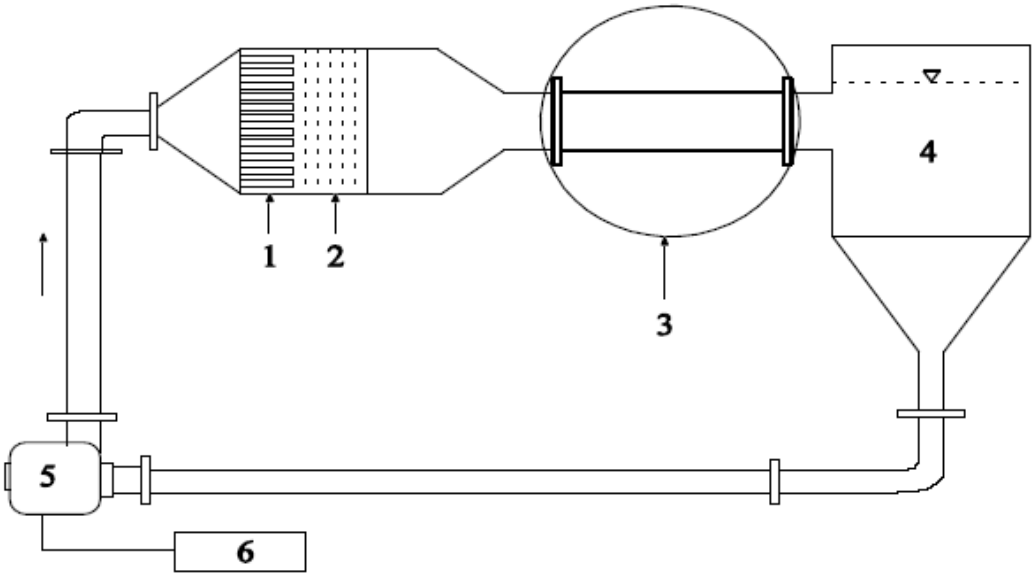

Figure 3.1: Schematic of a typical water tunnel indicating the main components where: 1- honeycomb, 2- perforated plate, 3- test section, 4- tank, - pump, and 6- variable speed controller (Paul, 2006).

Figure 3.2 shows a schematic representation of the experimental arrangement. Within the testing area, the models are fixed on flat acrylic plates. The origin of the model axis is 55.56h from the inlet of the test section and 27.78h downstream of the model (*h* is its height). The test model is placed within ± 1 mm of the test section's center during the test. At the channel's inlet, 36-grit sandpaper is used to strip the incoming flow and speed up the transition to turbulent flow. It is 100 mm long and covers the entire channel width (wall to wall). The water tunnel has a blockage ratio of 2.5%, which is way lower than the recommended 5% threshold value [277]. Therefore, no correction is required on the measured data [278]. The figure also displays the incoming flow direction and the laser system position.

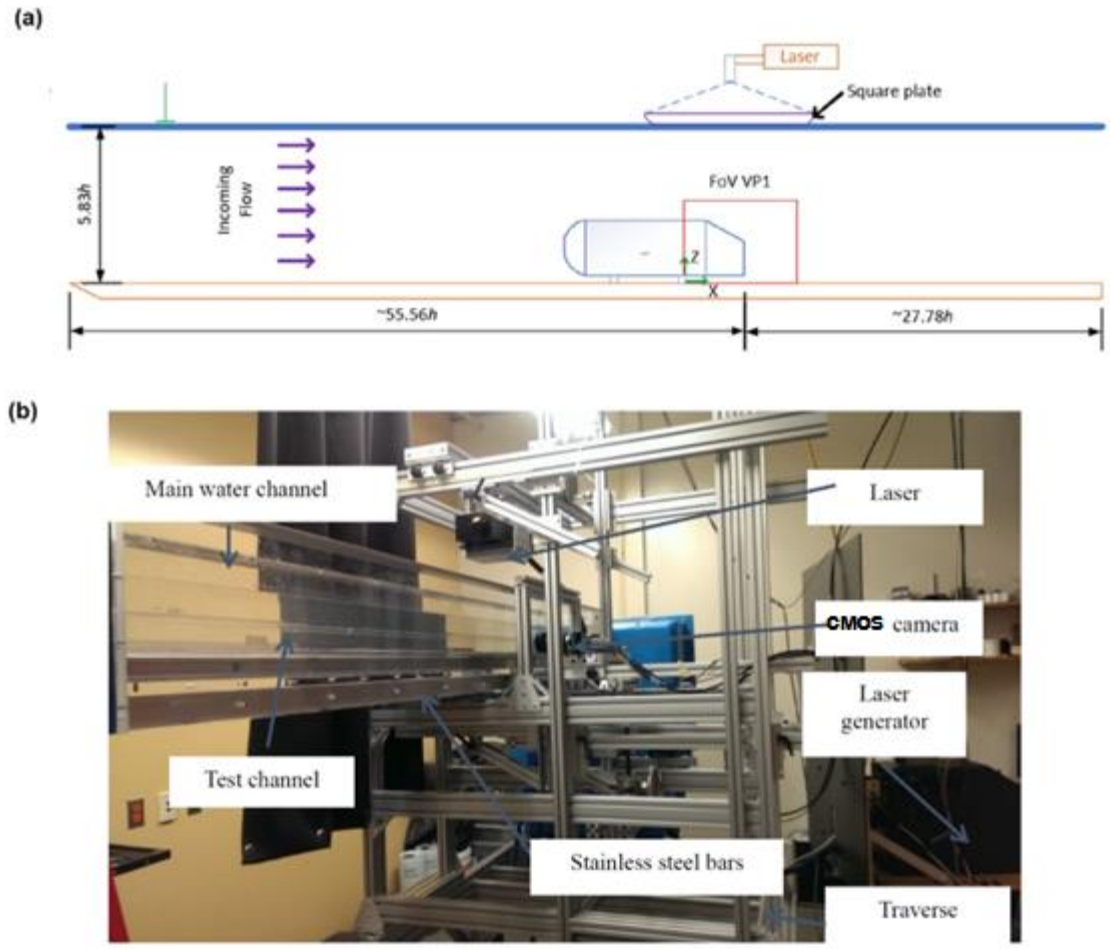

Figure 3.2: (a) The schematic of the experimental setup (b) Photo of the setup of the camera and laser for plane X-Z. Here FOV- Field of View.

3.1.2 Test model description

The standard Ahmed body (SAB) developed by Ahmed et al. [10] was 1044 mm in length, 389 mm in width, and 288 mm in height. The model is supported on small cylindrical rods 50 mm in height from the test floor. A quarter scaled-down version of the 25° SAB is used in this thesis with a height h = 72 mm. The general dimensions of the model are displayed in Figure 3.3, normalized with the model height.

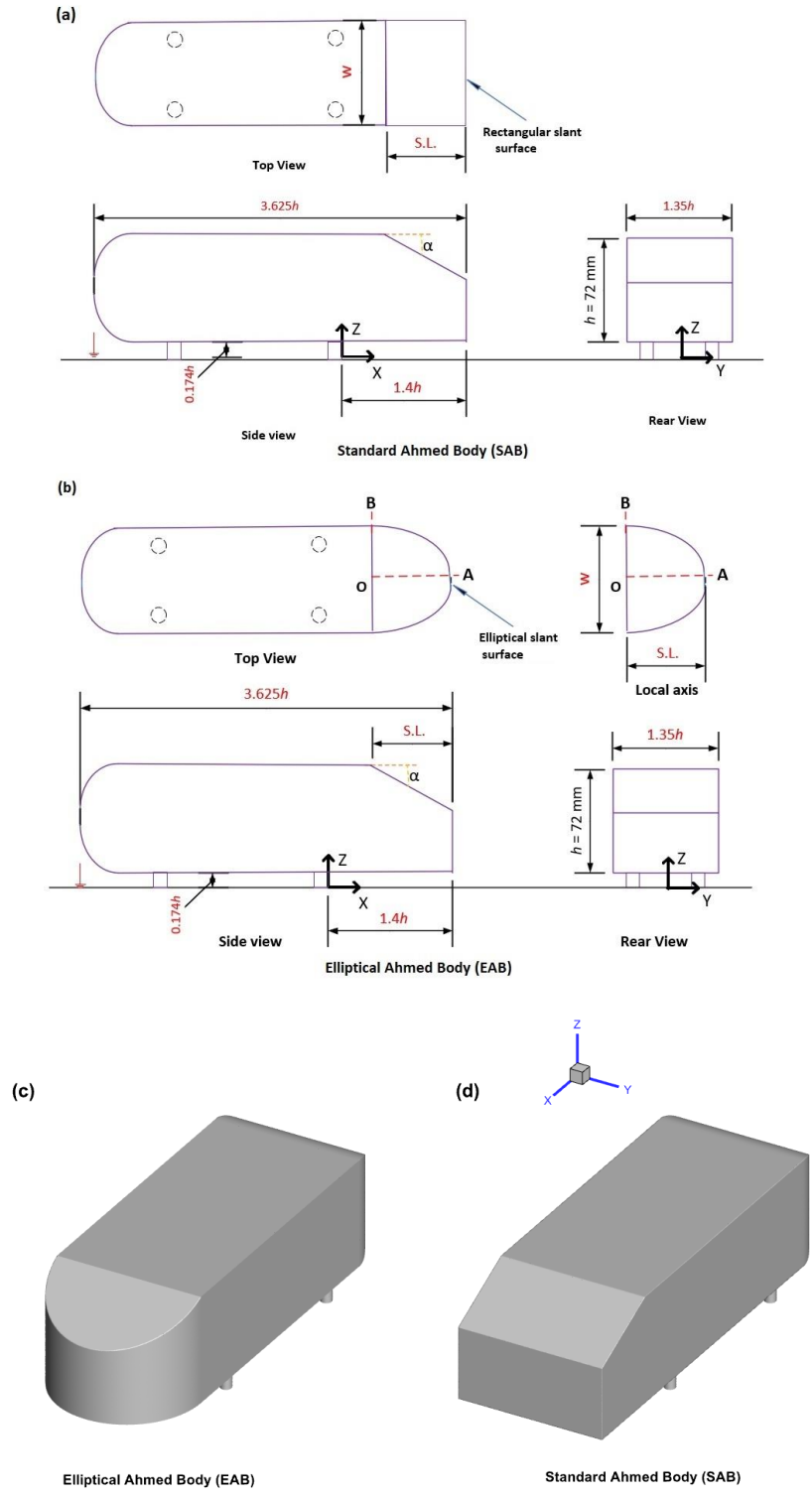

Figure 3.3: Dimensions of the standard Ahmed body (SAB) (a) and elliptical Ahmed body (EAB) (b) normalized by the model height, here *h* is the model height, S.L. is Slant length, α is the slant angle, W is the width. The Local axis in (b) is shown to calculate the equation of the ellipse. The Isometric views of the EAB and SAB are shown in (c) and (d), respectively.

Figure 3.3. shows the modified Ahmed body with elliptical curvature called the elliptical Ahmed body (EAB). The equation of the ellipse in the EAB can be expressed as:

$$\frac{A^2 \cos^2 \alpha}{(S.L.)^2} + \frac{B^2}{(W/2)^2} = 1 \quad (3.1)$$

Where the dimensions and variables are displayed in Figure 3.3. Note that OA = S.L. and OB = 0.5W. In terms of the normalized X, Y, and Z coordinate systems, the centre of the ellipse 'O' in the local coordinate axes is located at (0.7*h*, 0, 1.17*h*) from the model rear end. Eqn. (3.1) is designed for a constant slant surface length; hence it is limited to $0^{\circ} \leq \alpha \leq 55^{\circ}$.

On the Makerbot Z-18, the models are 3D printed using white polylactide acid, also known as PLA, in Fused Deposition Modeling. The PLA filament was used with a diameter of 1.75 mm, a layer height of 0.2 mm, 35% fill, and two layers on top, with four layers on the bottom. For the perimeter, the raster angle is 0°, and for the infill, it is 45°. Two SABs and two EABs are generated. The surface glare is minimized by painting each with non-reflective black paint. Furthermore, to provide the hydrophobic coating to the model, one SAB and one EAB are spray-coated with commercial hydrophobic paint (`Ultra Ever Dry'; UltraTech International Inc. Florida, USA) [279] and denoted as the hydrophobic SAB (or HSAB) and the hydrophobic EAB (or HEAB). The models are sprayed in several layers using bottom and top covers. After each layer of coating, sufficient time (as mentioned in the technical manual of the Ultra Tech) was provided to get the maximum strength.

3.1.2.1 Contact angle

The contact angle of the spray coating on the models was determined using the Keyence digital microscope, and a value of approximately 133º was obtained. This value is consistent with values obtained from other studies [268], [325]. The significantly higher contact angles than 90º confirmed that the coating possesses hydrophobic properties. Detailed results can be found in Appendix B.3.

3.1.2.2 Surface roughness

The surface roughness of the model surfaces was measured using the Filmetrics Profilm 3D instrument to obtain the arithmetic mean deviation roughness (R_a). R_a values of 0.18

μm and 0.35μm were obtained for the model surfaces without the hydrophobic coating and with the coating, respectively. The measured R_a values are considered smooth [335] and confirms that the coating did not significantly modify the surfaces roughness. More detailed information can be found in Appendix B.4.

3.1.3 Particle image velocimetry (PIV) technique

PIV has gained popularity as a non-intrusive optical measurement technique that can provide whole-field instantaneous velocity measurements. Its ability to estimate velocity gradients and derive quantities such as vorticity and various terms in the transport equations for turbulent kinetic energy and Reynolds stresses make it a useful tool in fluid mechanics and aerodynamics research. As such, PIV has been widely applied in these fields in recent years. This thesis employs two types of PIV techniques: Double-frame PIV (DF-PIV) and Time-resolved PIV (TR-PIV) supplied by LaVision Inc. A typical setup of the PIV is shown below in Figure 3.4. The PIV system involves three main components: a laser source, a camera, and a data acquisition system. The tracer particles are introduced into the flow and illuminated by a pulsed laser to generate images. The images are then divided into grids, and each grid is called an interrogation area (IA). The local displacement vector (Δx) of the tracer particles between the first and second image for each IA is calculated using a numerical correlation algorithm. Finally, the velocity vector map of the entire flow field is determined by dividing Δx by Δt for each IA. The details of basic components of the PIV are as follows:

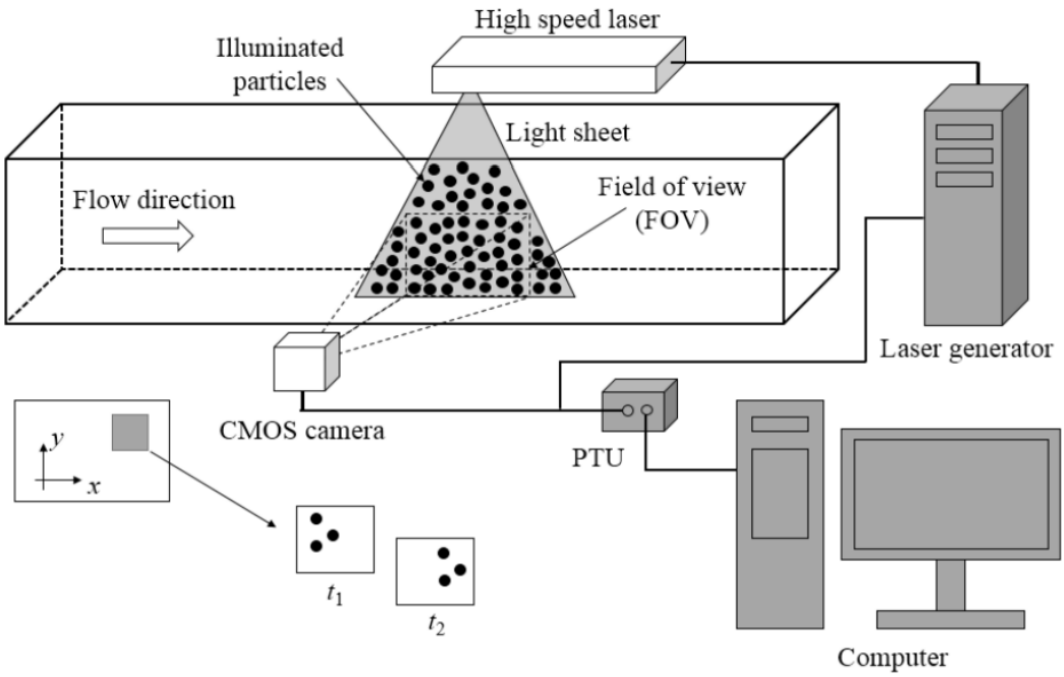

Figure 3.4: Typical setup of a Particle Image velocimetry (PIV) [280].

3.1.3.1 Laser

The experiment involved the use of a Photonics DM30–527DH laser, which was a diode pumped dual-cavity dual-head high-speed neodymium-doped yttrium lithium fluoride (Nd:YLF) laser. The laser produced a green light with a maximum energy of 30 mJ/pulse at wavelength λ= 532 nm. To adjust the thickness of the laser sheet, a combination of spherical and cylindrical lenses was employed, resulting in a thickness of approximately 1 mm.

3.1.3.2 Camera

Achieving precise and accurate PIV measurements requires the synchronization of cameras and lasers. Although CCD cameras have been traditionally used in PIV, they have limitations in terms of the image acquisition rate. High-speed cameras, such as the complementary metal-oxide semiconductor (CMOS) camera, have been developed to overcome this limitation and can achieve image acquisition rates of up to kilohertz (kHz). The CMOS camera is a valuable tool for TR-PIV measurements when used with high-repetition-rate lasers. In this study, a high-speed 12-bit CMOS Phantom VEO-430L camera

with a full resolution of 2560 × 1600 pixels and a pixel pitch of 10 μm to capture flow field images.

3.1.3.3 Seeding particles

In this study, the flow is seeded with a hollow glass sphere with a silver coating. The density of the seeding particles is 1400 kg/m^3, with a particle size (mean diameter) of 10μm. The ability of the particles to follow the flow faithfully is assessed by determining the Stokes number, S_k based on the particle response time, t_p and the characteristic temporal scale in the flow, t_f as follows (Eqn. (3.2):

$$S_k = \frac{t_p}{t_f} = \frac{d_p^2(\rho_p - \rho_f)}{18\rho_f t_f \nu} \tag{3.2}$$

Where ρ_p and ρ_f denote the density of the seeding particle and the fluid, respectively. The temporal scale in the flow field, t_f, is estimated to be of the order of the Taylor timescale, λ_T. Therefore, it is assumed here that $t_f \approx \lambda_T$. According to Tennekes and Lumley [281], the Taylor scale is calculated as:

$$\lambda_T = \frac{\sqrt{2\overline{u'u'}}}{(\frac{\partial u'}{\partial t})^2} \tag{3.3}$$

For the particle to be considered to accurately track the flow, the Stokes number should be smaller than 0.05 [282]. The present analysis has the Stokes number of 1.17×10^{-3} which satisfies the above conditions.

3.1.3.4 PIV measurement procedure

The PIV measurement is first made for the upstream of the test model before the model is installed to characterize the upstream boundary layer. This measurement plane is in the vertical plane (X-Z) and indicated as VP1 in Figure 3.5 with a camera field of view (FOV) of 224 mm × 140 mm (Shown in terms of model height). Secondly, the velocity measurements were performed in the downstream locations indicated as VP2 and VP3 in Figure 3.5 with the same FOV. Velocity measurements were also performed in the horizontal plane at 0.62*h* from the ground. The schematics of the vertical measurement planes are shown in Figure 3.5.

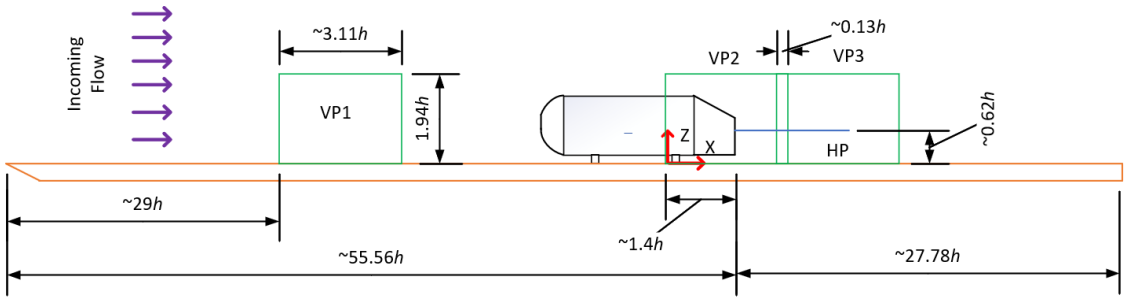

Figure 3.5: Schematic of the vertical measurement planes. All dimensions are non-dimensionalized with model height (h).

3.1.3.5 Data acquisition

The data acquisition is regulated by commercial software (DaVis version 10) developed by LaVision Inc. The time-resolved PIV (TR-PIV) measurements are performed by acquiring 48000 snapshots at a rate of 807Hz. At the same time, double-frame PIV (DF-PIV) measurements are taken at a rate of 6Hz for 9000 pairs of images. DF-PIV samples have more statistical independence, which allows them to provide a more accurate measure of the mean velocity and Reynolds stress. Thus, this study uses DF-PIV to compute time-averaged statistics, while TR-PIV is applied to compute time-dependent and spectral statistics. A 4-pass correlation method is used to calculate the velocity vectors. The initial interrogation area of TR-PIV was 128 × 128 pixels, with a 50% overlap, and DF-PIV's initial interrogation area was 64 × 64 pixels, with a 50% overlap. Following earlier experiments, the final interrogation area was chosen to be 24 × 24 pixels with 75% overlap [67].

3.1.4 Test conditions

In the experiment, all the tests are carried out at a Reynolds number of 0.431×10^5 based on the model height (h = 72) and the freestream velocity of U_∞= 0.60 m/s. The study is conducted at a room temperature of 25°C. The related Froude number $U_\infty/\sqrt{gH}$ is 0.50, and H denotes the water depth in the tunnel. Four different test models, namely, The SAB, EAB, HSAB, and HEAB, are investigated, focusing on the velocity measurement at the rear end in the vertical (X-Z at Y=0) and horizontal planes (X-Y at Z/h=0.62). The test conditions are listed in Table 3.1.

3.1.5 Error analysis

the present study followed the procedure of Casarsa & Giannattasio [283] for the error analysis in the experiment. Based on that, the mean velocity uncertainty at a 95% confidence level was estimated to be less than 2%, and that of the Reynolds stresses is 4% of their peaks. For further information on the statistical convergence and error analysis please see the appendix A.2.

Table 3.1: Experimental test conditions. DF-PIV (Double frame PIV) and TR-PIV (Time-resolved PIV).

Test model	Surface type	Reynolds number	Measurement plane	PIV type	No. of images DF-PIV/TR-PIV)
SAB	Non-hydrophobic	0.431×10^5	Y-0 (Symmetry Plane)	DF-PIV/TR-PIV	9000/48000
			Z/h=0.62 (Horizontal plane)	DF-PIV	9000
EAB			Y-0 (Symmetry Plane)	DF-PIV/TR-PIV	9000/48000
			Z/h=0.62 (Horizontal plane)	DF-PIV	9000
HSAB	Hydrophobic		Y-0 (Symmetry Plane)	DF-PIV/TR-PIV	9000/48000
			Z/h=0.62 (Horizontal plane)	DF-PIV	9000
HEAB			Y-0 (Symmetry Plane)	DF-PIV/TR-PIV	9000/48000
			Z/h=0.62 (Horizontal plane)	DF-PIV	9000

3.2 Numerical Method

The experimental technique employed for this study has some limitations. For example, the experiments were only performed in the vertical plane at the symmetry plane of the model and the horizontal plane. Also, the measurements are limited to low Reynolds

numbers. Therefore, numerical simulation was used to complement the experimental measurements. The numerical investigation of this thesis is conducted in two stages as follows.

For the initial investigation, a thorough numerical investigation is performed over the SAB by varying the slant angle from 25º to 30º in the 1º step. This slant angle range is called the transition angle range (TAR). Based on the model height, the Reynolds number is 0.147×10^5 at a freestream velocity of 3.1 m/s. For simplicity, the models are denoted according to the velocity (3.1 m/s) as the SAB_3.1.

After characterizing the flow features consistent with the literature at a low Reynolds number of 0.14×10^5, further numerical investigation for both the SAB and EAB is performed at the Reynolds number of the current experimental study of 0.43×10^5 at an air velocity $U_\infty = 9\ m/s$. In addition to this, the Reynolds number is raised in the moderate range of 1.90×10^5 found in the literature for on-road aerodynamics understanding at an air velocity $U_\infty = 40\ m/s$. This is the maximum Reynolds that can be achieved with the available computational resources. Consequently, the numerical investigation not only provides fresh information on the low Reynolds number but also documents the effect of a moderate Reynolds number on the SAB and EAB. For simplicity, the models are denoted according to the air velocity (9 m/s) as the SAB_9 and the EAB_9 for Reynolds number 0.43×10^5. While at Reynolds number 1.90×10^5 they are called the SAB_40 and the EAB_40 for air velocity of 40 m/s. The test conditions are summarized in Table 3.2.

Table 3.2: Test conditions for the numerical simulation.

Test model	Reynolds number	Slant angle	Simulation method
SAB_3.1	0.14×10^5	25º, 26º, 27º, 28º, 29º and 30º	IDDES
SAB_9	0.43×10^5	25º	
EAB_9		25º	
SAB_40	1.90×10^5	25º	
EAB_40		25º	

3.2.1 Detached eddy simulation

The detached eddy simulation (DES) is a hybrid model introduced by Spalart [158] that combines the RANS and LES and has become increasingly popular as a compromised method. Recent review papers highlight the development of such hybrid simulation methods used for both streamlines and bluff body flows [157], [159], [160]. It has been demonstrated through some foundational research that the DES is an appealing method for modeling the 25° Ahmed body, which represents a high-drag slant angle [137]. Moreover, Shur et al. [161] further developed the DES models by combining SST k-ω and Delayed Detached Eddy Simulation into the so-called Improved-Delayed Detached Eddy Simulation (IDDES). This particular model has shown superiority in capturing the flow field in both the TDS and QAS regions [29], [34], [111], [162]–[165]. Hence the IDDES method is employed for the current investigation.

3.2.2 Governing equations

The commercial software Ansys Fluent is used to do the numerical simulation. The finite volume method-based transient three-dimensional continuity and momentum equations is used in the simulation. Bounded second-order implicit time was employed to solve the resulting algebraic equations from the discretization. A spatial and temporal discretization of the governing equations is performed. Simply put, the equation can be expressed in its most basic form:

$$\frac{\partial}{\partial t}\int_{CV}\rho\varphi dV + \oint_A n.(\rho\varphi u)dA = \oint_A n.(\Gamma_\varphi \nabla_\varphi)dA + \int_{CV} S_\varphi dV \quad (3.4)$$

Here $\rho, u, n, \Gamma_\varphi, \nabla_\varphi$ values that correspond to density, speed, surface normal, diffusion coefficient, and gradient operator [147]. The convective fluxes are approximated using a bounded central differencing (BCD) scheme, which is a combination of a central difference scheme and a second-order upwind scheme. The SIMPLEC method couples pressure and velocity, and a second-order implicit scheme provides the temporal resolution, guaranteeing a robust numerical scheme [34].

The IDDES is used to conduct the current study because it provides more accurate predictions of the 25° Ahmed body. The IDDES is a hybrid of the Delayed Detached Eddy Simulation (DDES) and the Wall Modeled Large Eddy simulation [9], [14]. The IDDES prevents the log-layer mismatch or an excessive reduction in Reynolds stresses typically seen near the RANS- LES interface[285]. The TKE equation that is used in the RANS simulations is [284], [286]:

$$\frac{\partial(\rho k)}{\partial t} + \frac{\partial(\rho u_j k)}{\partial x_j} = \frac{\partial}{\partial x_j}\left[(\mu + \frac{\mu_t}{\partial_k})\frac{\partial k}{\partial x_j}\right] + \tau_{ij}\ S_{ij}\ - \frac{\sigma k^{1.5}}{L_{RANS}} \quad (3.5)$$

Where the time, TKE, density, velocity, molecular viscosity, turbulent viscosity, tensor of stress, and mean strain rate is represented by *t, k,* ρ, u_j, μ, μ_t, τ_{ij} *and* S_{ij} , respectively. The L_{RANS} is the turbulent length scale for the RANS. However, in the IDDES, L_{RANS} *length* scale is replaced by L_{IDDES}, which is the IDDES turbulent length scale [285], and is written as:

$$L_{IDDES} = \acute{f}_d\ (\acute{1} + f_e)L_{RANS} + (1 - \acute{f}_d)L_{LES} \quad (3.6)$$

Where $\acute{f}_d$ is the blending function, f_e is an elevating function, L_{RANS} is the length scale for the RANS and L_{LES} is for LES and is defined as:

$$L_{LES} = C_{DES}\Delta \text{ and } L_{RANS} = \frac{k^{1/2}}{\beta^*\acute{\omega}} \quad (3.7)$$

Here β^*=0.09 is a constant in the SST K- ω, $\Delta = \min[\max\{C_w\Delta_{max}, C_w d, \Delta_{min}\}, \Delta_{max}]$ is the sub-grid length-scale between Δ_{min}=

min $\{\Delta x, \Delta y, \Delta z\}$ and $\Delta_{max} = \max\{\Delta x, \Delta y, \Delta z\}$. C_w is the empirical constant, *d* is the nearest wall distance. The blending function is defined as $\acute{f_d} = \max\{(1 - f_{dt}), f_B\}$ where f_B is empirical blending function. When f_e is equal to zero, Eqn. (3.6 can be written as:

$$L_{IDDES} = L_{DDES} = \acute{f_d}\, L_{RANS} + \left(1 - \acute{f_d}\right) L_{LES} \tag{3.8}$$

Whereas, when f_e is higher than zero and $\acute{f_d}$ is equal to f_B, Eqn. (3.8) becomes:

$$L_{IDDES} = L_{WMLES} = f_B(1 + f_e)L_{RANS} + (1 - f_B)L_{LES} \tag{3.9}$$

Comprehensive explanations of the equations and coefficients can be found in [161], [284], [286].

The dimensions of the model are similar to the experiment shown in Figure 3.3. The computational domain setting is based on the results of the ERCOFTAC workshop on advanced turbulence modeling [287]. According to Figure 3.6, the domain has a length of 7.250*h* in front of the model, 18.125*h* in the back, a width of 6.493*h*, and a height of 4.861*h*. Here *h* is the model height. Domains with a blockage ratio of 4.28% are crucial for calculating aerodynamic coefficients [108], [111].

For the simulations of the SAB_3.1, the time step is set to 5×10^{-4} that ensures a Courant number of less than 1.5 [147]. The total simulation flow time is $t^* = tU_{in}/h$=67, and the flow statistics are collected over the last t^*=58 with ten iterations/time-step because the lift coefficient was less fluctuating while the drag coefficient became stable. Therefore, the time averaging of the last 1.25s is reliable to avoid contamination.

On the other hand, the SAB_9 & EAB_9 and the SAB_40 & EAB_40, the time step is set to 2×10^{-4} and 1×10^{-5}, respectively that ensures a Courant number of less than 1.5 [147]. The average simulation flow time is $t^* = tU_{in}/h$=150 and 70 for the SAB_9 and SAB_40 respectively. The flow statistics are collected with ten iterations/time-step when the drag coefficient becomes stable. Therefore, the time averaging of the last 0.8s and 0.125s of physical time is reliable to avoid contamination.

The solution is considered to have converged when residuals of continuity, momentum, TKE, and scalar dissipation rate fall below 10^{-4}, which is consistent with the study by He et al. [285]. In all the simulations, the outlet is subjected to constant pressure, and the left, right, and top surfaces are all designated as symmetry planes. The road is assumed to be stationary, and a no-slip boundary condition is used in the model.

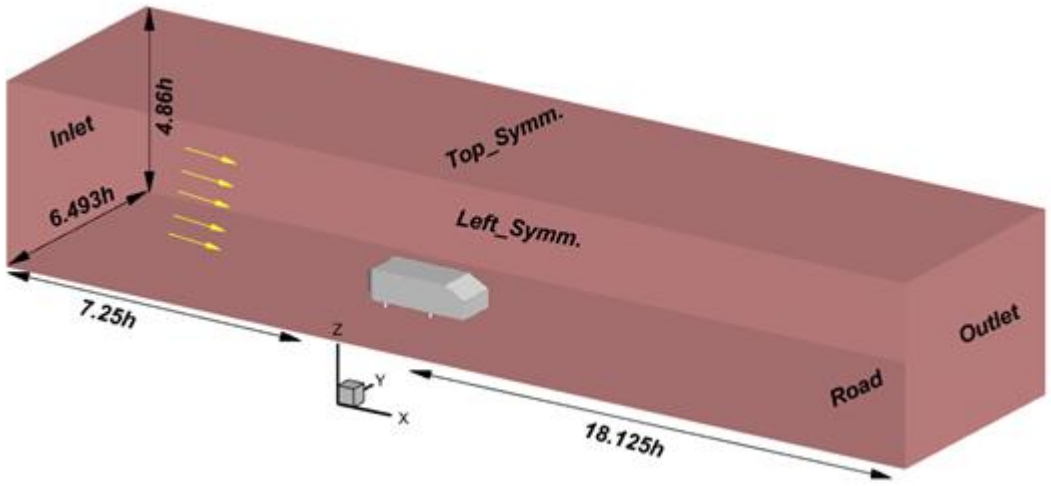

Figure 3.6: Computational domain of the simulation.

3.2.3 Mesh and grid independence

Accurately capturing the Ahmed body wake requires the estimation of turbulent length scales. As a result of these factors, the mesh grid size is determined by the Taylor (λ_T) and the Kolmogorov (η_k) length scales for the smallest turbulent length in the wake are shown in Table 3.3, normalized by the model height for the 25° Ahmed body [126], [288].

Table 3.3: Relevant length scale normalized by the model height.

Model	Reynolds number	L/h	λ_T/h	η_k/h
SAB_3.1	0.14×10^5	3.62	4.52×10^{-2}	8.86×10^{-4}
SAB_9 & EAB_9	0.43×10^5		2.65×10^{-2}	3.98×10^{-4}
SAB_40 & EAB_40	1.90×10^5		1.26×10^{-2}	1.31×10^{-4}

The simulation accuracy is confirmed by performing mesh sensitivity. The simulation used a structured polyhedral mesh. Reducing the element count improves the mesh quality while also dramatically reducing the cost and simulation time [25], [107], [289]. Along with the domain, two distinct refinement boxes surrounding the model precisely capture the length scale specified in Table 3.3. The grid resolution requirements for the smallest meshing cell size $\lambda_T/\Delta>1$ was achieved [147], where Δ is the sub-grid length scale mentioned in Eqs. 3.7 [161]. Consequently, as specified in Table 3.4, three different meshes are applied for the grid independence study. To capture the boundary layer over the model, inflation is used with a first layer height of 3.13×10^{-5} and 7.84×10^{-6} with 30 layers. Figure 3.7 shows the mesh used in the study.

Table 3.4: Mesh sensitivity analysis summary. (C_d is the drag coefficient).

Mesh type	**SAB_3.1**		**SAB_9**		**SAB_40**	
	Cell count/10^6	C_d	Cell count/10^6	C_d	Cell count/10^6	C_d
Mesh 1	3.6	0.449	4.4	0.383	5.4	0.350
Mesh 2	7.2	0.448	7.3	0.384	9.5	0.353
Mesh 3	13.5	0.448	14.4	0.385	18	0.354

It can be seen that Mesh 2 and 3 provide reasonably close drag coefficients for both the SAB_9 and SAB_40. Furthermore, $y^+ < 1$ is achieved for both Mesh 2 and Mesh 3; this demonstrates that the grid resolution is enough for capturing the viscous sublayer over the walls. As a result, Mesh 2 is chosen for the simulation to save processing time.

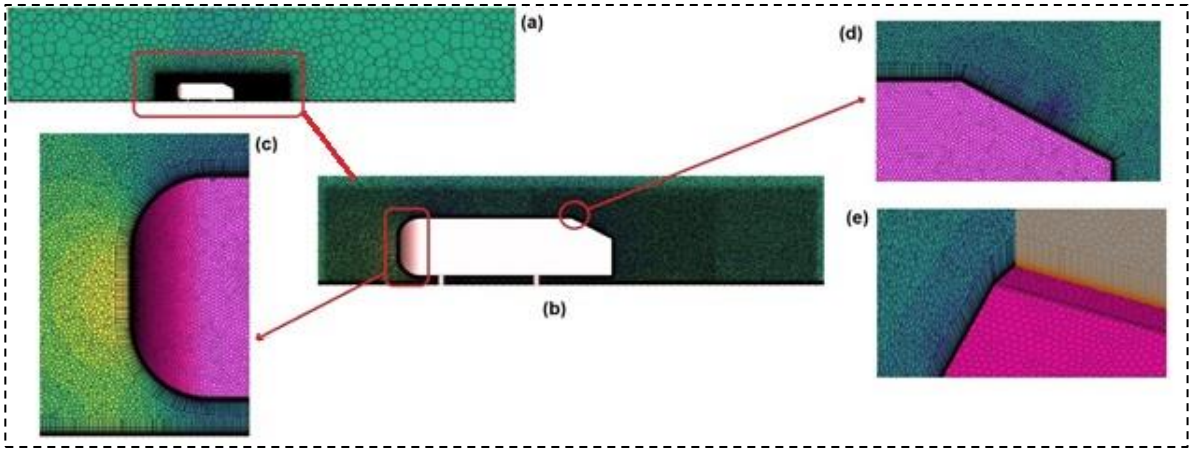

Figure 3.7: Computational mesh (a) Front view of the mesh at symmetry (Y =0), (b) Enlarged view with refinement boxes, (c) Enlarged view at the front-end, (d) Enlarged view at the slanted end, and (e) Isometric view.

3.2.4 Validation

At first, the simulation is validated using the aerodynamic drag coefficient. According to Table 3.5, the drag coefficient is scattered with respect to the Reynolds number. The drag values highlight that as the Reynolds number increases, the drag coefficient begins to reduce, and it varies between 0.285 to 0.437. The values found in the current IDDES simulation at both low Reynolds numbers and medium Reynolds numbers lie within the drag coefficient range. Secondly, Serre et al. [137] argued that the drag variation at the low Reynolds number is due to the large front roof bubble (FRB) at the front end. This FRB is also reported by Spohn and Gillieron [116] at low Reynolds number experimental investigation over a 25° SAB, which is also found in the current low Reynolds number model SAB_3.1 and the SAB_9 shown in Figure 3.8. Hence, the FRB is the distinctive feature of the low Reynolds number also supported by Krajnovic et al. and Mingueaz et al. [142], [148]. Thirdly, the most important features of the 25° SAB are the existence of SSB, recirculation region, URB, and LRB, as shown in Figure 3.8. In the current simulation as well, both the low and high Reynolds number shows the existence of these recirculation regions and the bubbles. The lengths of SSB (SBL) and wake recirculation region (Lr) are compared in

Table 3.6 with the existing studies. It can be seen that both the SBL and Lr are in close agreement with the existing literature [27] with minor differences due to the Reynolds number. It can be concluded that the IDDES simulation not only provides the basic flow features but also captures the FRB, SSB, Lr, URB, LRB, and drag coefficient according to the Reynolds number. Therefore, the current setup of the IDDES simulation is considered validated.

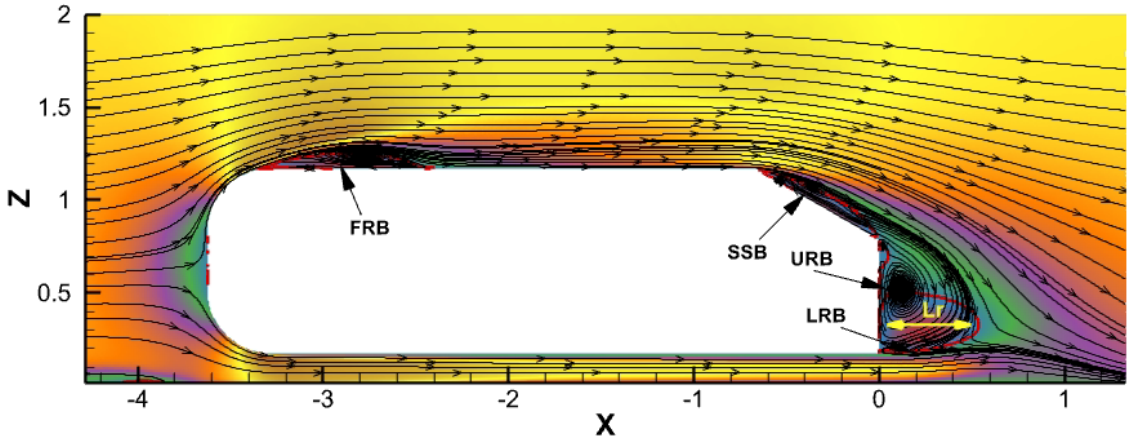

Figure 3.8: Basic flow recirculation regions over the 25° Standard Ahmed Body for the SAB_3.1 and the SAB_9.

Table 3.5: Comparison of the drag coefficient.

Reference	$\overline{C_d}$	Reynolds number	Method
Kohri et al. [26]	0.365	0.73×10^5	Experiment
Serre et al. [137]	0.431	7.68×10^5	LES
Guilmineau et al. [111]	0.437	7.68×10^5	DDES
Guilmineau et al. [111]	0.380	7.68×10^5	IDDES
Present study			
SAB_3.1	0.448	0.14×10^5	IDDES
SAB_9	0.382	0.43×10^5	
SAB_40	0.353	1.90×10^5	

Table 3.6: Comparison of the slant bubble length (SBL) and wake recirculation length (Lr). All the values are in terms of percentage slant length. Note, Exp. is experiment and Num. is Simulation, Re= Reynolds number.

	SAB_3.1.	SAB_9	SAB_40	(1)*	(2)*	(3)*	(4)*	(5)*	(6)*	(7)*
Re (10^5)	0.14	0.43	1.90	0.08	7.68	7.68	0.62	0.52	11.10	1.70
SBL	76	78	84		77	75			61	
Lr	76	76	73	78	67		80	84	84	96

(1)* Numerical study by Minguez et al.[148], (2)* Numerical study by Guilmineau[85], (3) *Experimental study by Rossitto[32], [170], (4)* Experimental study by Zhang et al.[72], (5)* Experimental study by Wang et al.[124], (6)* Experimental study by Sellappan.[77], (7)* Experimental study by Liu et al.[76]

3.3 Data Analysis Technique

In this section, the data analysis techniques used in the thesis are discussed. These include proper orthogonal decomposition (POD), dynamic mode decomposition (DMD), Two-point auto-correlation, Q-criterion and λ_2.

3.3.1 Proper orthogonal decomposition

Proper orthogonal decomposition (POD) is used as a model decomposition method in this study. According to their kinetic energy content, flow fields are classified into orthogonal spatial modes in the POD. Additionally, it can be applied to lessen small-scale turbulence and PIV uncertainty [290]. POD is composed of three matrices [291]:

$$X_{m\times n} = U_{m\times n}\Sigma_{n\times n}V^*{}_{n\times n} \tag{3.10}$$

A data set of matrix X is built by transforming each individual snapshot into the mean-removed vector fields. $x_1, x_2, \ldots x_n$ into an $m \times 1$ vector in which m is the number of velocity vectors times the number of velocity vector components and the number of snapshots is n. The order in which they were recorded in the X matrix determines how a flattened velocity vector field is then structured. Modal components of the POD are quantified as a share of

the fluctuating kinetic energy. The eigenvalues of a signal allow us to categorize the relative intensity of each mode (excluding mode 0). POD analysis of the Ahmed body has been used in previous studies [120], [139], [290], [292]. However, POD analysis of the wake region of the Ahmed body is not fully understood, especially the energy contribution and flow features.

3.3.2 Dynamic mode decomposition

Dynamic mode decomposition (DMD) is a spatial dimensionality-reduction technique that combines POD with the Fourier transforms in time. In this way, spatial modes now have a temporal frequency, possibly associated with a growth or decay rate. The DMD method, therefore, provides a spatiotemporal decomposition of data into dynamic modes derived from snapshots or measurements of a system in time. It has two main advantages; first, it is an equation-free architecture; and second, a future state prediction is possible to construct at any future time [293]. There are only a few studies of the DMD in the literature on the SAB [30], [294].

The DMD modes can be obtained by using a time series of measurement snapshot vectors, x_n at each time, step n is arranged in a matrix $X_1^N \leftarrow \{x_1, x_2, \dots \dots x_N\}$. The data matrix X_1^N is decomposed into two sets: $X_1^{N-1} \leftarrow \{x_1, x_2, \dots \dots x_{N-1}\}$ and $X_2^N \leftarrow \{x_2, x_2, \dots \dots x_N\}$. The first set is orthogonalized using the singular value decomposition (SVD): $[U, \Sigma, W] = svd(X_2^{N-1})$, where U includes the proper orthogonal modes of the first set of data X_1^{N-1}. It is thus possible to express the last data vector x_N as a linear combination of the previous elements in the form [30]:

$$S = U^H V_2^N W \tag{3.11}$$

Model structures are represented by the eigenvectors of S, whereas frequencies and growth/decay rates are represented by the eigenvalues. In order to quantify how many modes representations there are in the original dataset, the optimum amplitudes can be computed by QR-decomposition of the original data matrix V, the singular values Σ, and the modes (Eigenvectors of S). The discrete-time eigenvalue is used to study the stability characteristics of the DMD modes. The eigenvalues occur as complex conjugate pairs and lie on a unit circle in the complex domain representing the modes with zero growth rates.

However, the eigenvalues lying inside the unit circle represent the decaying of DMD modes, and outside existence shows growth with time [295].

3.3.3 Two-point autocorrelation

The two-point correlation functions are defined for two arbitrary quantities A and B in a plane at reference points separated by Δr1 and Δr2 as follows:

$$RAB = < A(\, r1, r2\,)\, B(\, r1 + \Delta r1, r2 + \Delta r2\,) > / \sigma A \sigma B \tag{3.12}$$

At positions ($r1$, $r2$), σA and σB refer to the standard deviations of A and B, respectively. A and B are the fluctuating velocities, while σA and σB represent the turbulent intensities in this research. For instance, in the x-y plane, σA and σB correspond to the streamwise (u) and wall-normal (v) fluctuating velocities. It's worth noting that the equation Eqn. (3.12) is also applicable to autocorrelations. As mentioned earlier, two-point correlations help to determine the distance and time scales that depict the correlation of the turbulence field across the flow. Additionally, they can be utilized to evaluate the integral, Taylor micro length, and time scales.

3.3.4 Q-criterion

One of the essential and critical means of vortex identification is the Q-criterion proposed by [296]. It is based on the tensor of the velocity gradient ∇u which is segregated into one symmetric strain tensor S_{ij} and one anti-symmetric rotational part Ω_{ij}. This is described as:

$$\nabla_u = u_{ij} = S_{ij} + \Omega_{ij} \tag{3.13}$$

$$S_{ij} = \frac{1}{2\left(u_{i,j} + u_{j,i}\right)} \tag{3.14}$$

$$\nabla_u = u_{ij} = S_{ij} + \Omega_{ij} \tag{3.15}$$

$$\Omega_{ij} = \frac{1}{2\left(u_{i,j} - u_{j,i}\right)} \tag{3.16}$$

Eqn. (3.13) is satisfied by the eigenvalues of ∇u is given by:

$$\sigma^3 - P\sigma^2 + Q\sigma - R = 0 \tag{3.17}$$

$$P = u_{i,j} = 0, \;\; Q = \frac{1}{2\left(u^2{}_{i,i} - u_{i,j}\, u_{i,j}\right)}, \qquad R = \det\left(u_{i,j}\right)$$

The Q-criterion is based on the second invariant of the velocity gradient, denoted as Q. It also includes the condition that ambient pressure should be higher than the pressure of the vortex to separate it. The full dynamics are presented as:

$$Q = \frac{1}{2}\left(u^2{}_{i,i} - u_{i,j}\, u_{i,j}\right) = -\frac{1}{2}u_{i,j}u_{i,j} = \frac{1}{2}\left(\|\Omega^2\| - \|S^2\|\right) \tag{3.18}$$

Q is a local term for balance vorticity magnitude Ω and strain rate S. By putting Q>0; it is possible to separate the regions where the strength of vorticity surpasses the strain rate. Since within a low-pressure tube with a small cross-section engulfed by isobaric layers of pressure, Laplacian will be positive if the flow has a uniform density. This variable is related to the Q, the second invariant, and Q must be positive.

3.3.5 λ_2-criterion

The λ_2 criterion extracts the coherent vortical structures based on regions where the second largest eigenvalue λ_2 of the tensor is negative [147].

$$S_{ik}S_{kj} + \Omega_{ik}\Omega_{kj} \tag{3.19}$$

Here are the symmetric and antisymmetric parts of the velocity gradient tensor $\frac{\partial U_i}{\partial x_j}$.

$$\mathrm{S_{ij}} = \left(\frac{\partial \mathrm{U_i}}{\partial \mathrm{x_j}} + \frac{\partial \mathrm{U_j}}{\partial \mathrm{x_i}}\right)/2 \text{ and } \Omega_{\mathrm{ij}} = \left(\frac{\partial \mathrm{U_i}}{\partial \mathrm{x_j}} - \frac{\partial \mathrm{U_j}}{\partial \mathrm{x_i}}\right)/2 \tag{3.20}$$

3.4 Non-dimensionalized parameters

Throughout this chapter, some common parameters are non-dimensionalzed and used to discuss the flow features. They are described here as follows:

The streamwise, spanwise, and wall-normal coordinates are normalized with the model height *h*:

$$X = \frac{x}{h}, \qquad Y = \frac{y}{h}, \qquad Z = \frac{z}{h} \tag{3.21}$$

The velocity component in the x, y, and z-direction is defined as:

$$U = \frac{u}{U_\infty}, V = \frac{v}{U_\infty}, W = \frac{w}{U_\infty} \tag{3.22}$$

Where U_∞ is the freestream velocity. The Reynolds shear stresses are:

$$UU = \frac{u'u'}{{U_\infty}^2}, UW = \frac{u'w'}{{U_\infty}^2}, VW = \frac{v'w'}{{U_\infty}^2}, UV = \frac{u'v'}{{U_\infty}^2}, WW = \frac{w'w'}{{U_\infty}^2}, \tag{3.23}$$

Similarly, the Q-criterion is defined as:

$$Q = Q'h^2/{U_\infty}^2 \tag{3.24}$$

Q is the second invariant of the velocity tensor. Finally, the pressure coefficient (C_p) is defined as:

$$C_p = \frac{P_i - P_\infty}{1/2\rho U_\infty^2} \tag{3.25}$$

Here, P_i is the pressure at the surface, p_∞ is the static reference pressure, ρ is the medium density. The Strouhal number is calculated as:

$$S_t = fh/U_\infty \tag{3.26}$$

Here frequency is *f* and *h* represents the height of the model. Until specified, 25° is the default slant angle of both the SAB and EAB. Note that all the data reported in the tables have an accuracy of ±0.5% in the normalized form.

Chapter 4: Result and Discussion

This chapter documents the results and discussions of the experimental and numerical analyses. The chapter is divided into three main sections as follows: Section 4.1 reports the experimental investigation of the standard Ahmed body (SAB) and the elliptical Ahmed body (EAB). Section 4.2 extends the investigation of the SAB and EAB using numerical simulation. Finally, Section 4.3 presents the experimental study of the effect of the hydrophobic coating on the SAB and EAB.

4.1 Experimental Results

This section provides a detailed experimental investigation of the effects of elliptical curvature on the Ahmed body. Hence, it employs the SAB as a base model and, with the application of elliptical curvature, creates an EAB. The investigation is conducted at a Reynold number of 0.431×10^5 based on the model height. In order to comprehend both the time-averaged and time-dependent flow characteristics, the mean velocities, Reynolds stresses, two-point auto-correlation, frequency spectra, proper orthogonal decomposition (POD), and Dynamic Mode Decomposition (DMD) approaches are used.

4.1.1 Upstream boundary condition

The profiles of velocity and Reynolds stress at the upstream are illustrated in Figure 4.1. It shows that, as the wall-normal distance increases, a monotonic increase in velocity is also observed. Similarly, Figure 4.1(b) reveals the averaged Reynolds stress profiles UU, UW, and WW. It can be seen that the stresses converged to lower levels after Z=1.5. The turbulent boundary layer thickness (BLT) at the upstream location is found at Z=1.05. Figure 4.1(a) depicts the extent of the model mid-height as a solid line with a long-dotted line denoting the TBL. The model's mid-height is observed to be within the BLT. The shape factor is 1.29, which is consistent with prior results, and the displacement and momentum thicknesses are 0.15h and 0.12h, respectively [67], [280]. The test model of the present study is within the boundary layer, which is similar to other water tunnel studies such as [67], [297]. However, the near-field flow structure is not significantly affected because of the fixed separation points of the Ahmed body, except for the potential effect on the magnitude of the upper and low recirculation bubbles in the wake. Furthermore, a comparison of the present study with similar studies in wind tunnels and water tunnels

[280], [298] shows consistent results in terms of shape factors in the range between 1.29-1.39.

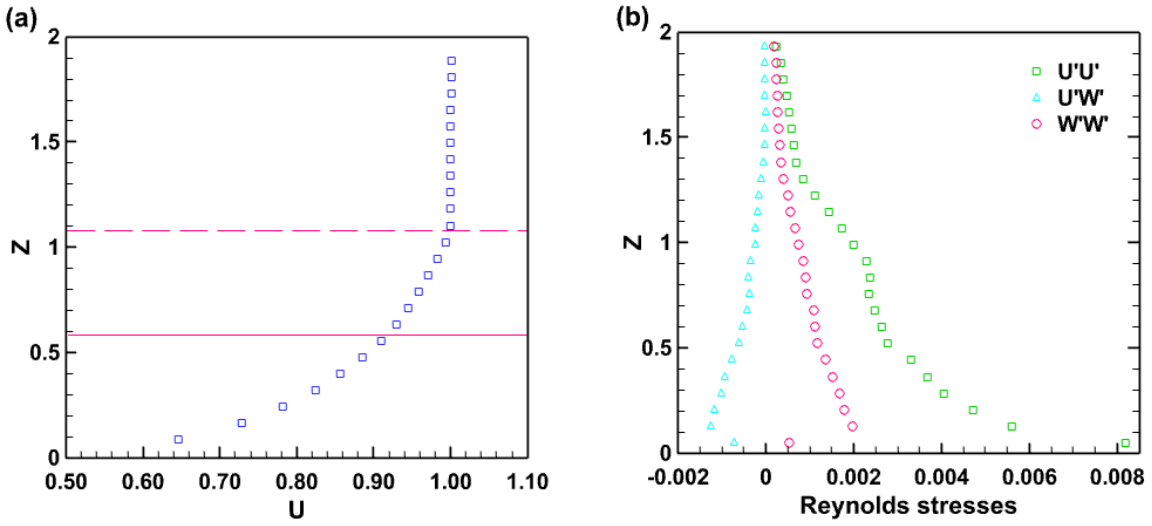

Figure 4.1: Profiles of the upstream flow (a) normalized streamwise velocity and (b) Reynolds stresses. The long dotted line in (a) represents the thickness of the boundary layer, while the solid line indicates the mid-height of the test model. These quantities are extracted at x=29h from the test section inlet.

4.1.2 Mean velocity

The time-averaged streamwise and wall-normal velocity contours at the symmetry plane Y=0 are presented in Figure 4.2. These figures provide both qualitative and quantitative flow characteristics by showing the velocity field and parameters of the recirculation region. They are crucial to understanding the effect of elliptical curvature on the Ahmed body wake flow structures.

(a) standard Ahmed body (SAB)

In Figure 4.2(a) and (b), streamwise and wall-normal velocity contours are shown for the SAB. The solid red lines show the contour of zero velocity to mark the reverse flow region. At first, it can be seen that the flow separates at the upper edge of the slant surface in the SAB (Figure 4.2(a)) and is reattached over the later part of the slant surface, thus, forming a slant separation bubble (SSB). The SSB is dominated by negative streamwise velocities. Additionally, due to the flow separation, the wall-normal velocity in Figure 4.2(b) is positive over the slant surface.

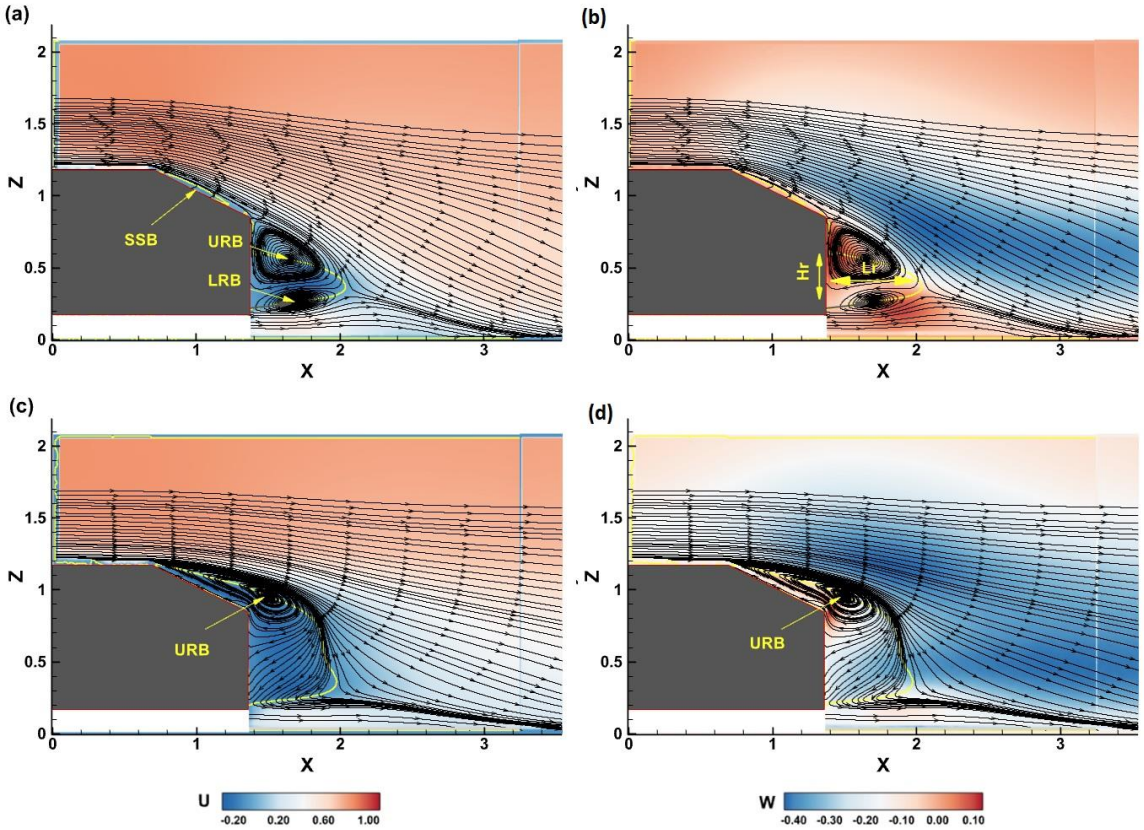

Figure 4.2: Contours of normalized streamwise mean velocity (a) & (c) and wall-normal mean velocity (b) & (d) at the symmetry plane. (a) & (b) are SAB and (c) & (d) are EAB. The streamlines of mean velocity are superimposed on the contours. The solid red line indicates U=0 velocity showing the extent of the recirculation region. In Figure4(a): Upper recirculation bubble (URB) and Lower recirculation bubble (LRB) And slant separation bubble (SSB Figure 4(b): L_r and H_r are the recirculation length and recirculation height.

This SSB is a typical flow characteristic of the 25° Ahmed body and is documented by many high and low Reynolds number studies [72], [73], [77]. Still, other low Reynolds number studies did not find the SSB [83], [127], [299]. Contrary to a study by Rao et al. [25] at a high Reynolds number of 2×10^6 also did not find the SSB. Consequently, the difference in the Reynolds number cannot be taken as a criterion for the absence of the SSB. Secondly, the present study found the reattachment length of the SSB in the SAB to be 62% of the length of the slant surface. This is close to the values reported as 77% from the IDDES simulation and 72% in the experiment reported by Guilmineau [85] at a Reynolds number of 7.68×10^5. Similarly, 75% is also documented by Rossitto et al. [32] based on an experiment at 7.68×10^5 Reynolds number. The difference in the reattachment length can be attributed to the different Reynolds numbers.

Thirdly, following the formation of the SSB, the flow again separates at the rear end of the slant surface, creating the wake recirculation region dominated by negative velocities. There are two recirculation bubbles, which are depicted in Figure 4.2(a), with the upper recirculation bubble (URB) and lower recirculation bubble (LRB). This causes the wall-normal velocity to increase in the wake recirculation region (Figure 4.2(b)) before decreasing afterward. The location of URB is at X=1.65 and Z= 0.57, while LRB is at X=1.7 and Z=0.3. These locations are also consistent with the values of Tunay et al. [127] at a low Reynolds number. However, unlike this study, they did not find the SSB over the slant surface at the 25° angle. Many studies have documented that slanted Ahmed bodies have these two recirculation bubbles [10], [72], [77]. Fourthly, the recirculation length indicated as L_r in Figure 4.2(b) is ~0.64, which is 85% of the slant length located at Z=0.36. This L_r is close to the ~ 0.64 of Zhang et al. [72], ~ 0.67 by Wang et al. [124], ~ 0.65 found using volumetric PIV by Sellappan et al. [77], and ~0.55 reported by Liu et al. [76]. Finally, several studies on the high-drag Ahmed body highlighted the existence of the C-vortices. The C-vortices are known to originate on the upper side of the slant surface and extend into the wake downstream. It is the interaction between the C-vortices with the flow over the slant surface and eventual merging with the URB that leads to distortion and dissipation of the URB further downstream [76], [77]. Thus, although the present study provides flow structure at the symmetry plane, the basic flow features of the SAB at the 25° angle strongly suggest the existence of both primary and secondary C-vortices over the slant surface [28], [72].

(b) elliptical Ahmed body (EAB)

The effect of curvature at the rear end of the slant surface is apparent in Figure 4.2(c) and (d) referred to as the EAB. Figure 4.2(c) shows the streamwise velocity contours of the EAB with the streamlines in the symmetry plane. The EAB shows a fully detached flow at the upper edge of the slant surface. It does not reattach over the slant surface; hence the SSB does not exist. Instead, the URB is enlarged and covers the entire slant surface along with the near wake and extends until X=1.98. Consequently, the wall-normal velocity increases over the slant surface. The streamlines suggest a stronger downwash compared to the SAB. Overall, significant flow modifications are observed.

Based on the literature on the SAB, the flow transition is reported to happen at or around a critical angle of 30°, whereas some reported post-32º as well [85]. The detachment from the upper edge of the slant surface facilitates the transition of TDS into QAS [10], [13], [25], [127]. The transition transforms the high-drag regime of the SAB into a low-drag flow field. An example would be the high-drag TDS present in the SAB at 25° (which the current study deals with) while absent from the SAB at 35° angle, which shows a low-drag QAS flow field [79], [85]. Interestingly, the EAB provides the flow transition at a significantly lesser angle of 25° and converts the flow structure similar to that of the SAB at 35°. However, the flow transition of the EAB is not exactly similar to the 35° SAB and differs in three important aspects. First, the wake recirculation height (H_r) has increased by more than 50% (Figure 4.2(c)) compared to the 25° SAB shown in Figure 4.2(a) but corresponds well with the SAB at a 35° angle found in the literature. Secondly, there is no significant increase in the recirculation length due to the EAB, and it remains close to the 25° SAB in Figure 4.2(a). Conversely, the 35° SAB shows a prolonged recirculation length along with the height. Thirdly, both the 25° and 35° SAB have URB and LRB, but the EAB only shows the URB [72], [79]. The location of URB is also moved towards the slant surface in the EAB compared to the 25° SAB in Figure 4.2(a). At the same time, the 35° SAB shifts the URB in the downstream direction. These three observations stated above are also different from the flow modification made using a rounded curvature at the upper and side edges of the slant surface of the 25° SAB [35]. The rounded curvature over the upper edge of the slant surface makes the flow attached over the slanted surface and creates two recirculation bubbles in the wake. Similarly, the C-vortices are weakened but do not vanish entirely.

On the other hand, the flow modification by the EAB differs from that of the elliptical curvature at the rear of the slanted aircraft fuselage studied previously [94]. Although both the SAB and slanted fuselage are considered critical geometries, the effect of curvature differs in a few aspects. Firstly, the slanted aircraft fuselage, even at a 45° angle, shows the SSB, while the EAB eliminates the SSB, which is one of the most important contributors to pressure drag in the Ahmed body [13]. Secondly, the aircraft fuselage is dominated by strong counter-rotating longitudinal vortices, called ‘vortex flow pattern’, due to hysteresis effects [300]. The Reynolds number is directly proportional to the length of the separation

bubble. In the vortex-dominated regime, the strength of the vortices correlates with the form of drag [301]. Furthermore, as pointed out above in the discussion of the SAB, the shear layer rolls up from the side edges and merges with the slant surface flow, which creates the C-vortices that coalesce into the near wake and merge with the URB [10], [72], [77]. However, the curvature in the SAB significantly affects the underbody flow leading to the elimination of the LRB. Such a modification also shifts the URB in the wall-normal direction at the level of the slant surface. Therefore, the non-existence of both the SSB and LRB and the shift in the URB suggest the weakening of the C-vortices. This is supported by Beaudoin and Aider [21], who found a fully detached flow similar to the low-drag Ahmed body by implementing flaps at the side edges of the slant surface. The side flap eradicated the longitudinal C-vortices that contributed to early separation. Thus, a fully separated flow is also accompanied by a suppression of longitudinal C-vortices and the SSB. Therefore, the elliptical curvature affects the Ahmed body differently by removing the SSB and LRB and weakening the C-vortices, which is different from the slanted cylinder [94]. Moreover, Zhang et al. [28] also found a similar flow modification where the active manipulation joined the URB with the SSB over the slant surface leading to a significant drag reduction of almost 29%. Therefore, the EAB not only transforms the TDS into similar low-drag flow features but also removes the LRB, which is a significant contributor to the soiling, causing surface contamination at the vehicle's rear window. These salient flow features suggest that the EAB has the potential to improve aerodynamic performance.

4.1.3 Reynolds stresses

The effect of curvature is analyzed using the contours of the Reynolds stresses. The normal stresses and shear stress are shown in Figure 4.3 at the symmetry plane. A few observations can be made.

(a) standard Ahmed body (SAB)

First, two peaks in the SAB are seen on the UU contours in Figure 4.3(a). One peak is located close to the top edge of the slant surface UU=0.12, and it is connected to the shear layer as a result of the flow separation. The value was lowered to UU=0.04 by more rearward reattachment at the slant surface. The second maxima have a value of UU=0.11 and are located at the model's lower edge. The UU=0.006 far downstream within the shear

layer is shown for comparison with the EAB. The two opposing peaks in the UW shear stress contour in the SAB are also visible in Figure 4.3(b). The upper shear layer stresses have a maximum negative value of UW= -0.017, which almost remains the same over the slant surface, including the rear end.

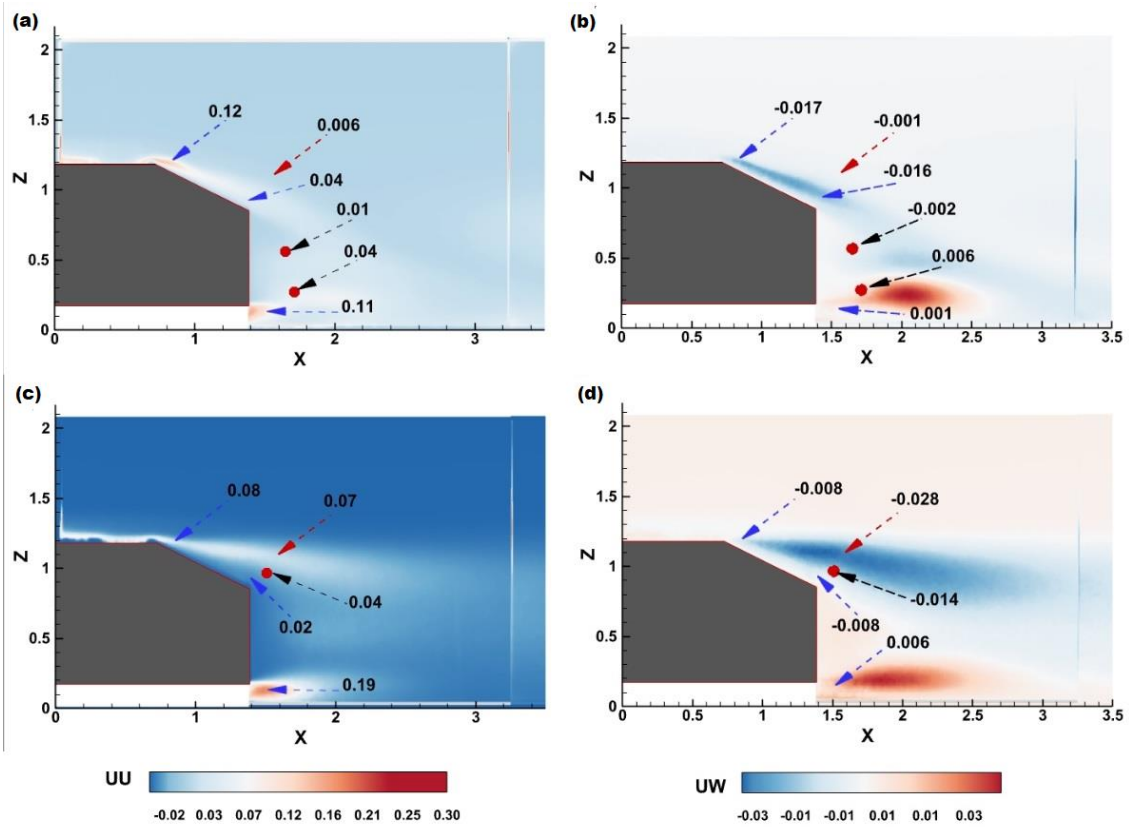

Figure 4.3: Contours of streamwise Reynolds normal stresses and Reynolds shear stresses at the symmetry plane Y=0 (a) & (b) are SAB (c) & (d) are EAB.

The lower shear layer from the underbody shows UW=0.001. The underbody shear layer also extends further downstream and is centred at X=2 when compared to the normal stresses. Finally, the two solid red circles represent the URB and LRB, respectively. The negative UW values are associated with the URB due to the downwash that has positive U and negative W velocities. At the same time, the positive UW in the LRB corresponds to the upwash because it has positive U and W velocities. These values are lower than the UW values reported previously [124] at the 25° slant angle Ahmed body.

(b) elliptical Ahmed body (EAB)

The effect of curvature on the Reynolds stresses is shown in Figure 4.3(c) and Figure 4.3(d). Due to the fully detached flow, the EAB shows a dominant upper shear layer. However, a reduction in normal stress to UU=0.08 is noticed, which represents a 33% reduction in the EAB. In contrast, the point inside the upper detached layer has a value of UU=0.07, which is 91% higher than that of the SAB. On the other hand, the shear stresses (UW) (Figure 4.3(d)) over the slant surface are found to be constant at UW=-0.008, which is almost 53% higher than that of the SAB. Similarly, the upper layer shows UW=-0.028, which is around 96% higher than that of the SAB. In comparison, the normal stresses in the lower shear layer are increased by 42%, whereas the shear stress has increased by almost 83% compared to the SAB. Furthermore, the lower shear layer in the EAB is more stretched in the downstream direction. Finally, the centre of the URB in the EAB (Figure 4.3(c)) has a value of UW=-0.014. It suggests that after shifting in the wall-normal direction, the effect of upwash increased in the EAB compared to the SAB since the shear stress increased by almost 86%. Thus, the shear stresses are higher at both the centre of the shifted recirculation bubble and within the separated shear layer.

4.1.4 Two-point auto correlation

Further investigation of the large-scale structures in the wake is achieved by extracting the two-point auto-correlations. Since the flow is predominantly streamwise, R_{uu} is explored in this direction [67]. A turbulence field's autocorrelation reveals how closely it is connected over a range of distances [302].

(a) standard Ahmed body (SAB)

As shown in Figure 4.4, five locations are selected to study the autocorrelations over the SAB. Point #1, indicated in Figure 4.4(a), is at the slant surface, whereas points #2 & #3 are associated with the bottom shear layer. The centre of the LRB and URB, respectively, are located at positions #4 and #5, as shown in Figure 4.4. Over the slant surface, the shape of R_{uu} is almost oval and elongated in the direction of flow (Figure 4.4 (a)). This indicates that the SAB has a higher degree of correlation in its fluctuating flow at the upper slant edge. Moreover, the flow reattachment causes a significant negative inclination (-45°) of the R_{uu} contours in the SAB toward the wall. Points #2 and #3 (Figure

4.4(b) & (c)) in the SAB exhibit R_{uu} contours in the lower shear layer that is more compressed and only slightly stretched in the streamwise direction than the slant surface (point #1). However, they are oriented at a positive 5° and 26° angle in the streamwise direction. The creation of the LRB is linked to the steady rise in positive angles. This means that the LRB's centre, located at point #4, stretches and correlates at an angle of around 11°, as seen in Figure 4.4(d). Finally, a R_{uu} with a negative inclination can be detected at the URB (point #5-Figure 4.4(e)) as a result of the SSB and its related downwash. These findings are consistent with the earlier discussions about the mean velocities and Reynold stresses.

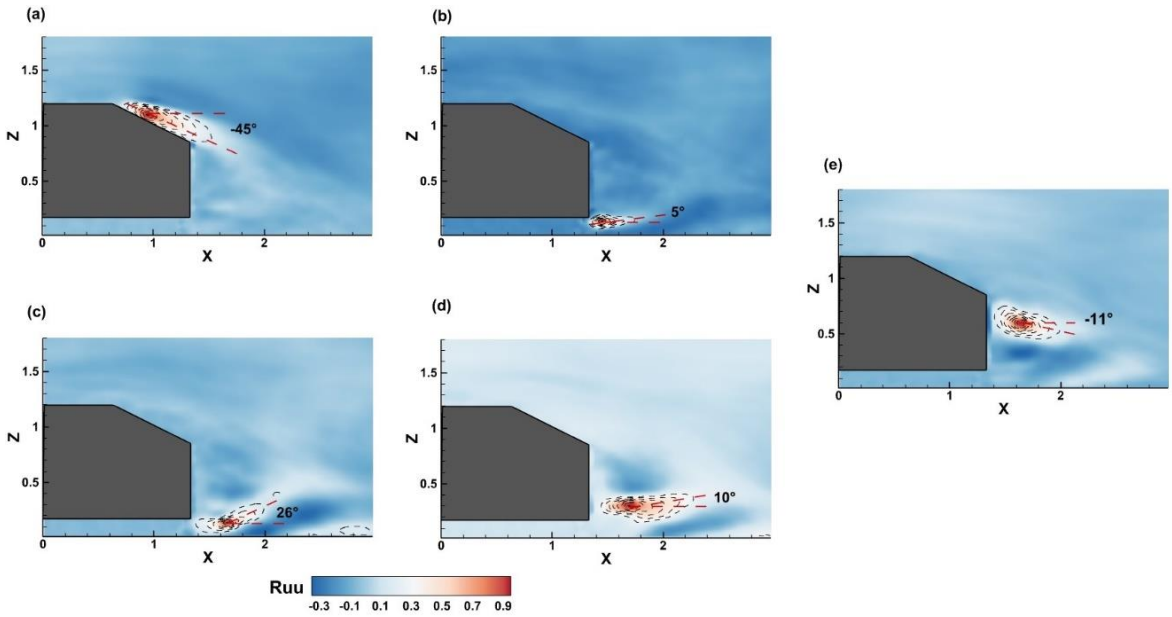

Figure 4.4: The SAB's autocorrelation contours for the streamwise fluctuating velocity R_{uu}, using slant and wake locations on the symmetry plane as reference points. Where (a) Point #1: X=0.96, Z=1.09 (b) Point #2: X=1.46, Z=0.121 (c) Point #3: X=1.66, Z=0.135 (d) Point #4: X=1.72, Z=0.284 (e) Point #5: X=1.65, Z=0.57.

(b) elliptical Ahmed body (EAB)

The two-point autocorrelation of the EAB is shown in Figure 4.5 for the six locations. Although identical in shape to R_{uu} in the SAB (at point #1), the EAB R_{uu} (Figure 4.5(a)) is far more diminutive. This indicates that there is a stronger correlation between velocity fluctuations in the SAB than the EAB. Having an inclination of only -10°, the EAB is more horizontal than the SAB (Figure 4.4(a)), which points to a separation of the flow from the slant surface. Point #2 is small and parallel to the streamwise flow in the lower shear layer

of the EAB (Figure 4.5(b)). On the other hand, point #3 in the lower shear layer is only inclined by 21° (Figure 4.5(c)) than the SAB. Since the effect of the LRB (point #4-Figure 4.5(d)) no longer exists, the shape of the recirculation region is changed. Over the inclined surface, the EAB flow separates, and the centre of the URB is shifted in the wall-normal direction. As illustrated for point #5, the repositioned URB is perpendicular to the direction of the flow (Figure 4.5(e)). Modification of the flow due to the EAB is supported by the two-point correlation and inclination patterns. As a result, the detached flow causes the size and inclination of the slant surface to be smaller than the SAB. Changes in the wake recirculation region, represented by the URB's movement, cause the patterns in the wake to diverge dramatically from the SAB.

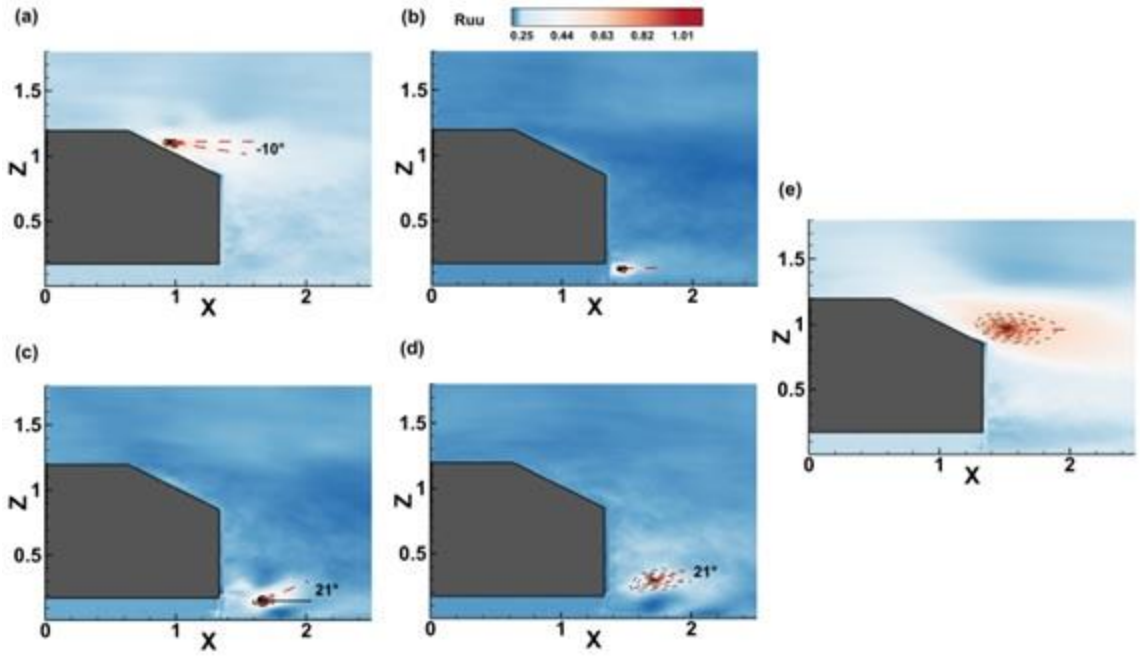

Figure 4.5: The EAB's autocorrelation contours for the streamwise fluctuating velocity R_{uu}, using slant and wake locations on the symmetry plane as reference points. Point locations are similar to Figure 4.4.

4.1.5 Frequency spectra

The effect of curvature is documented in terms of the frequency spectra in this section by calculating the associated Strouhal number. When the Strouhal number has the order of 1, then viscosity dominates the flow, and inertial separation does not occur, even at high Reynolds numbers [303]. For example, if the Strouhal number is 10^{-4}, then the flow is considered to be quasi-steady. In fact, there is a range between these orders where the flow does not behave in a quasi-steady manner due to inertial separation [303].

The velocity variations are more vigorous at low frequencies and weaken with increasing frequency [304]. Moreover, oscillations dominate the flow and are pushed away by the fast-moving fluid at a low Strouhal number. Between 0.2–0.3 Strouhal numbers, it is widely known that vortices are shed downstream of a bluff body [305]. Furthermore, Roshko [306] discovered that a decrease in the drag coefficient frequently coincides with a rise in the Strouhal number. Vino et al. [119] also observed an increased Strouhal number and associated it with drag reduction. Therefore, the investigation of the Strouhal number variations is important. The Strouhal number of the streamwise velocity fluctuations is investigated at a low Reynolds number over the slant surface and in the wake, as indicated in

Table 4.1, along with the coordinates of extracted points schematically shown in Figure 4.6.

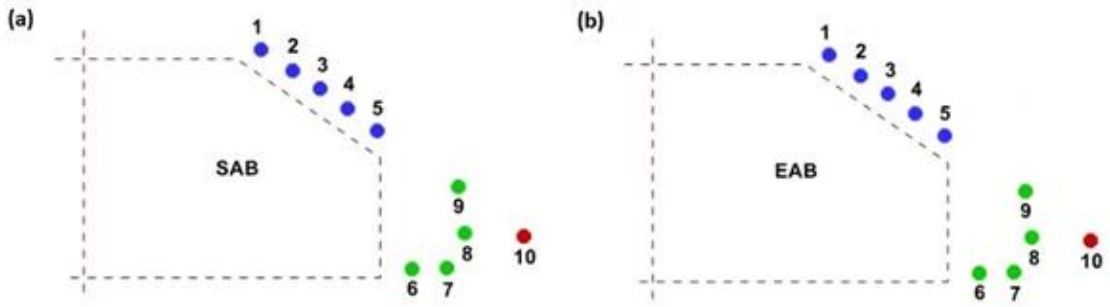

Figure 4.6: Schematic of the point location for the Strouhal number extraction. Here (a) SAB (b) EAB. The positions of the points are indicated in

Table 4.1: The Strouhal numbers for the SAB and EAB.

Re × 10^5							
4.3				**7.7 (1)***	**4.6-9.2 (2)***	**8.9 (3)***	**0.5 - 7.0 (4)***
Point No #	Locations (X, Z)	Strouhal #s					
		SAB	EAB	SAB without coating			
#1	0.84, 1.15	0.16	0.88	0.25	0.11	0.35	
#2	0.96, 1.09	0.16	0.65	0.21	0.11	-	0.20
#3	1.07, 1.04	0.16	0.95	0.21	0.11	-	-
#4	1.17,0.99	0.16	0.55	0.15	-	0.27	-
#5	1.31,0.95	0.30	0.70		-	-	-
#6	1.46,0.12	0.55	0.50	0.45	0.53	-	
#7	1.66,0.13	0.31	0.46	-	-	-	
#8	1.72,0.28	0.55	0.50	-	-	-	0.44
#9	1.65,0.57	0.61	0.23	-	-	-	
#10	2.05,0.35	0.56	0.48	0.45	-	0.42	

(1)* Numerical study by Delassaux et al. [34], (2)* Experimental study by Thacker et al. taken from [34], (3)* Minguez et al. [307] and (4)* Experimental study by [72].

(a) standard Ahmed body (SAB)

According to Table 4.1 a large area of the slant surface in the symmetry plane, a single dominant Strouhal number of S_t=0.16 is discovered. When compared to the constant S_t value of S_t=0.2 recorded by Zhang et al. [72] between points #1 and #4, the current value S_t=0.16 is close. Additionally, a sharp peak with a value of S_{t5}=0.3 can be noticed close to the rear edge of the slant surface (point #5). Even though this value is high, it still remains within the range of S_t values that have been explored in the literature. The literature reports a wide range of S_t values over the slant surface. The S_t=0.11 and 0.20, for example, are reported by Thacker et al. [308] and Zhang et al. [72], respectively, whereas S_t=0.25 and S_t=0.31 were reported by Delassaux et al. [34] and Minguez et al. [307], respectively.

According to Thacker et al. [308] the flapping of the three-dimensional separation bubble over the slanted surface is linked to a Strouhal number of S_t=0.11, whereas a small separation bubble is related to a Strouhal number of S_t=0.20 by [72]. Note that in

Table 4.1, Delassaux et al. [34] and Minguez et al. [307] are numerical studies, while Zhang et al. [72] and Thacker et al. [308] are experimental.

The S_t in the lower shear layer, LRB and URB, is shown with points #6 to #10 indicated schematically in Figure 4.6(a). A peak with the S_{t6}=0.55 (point #6) is found in the shear layer close to the model's vertical base, and this value is comparable to those reported by Delassaux et al. [34] and Thacker et al. [308]. Also, Tunay et al. [127] found St_6=0.31 and St_7=0.31 for a low Reynolds number around points #6 & 7, respectively. In addition, the LRB and URB make a major contribution to the construction of the wake structure; hence the Strouhal number is determined by their respective centre locations, indicated by points #8 and #9, respectively. The S_{t8}=0.55 and S_{t9}=0.61 show prominent frequency peaks at the centers of the LRB and URB, respectively. The fact that ordered structures are alternately emitted from the URB and LRB in the wake shows a peak at S_t=0.44 connected to quasiperiodic events discussed by Zhang et al. [72], which can be attributed to the current the SAB as well. The Saddle point (point #10) shows St_{10}=0.58, which is close to those reported by Delassaux et al. [34] and Minguez et al. [307].

(b) elliptical Ahmed body (EAB)

According to Table 4.1 due to the fully separated flow, the EAB has much higher S_t values over the slant surface than the SAB. Near the point of flow separation, S_{t1}=0.88 (Point #1), while the rear end shows S_{t5}=0.70. Here, there is no single dominant Strouhal number above the slant surface. In the EAB, a higher negative velocity is found near the wall of the slant surface than in the SAB, and the separating shear layer influences the reverse flow over the slant surface. For points #6 & #7, within the lower shear layer, the S_t values of the EAB are close to those of the SAB. A surprising difference between the EAB and the SAB is that the EAB does not show the LRB, but a higher S_{t8}=0.50 is found. However, the S_{t9}=0.23 is less than half of the SAB. The St_{10} values are similar to that of the SAB. Finally, since the URB in the EAB has shifted in the wall-normal direction, point #11 shows the centre of a shifted URB, where S_{t11}=1.14 is found. Whereas point #12 inside

the detached and separated shear layer, two dominant Strouhal numbers are present at S_{t12}=0.42 and 0.94. Overall, the flow detachment and the contribution from the shifting of URB in the wall-normal direction are responsible for the elevated S_t values over the slanted surface. The higher frequency (S_t >1) appears to be associated with the instability of the separating shear layer that initially undergoes exponential growth. This phenomenon is similar to a sphere having two modes Kim et al. [309] and also to an aircraft fuselage having high frequencies Zigunov et al. [94].

4.1.6 Proper orthogonal decomposition

The POD is used in this study to extract the dominant frequency in the wake of the SAB and EAB models. It is calculated based on the method used by Thacker et al. [304]. They reported that a wavelength (λ) could be calculated between alternate positive-negative regions of velocity and using the convection velocity as $U_o = 0.5 \times U_\infty$, the frequency of these alternate velocities can be found with $f = U_o/\lambda$ relation.

At first, Figure 4.7(a) & (b) shows the total energy percentage and the energy accumulated within the initial fifty modes. The POD is taken inside the limit of {X=1.15-3.3} and {Z=0.025- 2.05}. According to Figure 4.7(a), the relative energy captured in the 1st and 2nd POD modes in the SAB is 12.8% and 11.4%, respectively, and this drops to 4.5% in the 3rd mode. In addition, the EAB without the hydrophobic coating shows higher relative energy of 18.5% in the 1st POD mode but only 4.5% in the 2nd mode. In general, it can be observed from Figure 4.7(a) that fractional energy from the 1st POD mode to the 50th decays more steeply in the EAB compared to the SAB. Furthermore, the cumulative energy in Figure 4.7(b) shows an increasing trend, as expected. It is observed that the first 50 modes contribute to about 65% of energy in the SAB; in the EAB, the cumulative energy is closer to 55%. The results support the hypothesis that the modal energy is redistributed more gradually in the SAB compared to the EAB. These energy contributions are in a moderate range that is higher than 21.9% reported in [292] and less than 47% [304] over the SAB, depending on where the POD is applied. The first two modes are especially preferred which are used to discuss the mode patterns [310].

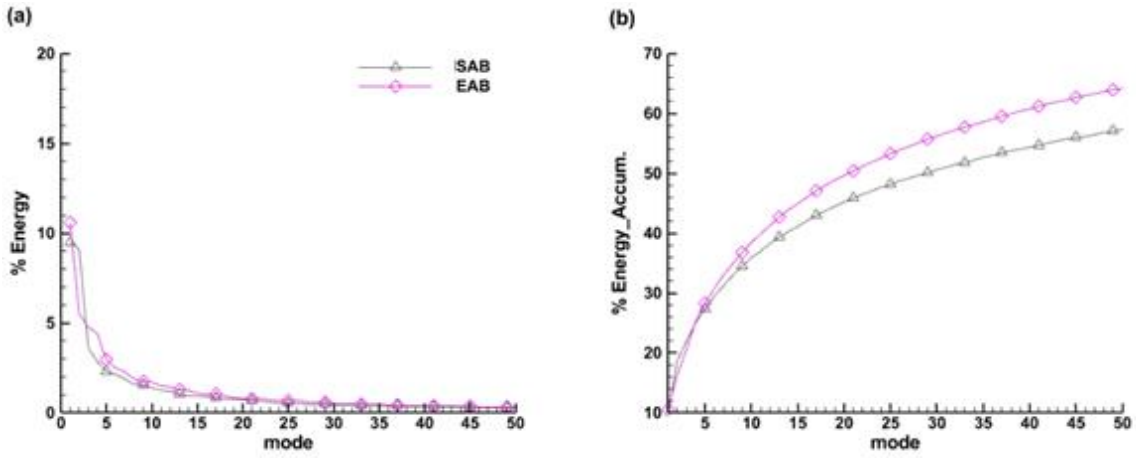

Figure 4.7: POD Energy contribution for four cases, where (a) percentage energy contribution, (b) percentage accumulative contribution

The streamwise velocity contours of the 1st and 2nd POD modes of the SAB are shown in Figure 4.8(a)-(b) and Figure 4.8(c)-(d). Thacker et al. [304] used the wall-normal velocity distribution to calculate the associated Strouhal numbers based on the $S_t=fh/U_\infty$, where h is model height. Subsequently, the 1st and 2nd mode of the SAB provides the frequency of f =0.33 & 0.48 Hz, resulting in Strouhal numbers of ~S_t=0.36 & 0.48. Even after accounting for measurement errors, these S_t values are consistent with those in

Table 4.1. Nevertheless, it is important to note that these S_t values correspond well with the S_t =0.33 discovered by [292] in the 1st and 2nd modes of the 25° the SAB. Such S_t values are attributed to quasiperiodic dynamics by [292] and [72], having S_t=0.44 and 0.54 in the wake. On the other hand, no existence of alternate negative-positive velocities is found in the EAB Figure 4.8(g)-(h). Therefore, the POD does not reveal any Strouhal number in the wake, suggesting that it might have a low value only.

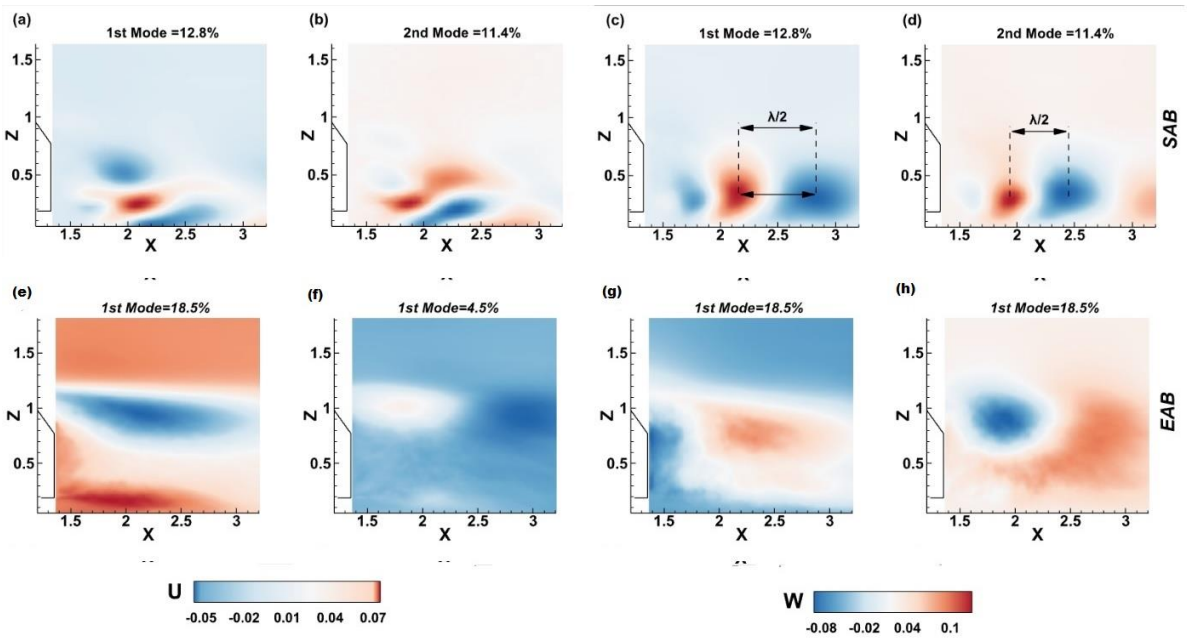

Figure 4.8: Contours of the POD modes. (a)-(d) SAB; (e)-(h)EAB; First two columns: Streamwise velocities; and last two columns: Wall-normal velocities.

4.1.7 Dynamic mode decomposition

An ideal spatial dimensionality-reduction technique is the dynamic mode decomposition (DMD), which combines the POD with Fourier transform in time. In this way, spatial modes now have a temporal frequency, possibly associated with a growth or decay rate. The DMD method, therefore, provides a spatiotemporal decomposition of data into dynamic modes derived from snapshots or measurements of a system in time. Therefore, it is possible to extract the inherent frequencies associated with the DMD modes. However, the selection of mode to represent the dynamics involved is a cumbersome issue and has been debated in the literature, which led to several variations of the DMD [311], [312]. Nonetheless, the application of DMD in the wake of the SAB and EAB provided a predominant Strouhal number calculated based on the $S_t = f_i\, h/U_\infty$). Here, $f_i = 2\pi\, \mathrm{Im}(\log(\lambda i))/\Delta t$ with λ_i as the complex eigenvalues, *h* being the model height, and U_∞ is the freestream velocity. The Strouhal number with associated DMD modes is shown in Figure 4.9(a) & (c) and Figure 4.9(b) & (d) for the SAB and EAB, respectively. It is interesting to note that the dominant Strouhal number in the SAB is S_t=0.27, which is close to the values found in the POD analysis. The corresponding DMD modes of the SAB show alternate positive and negative velocity contours in Figure 4.9(a), similar to that of the

POD. On the other hand, the DMD analysis provides a different understanding of the EAB. At first, the dominant Strouhal number for the EAB is close to S_t=0.013, and the corresponding DMD modes show an extended region of negative velocity fields. According to the literature, a lower DMD Strouhal number suggests a more energetic mode, and a higher one indicates less energetic[313]. Consequently, the mode in the SAB is less energetic than the EAB at this dominant Strouhal number.

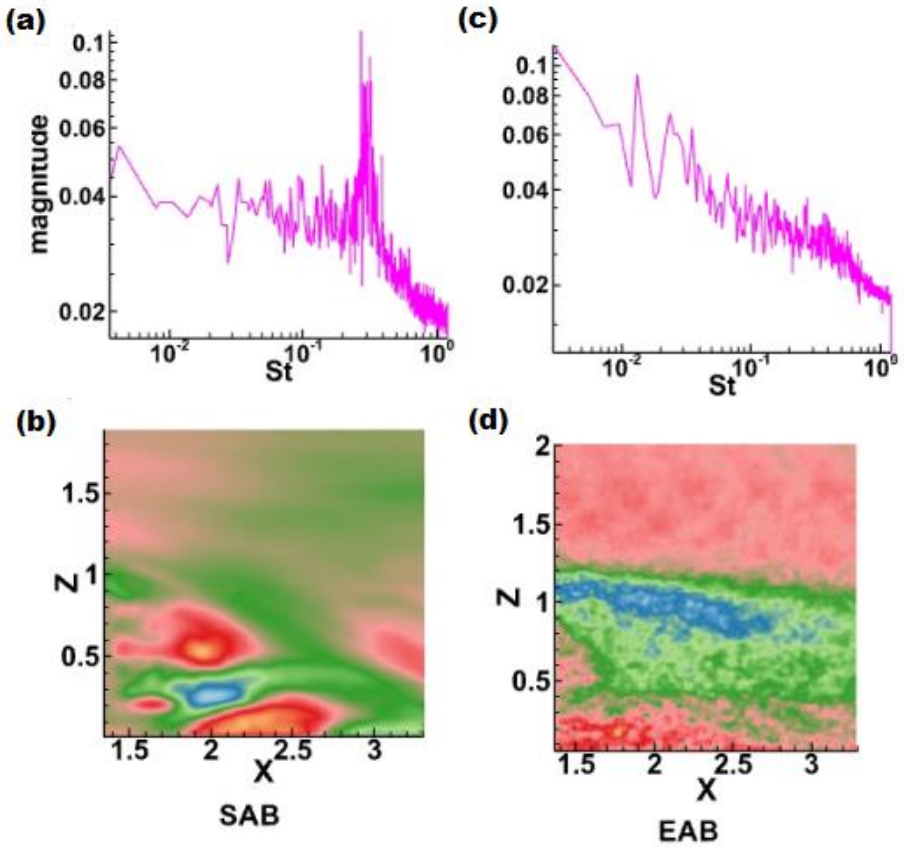

Figure 4.9: DMD analysis of the models. The first row indicates the dominant Strouhal number found in the wake of the model, and the second row shows the corresponding streamwise contour of the real part of streamwise velocity. Here (a) & (b)- SAB and (c) & (d) – EAB.

4.1.8 Flow features in the horizontal (X-Y) plane

Attention is now turned to the horizontal (X-Y) plane, where salient features of the flow will be discussed as well. It also provides some information to corroborate the discussion conducted in the symmetry plane. In order to maintain high spatial resolution, the entire flow field in this plane was not captured from the test section wall to wall, but it was ensured that the flow field from the test wall to a Y-location beyond the mid-section was

captured. Given that the Ahmed body is symmetric, the flow structures are similar with respect to its symmetric plane in this horizontal plane.

4.1.8.1 Mean velocity

Figure 4.10 shows the contours of the streamwise and wall-normal velocities superimposed with streamlines at Z=0.62. Note that this location lies close to the center of URB. The U=0 velocity line in a solid red captures the wake recirculation region. Figure 4.10(a) shows that the streamlines are in the direction of the flow as expected in the SAB. A low-velocity region exists in the wake; however, a trivial side recirculation bubble (SRB) is formed, indicated in a solid red line towards the side edge. These features are consistent with the results reported by Tunay et al. [70] who plotted the features at Z=0.67 and also captured the SRB. The spanwise velocities are observed to be higher in the wake than the streamwise velocities (see Figure 4.10(b)). On the other hand, the EAB shows two symmetric bubbles in the wake that are clearly visible in Figure 4.10(c). The symmetric bubble found in the horizontal plane at Z=0.62 in the EAB shares similarities with the wake flow structure of an elliptical cylinder as well. Within the aspect ratio of 0.25-0.67 and at a zero-degree angle of attack, the wake is dominated by a symmetric wake similar to that of the EAB and has a low drag coefficient value. Although not exactly similar to the elliptical cylinder, the EAB creates synchronous wake flow [314]. In addition to that, there is a large wake recirculation region shown by the U=0 velocity line in red (Figure 4.10(c)). The recirculation width identified as W_r in Figure 4.10(c) is 93% of the slant length. There are several studies reporting that a change in the length, height, and width of the wake recirculation region contributes to drag reduction [315]–[317].

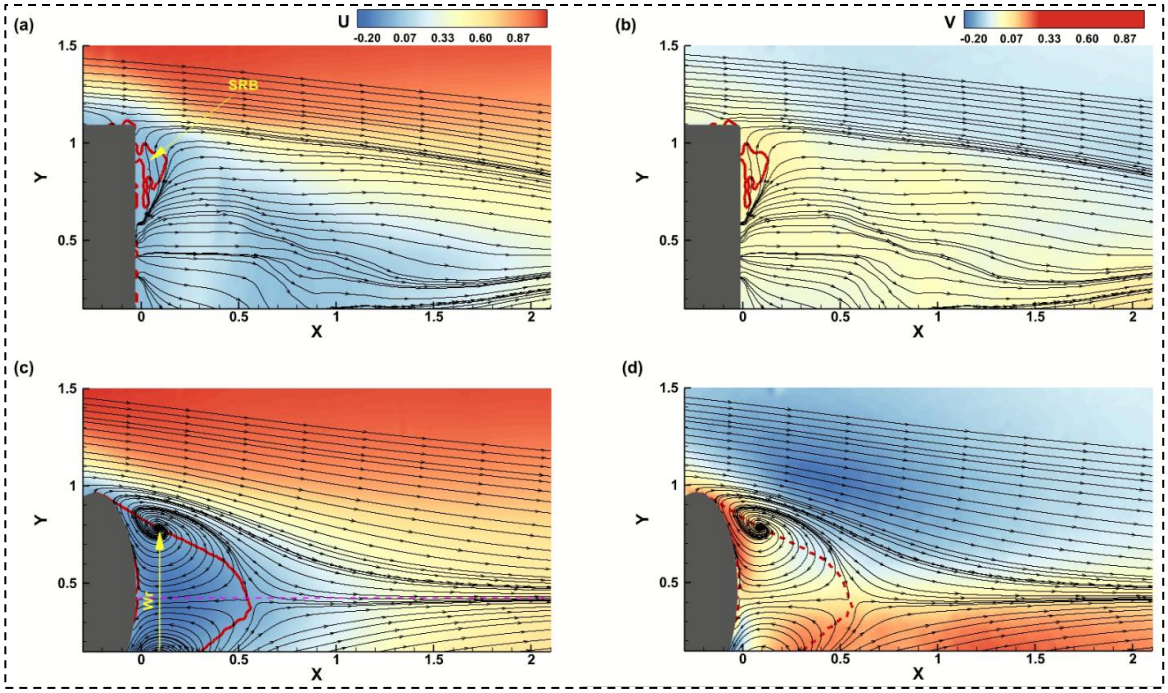

Figure 4.10: Contours of normalized streamwise mean velocity (a) & (c) and wall-normal mean velocity (b) & (d) at the horizontal plane Z=0.62 plane. Where (a) & (b) are SAB, and (c) & (d) is EAB. The streamlines of mean velocity are superimposed on the contours. The solid red line indicates U=0 velocity showing the extent of the recirculation region, and the dotted line in (c) marks the symmetry plane.

The EAB provides a significant increase in the wake width, which is one of the causes of drag reduction. The streamlines coming from the side edges merged at approximately X=0.6 and moved in a downstream direction which is not the case with the SAB. The existence of a symmetric bubble in the EAB increases the spanwise velocity, which is around 0.24, compared to the SAB, but which is only 0.05. It should be noted that the flow structure shown in the plane at Z=0.62 does not provide complete insight into the flow structure since it varies with the wall-normal distance, as reported by Tunay et al. [70]. Therefore, from the discussion above, the EAB promises to provide both drag and soiling benefits which are necessary for improved aerodynamics of the vehicle.

4.1.8.2 Reynolds stresses

The Reynolds stresses are shown in Figure 4.11 for both the SAB and EAB. It can be seen that adjacent to the model wake, a weak Reynolds normal stress exists that slightly increases in the downstream direction to around UU=0.9. This region is fed by the stresses coming out of the side edges as well. However, the existence of strong normal stresses is found at one end of the model only. In the EAB, strong normal stresses exist in the

downstream direction, similar to the SAB. Also, positive and negative shear stresses are alternately distributed. Figure 20 shows that high normal stresses (> 0.68) lie between X=0.3 and X=2.1, whereas the corresponding values in the EAB are more concentrated between only X=0.4 and X=1.3. In addition, the shear stresses are predominantly positive, with more dispersed high values over much of the wake region in the SAB. However, they are predominantly negative in the EAB. This is another demonstration of the curvature effect in the EAB.

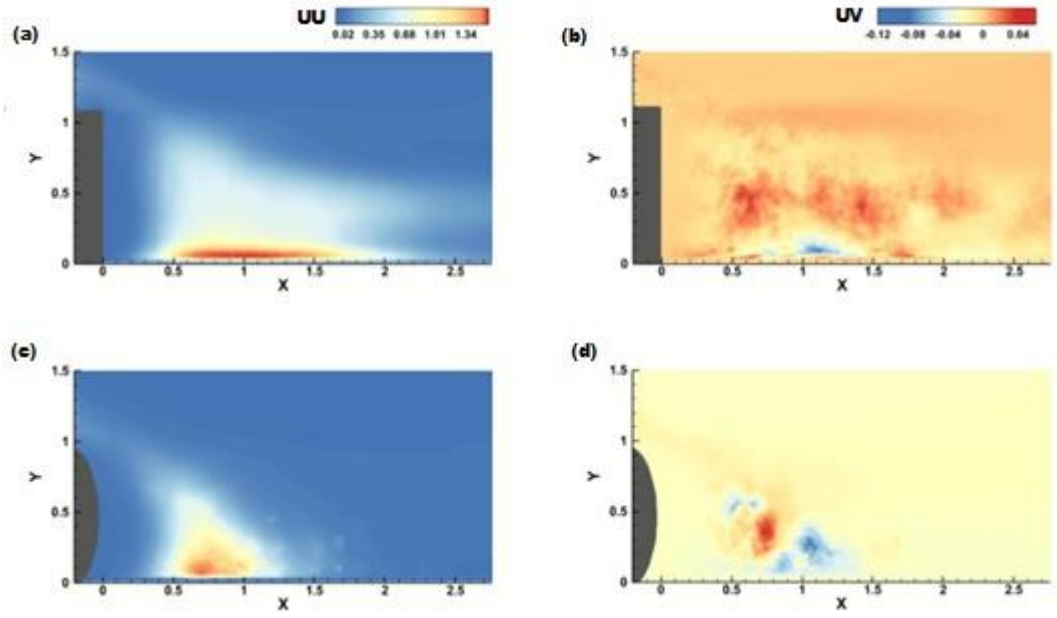

Figure 4.11: Contours of (a) & (c) streamwise Reynolds normal stresses and (b) & (d) Reynolds shear stresses at the horizontal plane Z=0.62 plane. Where (a) & (b) is SAB and (c) & (d) is EAB.

4.2 Numerical Results

In order to provide a comprehensive analysis of the effect of curvature, a detailed numerical investigation was conducted to complement the experimental studies. This section is divided into two subsections as follows: Section 4.2.1 presents the numerical analysis of the standard Ahmed body (SAB) by changing the slant angle from 25º-30º at a low Reynolds number. Section 4.2.2 reports the results of the numerical analysis of the SAB and elliptical Ahmed body (EAB) at low and medium Reynolds numbers. The simulations were performed at a slant angle of 25º and extended the Reynolds number to more applicable road vehicles.

4.2.1 Numerical Results of the Standard Ahmed body (SAB)

This section studies the effect of the slant angle on the flow structure of the standard Ahmed body (SAB). It intends to achieve an important aim to corroborate the experimental investigation reported in Section 4.1. The first aim is to understand the process of flow transition at a low Reynolds number in the SAB. The study by Guilmienau [85] found flow transition past 32º angle at a high Reynolds number. Therefore, whether such a flow transition is also found at a low Reynolds number is important to stress the critical importance of the EAB that provides a flow transition at 25º only. The flow transition is eminent since it significantly reduces the drag and changes the flow structure. There is no study to support the flow transition phenomena at a low Reynolds number, and this partly inspired this thesis to conduct a comprehensive investigation.

4.2.1.1 Mean flow

According to Yu and Bingfu [13], the pressure drag over the 25° Ahmed body is primarily generated by the rear end (64%) and the vertical base (30%), with only 6% coming from the front end. Furthermore, the rear end of the Ahmed body is subject to pressure drag caused by the separation bubbles along the slant, the C-vortices by the side edges, and the recirculation region (RR) in the wakes [10], [13]. These flow features are the focus of our analysis and discussion.

The time-averaged velocity streamlines in the symmetry plane are shown in Figure 4.12. The geometry of the front-end causes an adverse pressure gradient, resulting in an initial separation of the boundary layer from the front top roof, creating a front roof bubble

(FRB). The nature of the flow around the vehicle's front end is not exhaustively studied. A few studies are: [67], [142]. Since most of the studies only concentrate on the rear end flow, data on the front-end separation is scarce.

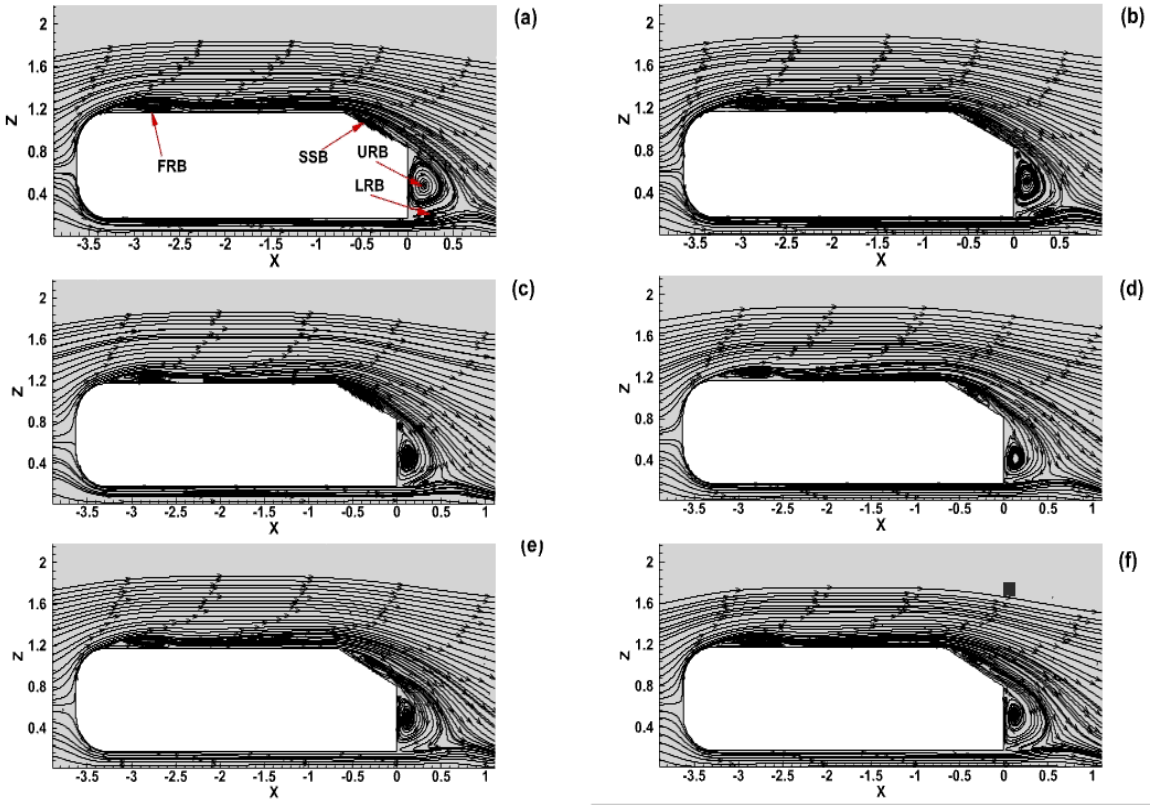

Figure 4.12: Time-averaged streamwise velocity streamlines in X-Z planet at Y=0. (a) 25° (b) 26° (c) 27°(d) 28° (e) 29° and (f) 30° slant angles. FRB- Front roof bubble, SSB- Slant separation bubble (SSB), URB- upper recirculation bubble, LRB- lower recirculation bubble.

The FRB can be seen at all the slant angles in Figure 4.12. After the creation of FRB at the front-end, the flow travels towards the rear end and separates at the upper edge of the slant surface. It is reattached at a later part of the slant surface, creating a slant separation bubble (SSB) that can be visualized at all slant angles in Figure 4.12. Following this, the flow separates again at the rear end of the slant surface and creates an upper recirculation bubble (URB) and the lower recirculation bubble (LRB), which begins to weaken after a 28° slant angle.

The iso-surface of the time-averaged velocity with an iso-value of zero to capture the various recirculation regions is shown in Figure 4.13. The dimensions of FRB are defined

as front bubble length (FBL), front bubble height (FBW), and front bubble width (FBW), SSB as slant bubble length (SBL), slant bubble length (SBH), and slant bubble width (SBW), and wake recirculation region including URB & LRB is defined as wake recirculation length (L_r), wake recirculation height (H_r), and wake recirculation width (W_r), as indicated in Figure 4.13(a). It can be visualized from Figure 4.13 that the shape of FRB for all slant angles appears similar except at 25° and 28°, where it is comparatively larger. On the contrary, the shape of SSB increases consistently in length with the slant angles. At 30°, it almost touches the rear end of the slant surface. Finally, the width of the wake looks nearly the same as the model width, which means there is no change in the wake width with the slant angle. However, it is not possible to visualize all the RR parameters from Figure 4.13. Therefore, the detailed features of these RRs are discussed as shown in Figure 4.13(a).

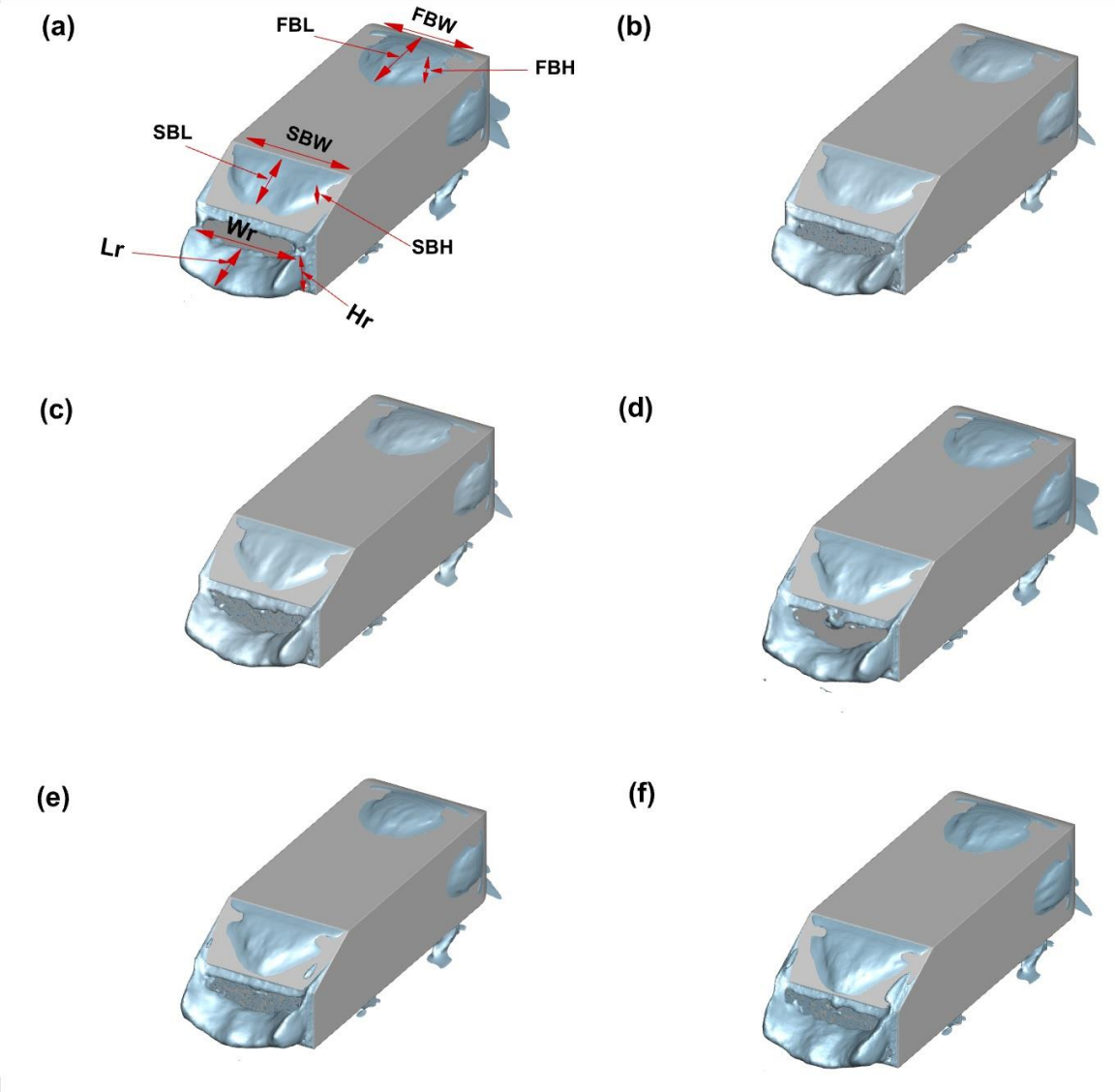

Figure 4.13: Iso-surface of the mean velocity at Iso-value of 0, where (a) 25° (b) 26° (c) 27°(d) 28° (e) 29° and (f) 30° slant angles. Here dimensions of FBL are as follows: front bubble length (FBL), front bubble height (FBW) and front bubble width (FBW), dimensions of SSB: slant bubble length (SBL), slant bubble height (SBH) and slant bubble width (SBW), recirculation length (L_r), recirculation height (H_r) , and recirculation width (W_r).

As discussed in Figure 4.13, the dimensions of RRs are listed in Table 4.2. The parameters FBL, FBH, and FBW do not vary much with the change in slant angle. The FBH varies only 0.1% of the roof length, while FBL & FBW show a variation of around 0.5% of the roof length. These results are apparent because SBL and SBW will be higher than FBH due to geometrical differences at the front-end and rear end. The existing literature does not report front-end recirculation lengths for every slant angle. However, the FBL is reported by Krajnovic and Davidson [142] with full-scale LES simulation

around the 25°Ahmed model at Reynolds number of 2×10^5 using different grid sizes. The FBL decreases when the grid size increases from coarse to fine. While a coarse mesh shows the FBL as 0.23*h*, the fine mesh is significantly reduced to 0.08*h* [142]. The present IDDES simulation found FBL to be 0.91*h*. This length is close to that of Minguez et al. [148] who found 0.95*h* at a low Reynolds number of 8322 and 0.7*h* at a high Reynolds number 7.68×10^5. Furthermore, the FBL at a 30° slant angle is reported in an experimental study by Sime-Williams and Dominy [82] using the full-scale 30° Ahmed model at a Reynolds number of 1.71×10^5. They reported a length of 0.2175*h*, while the present IDDES simulation found a value of 0.93*h*. It can be seen that the front-end recirculation region shows large differences. However, these differences can be attributed to the Reynolds numbers, as reported by Minguez et al. [148] that a low Reynolds number provides a higher FBL compared to a high Reynolds number.

Table 4.2: Dimensions of the recirculation regions. Refer to Figure 4.13 for nomenclature.

	Dimensions of FRB			**Dimensions of SSB**			**Dimensions of wake**			**(1)***	**(2)***	**(3)***	**(4)***
Ang.	FBL	FBH	FBW	SBL	SBH	SBW	L_r	H_r	W_r				
25°	116	10	105	75	3.2	137.5	76	43	159	77	75	83	71
26°	117	6	96	77	3.8	118	70.8	46	159				
27°	121	9	93.4	79.1	4.8	110.2	66	36	159				
28°	121	9	101	85	5.8	108.8	50	36	159				
29°	112	7.7	90.8	92.1	7.7	105	70	42	159				
30°	120	8	93.4	95	9.2	103.7	71	44	159	87			

(1)* Guilmineau [85] (2)* Rossitto et al. [32] (3)* Zhang et al. [72], (4)* Liu et al. [76]

Table 4.2 also shows the effect of the slant angle on the dimensions of SSB. There are a few important conclusions that can be drawn here. First, there is a consistent increase in the SBL with the slant angle. At 25°, the reattachment point of SBL is located at 76% of the slant length. This change is consistent with 77% of the slant length reported from the IDDES simulation and 72% by experiment at 7.68×10^5 Reynolds number [85]. Rossitto et al. [32] also reported the reattachment point to be 75% of the slant length. The SBL further increases with the slant angle, and at the critical angle of 30°, the reattachment point is 95% of the slant length. This is on the verge of transition from the slant surface. However, according to Guilmineau [85], the SBL is 87% at 30° and 95% at the 32° angle of the slant length. Consequently, he found flow transition above 32° slant angle. The current study at a low Reynolds number achieves a reattachment point of 95% of the slant length at a 30° angle; the flow does not show transition to QAS but is close to transitioning. Secondly, along with the SBL, the SBH also increases with the slant angle. The SBH increases from 25° with 3.2% of the slant length to 9.2% at 30°. Thus, the slant angle increases both SBL and SBH. Such an increase in the SBL and SBH of the SSB is advantageous for transition. Thirdly, SBH decreases with the slant angle except at 28°, where it slightly increases. All these conclusions can also be visualized in Figure 4.13. The SSB can grow in length and decrease in height with the slant angle. Compared with 25°, the iso-surface of the velocity at 30° demonstrated the facts presented above.

Furthermore, the percentage change in the L_r and H_r with respect to the slant angle is listed in Table 4.2. The L_r for the 25° is ~0.58, which is 76% of the slant length. This is close to the value of ~0.64 reported in [72], ~0.67 in [124], ~ 0.65 in [77] using volumetric PIV, and ~0.55 reported in [76]. The slant angle generally decreases the L_r and H_r, reaching a minimum of around 28° angle. The 28° slant angle has been investigated by Howard [134] using LES at 4.29×10^6. They found a fully detached flow which was similar to the post-critical angle (30°) low-drag regime Ahmed body. Nevertheless, other LES simulations captured the flow features of the 25° Ahmed body similar to the present study [98], [148]. Thus, the 28° Ahmed flow features are not completely understood. The present study as well found the variations at the 28° angle, which motivates studies to examine the physics behind such variations critically. Moreover, the effect of the length and height of the URB on the pressure drag is discussed by some existing studies [315]–[317].

Accordingly, an increased L_r and reduced H_r help reduce the pressure drag. Furthermore, the reduction in wake width is a strong indication of base pressure recovery [316]. For the TAR, the W_r does not change and implies it does not contribute to drag reduction.

4.2.1.2 Pressure coefficient

The pressure coefficient (C_p) over the Ahmed body is shown in Figure 4.14, according to Eqn. (3.25). The change in the slant angle does not affect the negative C_p area for the FRB. However, the C_p of SSB was reduced with a slant angle. The formation of the C-vortices can also be seen, and the increase in slant angle leads to pressure recovery in the C-vortices, as shown in Figure 4.14. However, to further investigate the changes in the pressure inside the RR's and C-vortices C_p is plotted in Figure 4.15(a) at the five different locations indicated in Figure 4.14(a), where C_{p1} is a point inside FRB (as defined in the caption for Figure 4.14). Also, C_{p2} & C_{p3} within SSB, C_{p4} shows the point at the vertical base, and C_{p5} indicates the C-vortices (See Figure 4.14(a)).

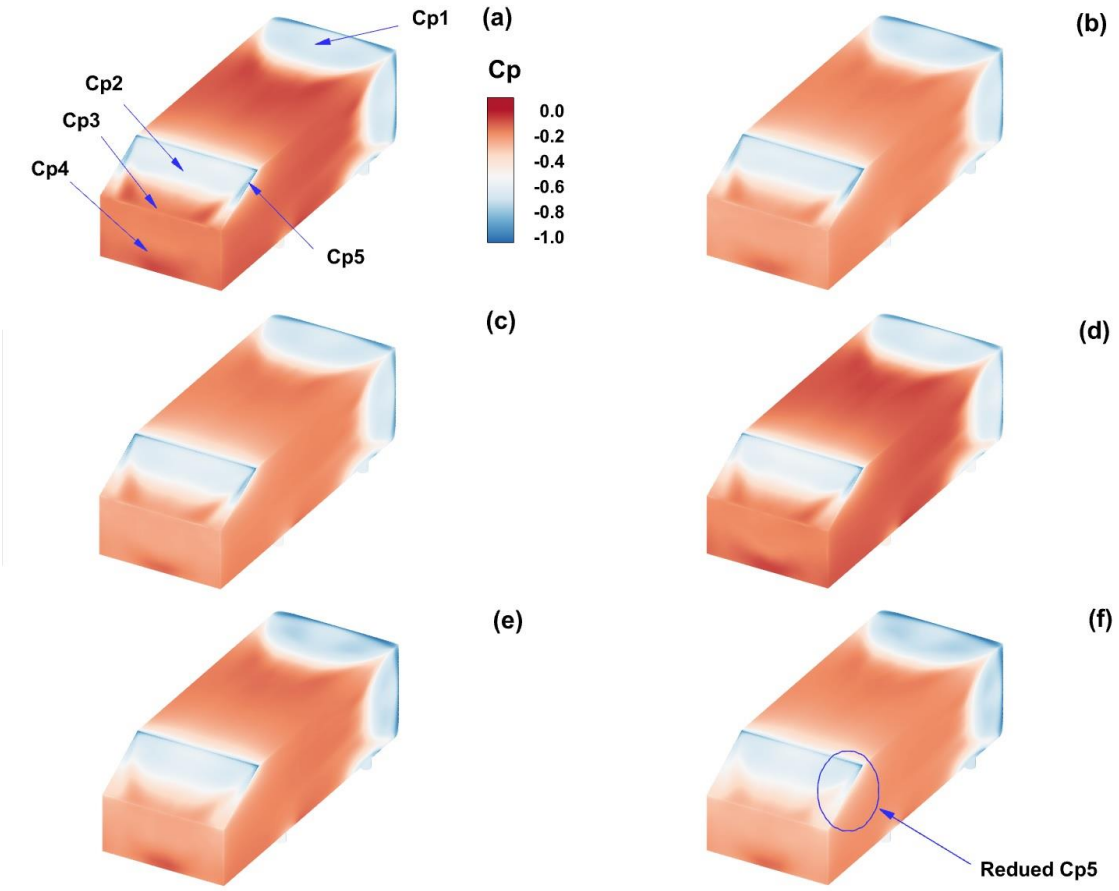

Figure 4.14: The distribution of pressure coefficient over the Ahmed body where (a) 25° (b) 26° (c) 27°(d) 28° (e) 29° and (f) 30°. Where Cp1 is taken at X=-0.28,Y=0, Z=1.17, Cp2 at X=-0.40, Y=0, Z=1.03, Cp3 at X=0, Y=0, Z=0.86, Cp4 at X=0, Y=0, Z=0.3 and Cp5 at X=0.48,Y=0.65,Z=1.05.

Figure 4.15(a) shows that C_{p1} increases with the slant angle up to 27° and decreases at 28° before rising again at 29°. The difference in the C_{p1} values is not significant with the slant angle. Similar trends are exhibited in C_{p2}, $C_{p3,}$ and C_{p4}. In all these cases, a slight pressure recovery is demonstrated at 28°, which is not consistent with the results of existing studies that show a consistent rise in drag coefficient with the slant angle. Consequently, the C_p at the rear end is expected to also decrease with a slant angle. The low pressure at the C_{p1} is due to the flow separation at the front-end, followed by the SSB, where the C_{p2} slightly increases compared to the front-end. However, compared to the C_{p1} and C_{p2}, a considerable pressure recovery is displayed at C_{p3} and C_{p4}. Inside the SSB, the C_{p2} =-0.6, and just after the SSB, it increased to $C_{p2=}$-0.2. Figure 4.15(b) shows the percentage change between the C_p values inside FRB and SSB. The %C_{p1-2} indicates the C_p recovery between

a point inside FRB and SSB, as shown in Figure 4.15(b). The flow shows a pressure recovery between C_{p1} to C_{p2} and is highest at a 30° angle with a 16% recovery.

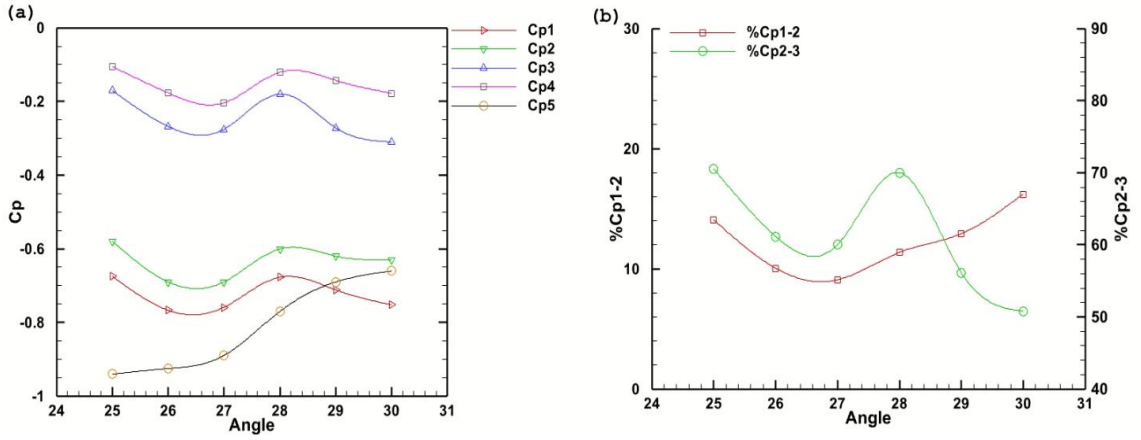

Figure 4.15: (a) Variation in the pressure coefficient with slant angle at symmetry plane (Y=0). (b) % Change between Cp1 & Cp2 denoted as %Cp1-2, Cp2 & Cp3 denoted as %Cp2-3. For location of Cp points, refer Figure 4.14.

On the other hand, $\%C_{p2-3}$ highlights the comparative pressure recovery between a point inside SSB and just outside. At 25°, C_{p2}=-0.58 and C_{p3}=-0.17 provided a recovery of around 70%. Nevertheless, at 30°, the C_p recovery drops to around 50% between the points at C_{p2}=-0.63 and C_{p3}=-0.31. Furthermore, the inside of the C-vortices C_{p5} shows consistent recovery with the slant angle. At 25°, the C_{p5} around the C-vortices has an approximate value of C_{p5}=-0.94, and at 30°, C_{p5}=-0.66. It shows a C_{p5} recovery of almost 30% at 30° compared to 25°. The impact of C_{p5} is emphasized in the next section. Similarly, from Figure 4.15(a), the change in the C_p can be seen for any particular slant angle as well. At a 25° angle, the C_p shows continuous pressure recovery from C_{p1} to C_{p4}. All the other angles follow this trend, and a significant pressure recovery is found after C_{p2} for all the angles.

All these RRs can also be observed in Figure 4.16, which shows the iso-surface of the pressure at an iso-value of C_p=-2 to display the necessary RRs and C-vortices. Along with the existence of low-pressure separation bubbles (FRB & SSB), C-vortices coming out of the side edges are also captured for all the slant angles. Especially the size of the SSB appears to increase with the slant angle except at the 28° angle. Another critical piece of information is the increased size of the C-vortices with slant angles. As the C-vortices grow in size, it merges with the SSB. The C-vortices constrain the flow at the slant surface to

spread spanwise. Consequently, the increased C-vortices at a 30° angle merged with the SSB and reduced the SBW. This explanation is supported by Table 4.2, where SBW decreases with the slant and is further discussed in the next section.

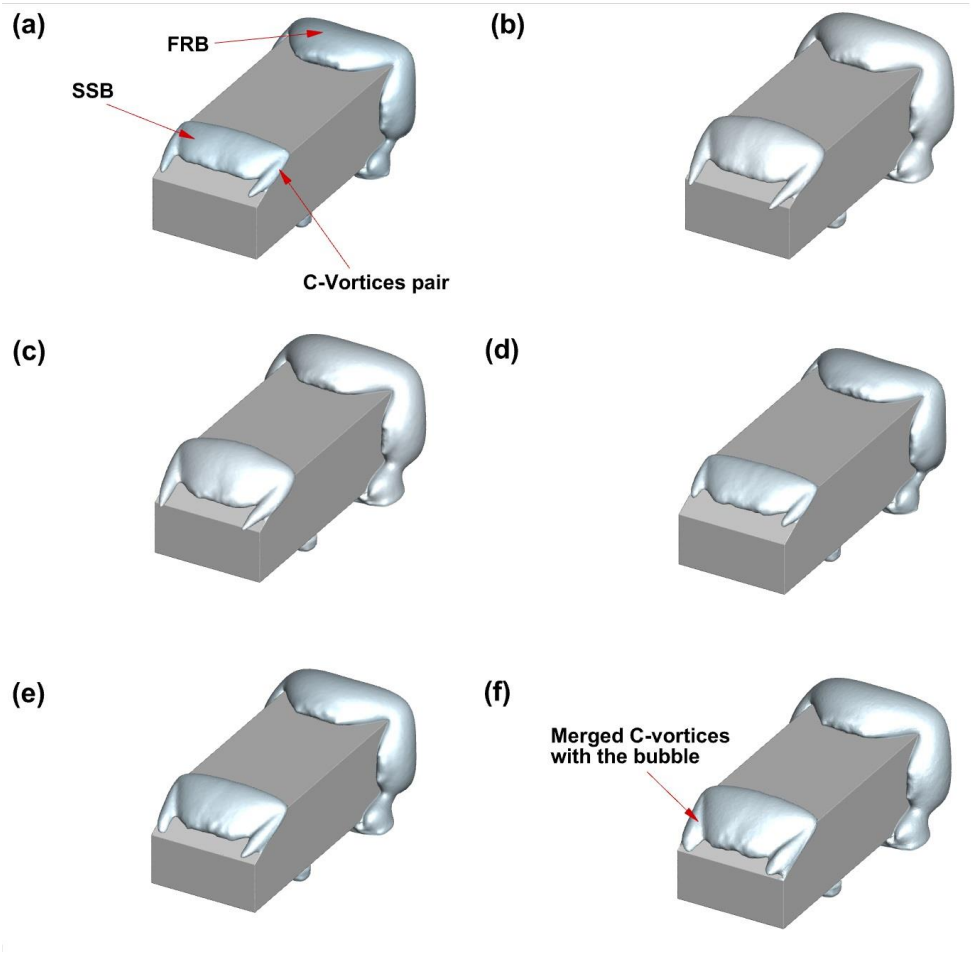

Figure 4.16: Iso-surface of the pressure at an Iso-value of -2, where (a) 25° (b) 26° (c) 27°(d) 28° (e) 29° and (f) 30° slant angles.

4.2.1.3 C-vortices

The discussion in the previous sections highlighted the effect of the slant angle on the geometric parameters of the RR's. However, the issue of transition from the slant surface, which is supposed to occur at a critical angle of 30°, needs further investigation [85], [127]. In the current study, the slant angle is reported to increase the SBL, which at the 30° angle extends to almost 95% of the slant length. This increase has a corresponding increase in SBH but a reduction in SBW with the slant angle [85]. The proceeding information helps to provide some insight into the effect of the slant angle on the C-vortices. Figure 4.17,

Figure 4.18 and Figure 4.19 show the time-averaged normalized streamwise velocity in the cross-section planes X=-0.35, X=0 and X=0.28.

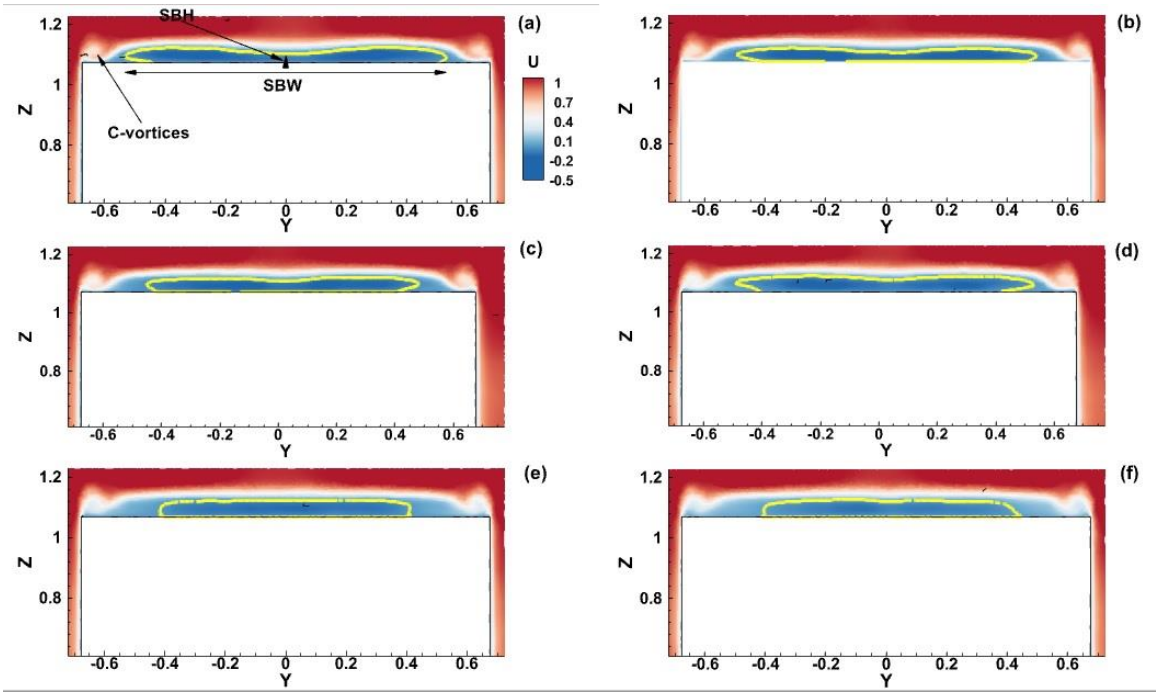

Figure 4.17: Normalized time-averaged streamwise velocity contours at the slant surface separation located at X=-0.35. The solid dashed yellow line shows the zero-velocity contour line to capture the RR. (a) 25° (b) 26° (c) 27°(d) 28° (e) 29° and (f) 30° slant angles.

The separating contour line at the core shows the zero streamwise velocity indicating the SSB over the slant surface. The existence of the C-vortices pair is found, and SBH and SBW are the parameters of SSB, as shown in Figure 4.17(a). At first, a consistent reduction in the SBW value with increasing slant angle can be observed, with the lowest SBW value at 30°. Additionally, SBH increases with the slant angle, reaching a maximum of 30°. These two images in Figure 4.17 agree with Figure 4.13(c) & (f). At 25°, however, the C-vortices show the highest streamwise velocity, but this value continuously reduces with the slant angle. For example, from the slant angles of 25° to 30°, the streamwise velocity decreased from 0.9 to 0.1, an 89% reduction.

Although the C-vortices lose energy with increasing slant angles, they grow in size with downstream distance. Figure 4.18(a) displays the time-averaged streamwise velocity contour at the slant rear end X= 0 for all the slant angles. The pair of C-vortices are shown with C-V1 in Figure 4.18(a). Along with C-V1, there are small negative C-vortices

indicated as C-V2 in Figure 4.18(a). Additionally, at X= 0, a positive streamwise velocity rear bubble can be seen, which exists outside the SSB. As the slant angle increases, C-V1 grows in size and becomes weaker. At 30°, C-V1 merges with the positive streamwise velocity rear bubble in Figure 4.18(f). Along with C-V1, C-V2 also grows in size with a slant angle. However, C-V2 is dominated by negative streamwise velocities. Furthermore, the C-vortices restrict the flow on the slant from spreading in the spanwise direction. This is one of the reasons found in the present analysis for reducing SBW as the slant angle increases.

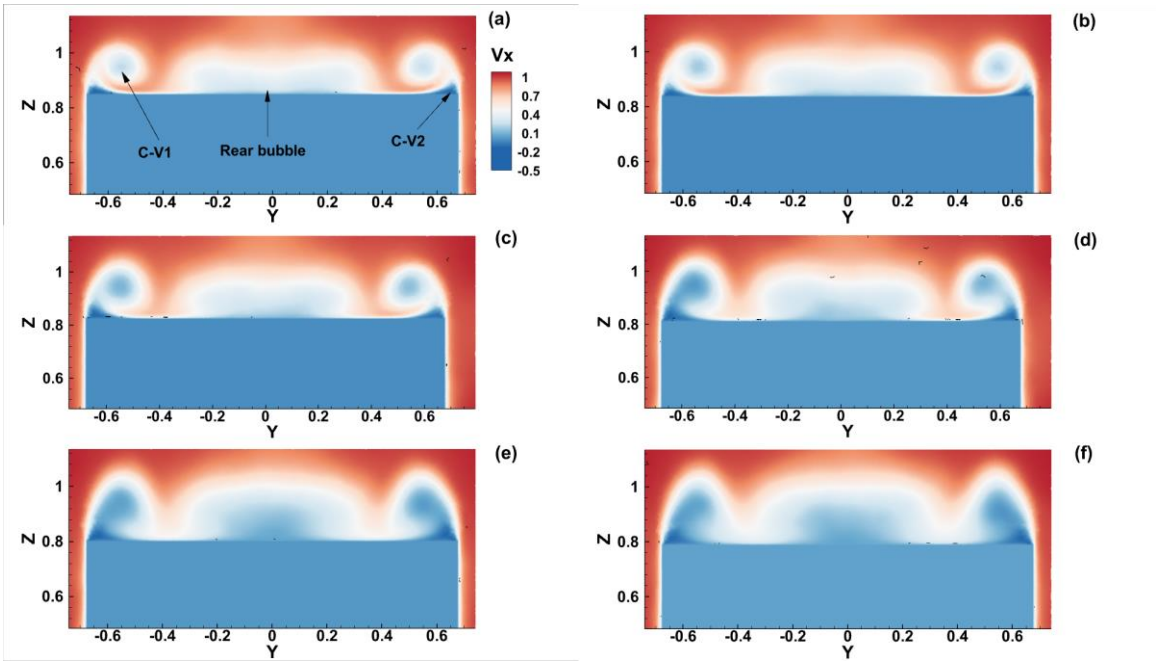

Figure 4.18: Normalized time-averaged streamwise velocity contours at the slant rear end located at X=0. (a) 25° (b) 26° (c) 27°(d) 28° (e) 29° and (f) 30° slant angles.

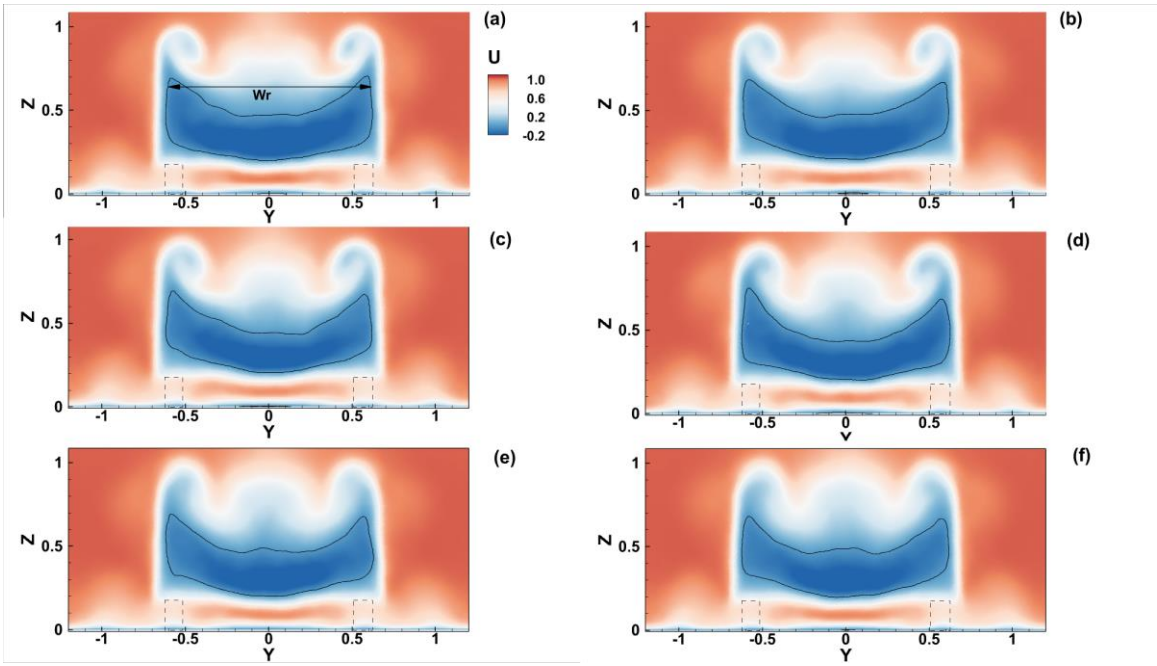

Figure 4.19: Normalized time-averaged streamwise velocity contours at X= 0.28. (a) 25° (b) 26° (c) 27°(d) 28° (e) 29° and (f) 30° slant angles.

In Figure 4.19, time-averaged streamwise velocity contours are shown just after the end of the slant surface inside the wake recirculation. At this location, the C-vortices can still be seen up to a slant angle of 28°, after which they merge with the shear layer from the top. Nonetheless, the change in slant angle does not affect the wake width (SBW), which remains consistent for all the slant angles and implies that it has no contribution to the pressure drag. Furthermore, according to Table 4.2, the percentage change in SBL and SBH is relatively small, and except for 28°, all of them are similar. It indicates that the shift in SBL, SBH, and SBW also depends on the slant height.

4.2.1.4 Vortex identification

Instantaneous vortices can help better understand the unsteady 3D wake structure around the Ahmed body. A variety of methods can be used, including the Q-criterion based on the complex eigenvalues of the velocity gradient tensor, Δ-criterion which is the second invariant of the velocity gradient tensor, the swirling strength λ_{ci} and the λ_2 criterion [147]. In this study, both the Q and λ_2 criteria are used to analyze the vortical structures around the Ahmed body.

(a) Q-criterion

Figure 4.20, Figure 4.21, and Figure 4.22 show the iso-surface of the Q-criterion colored by the normalized time-averaged streamwise velocity for all the slant angles. Figure 4.20 shows the three-dimensional isometric view, Figure 4.21 displays the top view, and Figure 4.22 exhibits the underbody vortical structures. For all the figures, an iso-value of -15 is chosen to extract the salient flow features from the data.

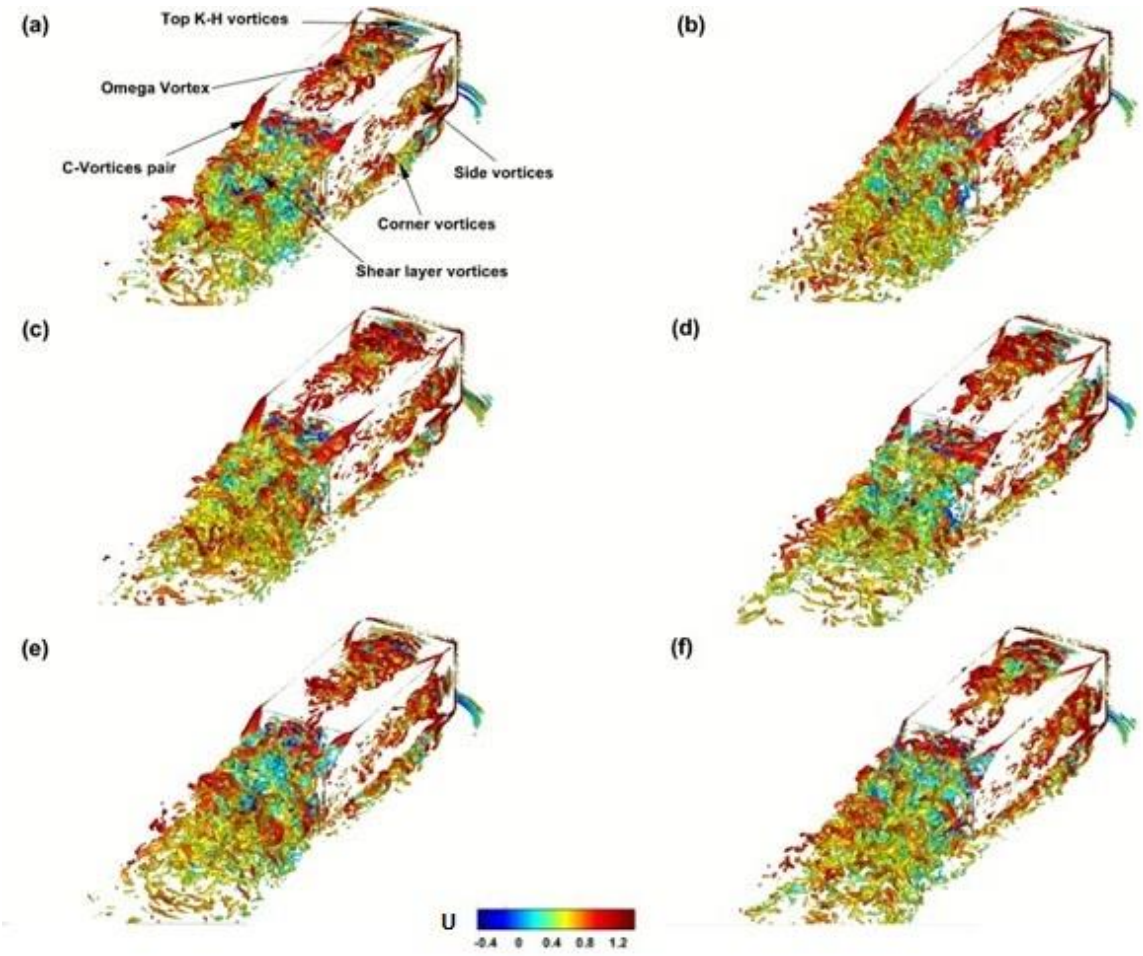

Figure 4.20: Three-dimensional Iso-surface of the Q-criterion colored by the normalized time-averaged streamwise velocity at an Iso-value of 15. (a) 25° (b) 26° (c) 27°(d) 28° (e) 29° and (f) 30° slant angles.

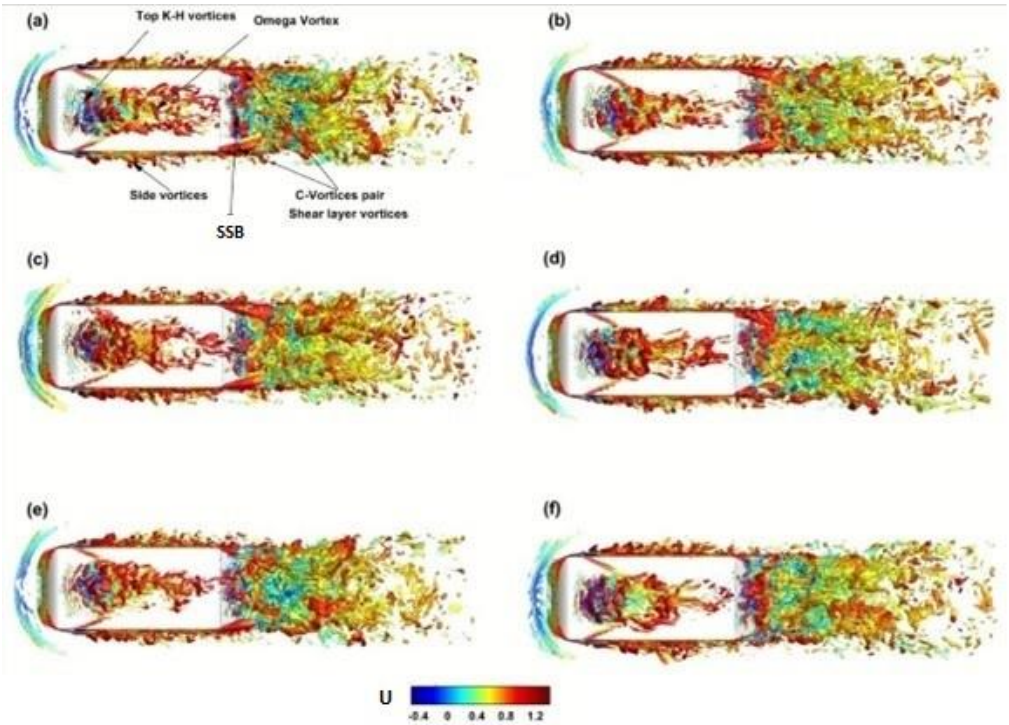

Figure 4.21: The top view of the Ahmed body Iso-surface of the Q-criterion colored by the normalized time-averaged streamwise velocity at an Iso-value of -15. (a) 25° (b) 26° (c) 27°(d) 28° (e) 29° and (f) 30° slant angles.

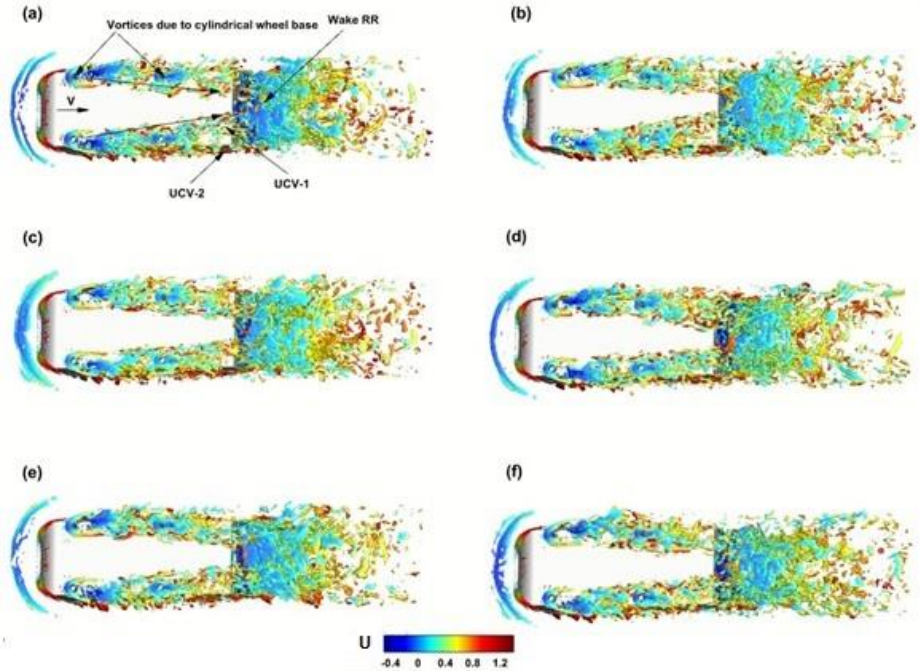

Figure 4.22: The underbody of the Ahmed body Iso-surface of the Q-criterion colored by the normalized time-averaged streamwise velocity at an Iso-value of -15. (a) 25° (b) 26° (c) 27°(d) 28° (e) 29° and (f) 30° slant angles.

In Figure 4.20, due to the separated shear layer, the vortices at the front end are dominated by the Kelvin-Helmholtz (KH) instability which can be seen at all the slant angles (indicated in Figure 4.20(a)) [147]. As the flow reattached to the roof, hairpin-like vortices (Figure 4.20(a) - Omega vortex) emerge due to boundary layer development with the corner vortices along the side edges. Similarly, the emergence of vortical structures can also be seen surrounding the side surface of the body. Especially the prominent distinguishing feature, the SSB at the slant and a pair of counter-rotating C-vortices, is also evident in all the cases. It can be seen that compared to the 25°; the C-vortices are dominated by less energetic vortices; as the slant angle increases, the angle and, at 30°, merge with the SSB. The underbody vortical structures that begin at the front end travel the body length to merge with the shear layer coming from the top to create interesting structures of the vortices in the wake of the body

Similarly, in Figure 4.21, the top view illustrates the hairpin-like vortices over the roof. The existence of FRB (visualized with negative velocity) can be seen due to flow separation at the front end at all angles. These vortices are joined by two small vortices (shown with a black circle in Figure 4.21(a)) coming from the side edges of the front end in all the cases. The hairpin vortices look almost symmetric to the Y=0 plane over the roof with slant angles. Afterward, the flow separates at the slant surface to form the SSB, where the negative velocities exist at all the angles shown in Figure 4.21(a)). Finally, the shear vortices in the wake are symmetrically distributed in the downstream direction.

Figure 4.22 captures the underbody vortical structures with slant angles. The vortices due to the cylindrical wheels can be seen at the front and then in the middle of the underbody. The vortices around the first pair of cylindrical stilts have more negative vortices compared to the second pair downstream. These vortical structures move towards the rear end but bifurcate into two underbody corner vortices (UCV), shown as UCV-1 and UCV-2 (Figure 4.22(a)). The UCV-1 flows inwardly towards the rear wake structure as indicated by black arrows and merges. Consequently, the UCV-2 remains corner vortices coming out of the underbody along with the side corners. However, it should be noted that the UCV-1 has negative vortices compared to the UCV-2, which has positive ones. Such a development displays a V shape flow (shown with arrows) under the body caused by the

presence of the cylindrical wheels. The vortices at the wake RR can be seen for all the slant angles and are symmetric around the symmetry plane.

(b) λ_2 criterion

The general flow structures captured by both the Q and λ_2 criteria are the same, which is also mentioned by Kang et al. [147]. However, the λ_2 criterion provides a more accurate vortical structure (Figure 4.23(a) highlighted with a circle at the front-end) of the K-H instability at the front part, which is not fully captured by the Q-criterion. All the slant angles show this trend of the matured effect of the front-end separation-reattachment phenomena. This effect is also visible on the side faces of the models, which show complex vortical structures associated with the front-end separation (Figure 4.23 and Figure 4.24). Furthermore, although the Q-criterion can show the existence of the C-vortices (Figure 4.20) for all the slant angles, the λ_2 criterion provides the more complex development of the C-vortices over the slant surface highlighted with a circle in (Figure 4.23(a)). On the other hand, the Q-criterion indicates vortical structures some distance downstream of the slant surface while λ_2 criterion displays starting with the upper slant edge. It can be seen in both the iso-metric (Figure 4.23 highlighted with a circle at the rear end) and top view (Figure 4.24 highlighted with a circle) of the λ_2 criterion. Finally, at the underbody (Figure 4.25), λ_2 criterion captures the vortical structures due to cylinders along with the UCV-1 and UCV-2, similar to the Q-criterion.

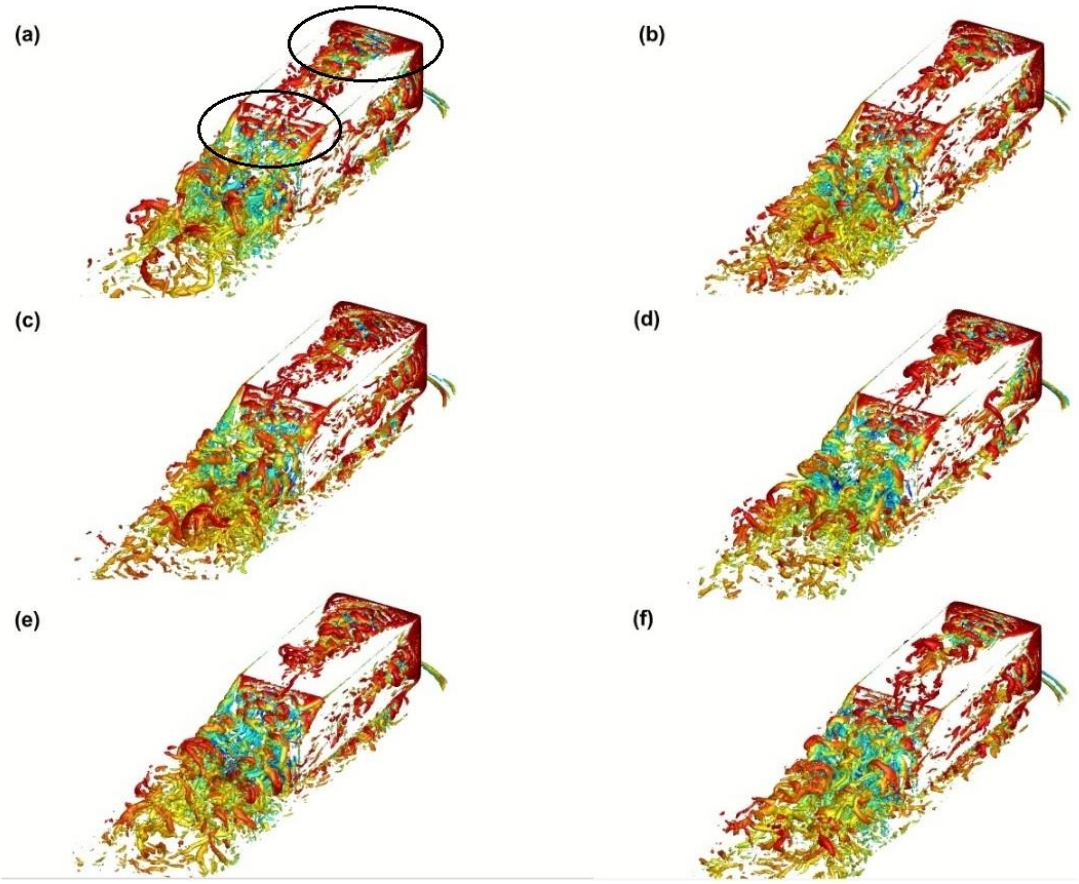

Figure 4.23: Three-dimensional Iso-surface of the λ_2 -criterion coloured by the normalized time-averaged streamwise velocity at an Iso-value of -1500. (a) 25° (b) 26° (c) 27°(d) 28° € 29° and (f) 30° slant angles.

Thus, the comparison between the Q-criterion and λ_2 criterion shows a general behavior in a similar manner. However, λ_2 criterion is more precise in extracting the front-end separation, flow separation at the upper slant edge, and complex system of the C-vortices development at all angles.

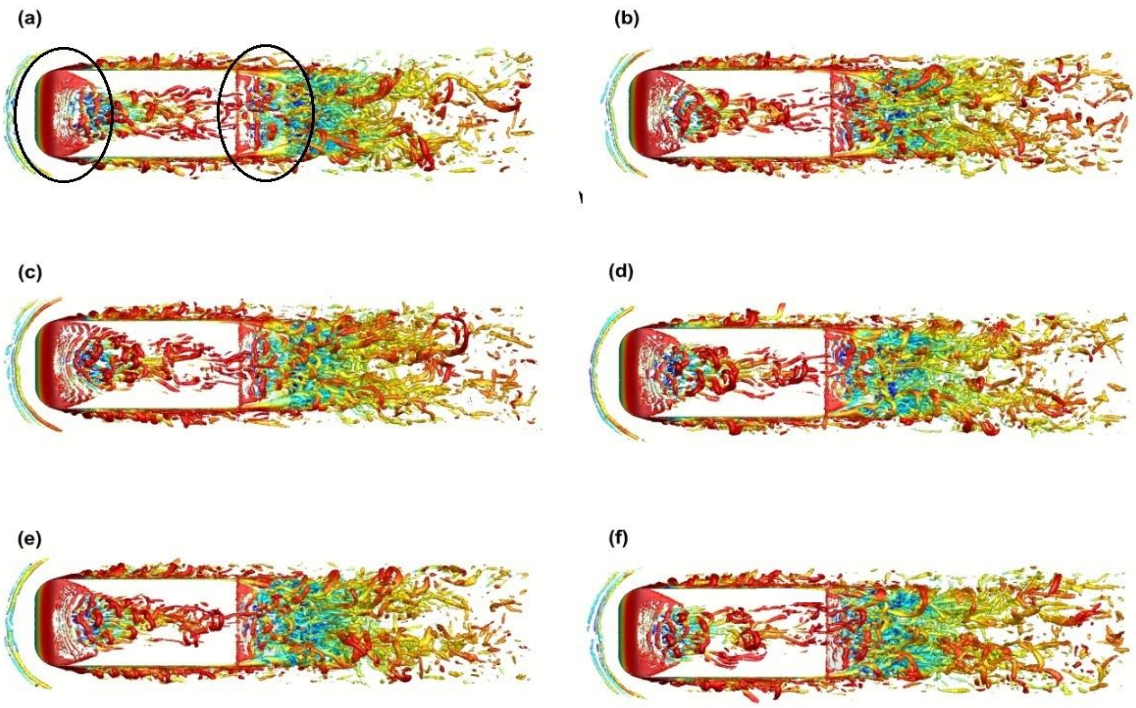

Figure 4.24: The Top view of the Ahmed body Iso-surface of the λ_2-criterion coloured by the normalized time-averaged streamwise velocity at an Iso-value of -1500. (a) 25° (b) 26° (c) 27°(d) 28° (e) 29° and (f) 30° slant angles.

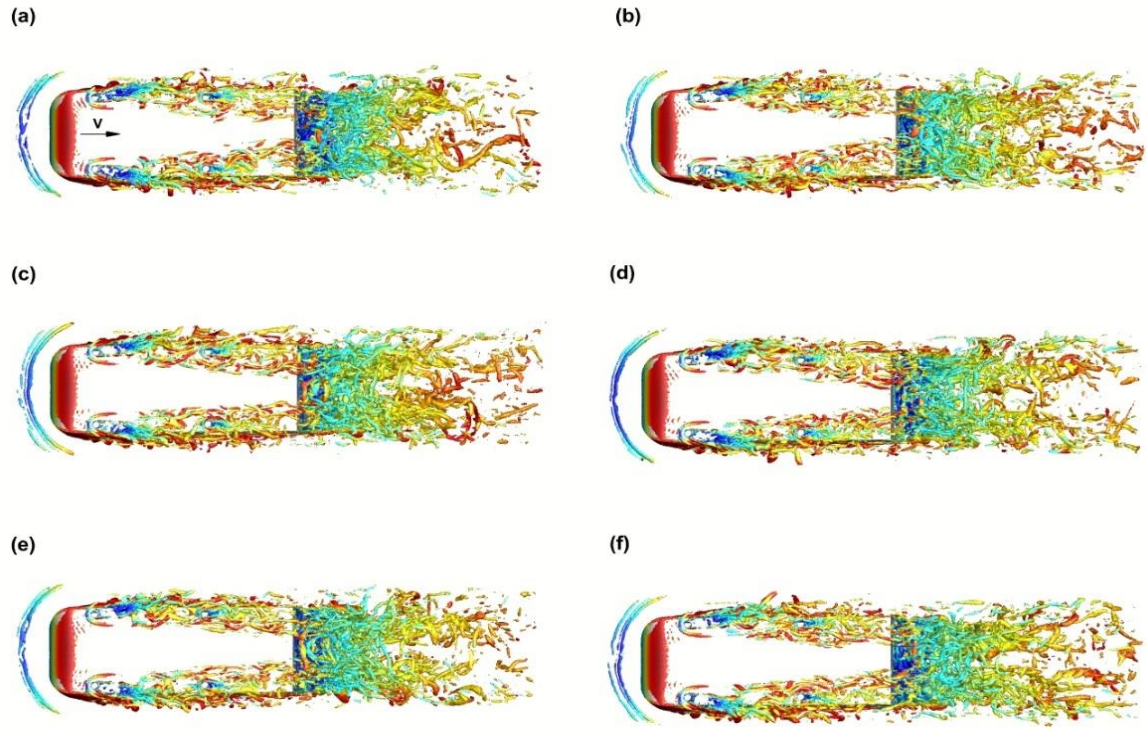

Figure 4.25: The underbody of the Ahmed body Iso-surface of the λ_2-criterion colored by the normalized time-averaged streamwise velocity at an Iso-value of -1500. (a) 25° (b) 26° (c) 27°(d) 28° (e) 29° and (f) 30° slant angles.

4.2.2 Numerical Results of the Elliptical Ahmed Body (EAB)

This section discusses the numerical analysis of the elliptical Ahmed Body (EAB) at the low and moderate Reynolds numbers of 0.43×10^5 and $1.90 \times 10^{5,}$ respectively, at a 25^o slant angle. It shows the similarity and comparison between the low and moderate Reynolds number flow features and the associated drag reduction achieved. It uses data analysis tools, including frequency analysis and vortex identification method, to quantify the unsteady coherent structures.

4.2.2.1 Mean velocity

The contours of the streamwise mean velocity superimposed with streamlines are shown in Figure 4.26. The contours are shown in the symmetry plane (Y=0) and near the side edge (Y=0.55). The models are identified by the inlet velocity, such that a test model of the SAB with an inlet velocity of 9 m/s is recognized as the SAB_9, and that with 40 m/s is also identified as the SAB_40. Similarly, the EAB is denoted as EAB_9 and EAB_40, respectively. There are a few observations that can be made.

(a) SAB_9 and SAB_40

First, Figure 4.26 in the Y=0 plane shows that the flow separates at the slant upper edge and reattaches over the slant surface, forming the reverse flow region (SSB) responsible for increased pressure drag [13]. This SSB is found in both the SAB_9 and SAB_40 (Figure 4.26(a) & (c)). Nonetheless, the effect of the Reynolds number on the magnitude of flow parameters is already highlighted in the existing studies [27], [83], [127], [146] and is documented in Table 4.3. Thus, the slant bubble length (SBL) is 78% and 84% for the SAB_9 and SAB_40, respectively, which is expected.

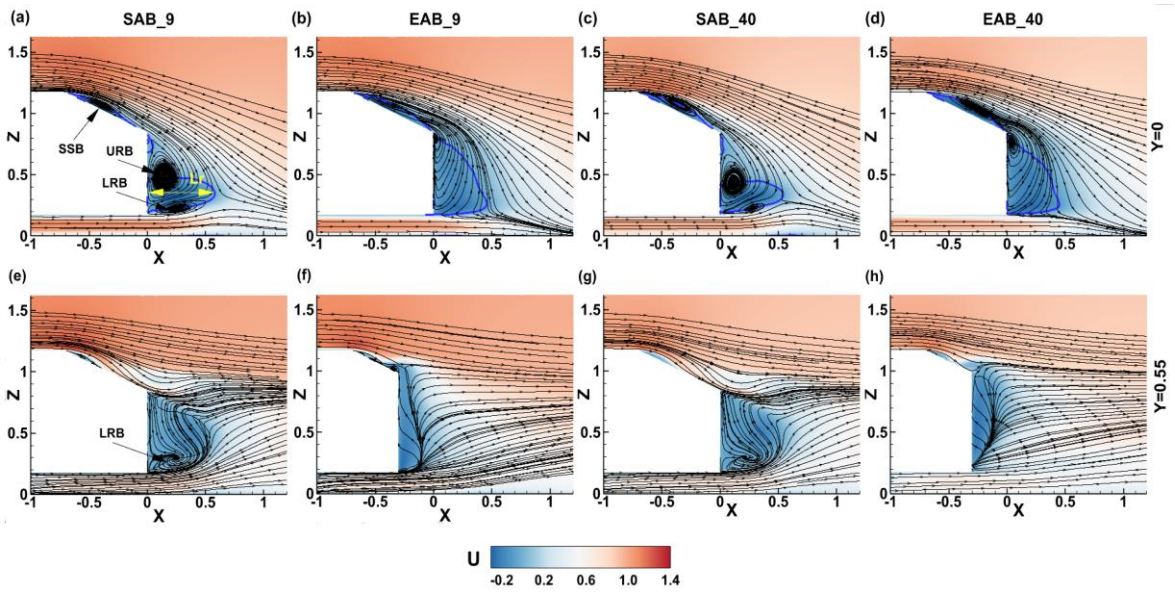

Figure 4.26: Contours of streamwise velocity at Y=0 (symmetry) and Y=0.04 (near side edge) superimposed by the velocity streamlines. The solid blue line indicates the U=0 velocity to demarcate the reverse flow region.

These SBL values are slightly higher than those found in the experimental SAB_9_Exp. but fall within the values reported in the literature [72], [77], [85], [170]. It should be noted that there are several low Reynolds numbers studies [83], [107], [127], [299] that did not report the occurrence of the SSB, including the high Reynolds number of 2×10^6 a study by Rao et al. [25] However, other studies such as [34], [79], [73] at high Reynolds numbers and [98] and [318] at low Reynolds numbers did report it. The present simulation also supports the existence of SSB both at low and high Reynolds numbers.

Secondly, beyond the SSB, the flow undergoes a secondary separation at the slant surface rear edge and creates the upper recirculation bubble (URB), lower recirculation bubble (LRB) and wake recirculation region, as indicated in Figure 4.26(a). Considering the wake recirculation lengths (L_r) reported in Table 4.3, both the SAB_9 (76%) and SAB_40 (73%) are close to those reported in some previous studies [85], [148] but are less than those in other previous studies [72], [76], [318]. At the same time, the heights of wake recirculation are less than the experimental values of the SAB_9_Exp. (Section 4.1).

Table 4.3: Dimensions of SBL, Lr, H_r and location of URB and LRB centers. All the values are in terms of percentage slant length. Note, Exp. is experiment and Num. is Simulation.

Re (10^5)	**0.43**	**1.9**	**0.43**	**1.9**	**0.43**	
	SAB_9	SAB_40	EAB_9	EAB_40	Experimental (Section 4.1)	
					SAB_9_Exp.	EAB_9_Exp.
	% lengths in terms of slant surface length					
SBL	78	84	93	95	62	Not exist
Lr	76	73	60	60	85	77
H_r	32	31	66	65	46	88
Dimensions are nondimensionalized by model height						
Center of URB	X=0.15, Z=0.48	X=0.11 Z=0.43	X=0.02 Z=0.80	X=0.05 Z=0.76	X=0.25 Z=0.57	X=0.25 Z=0.96
Center of LRB	X=0.24 Z=0.22	X=0.25 Z=0.23	Not exist	Not exist	X=0.3 Z=0.3	Not exist

In addition to that, near the side edges of the model at Y=0.55, both the SAB_9 and SAB_40 display similar flow features, as shown in Figure 4.26(e) & (f). Although they do not show the URB, the existence of LRB is found. The center point location of URB and LRB at the symmetry plane is close in both cases, as documented in Table 4.3. This is consistent with the volumetric PIV study of the 25° Ahmed body by Sellappan et al. [77] at the same Y=0.55 location. Thirdly, a more thorough description of the flow features is shown using the cross-section planes (Y-Z) over the slant surface and in the wake displayed in Figure 4.27 and Figure 4.28, respectively. The cross-section planes over the slant surface (Figure 4.27) clearly reveal the existence of counter-rotating C-vortices from the side edges and the side edge vortices (SEV) at the bottom for both the SAB_9 and SAB_40. The C-vortices become more pronounced, moving towards the rear edge along with the SSB. These features are consistent with those reported elsewhere [85].

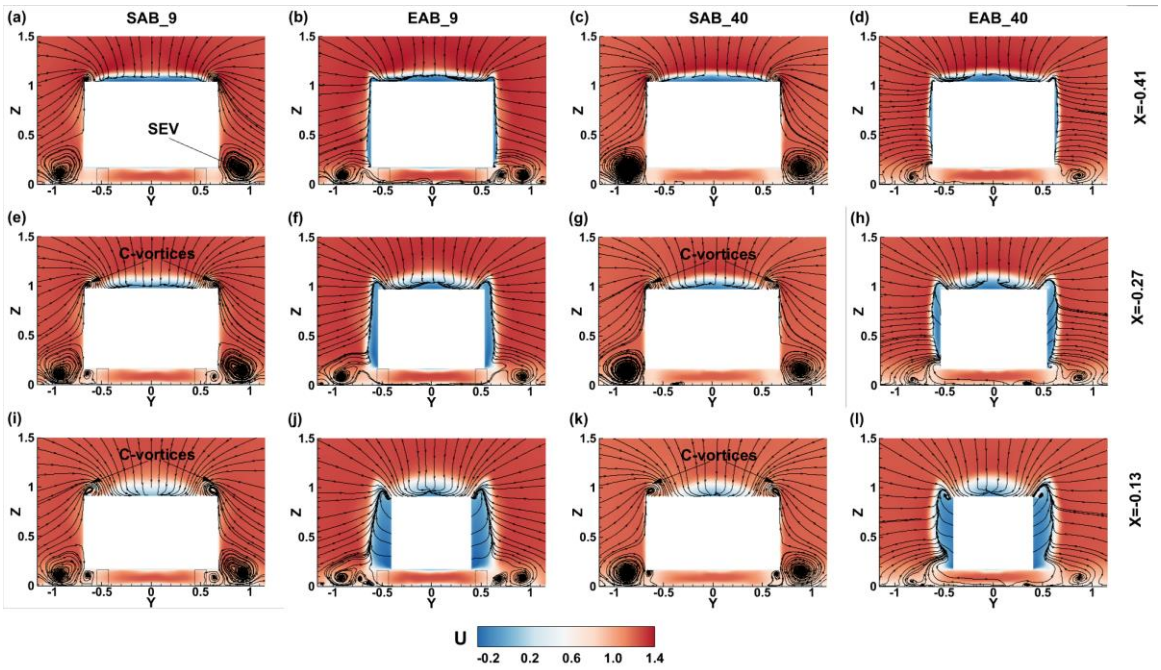

Figure 4.27: Contours of the streamwise velocity in the cross-section plane (Y-Z) at X=-0.41, X=-0.27, and X=-0.13 over the slant surface superimposed by the velocity streamlines.

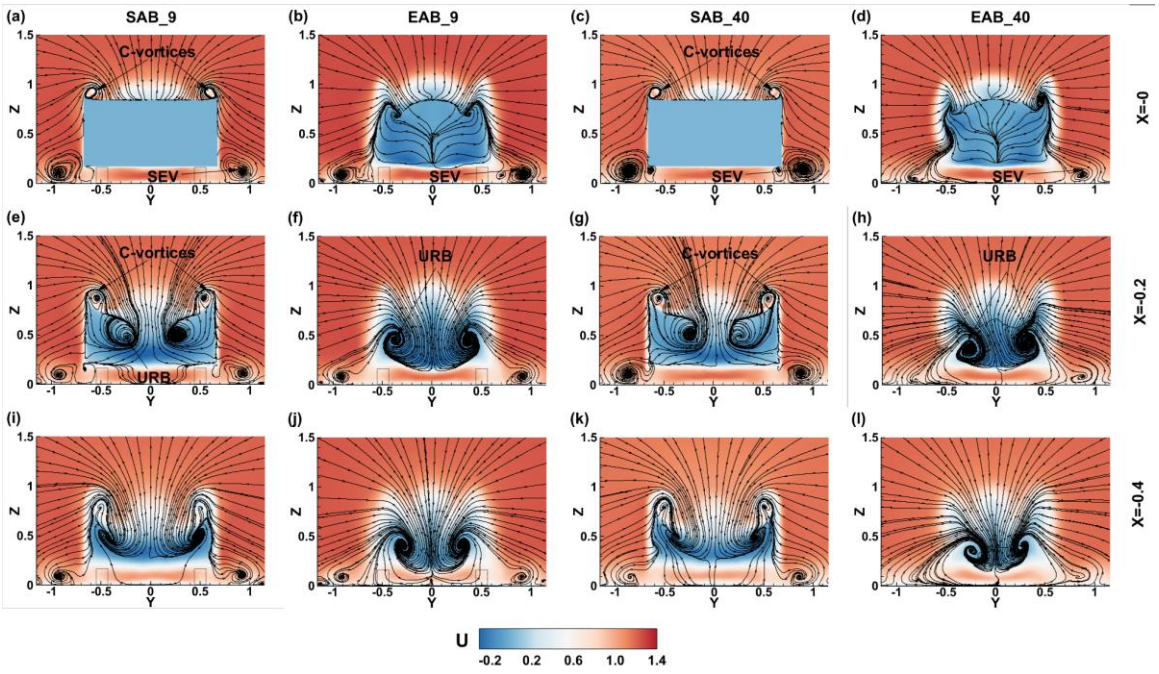

Figure 4.28: Contours of the streamwise velocity in the cross-section plane (Y-Z) at X=0, X=0.2, and X=0.4 in the wake superimposed by the velocity streamlines.

The existence of the C-vortices, along with the URB, can be seen in the cross-section planes of the wake (X=0.2 and X=0.4) in Figure 4.28. However, the URB and the C-vortices begin to merge in the far stream in the wake, and the beginning is found at X=0.4, which is also clearly documented in some previous studies [29], [77], [146]. These features exist both at the low (SAB_9) and high (SAB_40) Reynolds numbers, which stress the capability of low Reynolds numbers to reproduce the general flow features of the SAB.

(b) EAB_9 and EAB_40

The elliptical curvature has a significant effect on the overall flow features of the SAB. In fact, it creates a whole new dynamic of flow features that are seemingly disconnected from the SAB. The general flow features of the EAB are discussed as follows. At first, the flow separates and reattaches over the slant surface according to Figure 4.26 in the symmetry plane. The elliptical curvature provided an extended SBL of about 93% and 95% of the slant length at low (EAB_9) and high (EAB_40) Reynolds numbers, respectively, as documented in Table 4.3. It means that the after-flow separation at the slant upper edge, the flow reattachment points over the slant surface, which was around 78% and 84% in the SAB_9 and SAB_40, respectively, increased to almost the length of the slant due to curvature. Such an extended SBL is found by Guilmineau [85] but at a significantly higher slant angle of 32° SAB. It is due to the fact that in the IDDES simulation of Guilmineau [85] a fully detached flow was not achieved until 32°, which was also found in Figure 4.12 and Figure 4.13. The studies [85], [319] also showed that the SBL increases with the slant angle, and once SBL surpasses the slant length, the flow transition from TDS to the QAS provides significant drag reduction. Thus, such an extended SBL in the current analysis as well suggests that the flow is close to transitioning from the TDS to the fully detached flow low-drag regime due to the elliptical curvature. The experimental investigation (EAB_9_Exp.) revealed a fully detached flow at the 25° angle. However, due to obvious differences between the experimental and numerical methods, the IDDES method does not show a fully detached flow at a 25° angle. Nonetheless, it provides a clear indication of transition with an increased slant angle. However, a trivial reverse flow is found near the side edge of the EAB, which significantly differs from the SAB.

Secondly, the flow undergoes a secondary separation at the slant rear end. Nonetheless, the EAB provides a substantial restructuring of the wake flow. The wake recirculation region in both the EAB_9 and EAB_40, as documented in Table 4.3, is around 60% of the slant length. This is less than the SAB_9 and SAB_40., along with the SAB_9_Exp, which has 77%. It means the recirculation length is reduced due to curvature but unaffected by the Reynolds number. However, a dramatic increase in the height of the wake recirculation of around 52% is found in both the EAB_9 and EAB_40 compared to the SAB. Also, this is even more in the EAB_9_Exp, which is 64% higher than the SAB_9 and 25% than the EAB_9. It should be noted that such a restructuring by modifying the dimensions of the wake recirculation region, several studies have established drag reduction [315]–[317], [320]. Moreover, another peculiar characteristic of the EAB wake flow is the relocation of URB in the wall-normal direction and reduction in shape compared to the SAB. The URB in the EAB_9 and EAB_40 is not exactly similar to the EAB_9_Exp, but the underlying phenomena that connect the URB with the slant surface flow are the same, which is also found using an active control mechanism for drag reduction [28]. The center point location of the URB and LRB at the symmetry plane is close in both cases, as documented in Table 4.3. Additionally, a rather distinct and interesting result is the absence of the LRB in both the EAB_9 and EAB_40, similar to the EAB_9_Exp. The absence of the LRB provides a potential advantage in mitigating the problem of soiling at the rear window of vehicles. In this sense, the EAB offers a promising vehicle design that is potentially capable of providing both drag and soiling reduction.

Thirdly, surveying the cross-section plane flow features in Figure 4.27 provides a rather surprising result in which the counter-rotating C-vortices are not found at both the low (EAB_9) and high (EAB_40) Reynolds numbers. This can be more clearly seen at plane X=0.2 and X=0.4 in Figure 4.28. This is true over the slant surface and is transparent in the wake where the existence of shifted URB is noticed but not the LRB. The development of C-vortices from the side edges and its eventual merger with the URB has been documented and discussed by many studies [73], [77], [79]. In fact, the entrainment of the C-vortices can lead to the formation of SSB [72] and can affect the stability of vehicles. Almost 50% pressure drag is added to the SAB due to C-vortices compared to the square back Ahmed body [272]. Therefore, the elimination of the C-vortices has fundamental practical

implications. The indication of C-vortices weakening was highlighted in the experimental investigation [318]. The current simulation conclusively characterized the fundamental flow features of the EAB and established the absence of C-vortices. These unique features are not found [32], [34], [170] by rounding the upper and side edges of the slant surface. Although drag reduction was achieved, both the C-vortices and LRB are still present at a 25° angle. Consequently, the rounded curvature at the upper and side edges might not improve further with the slant angle because the C-vortices and LRB may exist. However, in the case of the EAB, an increase in angle will provide a fully detached flow, and the benefits gained by the absence of the C-vortices and LRB would likely increase further. Therefore, the EAB provides a reattached flow that is prone to transition along with the elimination of the C-vortices and LRB. It also shifts the URB parallel to the slant surface. It should also be noted that Reynold's number does not significantly affect the flow features of the EAB.

4.2.2.2 Reynolds stresses

The contours of the Reynolds shear stress are displayed in the streamwise and cross-sectional planes in Figure 4.29 and Figure 4.30, respectively. There are a few important observations as follows.

(a) SAB_9 and SAB_40

At first, the development of shear stress over the SAB has a similar mechanism at both low and high Reynolds numbers, as indicated in Figure 4.29(a) & (c). The shear layer, due to flow separation, provides negative peak UW values over the slant surface, which are almost the same in the SAB_9 and SAB_40. Another positive peak is associated with the underbody shear layer UW=0.04 & 0.06 in the SAB_9 and SAB_40, respectively. In addition, positive and negative UW values are related to the LRB and URB, shown as the solid red circle. The negative UW values are associated with the URB due to downwash that has positive streamwise and negative wall-normal velocities. At the same time, the positive UW in the LRB corresponds to the upwash since it has positive streamwise and wall-normal velocities. It should be noted that, due to the differences in the center points of the URB and LRB, differences exist in the UW values between the SAB_9 and SAB_40. These values, however, are not dissimilar to values reported previously [124], [318] at the

25° slant angle Ahmed body. Secondly, the cross-sectional plane in Figure 4.30 captures the shear stress associated with the counter-rotating C-vortices and the slant surface flow. Near the slant upper edge (X=-0.41), weak VW C-vortices begin to form, having opposite VW values at side edges. The values of VW are also not much offset between the low and high Reynolds numbers. As the flow trended towards the slant rear end, the contribution by the C-vortices also increased since it grew as well.

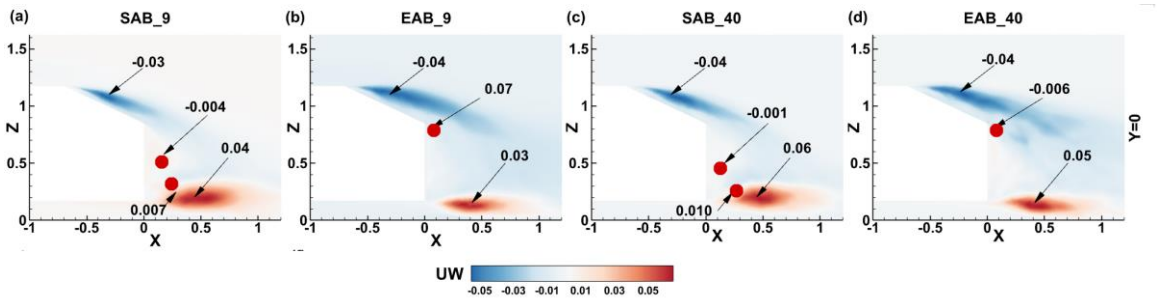

Figure 4.29: Reynolds shear stress (UW) in the streamwise plane at Y=0.

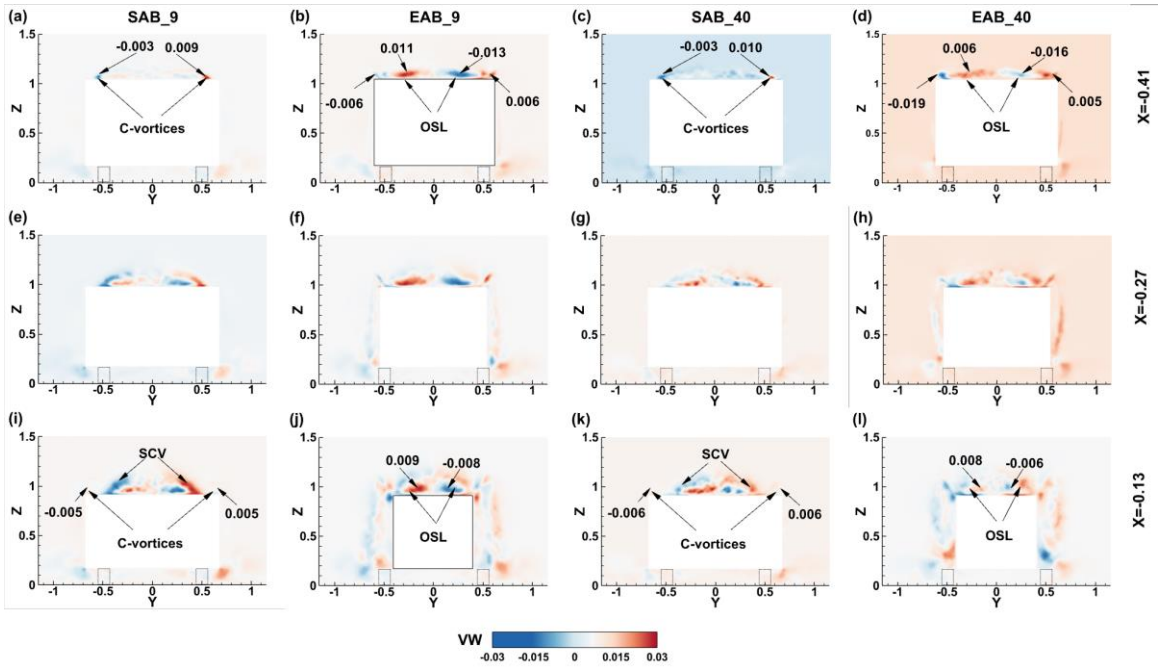

Figure 4.30: Reynolds shear stress (VW) in the cross-sectional plane at X=-0.41, X=-0.27, and X=-0.13.

However, it is accompanied by the emergence of secondary C-vortices (SCV), which is clearly discernible in X=0.13 and has the range of VW= ± 0.005-0.007 within the SAB_9

and SAB_40. Such a development is also supported in other studies as well [72]. It is due to the entrainment of the C-vortices over the slant surface. As the flow moves into the wake, it becomes more dominant. At the very rear end (X=0) in Figure 4.31(a) & (c), the SCV, along with the C-vortices, grows in size. The values of VW are almost the same between the SAB_9 and SAB_40 in all the cross-sectional planes in the wake. It is clear that the development of the shear stress over the slant surface and in the wake mostly follows the general trend reported in the literature. However, there are trivial differences in the magnitude of shear stress due to the Reynolds number, but the shape and size of the shear layers do not deviate much, which is consistent with the existing studies [27], [127], [318].

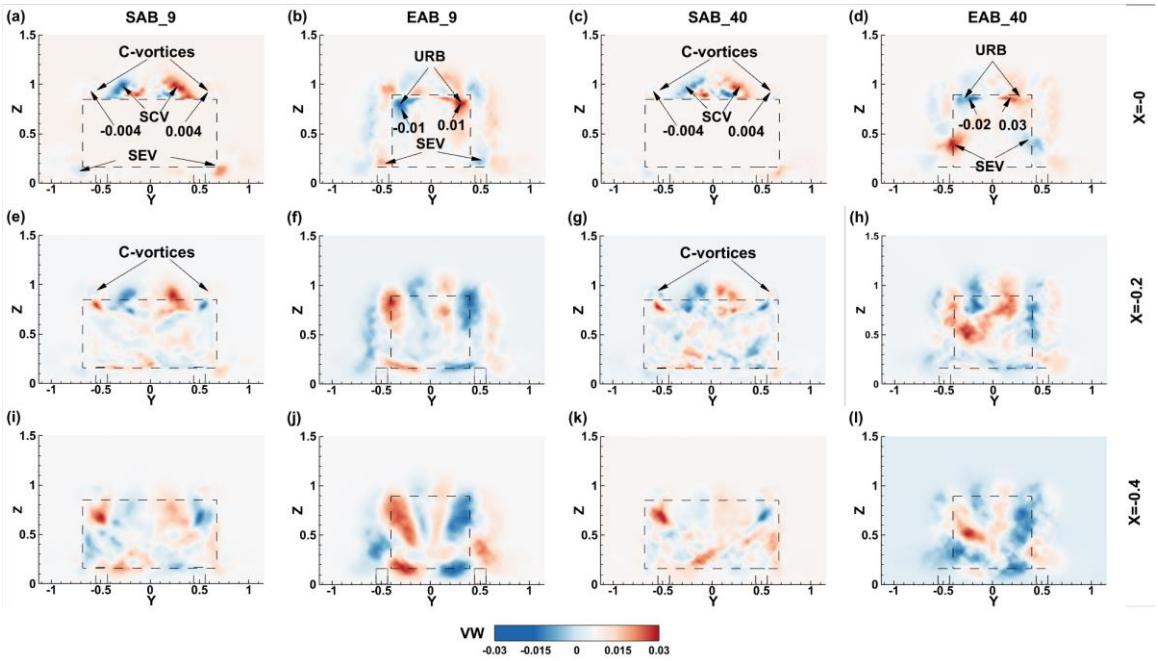

Figure 4.31: Reynolds shear stress (VW) in the cross-sectional plane at X=0, X=0.2, and X=0.4.

(b) EAB_9 and EAB_40

At first, due to the significantly different flow features of the EAB, the development of the shear stress is also unique. In the symmetry plane shown in Figure 4.29(b) & (d), there is a peak in the UW value over the slant surface, which is UW=-0.3-0.4 within the EAB_9 and EAB_40. The shear stress is rather extended in a streamwise direction and is also larger in size than in the SAB. This can be correlated with the comparatively larger SSB in the

EAB that is near transition. Such an upper shear layer is also seen in the low-drag regime SAB [79] but the UW value in the EAB is higher. Furthermore, the underbody shear layer shows the UW=0.03-0.5 in the EAB_9 and EAB_40, which is close to the SAB_9 and SAB_40. However, due to the absence of LRB and relocation of the URB near the slant surface, the UW at the center of this shifted URB has a positive peak value of 0.7 in the EAB_9. This value differs from the EAB_40 that shows a negative UW=-0.006, which is according to the trend found in the EAB_9_Exp. However, a direct comparison between the IDDES and experimental values of the EAB cannot be made since the experiment found a fully detached flow, however, since the UW in the EAB follows the SAB with the SSB.

Secondly, the cross-sectional plane above the slant surface shown in Figure 4.30(b) & (d) captures the two opposite VW=±0.006 at the side edges. It also displays an opposite shear layer (OSL) within the middle of the slant surface. The OSL has VW=0.011 and VW=-0.013 in the EAB_9 and VW=0.006 and VW=-0.016 in the EAB_40. Thus, there is not much difference due to the Reynolds number. However, as the flow moves towards the rear edge of the slant surface, the small side shear layer seen at X=-0.41 merged with the OSL. It is evident starting from plane X=-0.13 because, before that, SSB exist. As noted before in Section 4.2.2, the EAB shifts the URB near the slant surface and slowly merges with the slant surface flow. Due to this phenomenon, the OSL aligned with the URB and grew in size and is clearly discernible in planes X=0, 0.2, and 0.4. The development of the shear layer from the slant surface is also accompanied by the gradual enlargement of underbody side edge shear layers (Figure 4.31). Although there is not much difference between the VW values of the EAB_9 and EAB_40, the shear layers in the EAB_40 appear less organized downstream of the wake. The discussion reveals that the shear stress is increased in the EAB due to the shifted URB, which is indicative of the effect of upwash[124].

4.2.2.3 Pressure contours

The physical interest in vehicle aerodynamics is generally constrained to the drag and lift that significantly depends on the pressure distribution over the rear end. Similarly, vortex-induced drag and lift due to the cone-like structure at the back of some cars and the implication of soiling associated with particles of dirt and water all depend on the rear end.

These all can be well described with time-averaged surface patterns [143]. It is established from the earlier discussions that the flow structure is significantly influenced by the elliptical curvature. Therefore, a more thorough understanding of the flow mechanism over the rear end is required to investigate further and deepen our understanding of the physical mechanism. Figure 4.32 shows pressure contours over the rear of the SAB and EAB superimposed by the velocity streamlines showing the surface patterns.

(a) SAB_9 and SAB_40

At first, the flow separates at the slant upper edge (SUE), and the imprints a positive bifurcation line (PBL1) followed by a negative bifurcation line (NBL1) shown in Figure 4.32(a) and (c). Here, the NBL and PBL indicate the trajectories of the surface patterns as to where the bifurcation lines are diverging or converging. Subsequently, a PBL is associated with the flow attachment, while the separation is linked to NBL [321]. Accordingly, after separation at SUE, the flow reattached at the PBL1 and then separated again at the NBL1. Furthermore, after the NBL1, the flow evolves towards the slant surface downstream to again reattach at PBL2, which is the classical SSB (For clarity, it is highlighted with the dashed line in Figure 4.32(a). The flow inside the SSB is reversed in the upstream direction, as is visible from the surface streamlines. A recent study by Tran et al. (2022) found this SSB using the subgrid global luminescent oil-film (SGLOF) technique to study the skin-friction topology, but Salazar et al. (2022) using the same method does not find the SSB at several Reynolds numbers. Moreover, from the NBL1, the flow stretch in the spanwise direction, which is comparatively larger than the size of SSB. The consequence of such divergence in the spanwise is seen in the existence of a stable focus point (F) created due to the interaction of NBL1 and PBL2. It means that the stable focus point emerges due to the interface between the longitudinal C-vortices and the SSB, which is also reported in the [73], [116], [143] Towards the slant side edge (SSE), the streamlines are diverging from the PBL2 showing the existence of longitudinal C-vortices and secondary vortex related to NBL2 and PBL3 as highlighted in [73], [143]. It should be noted at first that, due to the symmetrical nature of the flow over the slant surface, these features exist at either side of the slant surface. Secondly, there is no significant change in the surface flow patterns between the SAB_9 and SAB_40.

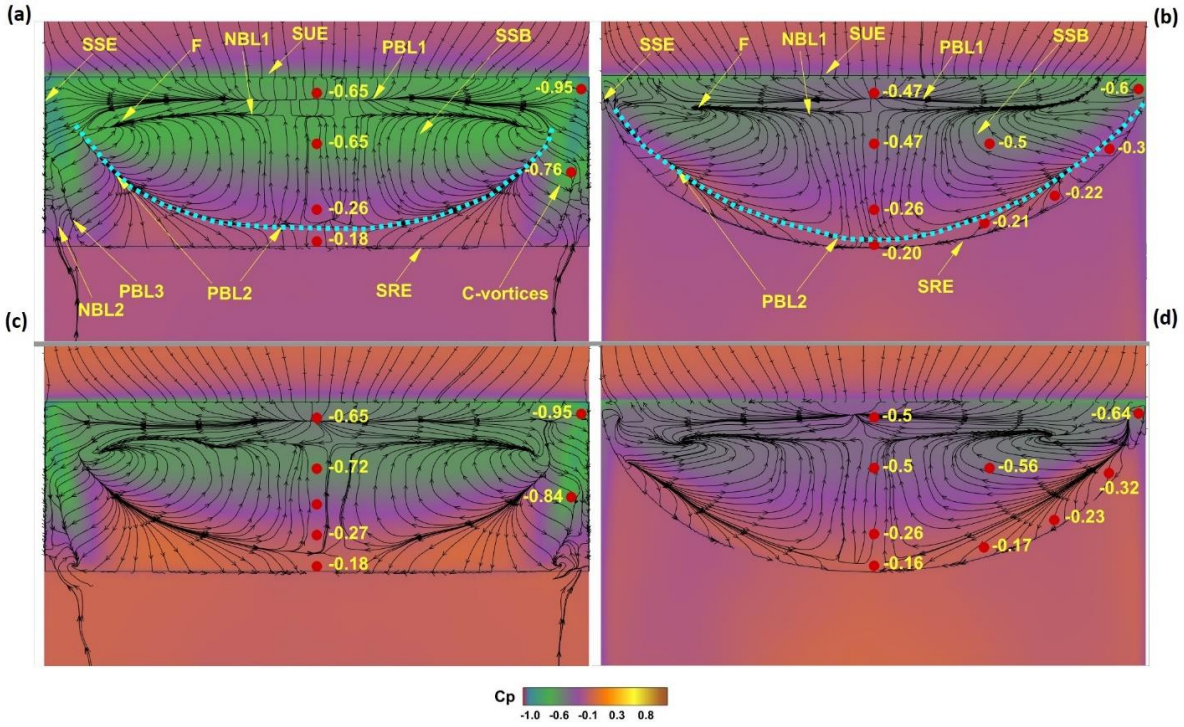

Figure 4.32: Pressure contours and the surface pattern. (a) SAB_9 (b) EAB_9 (c) SAB_40 and (d) EAB_40.

Second, with reference to the SAB_9, it can be seen at the Y=0 line, between the SUE and PBL1, the C_p=-0.65, which is maintained after the NBL1 at some distance but begins to decrease even within the SSB and just before the PBL2 reached C_p=-0.26. Also, the C_p=-0.18 value can be shown, and these values are close to those reported by Rossitto et al. [32] Due to the pressure difference at the reattachment point (at PBL2), the flow begins to migrate in the upstream direction within the SSB [319]. Furthermore, the existence of the C-vortices shows a significantly higher C_p=-0.95 near the intersection of SUE and SSE. As the C-vortices come towards the slant rear edge (SRE), an increased C_p=-0.76 is found and close to [32], [117], [319]. As it grows, the C_p increases, and the velocity decreases. In fact, this is exactly the dynamics of the C-vortices that constrain the flow on the slant surface from spreading in the spanwise direction. This modifies the dimensions of the SSB, as highlighted in the literature [72], [85], [319]. Therefore, the C-vortices not only contribute to the pressure drag independently but also contributes to modifying the entire slant surface flow pattern. Since after the SSB and C-vortices merge near the SRE, they coalesce into

the URB and influence the wake as well. In addition to that, the SAB_40 also provides similar C_p values with trivial differences in magnitude due to the Reynolds number.

Thirdly, the iso-surface of the Q criterion, which is based on the complex eigenvalues of the velocity gradients colored by mean pressure, is shown in Figure 4.33. The existence of the SSB shows the pressure recovery moving towards the SRE and engaging with the wake pressure vortices. Further down in the wake, vortices associated with the positive pressure can be seen to exist and blend with each other. It also reveals the low-pressure longitudinal C-vortices at either side of SSE in both the SAB_9 and SAB_40. The C-vortices are matured and more pronounced in the SAB_40. They also can be seen merging with the URB in the near-wake.

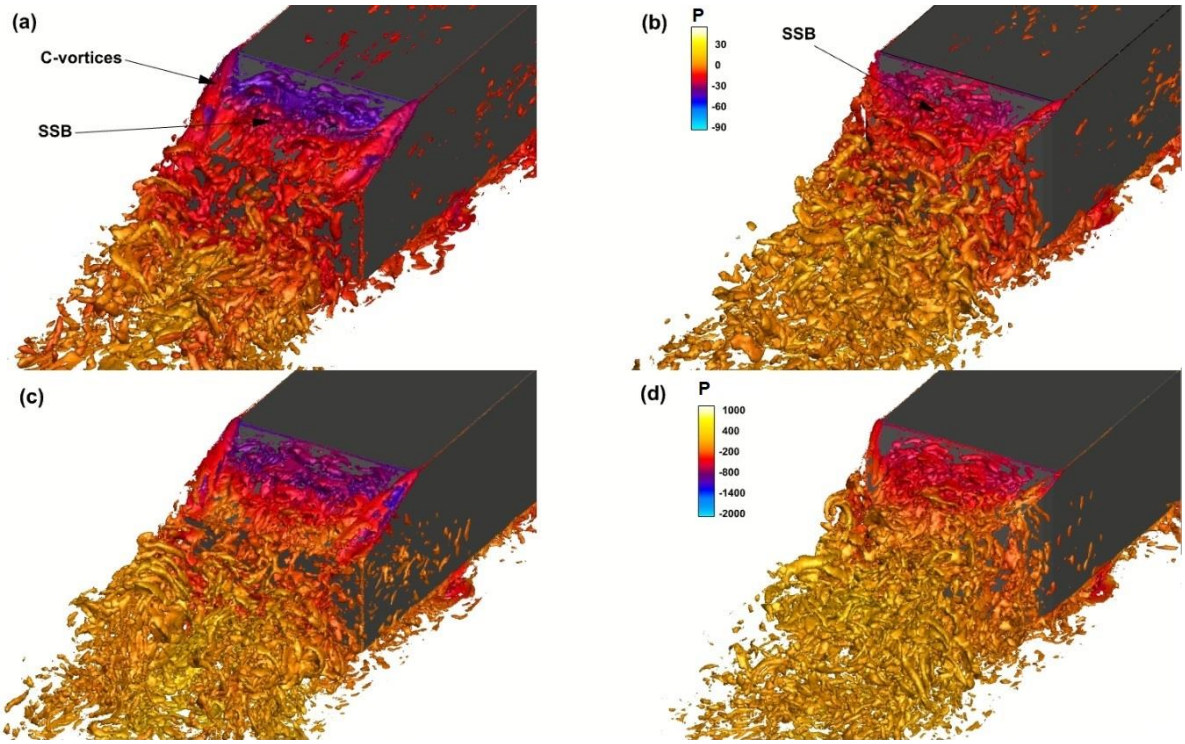

Figure 4.33: Iso-surface of the Q criterion colored by the mean pressure are (a) SAB_9, (b) EAB_9, (c) SAB_40 and (d) EAB_40. The iso-value of Q=22 for (a) & (b) while Q=900 for (c) & (d).

(b) EAB_9 and EAB_40

Given the nature of the elliptical curvature, the flow surface patterns significantly differed from the SAB, as shown in Figure 4.32(b) & (d). The flow separated at the SUE, and the existence of PBL1 is found nearby. From the PBL1, the flow converges towards

the SUE and diverges downstream until it reaches the NBL1, which is linked to separation. However, these surface patterns are close to those of the SAB, but their size is not the same. However, after the NBL1, the flow moves in the downstream direction towards the SRE until it reattaches at PBL2, forming the SSB. It can be clearly seen that the length of the SSB has increased, as documented in Table 4.3. Here, the surface pattern reveals that the spanwise size of the SSB is similar to the SABs. However, the existence of PBL3 and NBL2 is not found in the EABs. It means that the longitudinal C-vortices do not exist. Consequently, the entrainment of the slant surface flow that is usually caused by the C-vortices no more persists. This absence led to the dominance of the SSB over the slant surface that now covered almost the entire slant area. Since 50% of the pressure drag is contributed by the longitudinal C-vortices, the EAB should reduce the drag force as well [272]. Such a mechanism is possible due to the elliptical curvature, which alters the body near the SUE and stops the creation of C-vortices. Whether the EAB_9 or EAB_40, similar surface flow patterns are found in each case, this development over the elliptical slant surface is distinguished from the elliptical slant surface of the cylinder studied by Zigunov et al. [94]. They have reported the existence of a small SSB near the SUE with the longitudinal vortex along the SSE at a 45° slant angle.

Secondly, the distribution of the pressure coefficient C_p shows a general trend of C_p increase towards the SRE. At SUE, a C_p=-0.47 is found, which is ~27% pressure recovery. This is true for the most part of SSB except near the reattachment point C_p=-0.26, which is similar to that of the SAB. At the SRE, C_p=-0.20 is found, which is close to that of the SAB. The pressure difference again pushes the flow moving in the upstream slant direction. This is accompanied by a gradual increase in the C_p=-0.6 to C_p=-0.21 along the elliptical curvature shown for the right SSE. Such C_p values indicate ~37% pressure recovery at the SSE top corner, where the C-vortices begin to emerge in the SAB. The pressure recovery is associated with drag reduction. It should be noted again that there is no significant difference between the EAB_9 and EAB_40 in the pressure distribution.

Thirdly, the iso-surface in Figure 4.33 manifests the existence of recovered SSB compared to the SABs. In addition to that, the absence of the longitudinal C-vortices is evident as well. The vortices from the SSE coalesce with the SSB very early on, which

dominates the development downstream, catalyzing a sizable SSB. A more pronounced version of the iso-surface is apparent in the SAB_40. It is also ostensible that pressure is recovered not only over the slant surface but also in the wake in both the EABs and the SABs.

4.2.2.4 Frequency spectra

Here, the unsteady effects developed in the flow along the slanted rear surface and in the near wake of the body are characterized by spectral analysis of velocity fluctuations. The power spectral density is calculated based on the streamwise velocity fluctuations. The Strouhal numbers, along with the location of extraction, are listed in Table 4. Four different locations are selected to extract the S_t values, namely, point#1 at the slant surface, point#2 near the URB, point#3 near LRB, and point#4 around the saddle point.

Table 4: Strouhal number (S_t) of the streamwise velocity.

Point No.	**Location**	**Strouhal number (S_t)**				**Experiment**	
		SAB_9	EAB_9	SAB_40	EAB_40	SAB_9_ Exp	EAB_9_ Exp.
S_{t1}	X=-0.31 Z=1.05	0.20	0.39	0.25	0.42	0.16	0.88
S_{t2}	X=0.11 Z=0.50	0.29	0.42	0.78	0.21	0.61	0.23
S_{t3}	St3 X=0.25 Z=0.24	0.23	0.22	0.85	0.78	0.55	0.90
S_{t4}	St4 X=0.6 Z=0.3	0.35	0.24	0.67	0.72	0.56	0.48

(a) SAB_9 and SAB_40

At first, above the slant surface (point#1), the SAB_9 provides an S_t=0.20 while the SAB_40 has a value of S_t=0.25. These values are comparable with the S_t value found in the experimental analysis of the SAB_9_Exp. which was S_t=0.16. Similarly, the range of S_t reported in the literature is found from S_t=0.11-0.35, as listed in Table 4. Thus, the flow dynamics at the slant surface has both minimum and maximum associated Strouhal number. The lower S_t=0.11 is ascribed to the three-dimensional (3D) flapping of the SSB, while S_t=0.20 by Zhang et al. [72] has found a small SSB near the slant upper edge while S_t=0.18 is also found at the slant surface [103]. In the present simulation, the existence of the SSB is found at both the SAB_9 and SAB_40. Thus, the same phenomena of SSB flapping are ascribed to the Strouhal numbers.

Secondly, at point #2, point#3, and point#4, the SAB_9 at the low Reynolds number shows the S_t=0.29, 0.23, and 0.35, respectively, which is lower than the SAB_9_Exp. but lies within the values found in the literature S_t=0.36-0.53. However, a more pronounced Strouhal number is achieved at the high Reynolds number SAB_40 at point#2 and point#3 as S_t=0.78 & S_t=0.87, respectively. At a high Reynolds number, the values are on the level of the SAB_9_Exp. but are still higher than the values found in the literature ranging between S_t =0.36-0.53 [98], [100], [103]. Zhang et al. [72] associated such Strouhal number with the quasiperiodic events occurring in the wake of the SAB. It should be noted that [34] and [98] used simulation studies, while [72] and [308] used experimental studies. The effect of the Reynolds number on the S_t is also investigated by Zhang et al. [72] and they found that the S_t increases with the Reynolds number, which is also found in the present simulation. Nonetheless, in the wake, the SAB_9 has a range of S_t=0.23-0.35 that aligns with the literature, but as the Reynolds number increases, the SAB_40 shows a slightly higher range of S_t=0.67-0.85 than that of the SAB_9_Exp. Therefore, the values of S_t are scattered, and the effect of the Reynolds number on the S_t is also apparent in the present study.

(b) EAB_9 and EAB_40

The elliptical curvature has a significant effect on the flow structure, as discussed before. At first, over the slant surface at point #1, the S_t=0.39 and 0.42 is found for the

EAB_9 and EAB_40, in Table 4, respectively. Compared to the EAB_9_Exp, these values are less. In the experimental investigation (EAB_9_Exp.) a fully detached flow was achieved, leading to increased S_t values. However, in the present simulation, the flow is not fully detached. Thus, the existence of the SSB over the slant surface, similar to the SAB, constrained the S_t values to slightly higher values than those of the SAB, which is expected.

Secondly, in the wake region represented by points #2, #3, and #4, the EAB_9 has a S_t range of S_t=0.22-0.42 while the EAB_40 values vary from S_t=0.21-0.78. This range in the wake of the EAB lies within the experimental values recovered in the experiment of the EAB_9_Exp at a low Reynolds number. However, it is predicted that the Strouhal number will rise due to the elliptical curvature. A similarly slanted afterbody studied by Garmann et al. [323] reported Strouhal numbers up to 1.73. The same bluff body was also investigated by Zigunov [291] who reported an even higher Strouhal number of around 2.0, apparently generating more intense turbulent kinetic energy fluctuations. In addition to that, as highlighted before, Roshko [306] discovered that a decrease in the drag coefficient frequently coincides with a rise in the Strouhal number. Therefore, it is expected that even with the SSB, the EAB is promising to provide drag reduction, which will be discussed in subsequent sections.

4.2.2.5 Vortex identification

The instantaneous vortices can help to better understand the unsteady 3D wake structure around the Ahmed body and have been explored in the literature [147]. A variety of methods can be used, including the Q-criterion based on the complex eigenvalues of the velocity gradient tensor, Δ-2 criterion, which is the second invariant of the velocity gradient tensor, the swirling strength λ_{ci} and the λ_2 criterion. Here, rotational flow structures are visualized using iso-surfaces calculated based on the Q-criterion [296]. The isometric, top, and bottom view of the Q criterion of all the models is shown in Figure 4.34, Figure 4.35, and Figure 4.36, respectively. It is colored by the kinetic energy to understand the distribution of important components.

At first, the SSB at the slant and pair of counter-rotating C-vortices is evident in the SAB_9 and SAB_40. The energy associated with the C-vortices is high and begins to

reduce as it evolves towards the wake Figure 4.34(a) & (c). It is clearer in the top view of Figure 4.35(a) & (c), where fully developed C-vortices merge into the wake with reduced kinetic energy. Nevertheless, within the SSB, the vortices are found to have reduced kinetic energy than the C-vortices. The occurrence of higher and lower energetic vortex groups is identified over the slant surface and in the wake. However, since the flow becomes more refined with the Reynolds number and more fine vortices are seen over the slant surface and in the wake of the SAB_40. The SABs also show the corner vortices coming out of the bottom side edges. Furthermore, at the bottom view in Figure 4.36(a) & (c), the vortices emanated from the cylindrical wheel that has considerably less kinetic energy than the slant surface area and upper side of the wake.

On the other hand, a clear demarcation of sizable SSB can be seen in Figure 4.34(b) & (d). Around the SSE, a small portion of energetic vortices is found, which immediately merge with the flow at the slant surface. In fact, along the elliptical edge of the EAB, the kinetic energy is reduced, and this also affects the energy associated with the SSB. Since it can be visualized that the density of high and low vortices over the slant surface and in the wake is dissimilar to those of the SAB, these developments can also be seen in Figure 4.35 (b) & (d). In contrast, the merged vortices stress the surface flow patterns discussed before. Moreover, because of the elliptical rear end, the wake flow structure is mostly concentrated at the center, contrary to those of the SAB, due to the presence of the C-vortices moving in the downstream direction. Finally, Figure 4.36(b) & (d) produced mostly less energetic vortices in the near wake, which are also influenced by the vortices from the cylindrical support.

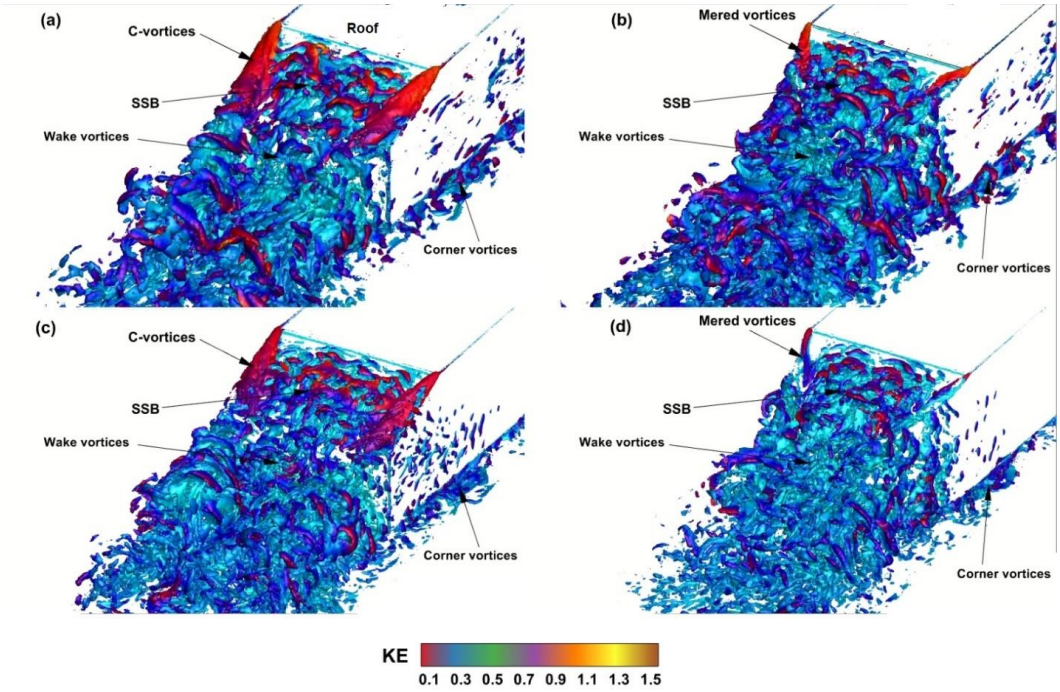

Figure 4.34: Isometric view: Q criterion colored by the kinetic energy where (a) SAB_9, (b) EAB_9, (c) SAB_40 and (d) EAB_40. The iso-value of Q=15 for (a) & (b) while Q=700 for (c) & (d).

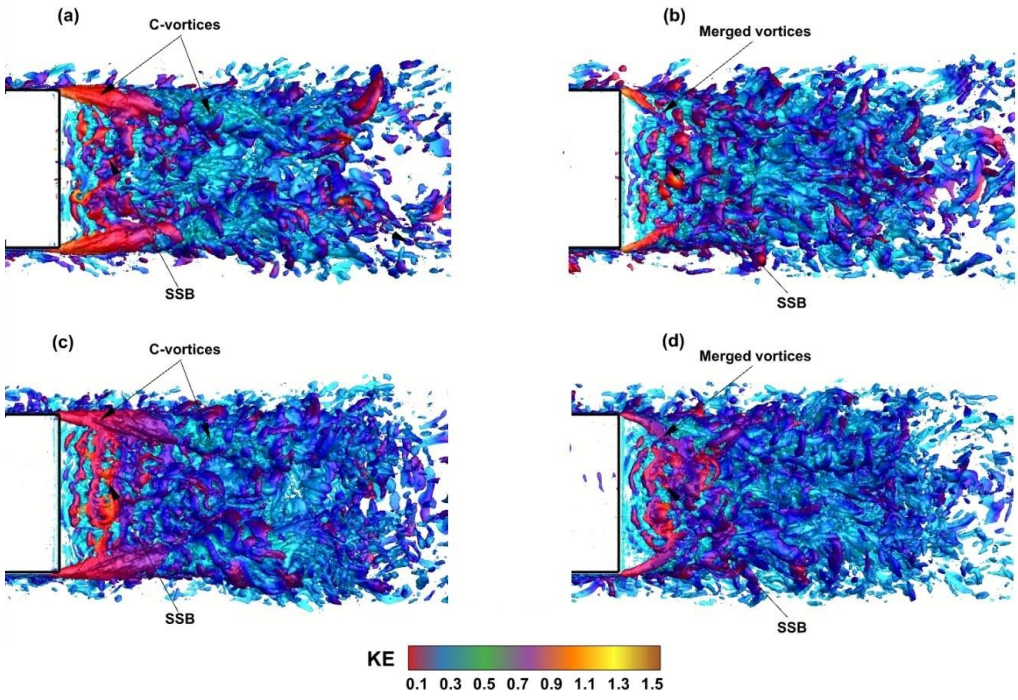

Figure 4.35: Top view: Iso-surface of the Q criterion colored by the kinetic energy where (a) SAB_9, (b) EAB_9, (c) SAB_40 and (d) EAB_40. The iso-value of Q=15 for (a) & (b) while Q=700 for (c) & (d).

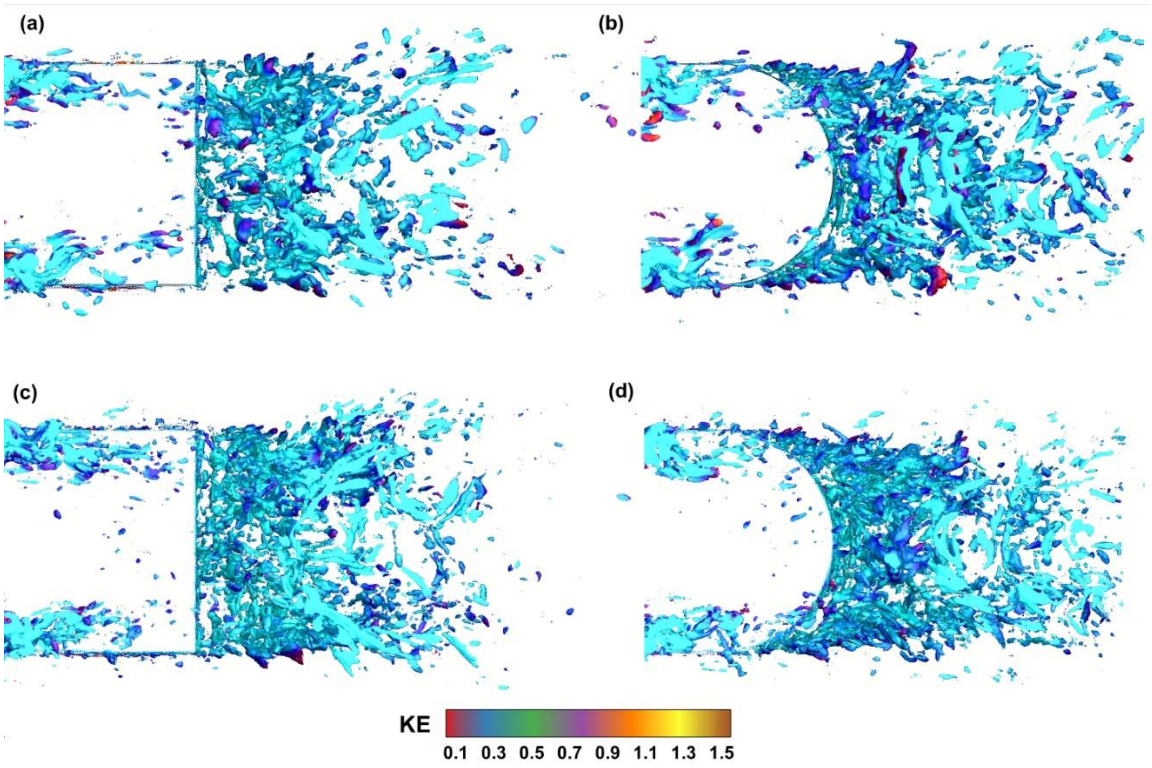

Figure 4.36: Bottom view: Iso-surface of the Q criterion colored by the kinetic energy where (a) SAB_9 (b) EAB_9 (c) SAB_40, and (d) EAB_40. The iso-value of Q=45 for (a) & (b) while Q=1800 for (c) & (d).

4.2.2.6 Mean velocity in the X-Y plane

The understanding of the flow features in the X-Y planes is shown in Figure 4.37 for planes at Z=0.27, z=0.62, and Z=0.97. Near the ground in the SAB_9, which is represented by plane Z=0.27, the flow separates from the side surfaces and creates a recirculation region that has a width of ~142% of the slant length. The flow then diverges in the downstream direction at both ends. A similar phenomenon is achieved at the high Reynolds number in the EAB_40, having a closer recirculation width of ~150% to the SAB_9. Furthermore, the slightly higher wall-normal distance at Z=0.62, both the SAB_9 and SAB_40, shows the two corner bubbles at each side end. This is exactly similar to the experimental investigation at the same plane in the SAB_9_Exp. [318]. Thus, the existence of a large recirculation region found at Z=0.27 no longer exists. In addition to that, the flow at low and high Reynolds numbers tends to flow inward in the downstream direction instead of parallel to the flow recovered at Z=0.27. Finally, further in the wall-normal direction, there are no more corner bubbles or the recirculation region at both the SAB_9 and SAB_40,

which is expected. After separation from the side surfaces, the flow moves inwardly, similar to that at Z=0.62.

On the other hand, in both the EAB_9 and EAB_40 at Z=0.27, the flow separated at the side surfaces and created the elliptical shape recirculation region. The width of the recirculation region is almost equal to the model width, which is ~175% of the slant length in the EAB_9 but reduced in the EAB_40 to ~150%. Thus, the recirculation region formed at the low Reynolds number is larger than the high Reynolds number. Nonetheless, the streamlines show that the flow moves slightly outwardly in the downstream direction. Similarly, at the Z=0.62 plane, the existence of symmetric wake bubbles (SWB) is found ostensibly in the EAB_9. In contrast, a more pronounced version of the SWB is found in the experimental investigation in the EAB_9_Exp. At the same plane, the experiment shows a large recirculation region with two concentric symmetric bubbles covering the area of the entire near wake. The present simulation captures similar bubbles, but they are smaller in size. Finally, towards plane Z=0.97, the flow separates from the side surfaces and moves downstream in the EAB_9. It also creates a small recirculation region in the wake. In the EAB_40, the flow moves parallel to the downstream flow after leaving the side surfaces. It also creates a comparatively larger recirculation region in the wake, similar to that in the Z=0.27 plane.

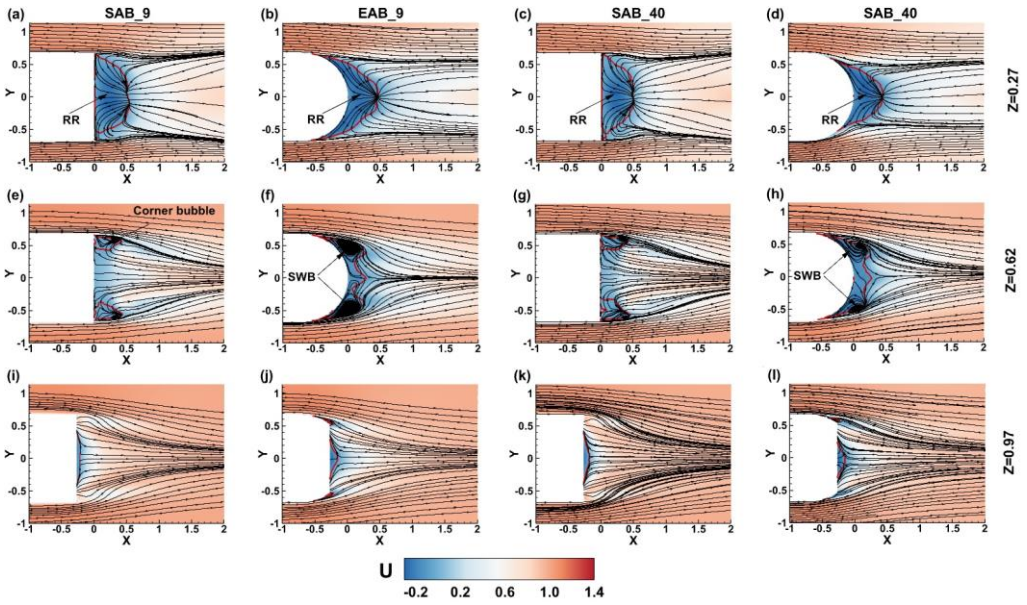

Figure 4.37: Contours of the streamwise velocity superimposed with the streamlines in the X-Y planes.

4.2.2.7 Reynolds shear stresses in the X-Y plane

The contours of the Reynolds shear stress (UW) are displayed in the spanwise (X-Y) plane in Figure 4.38 at Z=0.27, Z=0.62, and Z=0.97. A few important observations are discussed.

Firstly, near the ground at plane Z=0.27, the shear stress at the low Reynolds number SAB_9 is positive (~UW=0.026) in the near wake after X=0.3 but less than ~UV=0.009 between X= 0 – 0.3. The negative peaks (~UW>0.003) are found around the separated shear layer from the side surfaces. After X=0.8, the negative shear stress is concentrated around the symmetry plane (Y=0) up to X=1.7. Although a similar trend is also observed at the high Reynolds number SAB_40. Nevertheless, the area occupied by the positive peaks in the near wake is reduced to X= 0.4 – 0.7 in the streamwise and Y= -0.5 – 0.5 in the spanwise direction. In addition to that, the negative peaks due to side surface shear layers are more pronounced (~UW=-0.015). Furthermore, at the wall-normal height of plane Z=0.62, the shear stresses are reduced and become symmetric while having negative values ~0.009<UW<0 both in the SAB_9 and the SAB_40 after X=0.3. However, before X=0.3, the UV values remain positive. It is to be noted that, at a high Reynolds number, a major part of the wake is dominated by positive shear stresses. Finally, at the plane Z=0.97, the near wake becomes negative shear stress dominant and provides a well-defined symmetric structure around the Y=0. On the other hand, the separated side shear layer has a reduced negative UW value. These features are maintained at the SAB_40 as well but are more prominent.

At low Reynolds number plane Z=0.27 for the EAB_9, the elliptical curvature, on the other hand, exerts a side force that creates symmetric shear layers at each end with positive UW=0.025 - 0.03 values that extend until X=1.0. In between these two positive shear layers, the near wake is dominated by negative UW values that also extend far downstream. These features are also accompanied by a high Reynolds number as well with a slight reduction in positive UW values. However, the side surface separated shear layer is detached after X=0, which is dissimilar from the EAB_9. Subsequently, the size of such a positive UW region is smaller. Thus the Reynolds number seems to affect the size and magnitude of the shear stress.

Secondly, at the Z=0.62 plane, the symmetric layers become shorter and have negative UW values in the EAB_9. Furthermore, at high Reynolds number EAB_40, the symmetric layers remain but are smaller in size, and predominantly negative UW values are found. Finally, at Z=0.97, a rather significant difference is found. Two small symmetric layers exist along with the negative dominated wake at the low Reynolds number EAB_9. In contrast, at the high Reynolds number EAB_40, the symmetric shear layer is found after X=0.4 and is positive. It should be noted that the differences found between the EAB_9 and EAB_40 are due to the fact that the location of URB is not exactly similar at the low and high Reynolds numbers.

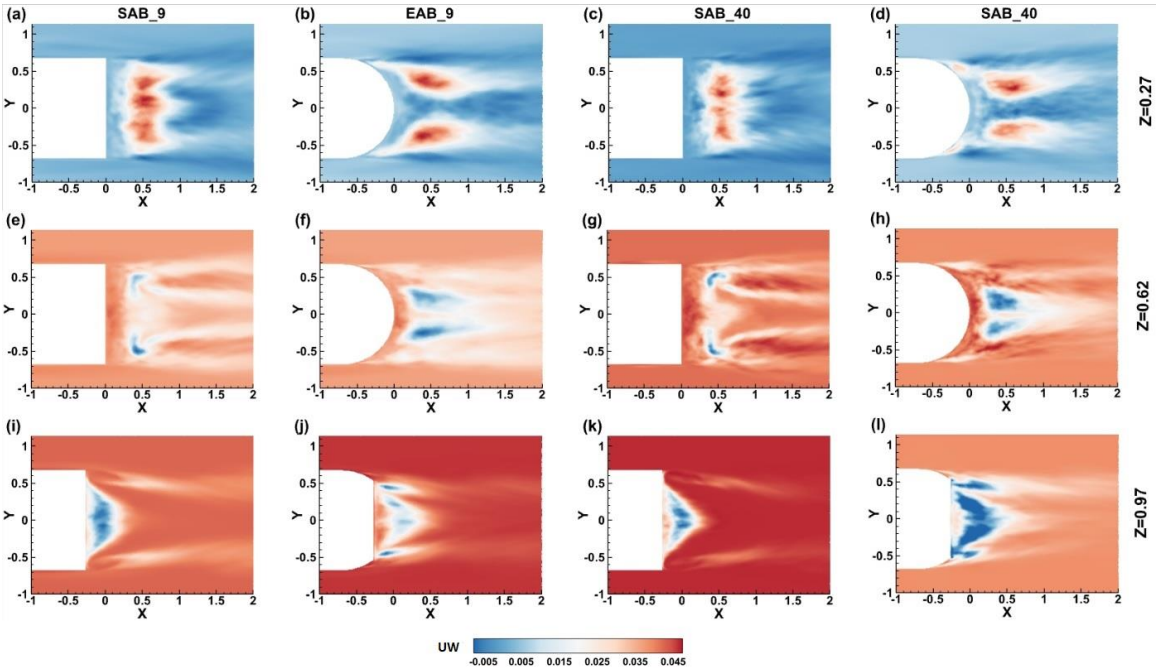

Figure 4.38: Reynolds shear stress (UW) in the spanwise (x-y) plane at Z=0.27, Z=0.62 and Z=0.97.

4.2.2.8 Drag reduction

The investigation so far has suggested that elliptical curvature is a promising feature for drag reduction. The curvature modifies the SSB, C-vortices and the wake recirculation region, however, it does not capture the fully separated flow similar to the experimental investigation of the SAB_9_Exp. At the 25° slant angle. Nonetheless, the present simulation reveals the absence of longitudinal C-vortices from the side edges responsible for a considerable increase in the pressure drag. Consequently, even at a low Reynolds

number, the EAB_9 provides a drag reduction of ~6.6%. On the other hand, at a high Reynolds number, the percentage reduction has increased to 10.4%, as documented in Table 4.4. Therefore, as far as SSB is present in the EAB, the drag reduction can reach up to 10.4% using the IDDES simulation.

Table 4.4: Drag reduction due to elliptical curvature.

	Drag Coefficient					
Angle	SAB_9	EAB_9	% reduction	SAB_40	EAB_40	% reduction
25°	0.384	0.359	6.6	0.353	0.316	10.4

4.3 Effects of the Hydrophobic Coating

As indicated in Chapter 1 and Chapter 2, the standard Ahmed body (SAB) is a larger part of the critical geometries having similar flow features. The flow around some submarines produces closer flow features to the Ahmed body at the rear end[14], [324]. There are other underwater applications of 3D bluff bodies, including large structures, such as caisson structures or oscillating water columns (OWC), wave energy converters (WECs) [16], and underwater energy storage systems [17]. Therefore, the study of the effects of HPS on the Ahmed body flow features has several underwater applications. The Ahmed body provides this unique combination where its flow structures can help understand the effect on both ground and underwater applications. This thesis is the first attempt to study the effect of the hydrophobic coating on the Ahmed body. Such a study provides a foundation to extrapolate the results found in the Ahmed body to other 3D bluff bodies. Hence, this section provides a detailed experimental description of the effects of the hydrophobic coating on the Ahmed body. The experiment is conducted at a Reynolds number of 0.431×10^5 based on the model height. To comprehend both the time-averaged and time-dependent flow characteristics, the mean velocities, Reynolds stresses, TKE, two-point auto-correlation, frequency spectra, proper orthogonal decomposition (POD), and Dynamic Mode Decomposition (DMD) approaches are used. Since the detailed results and discussion about the SAB and EAB without the hydrophobic coating are already presented in section 4.1, the same is not repeated here for the sake of comparison. However, according to necessity, the results will be contextualized in the discussion.

4.3.1 Mean velocity

The effect of the hydrophobic coating on the mean flow properties over the SAB and EAB provides new information not available in the open literature. Hence, Figure 4.39 shows the mean flow in the streamwise and wall-normal directions in the symmetry plane, respectively.

(a) hydrophobic standard Ahmed body (HSAB)

The streamwise and wall-normal velocity contours of the HSAB are shown in Figure 4.39(a)-(b). There are a few important observations. First, similar to the SAB, the flow separated at the upper edge of the slant surface and reattached over the rear end, thus

creating the SSB. However, due to the hydrophobic coating, the height of the SSB in the HSAB is increased. Additionally, the wall-normal velocity increases due to flow separation, as found in Figure 4.39(b). It suggests that the flow separation point and the SSB are modified due to the hydrophobic coating compared to the SAB. However, a hydrofoil at a 20° angle of attack investigated previously [268] showed results that are consistent with those of a bluff body. They reported no significant difference in the slant and wake flow features between the coated and non-coated hydrofoils, concluding that the effect of the hydrophobic coating is confined to a certain range of angles of attack. Nonetheless, in the current case, with the 25° slant angle, the effect of the hydrophobic coating is evident. Secondly, along with the modification of the SSB location, the hydrophobic coating also influences the length of the SSB. The reattachment point is found around 80% of the slant length, which is approximately 15% higher than the non-coated SAB. Guilmineau [85] reported an increasing trend in the length of the SSB with the slant angle, which was 95% at the 32° slant angle. Thus, the hydrophobic coating provided 80% SSB length at a quite low slant angle of 25°. Thirdly, when the flow separates at the rear edge of the slant surface, two recirculation bubbles form, similar to the SAB. It increases the wall-normal velocity (Figure 4.39(b)) and is reduced after the wake recirculation region. Nonetheless, the location of the upper recirculation bubble (URB) and lower recirculation bubble (LRB) shows a slight difference from the SAB. In the HSAB, the centre of the URB is at X=1.60, Z=0.60, while that of the LRB rests at X=1.6, Z=0.30. Whereas the streamwise location of the URB is similar to the SAB, the wall-normal distance is increased by 8%. Conversely, the streamwise location of the LRB is reduced by 6% without any changes in the wall-normal direction. However, these alterations may seem trivial but are necessary to document since they might be due to the extended length of the SSB over the slant surface. Fourthly, the formation of the wake recirculation region is also evident in the HSAB. Nonetheless, there is a fundamental difference with the SAB. The maximum recirculation length (L_r) in the case of the SAB was ~ 0.64 at Z=0.36. However, in the HSAB, the recirculation length at Z=0.36 is found to be ~ 0.60, which is 7.6% less than that of the SAB. It means that the location of the maximum recirculation length is modified in the HSAB. Consequently, the maximum wake recirculation length ~ 0.63 in the HSAB is now located at ~Z=0.42, which is ~14.2% shift in the wall-normal direction

compared to that of the SAB. Moreover, the height of the recirculation region taken at X=1.5 is ~ 0.33, which is slightly less than that of the SAB (~0.36). There are several studies using the hydrophobic coating that found a reduction in wake recirculation length due to delay in flow separation, for example [265], [325] on a circular cylinder [268] on hydrofoils and [270] with a bump inside the channel. In the present case, compared to the specific position of the maximum recirculation length of the SAB, the HSAB does reduce the wake recirculation length. However, the HSAB provides a similar maximum recirculation length but is located 14.2% above the corresponding SAB.

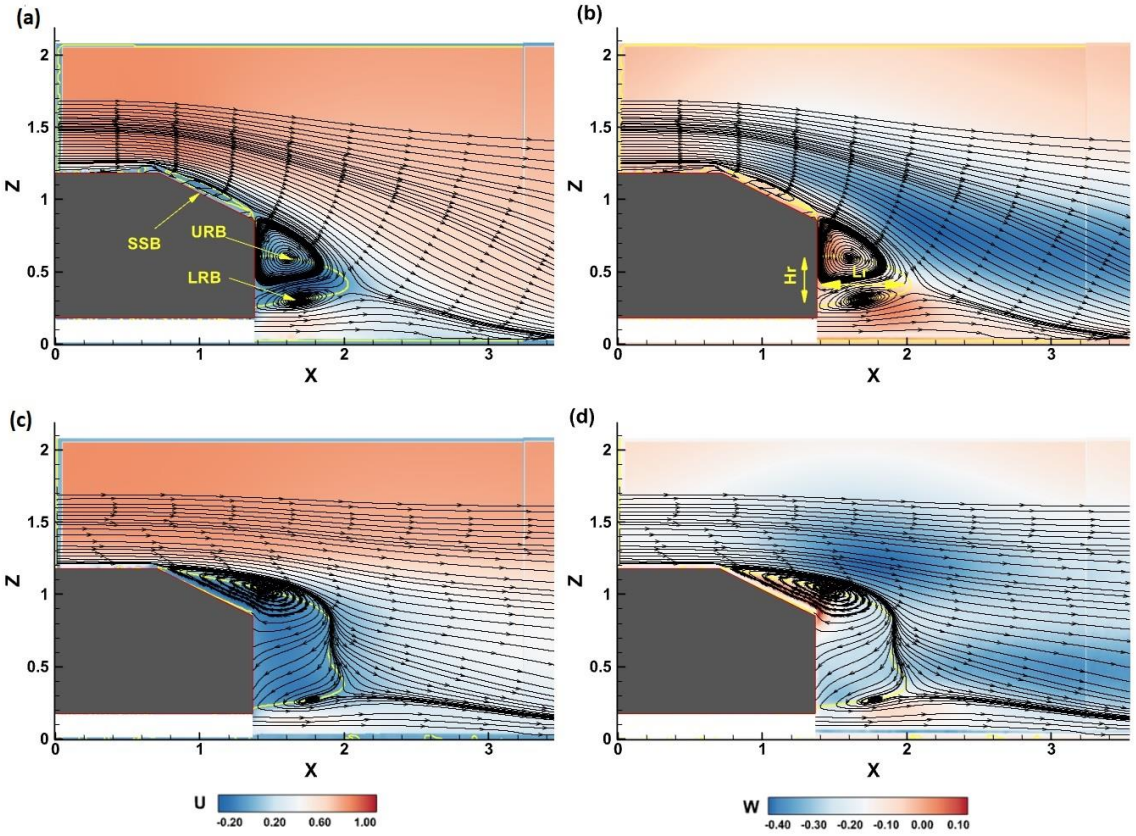

Figure 4.39: Time-averaged contours of the streamwise and wall-normal velocity at the symmetry plane (Y=0) superimposed by the mean streamlines. (a) & (b) HSAB and (c) & (d) HEAB. The solid red line denotes zero velocity (U=0), and it delimits the wake recirculation region. URB- Upper recirculation bubble, LRB- Lower recirculation bubble, SSB- Slant separation bubble.

(b) hydrophobic elliptical Ahmed body (HEAB)

The velocity contours of the HEAB are shown in Figure 4.39(c)-(d). Similar to the SAB, the flow separates at the upper edge of the slant surface. The point of separation is

almost the same for both the EAB and HEAB. Secondly, the existence of an enlarged wake is evidently similar to the EAB in size; however, the shape is dissimilar to that of the EAB. As a result, the location of the URB in the HEAB is slightly changed. The center of the URB is now at ~X=1.46, Z=1.03. In addition to that, a weak LRB is found away from the vertical base at ~X=1.8, Z=0.25, which is not available in the EAB. Finally, there are two maximum recirculation lengths in the HEAB. One is located at ~Z=0.80, providing a recirculation length of approximately ~ 0.52. A second maximum recirculation length exists at ~ Z=0.37, which is around ~ 0.62. Compared with the EAB, the second maximum length at ~Z=0.37 is around 6% larger, but at ~Z=0.80, it is around 10% lower than the EAB. Such a modification in the wake provides a slight change compared to the EAB.

4.3.2 Reynolds stresses

The effect of the hydrophobic coating on the SAB and EAB is analyzed using the contours of the Reynolds stresses. The normal and shear stresses are shown in Figure 4.40 at the symmetry plane. A few observations can be made.

(a) hydrophobic standard Ahmed body (HSAB)

The contours of the Reynolds stresses of the HSAB are shown in Figure 4.40(a)-(b). Near the upper edge of the slant surface, the normal stress values are reduced by 58% compared to the SAB to UU=0.05. Towards the rear end of the slant surface, no difference is found from the SAB. On the other hand, a dominant shear stress layer in Figure 4.40(b) can be observed over the slant surface, which is more pronounced in the HSAB than in the SAB. The values of the shear stresses at the upper and rear ends of the slant surface undergo a significant change and show around UW=-0.008, which is almost ~52% less than the SAB. However, the normal stresses in the HSAB are more shifted in the wall-normal direction and less inclined to a slant surface. This feature is different from that of the SAB. At the top shear layer, UU=0.01 shows an increase of 40% more than the SAB. Furthermore, the stresses at the lower shear layer are significantly reduced by almost 81% with respect to the SAB. In contrast, shear stress at the top shear layer is decreased in the HSAB by 80% with a value UW=-0.005. Finally, the shape and magnitude of UW in the HSAB decreased from positive in the SAB to negative UW=-0.0003 in the HSAB. Therefore, the general effect of the hydrophobic coating over the Ahmed body is providing

reduced normal and shear stresses both over the slant and wake. It has been noted in the literature that the hydrophobic coating reduces the Reynolds stresses and TKE [326], and it is associated with drag reduction. Finally, the negative and positive shear stresses associated with the URB and LRB are still maintained in the HSAB. This is expected since the center location of the URB and LRB is not changed much.

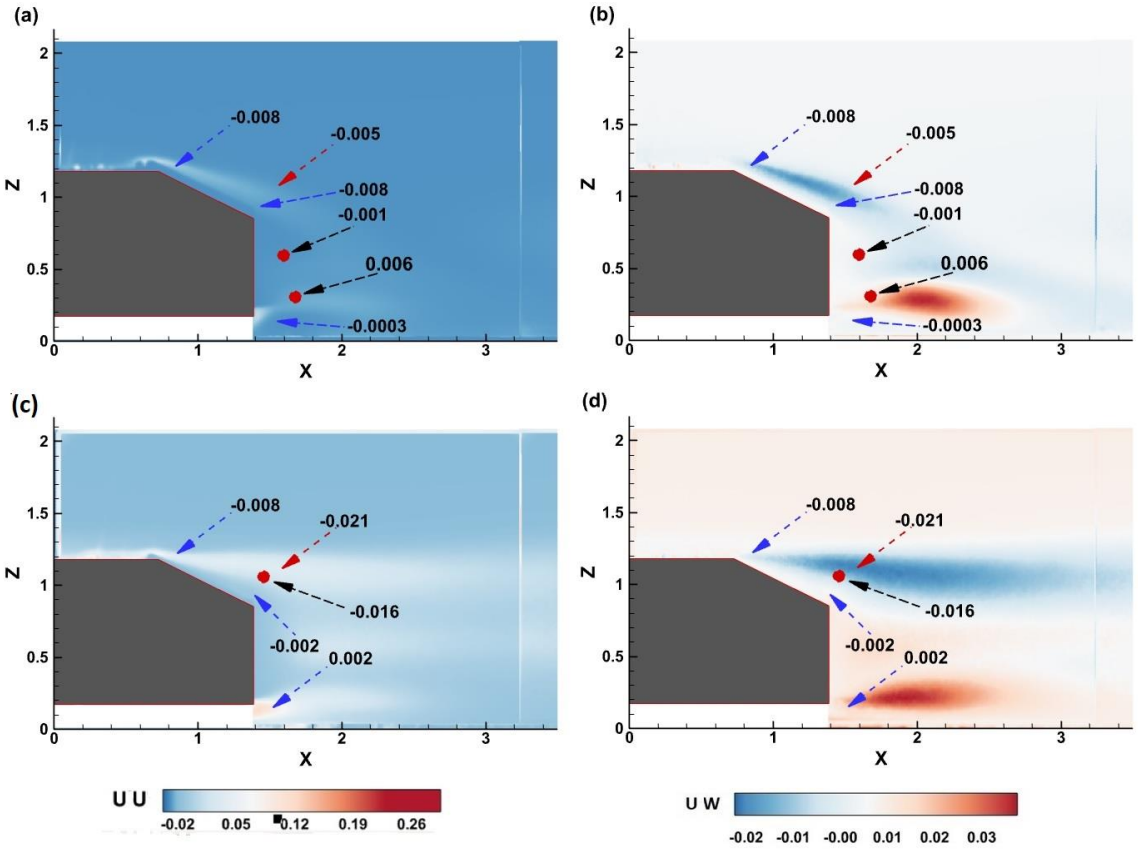

Figure 4.40: Contours of Reynolds normal and shear stresses at the symmetry plane Y=0, where (a) & (b) is HSAB and (c) & (d) is HEAB.

(b) hydrophobic elliptical Ahmed body (HEAB)

The effect of hydrophobic coating on the Reynolds stresses is discussed with respect to Figure 4.40(c)-(d). The major difference lies in the upper separated shear layer, which is more parallel to the streamwise direction than in the EAB. In addition, a small region of normal stress concentration is found between the upper and lower shear layers, which is not available in the EAB. Although the normal stress value is slightly higher near the upper edge of the slant surface, it is almost similar at the rear end. Similarly, the separated upper

layer shows closer values of UW=0.06 to that of the EAB. On the other hand, shear stress is reduced in the separated layer while it slightly gains at the centre of the shifted URB. Furthermore, both the normal and shear stresses are reduced in the lower separated layer, and no difference in the shape is found.

4.3.3 Two-point autocorrelation

This section describes the large-scale structures in the wake by extracting the two-point autocorrelations. Since the flow is predominantly streamwise, R_{uu} is explored in this direction [67].

(a) hydrophobic standard Ahmed body (HSAB)

Figure 4.41 shows the R_{uu} for the HSAB at the same five locations similar to the SAB (Figure 4.4). The shape of the R_{uu} at point #1 in the HSAB (Figure 4.41(a)) is close to that of the SAB, having a nearly elliptical shape but stretched in the flow direction. This implies that the HSAB is also connected with the variable flow at the top slant edge. However, the R_{uu} contours in the HSAB show a reduced negative inclination of -20° toward the slant surface. This is associated with the flow reattachment in the SAB, but as discussed with reference to Figure 4.39, the formation of the SSB in the HSAB significantly differs from that of the SAB. Since the reattachment length and location are different in the HSAB, and that is visible in the reduced inclination angle. More specifically, compared to the SAB, the HSAB's R_{uu} contours at locations #2 and #3 (Figure 4.41(b) and (c)) are flatter. Point #2 is almost parallel to the streamwise flow and less stretched compared to point #1. However, at point #3, the angle is 24 degrees in the streamwise direction, which is not the same as the slant surface and is 2° less than the SAB. The creation of the LRB coincides with this steady increase in the positive angles observed in the HSAB. Hence, the correlation is found at the center of the LRB at point #4 with an inclination of around 18°, shown in Figure 4.41(d). This inclination is 8° higher than that of the SAB. The formation of an SSB and its associated downwash has resulted in a negatively inclined R_{uu} at the URB (point #5). The above observations are consistent with the discussions of the mean velocities and Reynolds stresses.

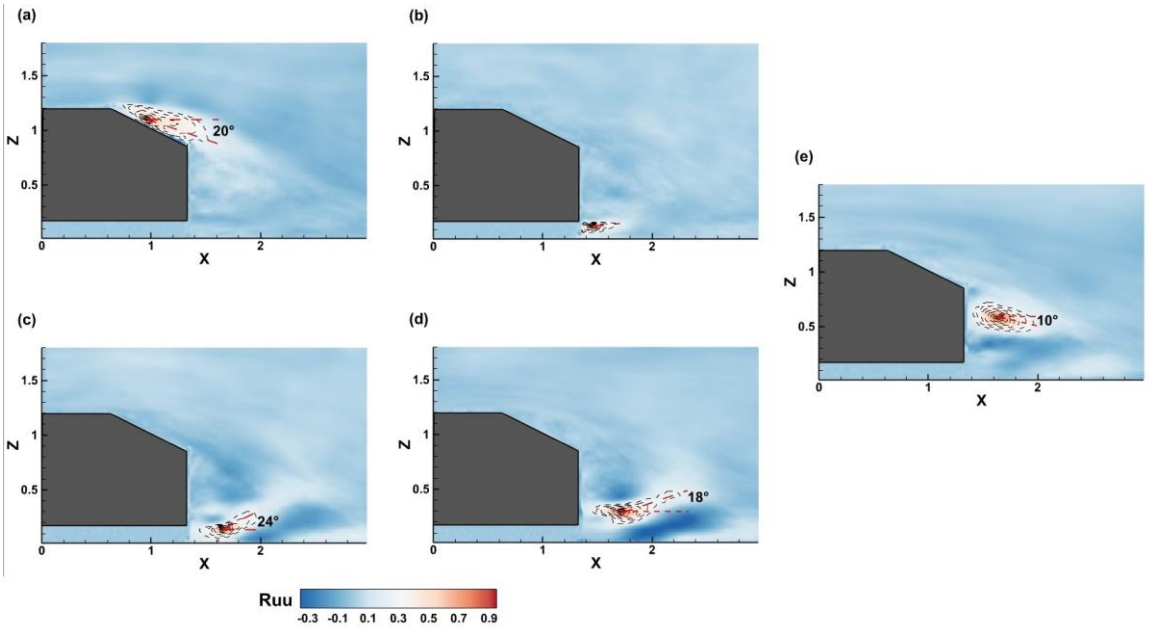

Figure 4.41: The HSAB's autocorrelation contours for the streamwise fluctuating velocity R_{uu}, using slant and wake locations on the symmetry plane as reference points. Where (a) Point #1: X=0.96, Z=1.09 (b) Point #2: X=1.46, Z=0.121 (c) Point #3: X=1.66, Z=0.135 (d) Point #4: X=1.72, Z=0.284 (e) Point #5: X=1.65, Z=0.57.

(b) hydrophobic elliptical Ahmed body (HEAB)

In Figure 4.42, the two-point autocorrelation of the HEAB is shown for the six locations indicated as similar to the EAB (Figure 4.5). The shape of R_{uu} in the HEAB (at point #1) is close to the EAB but larger in size. In the lower shear layer of the HEAB, the point near the vertical base of the model (point #2) is parallel to the streamwise flow but comparatively larger in size than that of the EAB (Figure 4.42(b)). Point #3 is similar to that of the EAB, with an inclination of 20° (Figure 4.42(c)). Point #5 is again parallel to the streamwise flow since the influence of the LRB (point #4) weakens around the lower shear layer. The centre of the URB is displaced in the direction of the wall-normal flow as a result of the HEAB flow detaching over the slant surface. As shown for point #5, the shape of the shifted URB is reduced but has a positive angle of 8° which does not exist in the EAB (Figure 4.42(e)). The patterns of the two-point correlation and inclination in the HEAB highlight the importance of the velocity correlation. Hence, the reduction in shape and inclination is observed both at the slant surface and in the wake due to the hydrophobic coating.

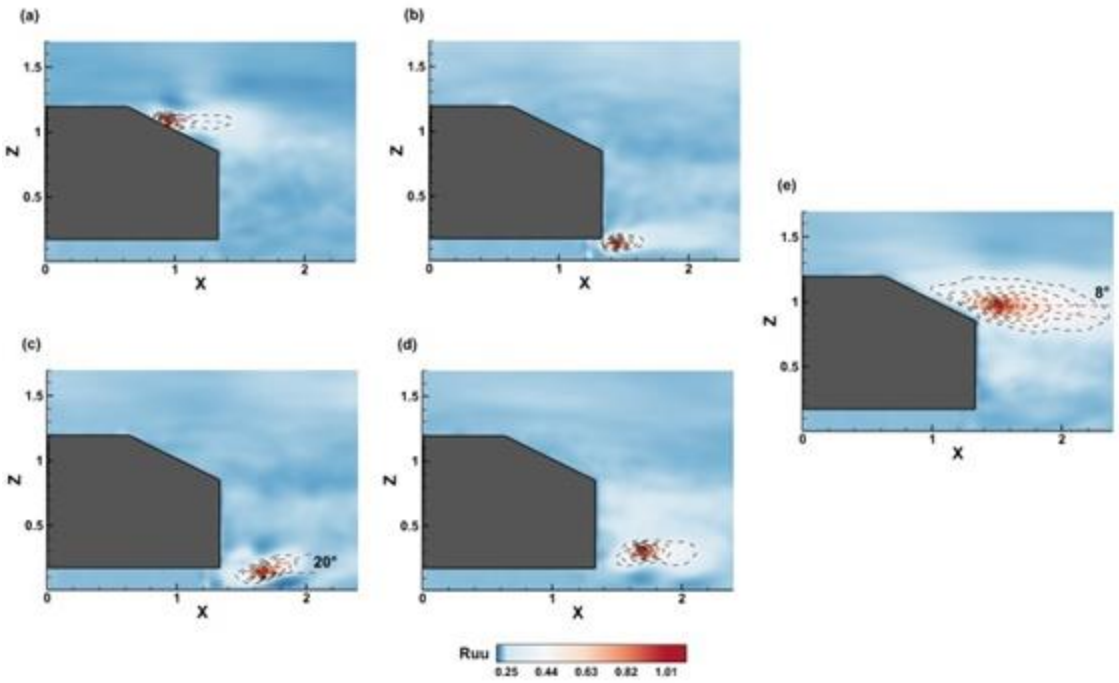

Figure 4.42: The HEAB's autocorrelation contours for the streamwise fluctuating velocity R_{uu}, using slant and wake locations on the symmetry plane as reference points. Where (a) Point #1: X=0.96, Z=1.09 (b) Point #2: X=1.46, Z=0.121 (c) Point #3: X=1.66, Z=0.135 (d) Point #4: X=1.72, Z=0.284 (e) Point #5: X=1.52, Z=0.96.

4.3.4 Frequency spectra

The Strouhal number of the streamwise velocity fluctuations is investigated in this section over the slant surface and the wake, as indicated in Figure 4.6 and documented in Table 4.5. The effect of the hydrophobic coating on the vortex shedding frequency or the Strouhal number has been reported on the bluff bodies in the literature. Xiong and Yang [327] studied the effect on the elongated bluff body and found that the SHPS increases the Strouhal number. Similarly, Zeinali et al. [44] also investigated the effect of the SHPS over a sphere and found that it increases the Strouhal number. The increasing trend in the Strouhal number is also reported over a circular cylinder as well [328].

Table 4.5: The Strouhal numbers for the HSAB and HEAB extracted at some specific locations indicated as point number #1 to #12. Please see Figure 4-12 for the schematics of the point locations.

Re × 10^5							
4.3				7.7 (1)*	4.6-9.2 (2)*	8.9 (3)*	0.5 - 7.0 (4)*
Point No #	Locations (X, Z)	Strouhal #s					
		HSAB	HEAB	SAB without coating			
#1	0.84, 1.15	0.24	0.48	0.25	0.11	0.35	
#2	0.96, 1.09	0.24	0.48	0.21	0.11	-	0.20
#3	1.07, 1.04	0.24	0.55	0.21	0.11	-	-
#4	1.17,0.99	0.24	0.40	0.15	-	0.27	-
#5	1.31,0.95	1.8	0.91		-	-	-
#6	1.46,0.12	0.48	0.62	0.45	0.53	-	
#7	1.66,0.13	0.23	0.85	-	-	-	
#8	1.72,0.28	0.16	0.25	-	-	-	0.44
#9	1.65,0.57	0.66	0.80	-	-	-	
#10	2.05,0.35	5.19	0.48	0.45	-	0.42	

(1)* Numerical study by Delassaux et al. [34], (2)* Experimental study by Thacker et al. taken from [34], (3)* Minguez et al. [307] and (4)* Experimental study by [72].

(a) hydrophobic standard Ahmed body (HSAB)

In the HSAB, over the slant surface in Table 4.5, increased S_t values are found, representing points #1 to point #4. Compared to the SAB, these S_t values are approximately 50% higher. Hence, similar to the SAB, a consistent dominant S_t=0.24 is discovered over the slant surface except at the rear end (point#5). This value remains close to the S_t values found in the literature. The rear end shows peak value S_t=1.8, at point #5. A value like this suggests an oscillating flow at the rear end of the slant. In the wake, however, various Strouhal numbers are observed except near the saddle point. Between point #6 to point #9, the S_t values are within the range of S_t=0.48-0.66, which is similar to those of the SAB. As

highlighted earlier, Zhang et al. [72] reported an S_t=0.44 in the wake showing quasiperiodic phenomena. Furthermore, in the near wake of a sphere, $S_{t=}$ 0.8 was reported by Zeinali et al. [44], which is consistent with the present study. Nevertheless, near the saddle point (point #10), the St_{10}=5.19 is large but consistent with the value reported in the near wake of a sphere for Reynolds number $>10^{4,}$ for example, in [309]. Therefore, the HPS increased the Strouhal number at the slant surface by 50%. Such a trend is also found in the literature and ascribed to drag reduction in Zeinali et al.[44] . The cause of this can be ascribed to the changes observed over the slant surface. However, once separated at the slant rear edge, the hydrophobic coating does not affect the flow structure and follows the Strouhal number trends found in the non-hydrophobic SAB which is related to quasiperiodic phenomena.

(b) hydrophobic elliptical Ahmed body (HEAB)

As discussed earlier, the effect of hydrophobic coating on the SAB is that it increased the Strouhal number, especially over the slant surface, however, the hydrophobic coating affects the HEAB differently. Over the slant surface, between points #1 and #4, a general consistency in the Strouhal number shows an average value of $S_t\approx0.47$. At the rear end, however, the Strouhal number increased to $S_t\approx0.91$, which is similar to the value for the EAB. In the wake of the HEAB, several high frequencies exist. The values at the lower end close to the ground are $S_{t6}\approx0.62$ and $S_{t7}\approx0.85$. Whereas point # 8 shows a reduced value of $S_t\approx0.25$, it again increased to $S_t\approx0.80$ at point #9. Point #10 shows a similar value of $S_{t10}\approx0.48$ for the EAB. These results indicate that the effect of the hydrophobic coating is more evident in the near wake of the EAB than over the slant surface. At the shifted URB, a high value of $S_{t11}\approx0.88$ is found, which is comparatively less than that for the EAB. Two Strouhal numbers, St_{12}=0.56 & 0.23, are also found in the shear layer, point #12. Therefore, it is inferred that since the EAB already has a fully detached flow, the existence of partial slip over the slant surface reduced the TKE the most at the slant surface. Such a reduction in TKE can lead to large scale instability and reduce the frequency in Kim and Durbin [309].

4.3.5 Turbulent kinetic energy variation

The literature suggests that the hydrophobic coating increases the turbulent kinetic energy (TKE) fluctuations due to the surface roughness pattern, which in turn reduces the wake recirculation dimensions. There are vortical structures induced by the wall pattern,

and these vortical structures transfer fluctuations to the surface of the no-slip interface and away from the wall. By increasing the fluctuations, the separation point is delayed, resulting in an earlier reattachment of the flow and a decrease in the form drag [270]. On the other hand, some other bluff body studies associate a reduction in TKE with an increase in the recirculation length, which reduces the pressure drag [315], [316]. Considering the recirculation region, it seems the mechanism of drag reduction with other passive/active flow control varies in nature in the hydrophobic coating. Accordingly, the TKE profiles over the slant surface and in the wake of the test model are displayed to study the effect of the hydrophobic coating.

In Figure 4.43(a), after the flow separation, at X=0.8, a maxima TKE=0.4 is found in the SAB, but the hydrophobic coating reduced the TKE to ~0.37 in the HSAB. In contrast, with flow separation having detached flow at the upper edge, the EAB shows a reduction in the TKE compared to the SAB & HSAB. However, this reduction in TKE due to fully separated flow is further augmented by the hydrophobic coating, and the HEAB demonstrates a 21% reduction in the TKE compared to the EAB. This trend corresponds to the area where no reverse flow is found near the upper edge of the slant surface.

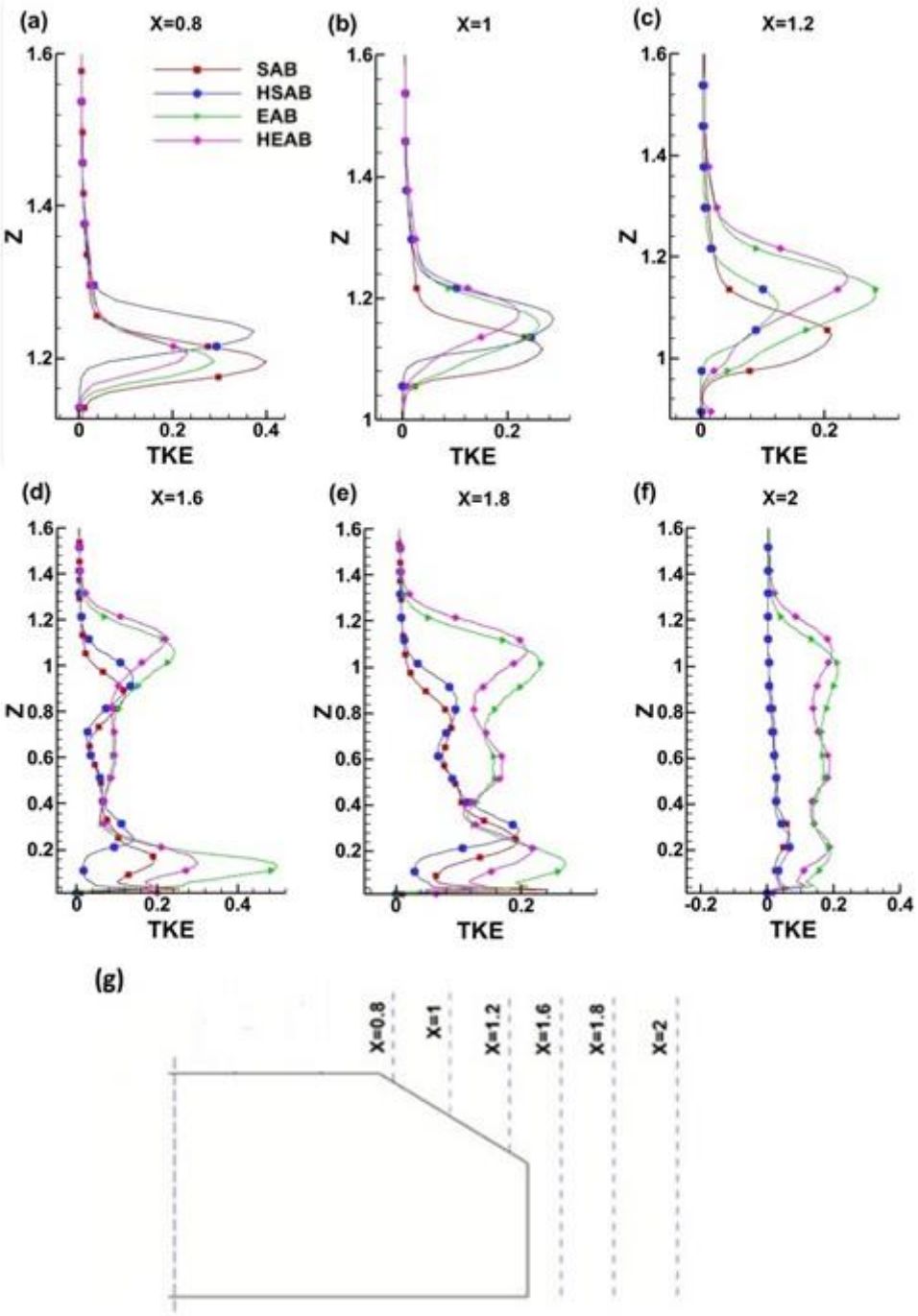

Figure 4.43: Turbulent kinetic energy (TKE) profiles in the symmetry plane at selected locations. Here (g) describes the extracted location for the TKE profile.

However, in the middle of the slant surface where the SSB exists (X=1.0) Figure 4.43 (b), not much difference is found between the SAB and HSAB, but the maxima of TKE=0.3 is found in the HSAB, whereas the HEAB has the lowest value of TKE=0.2, even less than

the EAB. Further downstream towards the rear end X=1.2 in Figure 4.43(c), the maxima of TKE=0.28 are shifted to the EAB, while the HSAB significantly reduced the TKE to 0.11, which is around 45% less than that of the SAB. In comparison, the HEAB is 21% less compared to the EAB. It indicates that, just outside the SSB, both the HSAB and HEAB reduce the TKE values. The existence of the SSB in the SAB and HSAB but not in the EAB and HEAB allows different peaks of the TKE to exist over the slant surface. Nonetheless, in the wake, the TKE is bifurcated by the existence of the wake recirculation region. Before the recirculation region, the EAB had high TKE values, while the HSAB shows the minimum both at X=1.6 & 1.8 locations. Inside the recirculation region, the TKE is less near the vertical base X=1.6 than at X=1.8. Also, above the recirculation region, the HEAB reduced the TKE compared to the EAB. The SAB and HSAB follow a similar trend; however, their TKE values are less than those of the EAB and HEAB.

Finally, at X=2, both the SAB and HSAB show a slight fluctuation near the floor, and then the profiles become smooth. However, the EAB and HEAB have higher TKE values compared to those of the SAB and HSAB, respectively. The TKE trend in the wake recirculation region differs for the SAB and EAB due to the nature of the flow separation and the formation of the URB and LRB in the SAB but only a large wake in the EAB. Furthermore, the reasons for the multiple peaks in the TKE are due to the nature of flow separation, which influences the mixing of turbulence eddies. For example, in the SAB and HSAB where the slant separation bubble exists, the TKE shows different peaks than the EAB and HEAB where the fully separated flow exists. The increase in the TKE in the shear layer due to fully separated flow is associated with the amplification of the Kelvin Helmholtz (KH) instability in the shear layer, which does not exist in the SAB and HSAB Moore and Amitay [329]. Also, due to the existence of the upper and lower recirculation regions in the SAB and HSAB, the TKE peaks are different from the EAB and HEAB, which only have an enlarged upper recirculation region.

The hydrophobic and non-hydrophobic models follow the same trend. In addition to that, it can be seen in Figure 4.43 that the early diffusion is only visible in the wake, but over the slant surface, the TKE profiles fluctuate depending on the existence of the slant separation bubble. The difference is also not evident at the near wake at X=1.6. However,

the early diffusion of the TKE at X=1.8 and then X=2 in the SAB/HSAB is due to the difference in the dimensions of the wake recirculation region. This early diffusion is associated with the higher mixing of turbulent structures, which depends on the nature of the flow separation. Therefore, the turbulent mixing is higher in the SAB/HSAB, which affects the recirculation region and the TKE diffused earlier compared to the EAB/HEAB.

Overall, the TKE trend in Figure 4.43 reveals that, in general, the hydrophobic coating reduced the TKE fluctuations over the slant surface and inside the wake recirculation region, which is consistent with previous studies[326], [330]. This is true for both the HSAB and the HEAB. Consequently, this reduction corresponds to a decrease in the recirculation length in the wake due to the hydrophobic coating and could lead to drag reduction [265], [270], [326], [331], [332]. However, other studies on axis-symmetric bluff bodies[315], [320] also associated the reduced TKE with increased recirculation length in the wake, which can reduce the drag. Therefore, it is conjectured that in the HSAB and HEAB, a reduction in the TKE might be related to reduced recirculation length at some locations, as indicated in previous studies.

4.3.6 Proper orthogonal decomposition

This section discusses the effect of hydrophobic coating on coherent structures and associated frequencies. The POD is used here to extract the dominant frequency in the wake of the HSAB and HEAB models similar to the SAB and EAB discussed in section 4.1.6.

At first, Figure 4.44(a) & (b) shows the total energy percentage and the energy accumulated within the initial fifty modes. The POD is taken inside the limit of {X=1.15-3.3} and {Z=0.025- 2.05}. According to Figure 4.44(a), the relative energy captured in the 1st and 2nd POD modes in the HSAB is 9.4% and 9%, respectively, and this drops to 3.8% in the 3rd mode. In addition, the HEAB shows higher relative energy of 10.5% in the 1st POD mode but only 5.5% in the 2nd mode. In general, it can be observed from Figure 4.44 (a) that fractional energy from the 1st POD mode to the 50th decays more steeply in the HSAB compared to the HEAB. Furthermore, the cumulative energy in Figure 4.44(b) shows an increasing trend, as expected. It is observed that the first 50 modes contribute to about 56% of energy in the HSAB and in the HEAB the cumulative energy is closer to

65%. These values are similar to the non-hydrophobic SAB and EAB. The first two modes contain the highest energy, which is discussed below.

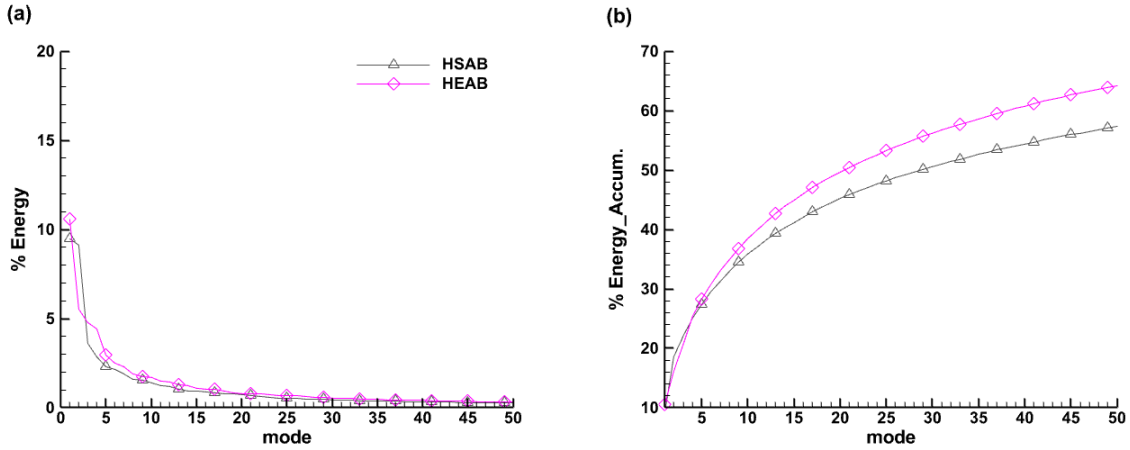

Figure 4.44: POD Energy contribution for four cases, where (a) percentage energy contribution, (b) percentage accumulative contribution.

(a) hydrophobic standard Ahmed body (HSAB)

The effect of the hydrophobic coating on the POD modes can be seen in Figure 4.45(a)-(d), where the streamwise velocity contours of 1st mode of the HSAB are shown. These are similar to the SAB, with two negative velocity regions divided by a positive velocity field. The 2nd mode, however, shows the exchange of the two dominant negative and positive regions compared to the SAB. It means the negative velocity region is replaced by a positive region and vice versa. Similarly, the wall-normal velocity (Figure 4.45(c)) of the 1st mode closely follows that of the SAB. However, in the 2nd mode in Figure 4.45(d), the alternating positive and negative velocity regions exchange locations compared to the SAB. It means that the positive velocity becomes negative and vice versa. Nevertheless, the calculated Strouhal number for both the 1st and 2nd modes remains the same as the SAB, which is St=0.36 and 0.48, respectively. It suggests that the hydrophobic coating has no significant effect on the coherent structures of the POD modes. Such S_t values are attributed to quasiperiodic dynamics similar to the SAB.

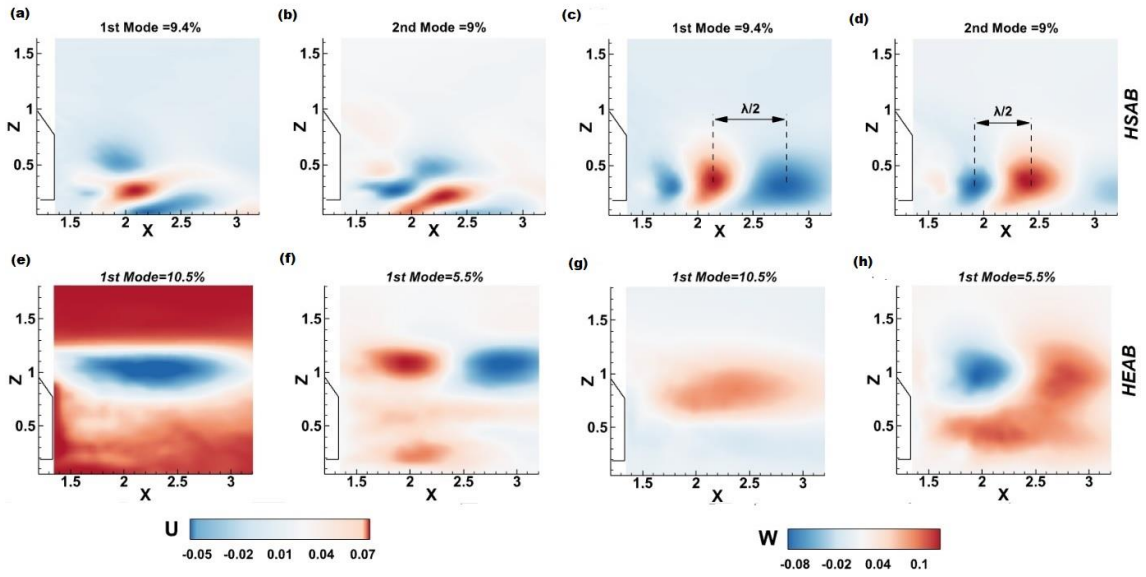

Figure 4.45: Contours of the POD Modes. The first row is HSAB, and the Second row is HEAB First two columns- Streamwise velocity, and the last two columns- Wall-normal velocity. Where (a)-(c), (e)-(g),: 1st mode and (b)-(d) & (f)-(h): 2nd mode.

(b) hydrophobic elliptical Ahmed body (HEAB)

The hydrophobic coating shows no effect on the 1st mode, as shown with streamwise velocity contours of the HEAB in Figure 4.45(e)-(f), whereas the 2nd mode in Figure 4.45(g)-(h) shows two alternate positive and negative velocity fields in the upper region. In addition, a positive velocity field exists in the lower region. These two features are not found in the POD modes of the EAB but are not similar to the EAB. In the wall-normal direction, the 1st mode in Figure 4.45(g) shows a predominantly positive velocity field, while the 2nd mode in Figure 4.45(h) is similar to the EAB. Therefore, no dominant Strouhal number can be achieved using the POD modes.

4.3.7 Dynamic mode decomposition

This section discusses the effect of hydrophobic coating on the coherent structures and associated frequencies using the DMD analysis.

The Strouhal number of the HSAB and HEAB with associated DMD modes is shown in Figure 4.46. It is interesting to note that the dominant Strouhal number in the HSAB is S_t=0.30, which is close to the values found in the POD analysis for the SAB. These values are within the Strouhal number found in the literature. It should be noted that the Strouhal number for both the SAB and HSAB in the POD analysis does not change, indicating that

the hydrophobic coating does not affect wake flow behavior. DMD supports this explanation by providing the same trend while highlighting the dominant Strouhal number of the wake. On the other hand, the dominant Strouhal number for the HEAB, is close to S_t=0.013, indicating the insensitivity of the hydrophobic coating similar to the POD. The corresponding DMD modes show energetic velocity fields without any alternate negative and velocity fields. According to the literature, a lower DMD Strouhal number suggests a more energetic mode, and a higher one indicates less energetic [313]. Consequently, the modes in the HSAB are less energetic than the HEAB at this dominant Strouhal number.

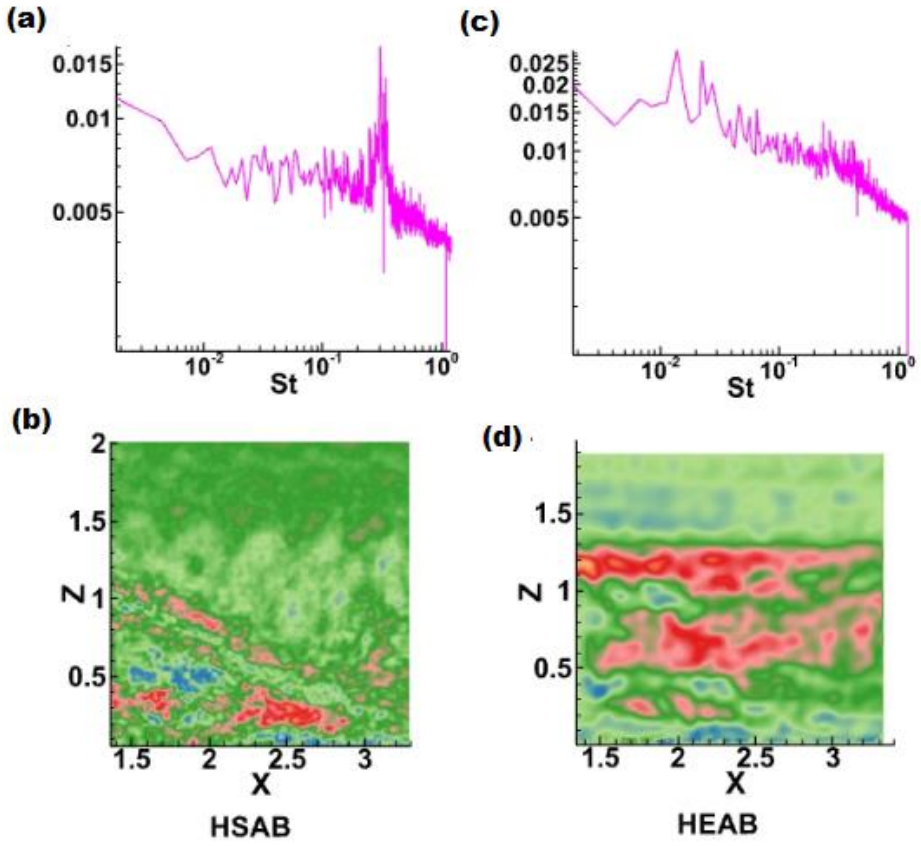

Figure 4.46: DMD analysis of the models. The first row indicates the dominant Strouhal number found in the wake of the model, and the second row shows the corresponding contour of the real part of streamwise velocity. Here (a) & (b) HSAB, (c) & (d) HEAB.

4.4 Chapter Summary

This chapter provided a comprehensive investigation of the standard Ahmed body (SAB) and elliptical Ahmed body (EAB) using both experimental and numerical methods. The important contribution can be summarized as follows:

The experimental results and discussions were described considering the effect of curvature on the SAB at 4.31×10^4 model-height based Reynolds number. It was found that the EAB at 25º slant angle provided a fully separated flow over the slant surface and eliminated the lower recirculation bubble. These modified flow structures suggested drag and rear end surface contamination reduction.

The experimental investigation was complemented with the numerical method using the detached eddy simulation (DES). At first, the effect of the slant angle (25º to 30º) was investigated over the SAB to establish the capability of the DES method to capture the flow structure at a model height-based Reynolds number 1.47×10^4. Also, it was intended to find out if a fully separated flow exists at the critical slant angle of 30º reported in the literature. The DES simulation found that it captured the SAB flow structures well with the slant angle variations. However, the fully separated flow was not found at the 30º slant angle using the DES. Secondly, the simulation around the SAB and EAB was conducted at 4.31×10^4 and 1.90×10^5 model height-based Reynolds numbers at a specific slant angle of 25º to complement the experiment. The investigation showed that at both the Reynolds numbers in the EAB, the flow separated and reattached around ~93 & 95% of the slant length, respectively, indicating a near flow transition phenomenon. It was also found that both the C-vortices and the LRB were eliminated. Although, the flow did not fully separated at 25°, it provided a drag reduction of ~10.4% at the 1.90×10^5 Reynolds number.

Finally, the experimental results of the effect of the hydrophobic coating on the SAB and EAB were discussed for 4.31×10^4 model-height based Reynolds number. Based on the findings of this study, the hydrophobic coating was comparatively more impactful on the SAB than the EAB. This can be attributed to the existence of the slant separation bubble in the SAB, which was greatly influenced by the hydrophobic coating but did not exist in the EAB.

Chapter 5: Conclusions and Recommendations

This chapter is divided into three sections to summarize the work undertaken in this thesis. The first section provides some conclusions on the main findings, and the second section provides some recommendations for future works.

5.1 Conclusions

This thesis conducted a detailed experimental and numerical study of 3D bluff bodies using the standard Ahmed body (SAB) at a 25º slant angle as a simplified representation of 3D bluff bodies. The SAB at 25º was studied because of its complex three-dimensional and unsteady flow structure at three Reynolds numbers, 1.47×10^4, 4.31×10^4 and 1.90×10^5 based on the model height. The time-averaged and time-dependent flow structures originated from the application of elliptical curvature, and the hydrophobic coating at the rear end has been investigated in detail using advanced vortex analysis techniques. The modified Ahmed body with elliptical curvature was defined as the elliptical Ahmed body (EAB).

The results show that the EAB at a 25º slant angle provided significant changes in the flow. The EAB created a fully separated flow, which was accompanied by the elimination of the slant separation bubble (SSB), C-vortices from the side edges and the lower recirculation bubble (LRB) near the ground while shifting the upper recirculation bubble (URB) towards the slant surface. These modifications were indicative of a significant drag reduction. Moreover, the presence of the LRB in the wake flow plays a significant role in the surface contamination at the rear end. The LRB, formed near the ground at the rear of the bluff body, entrains the surrounding particles and diffuses them towards the rear window, leading to undesirable contamination. Hence, the elimination of LRB in the EAB provided evidence of the suppression of the rear surface contamination. Furthermore, the Strouhal number (S_t) in the EAB is augmented to an averaged value of S_t=0.75 over the slant surface compared to the SAB, which showed a dominant value of S_t=0.16 only. However, the Strouhal number in the wake of EAB S_t=0.43 are closer to the S_t=0.50 of the SAB. The high S_t values are associated with the instability of the separating shear layer over the slant surface. Furthermore, the dominant Strouhal number provided by the dynamic mode decomposition (DMD) in the wake of the EAB is much smaller, S_t=0.013.

This lower Strouhal number suggested a more energetic mode. The unsteady flow dynamics suggested that the quasiperiodic phenomena associated with the alternate shedding of the URB and LRB found in the SAB are suppressed in the EAB due to the elimination of the LRB. In addition, the URB has grown in size over the slant surface in the EAB compared to the SAB. This increase in the URB indicates a corresponding increase in pressure over the slant surface. In fact, the numerical investigation showed a drag reduction of around ~6.6% at the Reynolds number of 4.31×10^4 and ~10.4% at the Reynolds number of 1.90×10^5.

In addition, the thesis examined the effects of the hydrophobic coating on the turbulent structure at the rear of the SAB and EAB. The SAB has a complex TDS at the rear end, whereas the EAB has a fully separated flow. It was found that the hydrophobic coating affected the flow structure on the SAB more significantly than on the EAB. This was attributed to the existence of the SSB in the SAB. The SSB was significantly affected by the hydrophobic coating and increased the reattachment length up to 80% of the slant length. This, in turn, led to a delay in the reattachment point at the rear edge of the slant surface. The turbulent kinetic energy (TKE) and shear stress were also reduced by 45% and 52%, respectively, on the slant surface in the SAB with a hydrophobic coating. The Strouhal number was increased by 50% in the SAB with the hydrophobic coating, with a dominant value of S_t=0.24 found over the slant surface compared to the SAB (S_t=0.16) without the hydrophobic coating. The proper orthogonal decomposition (POD) analysis showed that the Strouhal number for the first and second modes were S_t=0.36 and S_t=0.48, respectively, for the SAB with the hydrophobic coating. Similarly, the DMD analysis demonstrated a dominant Strouhal number of S_t=0.30 in the SAB with the hydrophobic coating. These results suggested a comparatively higher impact of the hydrophobic coating at the slant surface than in the wake. Since the SSB modification and increase in the Strouhal number were found over the slant surface, both mean, and unsteady wake structures were similar to the SAB without the hydrophobic coating.

On the other hand, the hydrophobic coating affected the EAB flow structure differently. Here, the wake recirculation length was increased by 6%, whereas the TKE recovery was reduced by 21% over the slant and 66% in the wake, respectively, compared to the EAB

without the hydrophobic coating. In addition, an averaged Strouhal number of S_t=0.47 was found over the slant surface and S_t=0.64 in the wake of the EAB with the hydrophobic coating. Compared to the EAB without the hydrophobic coating, these values suggest that the hydrophobic coating reduced the Strouhal number by 36% over the slant surface and a 39% increase in the wake. Furthermore, the POD analysis did not show any dominant Strouhal numbers in the wake, whereas the DMD found a dominant Strouhal number of S_t=0.013 in the wake of EAB with the hydrophobic coating. This low Strouhal number suggested the existence of energetic modes. Therefore, the results on the effect of hydrophobic coating focusing on the rear end of the EAB and SAB suggested that the effectiveness of the hydrophobic coating used in this study depends on the nature of flow separation at the rear end. However, more research is required to draw a generalized conclusion on the effects of hydrophobic coating on the 3D bluff bodies.

5.2 Recommendations for Future Work

Based on the work undertaken in the current thesis, the recommendations are expected to provide future research directions to extend the body of knowledge generated in this thesis.

1. The current study provides ample evidence of the effects an elliptical curvature creates, it is recommended that the slant angle variations can provide further information, such as the effects on the flow structure.

2. The elliptical Ahmed body (EAB) provided an in-depth effect of the curvature focusing on the rear end of the Ahmed body.

3. Also, the elliptical curvature is proven to be a significant geometric factor in influencing flow structure. Therefore, more variations of the curvature can be examined to extend the idea of curvature as a flow control method.

4. The current work is the first attempt to study the effect of the hydrophobic coating on complex three-dimensional bluff bodies. Future investigation can focus on the numerical and experimental investigation at different Reynolds numbers to confirm and extend the present results.

References

[1] National Research Council, “Twenty-First Symposium on Naval Hydrodynamics,” Twenty-First Symposium on Naval Hydrodynamics, Aug. 1997. doi: 10.17226/5870.

[2] P. W. Bearman, “Developments in the Understanding of Bluff Body Flows.,” JSME International Journal Series B, vol. 41, no. 1, pp. 103–114, Feb. 1998. doi: 10.1299/jsmeb.41.103.

[3] M. R. Lekkala et al., “Recent advances in understanding the flow over bluff bodies with different geometries at moderate Reynolds numbers,” Ocean Engineering, vol. 261, p. 111611, Oct. 2022. doi: 10.1016/J.OCEANENG.2022.111611

[4] H. Choi, W.-P. Jeon, and J. Kim, “Control of Flow Over a Bluff Body,” Annual Review of Fluid Mechanics, vol. 40, no. 1, pp. 113–139, Jan. 2008. doi: 10.1146/annurev.fluid.39.050905.110149.

[5] S. Sarraf, M. Abbaspour, K. M. Dolatshahi, S. Sarraf, and M. Sani, “Experimental and numerical investigation of squat submarines hydrodynamic performances,” Ocean Engineering, vol. 266, p. 112849, Dec. 2022. doi: 10.1016/J.OCEANENG.2022.112849.

[6] Wolf-Heinrich Hucho, Aerodynamics of Road Vehicles, 4th ed. SAE International, 1998.

[7] J. Howell and G. le Good, “The Effect of Backlight Aspect Ratio on Vortex and Base Drag for a Simple Car-Like Shape,” SAE Technical Papers, Apr. 2008. doi: 10.4271/2008-01-0737.

[8] G. Bonnavion et al., “On multistabilities of real car’s wake,” Journal of Wind Engineering and Industrial Aerodynamics, vol. 164, pp. 22–33, May 2017. doi: 10.1016/J.JWEIA.2017.02.004.

[9] B. Conan, J. Anthoine, and P. Planquart, “Experimental aerodynamic study of a car-type bluff body,” Experiments in Fluids 2010 50:5, vol. 50, no. 5, pp. 1273–1284, Oct. 2010. doi: 10.1007/S00348-010-0992-Z.

[10] S. R. Ahmed, G. Ramm, and G. Faltin, “Some Salient Features Of The Time-Averaged Ground Vehicle Wake,” SAE Transactions, vol. 93, no. 2, pp. 473–503, Feb. 1984. doi: 10.4271/840300.

[11] W.-H. Hucho, “The Aerodynamic Drag of Cars Current Understanding, Unresolved Problems, and Future Prospects,” in Aerodynamic Drag Mechanisms of Bluff Bodies and Road Vehicles, Boston, MA: Springer US, 1978, pp. 7–44. doi: 10.1007/978-1-4684-8434-2_2.

[12] Wolf-Heinrich Hucho, Aerodynamics of road vehicles. 2016.

[13] Z. Yu and Z. Bingfu, “Recent Advances in Wake Dynamics and Active Drag Reduction of Simple Automotive Bodies,” Applied Mechanical Review, vol. 73, no. 6, Nov. 2021. doi: 10.1115/1.4053132/1129077.

[14] H Tanaka, “A Study of Resistance of Shallow-Running Flat Submerged Bodies,” Journal of the Society of Naval Architects of Japan, vol. 137, 1974.

[15] C. Huo, Y. Zheng, and X. peng Gao, “Free-running tests on a self-propelled submersible multi-state vehicle model,” Ocean Engineering, vol. 236, p. 109575, Sep. 2021. doi: 0.1016/J.OCEANENG.2021.109575.

[16] O. Lancaster, R. Cossu, M. Wilson, and T. E. Baldock, “A 3D numerical and experimental parametric study of wave-induced scour around large bluff body structures,” Ocean Engineering, vol. 266, p. 112766, Dec. 2022. doi: 10.1016/J.OCEANENG.2022.112766.

[17] Z. Wang, J. Wang, H. Cen, D. S. K. Ting, R. Carriveau, and W. Xiong, “Large-eddy simulation of a full-scale underwater energy storage accumulator,” Ocean Engineering, vol. 234, p. 109184, Aug. 2021. doi: 10.1016/J.OCEANENG.2021.109184

[18] R. Li, “Aerodynamic Drag Reduction of a Square-Back Car Model Using Linear Genetic Programming and Physic-Based Control,” ISAE-ENSMA Ecole Nationale Supérieure de Mécanique et d’Aérotechique, 2017.

[19] A. Booysen, “Characterization and passive control of the wake behind a square-back Ahmed body at yaw,” University of Alberta, 202. . doi: 10.7939/R3-JS8K-QY50.

[20] G. M. le Good and K. P. Garry, “On the Use of Reference Models in Automotive Aerodynamics,” SAE Technical papers, Mar. 2004. doi: 10.4271/2004-01-1308.

[21] J.-F. Beaudoin and J.-L. Aider, “Drag and lift reduction of a 3D bluff body using flaps,” Experiment in Fluids, vol. 44, no. 4, pp. 491–501, Apr. 2008, doi: 10.1007/s00348-007-0392-1.

[22] T. Morel, “The Effect of Base Slant on the Flow Pattern and Drag of Three-Dimensional Bodies with Blunt Ends,” pp. 191–226, 1978. doi: 10.1007/978-1-4684-8434-2_8.

[23] K. Xu, X. Su, R. Bensow, and S. Krajnovic, “Drag reduction of ship airflow using steady Coanda effect,” Ocean Engineering, vol. 266, p. 113051, Dec. 2022. doi: 10.1016/J.OCEANENG.2022.113051.

[24] Y. Haffner, J. Boreé, A. Spohn, and T. Castelain, “Mechanics of bluff body drag reduction during transient near-wake reversals,” Journal of Fluid Mechanics, vol. 894, 2020. doi: 10.1017/JFM.2020.275.

[25] A. Rao, G. Minelli, B. Basara, and S. Krajnović, “On the two flow states in the wake of a hatchback Ahmed body,” Journal of Wind Engineering and Industrial Aerodynamics, vol. 173, pp. 262–278, Feb. 2018. doi: 10.1016/j.jweia.2017.10.021.

[26] I. Kohri, T. Yamanashi, T. Nasu, Y. Hashizume, and D. Katoh, “Study on the Transient Behaviour of the Vortex Structure behind Ahmed Body,” SAE International Journal of Passenger Cars - Mechanical Systems, vol. 7, no. 2, pp. 586–602, Apr. 2014. doi: 10.4271/2014-01-0597.

[27] T. Avadiar, M. C. Thompson, J. Sheridan, and D. Burton, “The influence of reduced Reynolds number on the wake of the DrivAer estate vehicle,” Journal of Wind Engineering and Industrial Aerodynamics, vol. 188, pp. 207–216, May 2019. doi: 10.1016/J.JWEIA.2019.02.024.

[28] B. F. Zhang, K. Liu, Y. Zhou, S. To, and J. Y. Tu, “Active drag reduction of a high-drag Ahmed body based on steady blowing,” Journal of Fluid Mechanics, vol. 856, pp. 351–396, Dec. 2018. doi: 10.1017/JFM.2018.703.

[29] E. Guilmineau, “Computational study of flow around a simplified car body,” Journal of Wind Engineering and Industrial Aerodynamics, vol. 96, no. 6–7, pp. 1207–1217, Jun. 2008. doi: 10.1016/J.JWEIA.2007.06.041.

[30] O. Evstafyeva, A. S. Morgans, and L. Dalla Longa, “Simulation and feedback control of the Ahmed body flow exhibiting symmetry breaking behaviour,” Journal of Fluid Mechanics, vol. 817, p. R2, Apr. 2017. doi: 10.1017/jfm.2017.118.

[31] M. Grandemange, M. Gohlke, and O. Cadot, “Turbulent wake past a three-dimensional blunt body. Part 1. Global modes and bi-stability,” Journal of Fluid Mechanics, vol. 722, pp. 51–84, May 2013. doi: 10.1017/jfm.2013.83.

[32] G. Rossitto, C. Sicot, V. Ferrand, J. Borée, and F. Harambat, “Influence of afterbody rounding on the pressure distribution over a fastback vehicle,” Experiment in Fluids, vol. 57, no. 3, pp. 1–12, Mar. 2016. , doi: 10.1007/S00348-016-2120-1/FIGURES/18.

[33] A. Thacker, S. Aubrun, A. Leroy, and P. Devinant, “Effects of suppressing the 3D separation on the rear slant on the flow structures around an Ahmed body,” Journal of Wind Engineering and Industrial Aerodynamics, vol. 107–108, pp. 237–243, Aug. 2012. doi: 10.1016/j.jweia.2012.04.022.

[34] F. Delassaux, I. Mortazavi, E. Itam, V. Herbert, and C. Ribes, “Sensitivity analysis of hybrid methods for the flow around the ahmed body with application to passive control with rounded edges,” Computer & Fluids, vol. 214, p. 104757, Jan. 2021. doi: 10.1016/j.compfluid.2020.104757.

[35] G. Rossitto, C. Sicot, V. Ferrand, J. Borée, and F. Harambat, “Aerodynamic performances of rounded fastback vehicle,” Proceedings of the Institution of Mechanical Engineers, Part D: Journal of Automobile Engineering, vol. 231, no. 9, pp. 1211–1221, Aug. 2017. doi: 10.1177/0954407016681684.

[36] J. Bico, C. Marzolin, and D. Quéré, “Pearl drops,” Europhys Lett, vol. 47, no. 6, p. 743, Sep. 1999. doi: 10.1209/EPL/I1999-00453-Y.

[37] N. Kim, H. Kim, and H. Park, “An experimental study on the effects of rough hydrophobic surfaces on the flow around a circular cylinder,” Physics of Fluids, vol. 27, no. 8, p. 085113, Aug. 2015, doi: 10.1063/1.4929545.

[38] J. P. Rothstein, “Slip on Superhydrophobic Surfaces,” Annual Reviw of Fluid Mechanics, vol. 42, pp. 89–109, Dec. 2009, doi: 10.1146/ANNUREV-FLUID-121108-145558.

[39] K. Moaven, M. Rad, and M. Taeibi-Rahni, “Experimental investigation of viscous drag reduction of superhydrophobic nano-coating in laminar and turbulent flows,” Experimental Thermal and Fluid Science, vol. 51, 2013, doi: 10.1016/j.expthermflusci.2013.08.003.

[40] S. Farhadi, M. Farzaneh, and S. A. Kulinich, “Anti-icing performance of superhydrophobic surfaces,” Applied Surface Science, vol. 257, no. 14, 2011, doi: 10.1016/j.apsusc.2011.02.057.

[41] H. Li and S. Yu, “A robust superhydrophobic surface and origins of its self-cleaning properties,” Applied Surface Science, vol. 420, 2017, doi: 10.1016/j.apsusc.2017.05.131.

[42] P. Sooraj, M. S. Ramagya, M. H. Khan, A. Sharma, and A. Agrawal, “Effect of superhydrophobicity on the flow past a circular cylinder in various flow regimes,” Journal of Fluid Mechanics, vol. 897, 2020, doi: 10.1017/JFM.2020.371.

[43] Canada Energy Regulator, “Provincial and Territorial Energy Profiles – Alberta,” Cer-Rec.Gc.Ca, 2021.

[44] “Greenhouse gas sources and sinks: executive summary 2021 - Canada.ca.” https://www.canada.ca/en/environment-climate-change/services/climate-change/greenhouse-gas-emissions/sources-sinks-executive-summary-2021.html (accessed Jul. 23, 2021).

[45] G. H. L. Y. Y. Y. C. S. Yuan Gao, “Numerical Study of Flow Characteristics Around Underwater Vehicle Model at High Reynolds Number,” in International Ocean and Polar Engineering Conference, 2019.

[46] B. Zeinali and J. Ghazanfarian, “Turbulent flow over partially superhydrophobic underwater structures: The case of flow over sphere and step,” Ocean Engineering, vol. 195, p. 106688, Jan. 2020, doi: 10.1016/J.OCEANENG.2019.106688.

[47] P. W. Bearman, “The Effect of Base Bleed on the Flow behind a Two-Dimensional Model with a Blunt Trailing Edge,” Aeronautical Quarterly, vol. 18, no. 3, pp. 207–224, Aug. 1967, doi: 10.1017/s0001925900004212.

[48] P. R. Viswanath, “Flow management techniques for base and afterbody drag reduction,” Progress in Aerospace Sciences, vol. 32, no. 2–3. Pergamon, pp. 79–129, Jan. 01, 1996. doi: 10.1016/0376-0421(95)00003-8.

[49] V. Parezanović and O. Cadot, “Experimental sensitivity analysis of the global properties of a two-dimensional turbulent wake,” Journal of Fluid Mechanics, vol. 693, pp. 115–149, Feb. 2012, doi: 10.1017/jfm.2011.495.

[50] B. Thiria, O. Cadot, and J. F. Beaudoin, “Passive drag control of a blunt trailing edge cylinder,” Journal of Fluids and Structure, vol. 25, no. 5, pp. 766–776, Jul. 2009, doi: 10.1016/j.jfluidstructs.2008.07.008.

[51] M. Grandemange, “Analysis and Control of Three-dimensional Turbulent Wakes: from Axisymmetric Bodies to Road Vehicles,” École Polytechnique — ENSTA ParisTech, 2013.

[52] B. Forouzi Feshalami, S. He, F. Scarano, L. Gan, and C. Morton, “A review of experiments on stationary bluff body wakes,” Physics of Fluids, vol. 34, no. 1, p. 011301, Jan. 2022, doi: 10.1063/5.0077323.

[53] H. Choi, J. Lee, and H. Park, “Aerodynamics of Heavy Vehicles,” Annu Rev Fluid Mech, vol. 46, no. 1, pp. 441–468, Jan. 2014, doi: 10.1146/annurev-fluid-011212-140616.

[54] W. Hucho and G. Sovran, “Aerodynamics of Road Vehicles,” Annual Review of Fluid Mechanics, vol. 25, no. 1, pp. 485–537, Jan. 1993, doi: 10.1146/annurev.fl.25.010193.002413.

[55] Y. Yang, D. Zhang, and Z. Liu, “Optimization and design method for a rough rear surface on the notchback MIRA model,” Proceedings of the Institution of Mechanical Engineers, Part D: Journal of Automobile Engineering, vol. 232, no. 10, pp. 1297–1309, Sep. 2018, doi: 10.1177/0954407017728840.

[56] M. Abdolmaleki, A. Mashhadian, S. Amiri, V. Esfahanian, and H. Afshin, “Numerical-Experimental Geometric Optimization of the Ahmed Body and Analyzing Boundary Layer Profiles,” Journal of Optimization Theory and Applications 2021 192:1, vol. 192, no. 1, pp. 1–35, Sep. 2021, doi: 10.1007/S10957-021-01932-W.

[57] R. Li, B. R. Noack, L. Cordier, J. Borée, and F. Harambat, “Drag reduction of a car model by linear genetic programming control,” Experiment in Fluids, vol. 58, no. 8, pp. 1–20, Aug. 2017, doi: 10.1007/s00348-017-2382-2.

[58] Y. Li et al., “Explorative gradient method for active drag reduction of the fluidic pinball and slanted Ahmed body,” Journal of Fluid Mechanics, vol. 932, p. A7, Feb. 2022, doi: 10.1017/JFM.2021.974.

[59] G. M. le Good and K. P. Garry, “On the Use of Reference Models in Automotive Aerodynamics,” SAE Technical Papers, Mar. 2004, doi: 10.4271/2004-01-1308.

[60] M. Moonesun et al., “Optimization on submarine stern design,” http://dx.doi.org/10.1177/1475090215625673, vol. 231, no. 1, pp. 109–119, Feb. 2016, doi: 10.1177/1475090215625673.

[61] T. Morel, “The Effect of Base Slant on the Flow Pattern and Drag of Three-Dimensional Bodies with Blunt Ends,” in Aerodynamic Drag Mechanisms of Bluff Bodies and Road Vehicles, Boston, MA: Springer US, 1978, pp. 191–226. doi: 10.1007/978-1-4684-8434-2_8.

[62] A. I. Heft, T. Indinger, and N. A. Adams, “Introduction of a New Realistic Generic Car Model for Aerodynamic Investigations,” SAE Technical Papers, Apr. 2012, doi: 10.4271/2012-01-0168.

[63] F. Zigunov, P. Sellappan, and F. Alvi, “Reynolds number and slant angle effects on the flow over a slanted cylinder afterbody,” Journal of Fluid Mechanics, vol. 893, 2020, doi: 10.1017/JFM.2020.214.

[64] L. Dalla Longa, O. Evstafyeva, and A. S. Morgans, “Simulations of the bi-modal wake past three-dimensional blunt bluff bodies,” Journal of Fluid Mechanics, vol. 866, pp. 791–809, May 2019, doi: 10.1017/JFM.2019.92.

[65] E. Essel, S. Das, and R. Balachandar, “Effects of Rear Angle on the Turbulent Wake Flow between Two in-Line Ahmed Bodies,” Atmosphere 2020, Vol. 11, Page 328, vol. 11, no. 4, p. 328, Mar. 2020, doi: 10.3390/ATMOS11040328.

[66] D. Burton, S. Wang, D. Tudball Smith, H. N. Scott, T. N. Crouch, and M. C. Thompson, “The influence of background turbulence on Ahmed-body wake bistability,” Journal of Fluid Mechanics, vol. 926, p. R1, 2021, doi: 10.1017/JFM.2021.706.

[67] S. S. Aleyasin, M. F. Tachie, and R. Balachandar, “Characteristics of flow past elongated bluff bodies with underbody gaps due to varying inflow turbulence,” Physics of Fluids, vol. 33, no. 12, p. 125106, Dec. 2021, doi: 10.1063/5.0072390.

[68] D. Fan, B. Zhang, Y. Zhou, and B. R. Noack, “Optimization and sensitivity analysis of active drag reduction of a square-back Ahmed body using machine learning control,” Physics of Fluids, vol. 32, no. 12, p. 125117, Dec. 2020, doi: 10.1063/5.0033156.

[69] B. Sims-Williams, David, “Self-Excited Aerodynamic Unsteadiness Associated with Passenger Cars,” Durham University, 2001.

[70] T. Tunay, E. Firat, and B. Sahin, “Experimental investigation of the flow around a simplified ground vehicle under effects of the steady crosswind,” International Journal of Heat Fluid Flow, vol. 71, pp. 137–152, Jun. 2018, doi: 10.1016/J.IJHEATFLUIDFLOW.2018.03.020.

[71] J. Venning, T. McQueen, D. lo Jacono, D. Burton, M. Thompson, and J. Sheridan, “Aspect ratio and the dynamic wake of the Ahmed body,” Experimental Thermal and Fluid Science, vol. 130, p. 110457, Jan. 2022, doi: 10.1016/J.EXPTHERMFLUSCI.2021.110457.

[72] B. F. Zhang, Y. Zhou, and S. To, “Unsteady flow structures around a high-drag Ahmed body,” Journal of Fluid Mechanics, vol. 777, pp. 291–326, Aug. 2015, doi: 10.1017/jfm.2015.332.

[73] T. H. Tran, M. Anyoji, T. Nakashima, K. Shimizu, and A. D. Le, “Experimental Study of the Skin-Friction Topology Around the Ahmed Body in Cross-Wind Conditions,” Journal of Fluids Engineering, vol. 144, no. 3, Mar. 2022, doi: 10.1115/1.4052418.

[74] Md. Shehab Uddin and F. Rashid, “Effect of Rear Wing on Time-Averaged Ground Vehicle Wake With Variable Slant Angle,” Journal of Fluids Engineering, vol. 143, no. 7, Jul. 2021, doi: 10.1115/1.4050373.

[75] Y. Huang, S. Wang, Y. Ji, and Z. Liu, “Study of the automotive aerodynamic performance affected by entrance structure of forecabin,” Energy and Built Environment, vol. 2, no. 3, pp. 327–335, Jul. 2021, doi: 10.1016/J.ENBENV.2020.06.012.

[76] K. Liu, B. Zhang, and Y. Zhou, “Correlation between drag variation and rear surface pressure of an Ahmed body,” Experiment in Fluids, vol. 62, no. 6, p. 124, Jun. 2021, doi: 10.1007/s00348-021-03214-7.

[77] P. Sellappan, J. McNally, and F. S. Alvi, “Time-averaged three-dimensional flow topology in the wake of a simplified car model using volumetric PIV,” Experiments in Fluids 2018 59:8, vol. 59, no. 8, pp. 1–13, Jul. 2018, doi: 10.1007/S00348-018-2581-5.

[78] S.-Y. Cheng, K.-Y. Chin, S. Mansor, and A. B. Abd Rahman, “Experimental study of yaw angle effect on the aerodynamic characteristics of a road vehicle fitted with a rear spoiler,” Journal of Wind Engineering and Industrial Aerodynamics, vol. 184, pp. 305–312, Jan. 2019, doi: 10.1016/J.JWEIA.2018.11.033.

[79] K. Liu, B. F. Zhang, Y. C. Zhang, and Y. Zhou, “Flow structure around a low-drag Ahmed body,” Journal of Fluid Mechanics, vol. 913, 2021, doi: 10.1017/jfm.2020.1136.

[80] Y. Kobayashi, I. Kohri, A. Kasai, T. Nasu, D. Katoh, and Y. Hashizume, “Numerical Analysis on the Transitional Mechanism of the Wake Structure of the Ahmed Body,” SAE Technical Papers, Apr. 2016, doi: 10.4271/2016-01-1592.

[81] A. Kasai et al., “Large-Scale Separated Vortex Generated in a Wake Flow of Ahmed’s Body,” Flow, Turbulence and Combustion 2018 102:2, vol. 102, no. 2, pp. 373–388, Jun. 2018, doi: 10.1007/S10494-018-9950-2.

[82] D. B. Sims-Williams and R. G. Dominy, “Experimental Investigation into Unsteadiness and Instability in Passenger Car Aerodynamics,” SAE Technical Papers, Feb. 1998, doi: 10.4271/980391.

[83] I. Kohri, Y. Kobayashi, A. Kasai, T. Nasu, D. Katoh, and Y. Hashizume, “Experimental Analysis on the Transitional Mechanism of the Wake Structure of the Ahmed Body,” SAE International Journal of Passenger Cars - Mechanical Systems, vol. 9, no. 2, pp. 612–624, Apr. 2016, doi: 10.4271/2016-01-1591.

[84] A. Kasai et al., “Large-Scale Separated Vortex Generated in a Wake Flow of Ahmed’s Body,” Flow, Turbulence and Combustion 2018 102:2, vol. 102, no. 2, pp. 373–388, Jun. 2018, doi: 10.1007/S10494-018-9950-2.

[85] E. Guilmineau, “Effects of Rear Slant Angles on the Flow Characteristics of the Ahmed Body by IDDES Simulations,” SAE Technical Papers, vol. 2018-April, Apr. 2018, doi: 10.4271/2018-01-0720.

[86] K. He, G. Minelli, X. Su, G. Gao, and S. Krajnović, “On state instability of the bi-stable flow past a notchback bluff body,” Journal of Fluid Mechanics, vol. 931, p. R6, Jan. 2022, doi: 10.1017/JFM.2021.1025.

[87] K. He, G. Minelli, J. Wang, G. Gao, and S. Krajnović, “Assessment of LES, IDDES and RANS approaches for prediction of wakes behind notchback road vehicles,” Journal of Wind Engineering and Industrial Aerodynamics, vol. 217, p. 104737, Oct. 2021, doi: 10.1016/J.JWEIA.2021.104737.

[88] K. He, G. Minelli, X. Su, G. Gao, and S. Krajnović, “Blockage influence on bi-stable flows of a notchback bluff body,” Physics of Fluids, vol. 33, no. 12, p. 125113, Dec. 2021, doi: 10.1063/5.0077251.

[89] K. He, G. Minelli, X. Su, G. Gao, and S. Krajnović, “Influence of the rounded rear edge on wake bi-stability of a notchback bluff body,” Physics of Fluids, vol. 33, no. 11, p. 115107, Nov. 2021, doi: 10.1063/5.0071925.

[90] A. Sciacchitano and D. Giaquinta, “Investigation of the Ahmed body cross-wind flow topology by robotic volumetric PIV,” in 13th International Symposium on Particle Image Velocimetry – ISPIV 2019, Munich, Jul. 2019.

[91] T. Nakashima, C. Yan, T. Moriuchi, I. Kohri, H. Mutsuda, and Y. Doi, “Active aerodynamics control of simplified vehicle body in a crosswind condition,” The Journal of Engineering, vol. 2020, no. 14, pp. 1005–1011, Nov. 2020, doi: 10.1049/JOE.2020.0062.

[92] I. Gursul, “Recent developments in delta wing aerodynamics,” The Aeronautical Journal, vol. 108, no. 1087, pp. 437–452, 2004, doi: 10.1017/S0001924000000269.

[93] F. Zigunov, P. Sellappan, and F. Alvi, “Reynolds number and slant angle effects on the flow over a slanted cylinder afterbody,” Journal of Fluid Mechanics, vol. 893, p. A11, 2020, doi: 10.1017/JFM.2020.214.

[94] F. Zigunov, P. Sellappan, and F. Alvi, “Reynolds number and slant angle effects on the flow over a slanted cylinder afterbody,” Journal of Fluid Mechanics, vol. 893, 2020, doi: 10.1017/JFM.2020.214.

[95] A. P. Gaylard, “Vehicle surface contamination, unsteady flow and aerodynamic drag,” University of Warwick, 2019.

[96] A. Kabanovs, M. Varney, A. Garmory, M. Passmore, and A. Gaylard, “Experimental and Computational Study of Vehicle Surface Contamination on a Generic

Bluff Body," in SAE Technical Papers, SAE International, Apr. 2016. doi: 10.4271/2016-01-1604.

[97] J. Jilesen, A. Gaylard, and J. Escobar, "Numerical Investigation of Features Affecting Rear and Side Body Soiling," SAE International Journal of Passenger Cars - Mechanical Systems, vol. 10, no. 1, pp. 299–308, Mar. 2017, doi: 10.4271/2017-01-1543.

[98] M. Minguez, R. Pasquetti, and E. Serre, "High-order large-eddy simulation of flow over the 'Ahmed body' car model," Physics of Fluids, vol. 20, no. 9, 2008, doi: 10.1063/1.2952595.

[99] S. Krajnović, "Large eddy simulation exploration of passive flow control around an Ahmed body," Journal of Fluids Engineering, Transactions of the ASME, vol. 136, no. 12, Dec. 2014, doi: 10.1115/1.4027221.

[100] P. Joseph, X. Amandolèse, and J.-L. Aider, "Drag reduction on the 25° slant angle Ahmed reference body using pulsed jets," Experiment in Fluids, vol. 52, no. 5, pp. 1169–1185, May 2012, doi: 10.1007/s00348-011-1245-5.

[101] J. McNally, E. Fernandez, R. Kumar, and F. Alvi, "Near wake dynamics for an Ahmed body with active flow control," 6th AIAA Flow Control Conference 2012, 2012, doi: 10.2514/6.2012-3041.

[102] A. Thacker, S. Aubrun, A. Leroy, and P. Devinant, "Experimental characterization of flow unsteadiness in the centerline plane of an Ahmed body rear slant," Experiments in Fluids 2013 54:3, vol. 54, no. 3, pp. 1–16, Feb. 2013, doi: 10.1007/S00348-013-1479-5.

[103] V. Boucinha, R. Weber, and A. Kourta, "Drag reduction of a 3D bluff body using plasma actuators," International Journal of Aerodynamics, vol. 1, no. 3/4, p. 262, 2011, doi: 10.1504/ijad.2011.038845.

[104] J. R. Bell, D. Burton, M. C. Thompson, A. H. Herbst, and J. Sheridan, "Dynamics of trailing vortices in the wake of a generic high-speed train," Journal of Fluids and Structure, vol. 65, pp. 238–256, Aug. 2016, doi: 10.1016/J.JFLUIDSTRUCTS.2016.06.003.

[105] A. Khan, P. Rajendran, and J. S. S. Sidhu, "Passive Control of Base Pressure: A Review," Applied Sciences, vol. 11, no. 3, p. 1334, Feb. 2021, doi: 10.3390/app11031334.

[106] Y. Zhou and B. Zhang, "Recent Advances in Wake Dynamics and Active Drag Reduction of Simple Automotive Bodies," Applied Mechanical Review, Dec. 2021, doi: 10.1115/1.4053132.

[107] M. Corallo, J. Sheridan, and M. C. Thompson, "Effect of aspect ratio on the near-wake flow structure of an Ahmed body," Journal of Wind Engineering and Industrial Aerodynamics, vol. 147, pp. 95–103, Dec. 2015, doi: 10.1016/J.JWEIA.2015.09.006.

[108] J. Keogh, T. Barber, S. Diasinos, and G. Doig, “The aerodynamic effects on a cornering Ahmed body,” Journal of Wind Engineering and Industrial Aerodynamics, vol. 154, pp. 34–46, Jul. 2016, doi: 10.1016/J.JWEIA.2016.04.002.

[109] N. Ashton and A. Revell, “Key factors in the use of DDES for the flow around a simplified car,” International Journal of Heat Fluid Flow, vol. 54, pp. 236–249, 2015, doi: 10.1016/j.ijheatfluidflow.2015.06.002.

[110] E. Fares, “Unsteady flow simulation of the Ahmed reference body using a lattice Boltzmann approach,” Computer & Fluids, vol. 35, no. 8–9, pp. 940–950, Sep. 2006, doi: 10.1016/J.COMPFLUID.2005.04.011.

[111] E. Guilmineau, G. B. Deng, A. Leroyer, P. Queutey, M. Visonneau, and J. Wackers, “Assessment of hybrid RANS-LES formulations for flow simulation around the Ahmed body,” Computer & Fluids, vol. 176, pp. 302–319, Nov. 2018, doi: 10.1016/J.COMPFLUID.2017.01.005.

[112] B. Podvin, S. Pellerin, Y. Fraigneau, A. Evrard, and O. Cadot, “Proper orthogonal decomposition analysis and modelling of the wake deviation behind a squareback Ahmed body,” Physical Review of Fluids, vol. 5, no. 6, p. 064612, Jun. 2020,doi:10.1103/PHYSREVFLUIDS.5.064612/FIGURES/20/MEDIUM.

[113] B. Podvin, S. Pellerin, Y. Fraigneau, G. Bonnavion, and O. Cadot, “Relationship between the base pressure and the velocity in the near-wake of an Ahmed body,” Physical Review of Fluids, vol. 7, no. 5, p. 054602, May 2022, doi: 10.1103/PHYSREVFLUIDS.7.054602/FIGURES/14/MEDIUM.

[114] E. G. Duell and A. R. George, “Experimental Study of a Ground Vehicle Body Unsteady Near Wake,” SAE Technical Papers, Mar. 1999, doi: 10.4271/1999-01-0812.

[115] B. Khalighi, K. H. Chen, and G. Iaccarino, “Unsteady aerodynamic flow investigation around a simplified square-back road vehicle with drag reduction devices,” Journal of Fluids Engineering, Transactions of the ASME, vol. 134, no. 6, Jun. 2012, doi: 10.1115/1.4006643/456319.

[116] A. Spohn and P. Gillieron, “Flow separations generated by a simplified geometry of an automotive vehicle,” in IUTAM Symposium: Unsteady separated Flows, Toulouse, Toulouse, 2002.

[117] H. Lienhart, C. Stoots, and S. Becker, “Flow and Turbulence Structures in the Wake of a Simplified Car Model (Ahmed Modell),” in New Results in Numerical and Experimental Fluid Mechanics III, Springer Berlin Heidelberg, 2002, pp. 323–330. doi: 10.1007/978-3-540-45466-3_39.

[118] David B. Sims-Williams and Bradley D. Duncan, “The Ahmed Model Unsteady Wake: Experimental and Computational Analyses ,” Journal of Passenger Car: Mechanical Systems Journal, vol. 112, no. 6, pp. 1385–1396, 2003, Accessed: Jan. 08, 2022. [Online]. Available: https://www.jstor.org/stable/44745512

[119] G. Vino, S. Watkins, P. Mousley, J. Watmuff, and S. Prasad, “Flow structures in the near-wake of the Ahmed model,”

Journal of Fluids and Structure, vol. 20, no. 5, pp. 673–695, Jul. 2005, doi: 10.1016/J.JFLUIDSTRUCTS.2005.03.006.

[120] A. Thacker, S. Aubrun, A. Leroy, and P. Devinant, “Unsteady analyses of the flow separation on the rear window of a simplified ground vehicle model,” 28th AIAA Applied Aerodynamics Conference, vol. 1, 2010, doi: 10.2514/6.2010-4569.

[121] A. I. Heft, T. Indinger, and N. A. Adams, “Investigation of unsteady flow structures in the wake of a realistic generic car model,” in 29th AIAA Applied Aerodynamics Conference 2011, American Institute of Aeronautics and Astronautics Inc., 2011. doi: 10.2514/6.2011-3669.

[122] M. Grandemange, O. Cadot, and M. Gohlke, “Reflectional symmetry breaking of the separated flow over three-dimensional bluff bodies,” Physical Review E, vol. 86, no. 3, p. 035302, Sep. 2012, doi: 10.1103/PHYSREVE.86.035302/FIGURES/5/MEDIUM.

[123] M. Grandemange, M. Gohlke, and O. Cadot, “Turbulent wake past a three-dimensional blunt body. Part 2. Experimental sensitivity analysis,” Journal of Fluid Mechanics, vol. 752, no. 5, pp. 439–461, Aug. 2014, doi: 10.1017/jfm.2014.345.

[124] X. W. Wang, Y. Zhou, Y. F. Pin, and T. L. Chan, “Turbulent near wake of an Ahmed vehicle model,” Experiments in Fluids 2013 54:4, vol. 54, no. 4, pp. 1–19, Apr. 2013, doi: 10.1007/S00348-013-1490-X.

[125] A. Lahaye, A. Leroy, and A. Kourta, “Aerodynamic characterisation of a square back bluff body flow,” International Journal of Aerodynamics, vol. 4, no. 1/2, p. 43, 2014, doi: 10.1504/IJAD.2014.057804.

[126] T. Tunay, B. Sahin, and H. Akilli, “Experimental and numerical studies of the flow around the Ahmed body,” Wind and Structures, vol. 17, no. 5, pp. 515–535, Nov. 2013, doi: 10.12989/WAS.2013.17.5.515.

[127] T. Tunay, B. Sahin, and V. Ozbolat, “Effects of rear slant angles on the flow characteristics of Ahmed body,” Experimental Thermal and Fluid Science, vol. 57, pp. 165–176, Sep. 2014, doi: 10.1016/J.EXPTHERMFLUSCI.2014.04.016.

[128] O. Cadot, A. Evrard, and L. Pastur, “Imperfect supercritical bifurcation in a three-dimensional turbulent wake,” Physical Review E, vol. 91, no. 6, p. 063005, Jun. 2015, doi: 10.1103/PHYSREVE.91.063005/FIGURES/12/MEDIUM.

[129] J. Venning, D. Lo Jacono, D. Burton, M. Thompson, and J. Sheridan, “The effect of aspect ratio on the wake of the Ahmed body,” Experiment in Fluids, vol. 56, no. 6, p. 126, Jun. 2015, doi: 10.1007/s00348-015-1996-5.

[130] R. Volpe, P. Devinant, and A. Kourta, “Experimental characterization of the unsteady natural wake of the full-scale square back Ahmed body: flow bi-stability and

spectral analysis," Experiments in Fluids 2015 56:5, vol. 56, no. 5, pp. 1–22, May 2015, doi: 10.1007/S00348-015-1972-0.

[131] D. Barros, J. Borée, B. R. Noack, and A. Spohn, "Resonances in the forced turbulent wake past a 3D blunt body," Physics of Fluids, vol. 28, no. 6, p. 065104, Jun. 2016, doi: 10.1063/1.4953176.

[132] T. Han, "Computational analysis of three-dimensional turbulent flow around a bluff body in ground proximity," AIAA Journal, vol. 27, no. 9, pp. 1213–1219, 1989, doi: 10.2514/3.10248.

[133] F. T. Makowski and S.-E. Kim, "Advances in External-Aero Simulation of Ground Vehicles Using the Steady RANS Equations," Mar. 2000. doi: 10.4271/2000-01-0484.

[134] R. J. A. Howard and M. Pourquie, "Large eddy simulation of an Ahmed reference model," Journal of Turbulence, vol. 3, 2011, doi: 10.1088/1468-5248/3/1/012.

[135] S.-G. Cai, S. Mozaffari, J. Jacob, and P. Sagaut, "Application of immersed boundary based turbulence wall modeling to the Ahmed body aerodynamics," Physics of Fluids, vol. 34, no. 9, p. 095106, Sep. 2022, doi: 10.1063/5.0098232.

[136] D. E. Aljure, O. Lehmkuhl, I. Rodríguez, and A. Oliva, "Flow and turbulent structures around simplified car models," Comput Fluids, vol. 96, pp. 122–135, Jun. 2014, doi: 10.1016/j.compfluid.2014.03.013.

[137] E. Serre et al., "On simulating the turbulent flow around the Ahmed body: A French-German collaborative evaluation of LES and DES," Computer & Fluids, vol. 78, pp. 10–23, Apr. 2013, doi: 10.1016/j.compfluid.2011.05.017.

[138] J.-M. Lucas, O. Cadot, V. Herbert, S. Parpais, and J. Délery, "A numerical investigation of the asymmetric wake mode of a squareback Ahmed body – effect of a base cavity," Journal of Fluid Mechanics, vol. 831, pp. 675–697, Nov. 2017, doi: 10.1017/jfm.2017.654.

[139] J. Östh, B. R. Noack, S. Krajnović, D. Barros, and J. Borée, "On the need for a nonlinear subscale turbulence term in POD models as exemplified for a high-Reynolds-number flow over an Ahmed body," Journal of Fluid Mechanics, vol. 747, no. 3, pp. 518–544, Apr. 2014, doi: 10.1017/JFM.2014.168.

[140] M. Mirzaei, S. Krajnović, and B. Basara, "Partially-Averaged navier-stokes simulations of flows around two different ahmed bodies," Computer & Fluids, vol. 117, 2015, doi: 10.1016/j.compfluid.2015.05.010.

[141] S. Krajnović and L. Davidson, "Numerical study of the flow around a bus-shaped body," Journal of Fluids Engineering, Transactions of the ASME, vol. 125, no. 3, pp. 500–509, May 2003, doi: 10.1115/1.1567305.

[142] S. Krajnović and L. Davidson, “Flow Around a Simplified Car, Part 1: Large Eddy Simulation,” ,” Journal of Fluids Engineering, vol. 127, no. 5, pp. 907–918, Sep. 2005, doi: 10.1115/1.1989371.

[143] S. Krajnović and L. Davidson, “Flow Around a Simplified Car, Part 2: Understanding the Flow,” ,” Journal of Fluids Engineering, vol. 127, no. 5, pp. 919–928, Sep. 2005, doi: 10.1115/1.1989372.

[144] C. Hinterberger, M. García-Villalba, and W. Rodi, “Large eddy simulation of flow around the Ahmed body,” Springer, Berlin, Heidelberg, 2004, pp. 77–87. doi: 10.1007/978-3-540-44419-0_7.

[145] F. Hesse and A. S. Morgans, “Simulation of wake bimodality behind squareback bluff-bodies using LES,” Computer & Fluids, vol. 223, p. 104901, Jun. 2021, doi: 10.1016/J.COMPFLUID.2021.104901.

[146] T. Tunay, B. Yaniktepe, and B. Sahin, “Computational and experimental investigations of the vortical flow structures in the near wake region downstream of the Ahmed vehicle model,” Journal of Wind Engineering and Industrial Aerodynamics, vol. 159, pp. 48–64, Dec. 2016, doi: 10.1016/J.JWEIA.2016.10.006.

[147] N. Kang, E. E. Essel, V. Roussinova, and R. Balachandar, “Effects of approach flow conditions on the unsteady three-dimensional wake structure of a square-back Ahmed body,” Physical Review Fluids, vol. 6, no. 3, p. 034613, Mar. 2021, doi: 10.1103/PHYSREVFLUIDS.6.034613/FIGURES/21/MEDIUM.

[148] M. Minguez, R. Pasquetti, and E. Serre, “High-order LES of the flow over a simplified car model,” European Journal of Computational Mechanics, vol. 18, no. 7–8, pp. 627–646, 2009, doi: 10.3166/EJCM.18.627-646.

[149] C.-H. Bruneau, I. Mortazavi, and P. Gilliéron, “Passive Control Around the Two-Dimensional Square Back Ahmed Body Using Porous,” Journal of fluid engineering, vol. 130, no. 6, pp. 1–12, 2008, doi: 10.1115/1.2917423.

[150] C. H. Bruneau, E. Creusé, D. Depeyras, P. Gilliéron, and I. Mortazavi, “Coupling active and passive techniques to control the flow past the square back Ahmed body,” Computer & Fluids, vol. 39, no. 10, pp. 1875–1892, Dec. 2010, doi: 10.1016/j.compfluid.2010.06.019.

[151] S. Krajnović and L. Davidson, “Large-Eddy Simulation of the Flow around Simplified Car Model,” SAE Technical Papers, Mar. 2004, doi: 10.4271/2004-01-0227.

[152] S. Krajnović and L. Davidson, “Numerical study of the flow around a bus-shaped body,” Journal of Fluids Engineering, Transactions of the ASME, vol. 125, no. 3, pp. 500–509, May 2003, doi: 10.1115/1.1567305.

[153] H. Choi and P. Moin, “Grid-point requirements for large eddy simulation: Chapman’s estimates revisited,” Physics of Fluids, vol. 24, no. 1, p. 011702, Jan. 2012, doi: 10.1063/1.3676783.

[154] S. T. Bose and G. I. Park, “Wall-Modeled Large-Eddy Simulation for Complex Turbulent Flows,” Annual Review of Fluid Mechanics, vol. 50, pp. 535–561, Jan. 2018, doi: 10.1146/ANNUREV-FLUID-122316-045241.

[155] J. Larsson, S. Kawai, J. Bodart, and I. Bermejo-moreno, “Large eddy simulation with modeled wall-stress: recent progress and future directions,” Mechanical Engineering Reviews, vol. 3, no. 1, pp. 15–00418, 2016, doi: 10.1299/MER.15-00418.

[156] P. R. Spalart and V. Venkatakrishnan, “On the role and challenges of CFD in the aerospace industry,” The Aeronautical Journal, vol. 120, no. 1223, pp. 209–232, Jan. 2016, doi: 10.1017/AER.2015.10.

[157] S. Heinz, “A review of hybrid RANS-LES methods for turbulent flows: Concepts and applications,” Progress in Aerospace Sciences, vol. 114, p. 100597, Apr. 2020, doi: 10.1016/J.PAEROSCI.2019.100597.

[158] SPALART and PR, “Comments on the feasibility of LES for wings, and on a hybrid RANS/LES approach,” Proceedings of first AFOSR international conference on DNS/LES, 1997, Accessed: Nov. 02, 2020. [Online]. Available: https://ci.nii.ac.jp/naid/20001674527

[159] F. Menter, A. Hüppe, A. Matyushenko, and D. Kolmogorov, “An Overview of Hybrid RANS–LES Models Developed for Industrial CFD,” Applied Sciences 2021, Vol. 11, Page 2459, vol. 11, no. 6, p. 2459, Mar. 2021, doi: 10.3390/APP11062459.

[160] B. Chaouat and B. Chaouat BrunoChaouat, “The State of the Art of Hybrid RANS/LES Modeling for the Simulation of Turbulent Flows,” Flow, Turbulence and Combustion 2017 99:2, vol. 99, no. 2, pp. 279–327, Jul. 2017, doi: 10.1007/S10494-017-9828-8.

[161] M. L. Shur, P. R. Spalart, M. K. Strelets, and A. K. Travin, “A hybrid RANS-LES approach with delayed-DES and wall-modelled LES capabilities,” International Journal of Heat Fluid Flow, vol. 29, no. 6, pp. 1638–1649, Dec. 2008, doi: 10.1016/j.ijheatfluidflow.2008.07.001.

[162] Y. Fan, C. Xia, S. Chu, Z. Yang, and O. Cadot, “Experimental and numerical analysis of the bi-stable turbulent wake of a rectangular flat-backed bluff body,” Physics of Fluids, vol. 32, no. 10, p. 105111, Oct. 2020, doi: 10.1063/5.0019794.

[163] D. L. Barsotti, E. A. Divo, and S. K. S. Boetcher, “Optimizing jets for active control of wake refinement for ground vehicles,” Journal of Fluids Engineering, Transactions of the ASME, vol. 137, no. 12, Dec. 2015, doi: 10.1115/1.4030913/372664.

[164] J. Zhang, Z. Guo, S. Han, S. Krajnović, J. Sheridan, and G. Gao, “An IDDES study of the near-wake flow topology of a simplified heavy vehicle,” Transportation Safety and Environment, vol. 4, no. 2, Jun. 2022, doi: 10.1093/TSE/TDAC015.

[165] J. Zhang, F. Wang, Z. Guo, S. Han, G. Gao, and J. Wang, “Investigation of the wake flow of a simplified heavy vehicle with different aspect ratios,” Physics of Fluids, vol. 34, no. 6, p. 065135, Jun. 2022, doi: 10.1063/5.0094534.

[166] K. Gosse, P. Paranthoën, B. Patte-Rouland, and M. Gonzalez, “Dispersion in the near wake of idealized car model,” International Journal of Heat and Mass Transfer, vol. 49, no. 9–10, pp. 1747–1752, May 2006, doi: 10.1016/J.IJHEATMASSTRANSFER.2005.12.003.

[167] W. Meile, G. Brenn, A. Reppenhagen, B. Lechner, and A. Fuchs, “Experiments and numerical simulations on the aerodynamics of the Ahmed body,” CFD letters, vol. 3, no. March 2011, pp. 32–39, 2012.

[168] D. Burton, S. Wang, D. Tudball Smith, H. N. Scott, T. N. Crouch, and M. C. Thompson, “The influence of background turbulence on Ahmed-body wake bistability,” Journal of Fluid Mechanics, vol. 926, p. 1, 2021, doi: 10.1017/JFM.2021.706.

[169] J. Venning, D. Lo Jacono, D. Burton, M. Thompson, and J. Sheridan, “The effect of aspect ratio on the wake of the Ahmed body,” Experiment in Fluids, vol. 56, no. 6, pp. 1–11, Jun. 2015, doi: 10.1007/s00348-015-1996-5.

[170] G. Rossitto, “Influence of afterbody rounding on the aerodynamics of a fastback vehicle,” Phd, Ecole Nationale Sup erieure de M ecanique et d’A erotechnique, 2016.

[171] A. P. Gaylard, K. Kirwan, and D. A. Lockerby, “Surface contamination of cars: A review,” Proceedings of the Institution of Mechanical Engineers, Part D: Journal of Automobile Engineering, vol. 231, no. 9, pp. 1160–1176, Aug. 2017, doi: 10.1177/0954407017695141.

[172] J. Jilesen, A. P. Gaylard, B. Duncan, A. Konstantinov, and J. Wanderer, “Simulation of Rear and Body Side Vehicle Soiling by Road Sprays Using Transient Particle Tracking,” SAE International Journal of Passenger Cars - Mechanical Systems, vol. 6, no. 1, pp. 424–435, Apr. 2013, doi: 10.4271/2013-01-1256.

[173] T. Lajos, L. Preszler, and L. Finta, “A wind tunnel investigation of mud deposits on the body of a bus,” International Journal of Vehicle Design, 2014.

[174] G. Fourrié, L. Keirsbulck, L. Labraga, and P. Gilliéron, “Bluff-body drag reduction using a deflector,” Experiment in Fluids, vol. 50, no. 2, pp. 385–395, Feb. 2011, doi: 10.1007/s00348-010-0937-6.

[175] J. Tian, Y. Zhang, H. Zhu, and H. Xiao, “Aerodynamic drag reduction and flow control of Ahmed body with flaps,” Advances in Mechanical Engineering, vol. 9, no. 7, pp. 1–17, 2017, doi: 10.1177/1687814017711390.

[176] W. Hanfeng, Z. Yu, Z. Chao, and H. Xuhui, “Aerodynamic drag reduction of an Ahmed body based on deflectors,” Journal of Wind Engineering and Industrial Aerodynamics, vol. 148, pp. 34–44, Jan. 2016, doi: 10.1016/j.jweia.2015.11.004.

[177] J. L. Aider, J. F. Beaudoin, and J. E. Wesfreid, “Drag and lift reduction of a 3D bluff-body using active vortex generators,” Experiment in Fluids, vol. 48, no. 5, pp. 771–789, May 2010, doi: 10.1007/s00348-009-0770-y.

[178] G. Filip, K. Maki, P. Bachant, and R. Lietz, “Simulation of Flow Control Devices in Support of Vehicle Drag Reduction,” in SAE Technical Papers, SAE International, Apr. 2018. doi: 10.4271/2018-01-0713.

[179] S. O. Kang et al., “Actively translating a rear diffuser device for the aerodynamic drag reduction of a passenger car,” International Journal of Automotive Technology, vol. 13, no. 4, pp. 583–592, 2012.

[180] T. Heinemann, M. Springer, H. Lienhart, S. Kniesburges, C. Othmer, and S. Becker, “Active flow control on a 1:4 car model,” Experiment in Fluids, vol. 55, no. 5, pp. 1–11, May 2014, doi: 10.1007/s00348-014-1738-0.

[181] R. Mestiri, A. Ahmed-Bensoltane, L. Keirsbulck, F. Aloui, and L. Labraga, “Active flow control at the rear end of a generic car model using steady blowing,” Journal of Applied Fluid Mechanics, vol. 7, no. 4, pp. 565–571, 2014, doi: 10.36884/jafm.7.04.21752.

[182] M. Rouméas, P. Gilliéron, and A. Kourta, “Analysis and control of the near-wake flow over a square-back geometry,” Computer & Fluids, vol. 38, no. 1, pp. 60–70, Jan. 2009, doi: 10.1016/j.compfluid.2008.01.009.

[183] E. Wassen and F. Thiele, “Drag reduction for a generic car model using steady blowing,” in 4th AIAA Flow Control Conference, 2008. doi: 10.2514/6.2008-3771.

[184] D. Krentel, R. Muminovic, A. Brunn, W. Nitsche, and R. King, “Application of active flow control on generic 3d car models,” Notes on Numerical Fluid Mechanics and Multidisciplinary Design, vol. 108, pp. 223–239, 2010, doi: 10.1007/978-3-642-11735-0_15.

[185] E. Wassen, S. Eichinger, and F. Thiele, “Simulation of active drag reduction for a square-back vehicle,” Notes on Numerical Fluid Mechanics and Multidisciplinary Design, vol. 108, pp. 241–255, 2010, doi: 10.1007/978-3-642-11735-0_16.

[186] S. Aubrun, J. McNally, F. Alvi, and A. Kourta, “Separation flow control on a generic ground vehicle using steady microjet arrays,” Experiment in Fluids, vol. 51, no. 5, pp. 1177–1187, Nov. 2011, doi: 10.1007/s00348-011-1132-0.

[187] J. McNally et al., “Drag reduction on a flat-back ground vehicle with active flow control,” Journal of Wind Engineering and Industrial Aerodynamics, vol. 145, pp. 292–303, Oct. 2015, doi: 10.1016/j.jweia.2015.03.006.

[188] H. Park, J. H. Cho, J. Lee, D. H. Lee, and K. H. Kim, “Aerodynamic Drag Reduction of Ahmed Model Using Synthetic Jet Array,” SAE International Journal of Passenger Cars - Mechanical Systems, vol. 6, no. 1, pp. 1–6, Mar. 2013, doi: 10.4271/2013-01-0095.

[189] A. Kourta and C. Leclerc, “Characterization of synthetic jet actuation with application to Ahmed body wake,” Sensors and Actuators A: Physical, vol. 192, pp. 13–26, 2013, doi: 10.1016/j.sna.2012.12.008.

[190] N. Tounsi, R. Mestiri, L. Keirsbulck, H. Oualli, S. Hanchi, and F. Aloui, “Experimental study of flow control on bluff body using piezoelectric actuators,” Journal of Applied Fluid Mechanics, vol. 9, no. 2, pp. 827–838, 2016, doi: 10.18869/acadpub.jafm.68.225.24488.

[191] P. Gilliéron et al., “Drag reduction by pulsed jets on strongly unstructured wake: towards the square back control,” International Journal of Aerodynamics, vol. 1, no. 3/4, p. pages 282-298, 2011.

[192] P. Gillieron and A. Kourta, “Massive separation control analysis of the pulsed jet actuators effects | Mechanics & Industry | Cambridge Core,” Mechanics & Industry, vol. 14, no. 6, pp. 441–445, Feb. 2013.

[193] A. Kourta and P. Gilliéron, “Impact of the automotive aerodynamic control on the economic issues,” Journal of Applied Fluid Mechanics, vol. 2, no. 2, pp. 69–75, 2009.

[194] B. Lehugeur, P. Gilliéron, and A. Kourta, “Experimental investigation on longitudinal vortex control over a dihedral bluff body,” Experiment in Fluids, vol. 48, no. 1, pp. 33–48, Jan. 2010, doi: 10.1007/s00348-009-0707-5.

[195] E. Wassen and F. Thiele, “Road vehicle drag reduction by combined steady blowing and suction,” in 39th AIAA Fluid Dynamics Conference, 2009. doi: 10.2514/6.2009-4174.

[196] J. T. Whiteman and M. Zhuang, “Active flow control schemes for bluff body drag reduction,” in American Society of Mechanical Engineers, Fluids Engineering Division (Publication) FEDSM, American Society of Mechanical Engineers (ASME), Dec. 2016. doi: 10.1115/FEDSM2016-7520.

[197] S Shadmani, S. M. Mousavi Nainiyan, Ramin Ghasemiasl, and Masoud Mirzaei, “Experimental Study of Flow Control Over an Ahmed Body Using Plasma Actuator,” Mechanics and Mechanical Engineering, vol. 22, no. 1, pp. 239–251, Jun. 2018.

[198] B. Khalighi, J. Ho, J. Cooney, B. Neiswander, T. C. Corke, and T. Han, “Aerodynamic drag reduction investigation for a simplified road vehicle using plasma flow control,” in American Society of Mechanical Engineers, Fluids Engineering Division (Publication) FEDSM, American Society of Mechanical Engineers (ASME), Dec. 2016. doi: 10.1115/FEDSM2016-7927.

[199] I. Kim and H. Chen, “Reduction of aerodynamic forces on a minivan by a pair of vortex generators of a pocket type,” International Journal of Vehicle Design, vol. 53, no. 4, pp. 300–316, Jul. 2010, doi: 10.1504/IJVD.2010.034103.

[200] G. Pujals, S. Depardon, and C. Cossu, “Drag reduction of a 3D bluff body using coherent streamwise streaks,” Experiment in Fluids, vol. 49, no. 5, pp. 1085–1094, Nov. 2010, doi: 10.1007/s00348-010-0857-5.

[201] Walid Ibrahim Mazyan, “Numerical simulations of drag-reducing devices for ground vehicles ,” American University of Sharjah, Sharjah, 2013.

[202] G. Shankar and G. Devaradjane, “Experimental and computational analysis on aerodynamic behavior of a car model with vortex generators at different yaw angles,” Journal of Applied Fluid Mechanics, vol. 11, no. 1, pp. 285–295, 2018, doi: 10.29252/jafm.11.01.28357.

[203] I. Kim, H. Chen, and R. C. Shulze, “A rear spoiler of a new type that reduces the aerodynamic forces on a mini-van,” in SAE Technical Papers, SAE International, Apr. 2006. doi: 10.4271/2006-01-1631.

[204] D. Kim, H. Lee, W. Yi, and H. Choi, “A bio-inspired device for drag reduction on a three-dimensional model vehicle,” Bioinspired Biomimemetics, vol. 11, no. 2, p. 026004, Mar. 2016, doi: 10.1088/1748-3190/11/2/026004.

[205] J. Marklund, L. Lofdahl, H. Danielsson, and G. Olsson, “Performance of an Automotive Under-Body Diffuser Applied to a Sedan and a Wagon Vehicle,” SAE International Journal of Passenger Cars - Mechanical Systems, vol. 6, no. 1, pp. 293–307, Apr. 2013, doi: 10.4271/2013-01-0952.

[206] J. Cho, T. K. Kim, K. H. Kim, and K. Yee, “Comparative investigation on the aerodynamic effects of combined use of underbody drag reduction devices applied to real sedan,” International Journal of Automotive Technology, vol. 18, no. 6, pp. 959–971, Dec. 2017, doi: 10.1007/s12239-017-0094-5.

[207] K. S. Song et al., “Aerodynamic design optimization of rear body shapes of a sedan for drag reduction,” International Journal of Automotive Technology, vol. 13, no. 6, pp. 905–914, Oct. 2012, doi: 10.1007/s12239-012-0091-7.

[208] X. Hu et al., “Automotive shape optimization using the radial basis function model based on a parametric surface grid,” Proceedings of the Institution of Mechanical Engineers, Part D: Journal of Automobile Engineering, vol. 230, no. 13, pp. 1808–1821, Nov. 2016, doi: 10.1177/0954407015624042.

[209] Y. Wang, C. Wu, G. Tan, and Y. Deng, “Reduction in the aerodynamic drag around a generic vehicle by using a non-smooth surface,” Proceedings of the Institution of Mechanical Engineers, Part D: Journal of Automobile Engineering, vol. 231, no. 1, pp. 130–144, Jan. 2017, doi: 10.1177/0954407016636970.

[210] J. Katz, “Aerodynamics of Race Cars,” Annual Review of Fluid Mechanics, vol. 38, no. 1, pp. 27–63, Jan. 2006, doi: 10.1146/annurev.fluid.38.050304.092016.

[211] O. H. Ehirim, K. Knowles, and A. J. Saddington, “A review of ground-effect diffuser aerodynamics,” Journal of Fluids Engineering, Transactions of the ASME, vol. 141, no. 2, Feb. 2018, doi: 10.1115/1.4040501.

[212] A. Huminic, G. Huminic, M. Carauleanu, and C. Ciolofan, “Comparative Study on the Performances of Aerodynamic Devices Used in Decreasing of the Automobiles Lift Force,” in CONAT 2016 International Congress of Automotive and Transport Engineering, Springer International Publishing, 2017, pp. 48–54. doi: 10.1007/978-3-319-45447-4_5.

[213] H. Taiming, Z. Xiaodong, W. Zhongmin, and G. Zhengqi, “Experimental and numerical investigations of the vehicle aerodynamic drag with single-channel rear diffuser,” Proceedings of the Institution of Mechanical Engineers, Part D: Journal of Automobile Engineering, vol. 234, no. 8, pp. 2216–2227, Jul. 2020, doi: 10.1177/0954407019893849.

[214] A. Huminic and G. Huminic, “Aerodynamics of curved underbody diffusers using CFD,” Journal of Wind Engineering and Industrial Aerodynamics, vol. 205, p. 104300, Oct. 2020, doi: 10.1016/j.jweia.2020.104300.

[215] F. F. Buscariolo, G. R. S. Assi, and S. J. Sherwin, “Computational study on an Ahmed Body equipped with simplified underbody diffuser,” Journal of Wind Engineering and Industrial Aerodynamics, vol. 209, p. 104411, Feb. 2021, doi: 10.1016/j.jweia.2020.104411.

[216] Z. M. Saleh and A. H. Ali, “Numerical Investigation of Drag Reduction Techniques in a Car Model,” in IOP Conference Series: Materials Science and Engineering, Institute of Physics Publishing, Jan. 2020, p. 012160. doi: 10.1088/1757-899X/671/1/012160.

[217] M. Gohlke, J. F. Beaudoin, M. Amielh, and F. Anselmet, “Shape influence on mean forces applied on a ground vehicle under steady cross-wind,” Journal of Wind Engineering and Industrial Aerodynamics, vol. 98, no. 8–9, pp. 386–391, Aug. 2010, doi: 10.1016/J.JWEIA.2009.12.003.

[218] T. Schuetz, L. Kruger, and M. Lentzen, “Aerodynamic forces and their influence on passenger vehicles,” in Aerodynamics of road vehicles, T. Schuetz, Ed., SAE International, 2016.

[219] J.P. Howell, “Shape features which influence crosswind sensitivity,” in International conference, Vehicle ride and handling, in Vehicle ride and handling. Institution of Mechanical Engineers Conference Publications, 1993, pp. 43–52.

[220] A. M. Gilhaus and V. E. Renn, “Drag and Driving-Stability-Related Aerodynamic Forces and Their Interdependence-Results of Measurements on 3/8-Scale Basic Car Shapes,” SAE Technical Papers, Mar. 1986, doi: 10.4271/860211.

[221] R. Buchheim, K. R. Deutenbach, and H. J. Lückoff, “Necessity and Premises for Reducing the Aerodynamic Drag of Future Passenger Cars,” SAE Technical Papers, Feb. 1981, doi: 10.4271/810185.

[222] John P Davis, “Wind tunnel investigations of road vehicle wakes,” Imperial college London, London, 1982. Accessed: Jun. 25, 2022.

[223] J. Fuller and M. A. Passmore, “The importance of rear pillar geometry on fastback wake structures,” Journal of Wind Engineering and Industrial Aerodynamics, vol. 125, pp. 111–120, Feb. 2014, doi: 10.1016/J.JWEIA.2013.11.002.

[224] F. Zigunov, P. Sellappan, and F. Alvi, “Reynolds number and slant angle effects on the flow over a slanted cylinder afterbody,” Journal of Fluid Mechanics, vol. 893, 2020, doi: 10.1017/JFM.2020.214.

[225] B. Mohammadikalakoo, P. Schito, and M. Mani, “Passive flow control on Ahmed body by rear linking tunnels,” Journal of Wind Engineering and Industrial Aerodynamics, vol. 205, p. 104330, Oct. 2020, doi: 10.1016/j.jweia.2020.104330.

[226] A. Reif, W. E., & Dinkelacker, “Hydrodynamics of the squamation infast swimming sharks,” Neues Jahrbuch fuer Geologie Palaeontologie, pp. 184–187, 1982.

[227] Y. Luo, X. Xu, D. Li, and W. Song, “Recent developments in fabricating drag reduction surfaces covering biological sharkskin morphology,” Reviews in Chemical Engineering, vol. 32, no. 1, pp. 93–113, Jan. 2016, doi: 10.1515/revce-2015-0015.

[228] M. Walsh, “Turbulent boundary layer drag reduction using riblets,” in 20th Aerospace Sciences Meeting, Reston, Virigina: American Institute of Aeronautics and Astronautics, Jan. 1982. doi: 10.2514/6.1982-169.

[229] M. J. Walsh, “Riblets as a Viscous Drag Reduction Technique,” AIAA Journal, vol. 21, no. 4, pp. 485–486, Apr. 1983, doi: 10.2514/3.60126.

[230] D. W. Bechert and M. Bartenwerfer, “The viscous flow on surfaces with longitudinal ribs,” Journal of Fluid Mechanics, vol. 206, pp. 105–129, Sep. 1989, doi: 10.1017/S0022112089002247.

[231] D. W. Bechert, M. Bruse, W. Hage, J. G. T. van der Hoeven, and G. Hoppe, “Experiments on drag-reducing surfaces and their optimization with an adjustable geometry,” Journal of Fluid Mechanics, vol. 338, pp. 59–87, May 1997, doi: 10.1017/S0022112096004673.

[232] B. Nugroho, N. Hutchins, and J. P. Monty, “Large-scale spanwise periodicity in a turbulent boundary layer induced by highly ordered and directional surface roughness,” International Journal of Heat Fluid Flow, vol. 41, pp. 90–102, 2013, doi: 10.1016/j.ijheatfluidflow.2013.04.003.

[233] G. Cui, C. Pan, D. Wu, Q. Ye, and J. Wang, “Effect of drag reducing riblet surface on coherent structure in turbulent boundary layer,” Chinese Journal of Aeronautics, May 2019, doi: 10.1016/J.CJA.2019.04.023.

[234] D. W. Bechert, M. Bruse, W. HAGE, J. G. T. van der Hoeven, and G. Hoppe, “Experiments on drag-reducing surfaces and their optimization with an adjustable geometry,” Journal of Fluid Mechanics, vol. 338, pp. 59–87, May 1997, doi: 10.1017/S0022112096004673.

[235] W. Li et al., “Turbulent drag reduction by spanwise traveling ribbed surface waves,” European Journal of Mechanics - B/Fluids, vol. 53, pp. 101–112, Sep. 2015, doi: 10.1016/J.EUROMECHFLU.2015.03.009.

[236] Y. Luo, Y. Liu, D. Zhang, and E. Y. K. Ng, “Influence of morphology for drag reduction effect of sharkskin surface,” Journal of Mechanics in Medicine and Biology, vol. 14, no. 02, p. 1450029, Apr. 2014, doi: 10.1142/S0219519414500298.

[237] S. Martin and B. Bhushan, “Modeling and optimization of shark-inspired riblet geometries for low drag applications,” Journal of Colloid and Interface Science, vol. 474, pp. 206–215, Jul. 2016, doi: 10.1016/J.JCIS.2016.04.019.

[238] L. Tian, L. Ren, Z. Han, and S. Zhang, “Experiment about drag reduction of bionic non-smooth surface in low speed wind tunnel,” Journal of Bionic Engineering, vol. 2, no. 1, pp. 15–24, Mar. 2005, doi: 10.1007/BF03399477.

[239] D. Zhang, Y. Luo, X. Li, and H. Chen, “Numerical simulation and experimental study of drag-reducing surface of a real shark skin,” Journal of Hydrodynamics, Ser. B, vol. 23, no. 2, pp. 204–211, Apr. 2011, doi: 10.1016/S1001-6058(10)60105-9.

[240] A. W. Lang, P. Motta, P. Hidalgo, and M. Westcott, “Bristled shark skin: a microgeometry for boundary layer control?,” Bioinspiration & Biomimetics, vol. 3, no. 4, p. 046005, Dec. 2008, doi: 10.1088/1748-3182/3/4/046005.

[241] A. G. Domel, M. Saadat, J. C. Weaver, H. Haj-Hariri, K. Bertoldi, and G. v. Lauder, “Shark skin-inspired designs that improve aerodynamic performance,” Journal of the Royal Society Interface, vol. 15, no. 139, p. 20170828, Feb. 2018, doi: 10.1098/rsif.2017.0828.

[242] F.-W. Patricia, D. Guzman, B. Iñigo, I. Urtzi, B. J. Maria, and S. Manu, “Morphological Characterization and Hydrodynamic Behavior of Shortfin Mako Shark (Isurus oxyrinchus) Dorsal Fin Denticles,” Journal of Bionic Engineering, vol. 16, no. 4, pp. 730–741, Jul. 2019, doi: 10.1007/s42235-019-0059-7.

[243] C. Zhang and K. Saurav Bijay, “Investigation on drag reduction performance of aero engine blade with micro-texture,” Aerospace Science and Technology, vol. 72, pp. 380–396, Jan. 2018, doi: 10.1016/J.AST.2017.11.007.

[244] Y. Luo, D. Zhang, and Y. Liu, “Recent drag reduction developments derived from different biological functional surfaces: a review,” Journal of Mechanics in Medicine and Biology, vol. 16, no. 02, p. 1630001, Mar. 2016, doi: 10.1142/S0219519416300015.

[245] S. Nakao, “Application of V Shape Riblets to Pipe Flows,” Journal of Fluids Engineering, vol. 113, no. 4, p. 587, Dec. 1991, doi: 10.1115/1.2926519.

[246] M. Nili-Ahmadabadi, O. Nematollahi, and K. C. Kim, “Effects of coarse riblets on air flow structures over a slender delta wing using particle image velocimetry,” Chinese Journal of Aeronautics, vol. 32, no. 6, pp. 1367–1379, Jun. 2019, doi: 10.1016/J.CJA.2019.03.019.

[247] V. Stenzel, Y. Wilke, and W. Hage, “Drag-reducing paints for the reduction of fuel consumption in aviation and shipping,” Progress in Organic Coating, vol. 70, no. 4, pp. 224–229, Apr. 2011, doi: 10.1016/J.PORGCOAT.2010.09.026.

[248] N. West, K. Sammut, and Y. Tang, “Material selection and manufacturing of riblets for drag reduction: An updated review,” Proceedings of the Institution of Mechanical Engineers, Part L: Journal of Materials: Design and Applications, vol. 232, no. 7, pp. 610–622, Jul. 2018, doi: 10.1177/1464420716641452.

[249] H. H. Zhang, S. S. Nunayon, and A. C. K. Lai, “Experimental study on deposition enhancement of ultrafine particles in a duct flow by riblets,” Applied Thermal Engineering, vol. 147, pp. 886–894, Jan. 2019, doi: 10.1016/J.APPLTHERMALENG.2018.10.112.

[250] W. Sagong, C. Kim, S. Choi, W. P. Jeon, and H. Choi, “Does the sailfish skin reduce the skin friction like the shark skin?,” in Physics of Fluids, American Institute of Physics Inc., 2008. doi: 10.1063/1.3005861.

[251] W. Barthlott and C. Neinhuis, “Purity of the sacred lotus, or escape from contamination in biological surfaces,” Planta, vol. 202, no. 1, pp. 1–8, Apr. 1997, doi: 10.1007/s004250050096.

[252] B. Bhushan and Y. C. Jung, “Micro- and nanoscale characterization of hydrophobic and hydrophilic leaf surfaces,” Nanotechnology, vol. 17, no. 11, pp. 2758–2772, Jun. 2006, doi: 10.1088/0957-4484/17/11/008.

[253] M. A. Samaha, H. V. Tafreshi, and M. Gad-el-Hak, “Superhydrophobic surfaces: From the lotus leaf to the submarine,” Comptes Rendus Mécanique, vol. 340, no. 1–2, 2012, doi: 10.1016/j.crme.2011.11.002.

[254] X. Han, D. Zhang, X. Li, and Y. Li, “Bio-replicated forming of the biomimetic drag-reducing surfaces in large area based on shark skin,” Science Bulletin (Beijing), vol. 53, no. 10, pp. 1587–1592, May 2008, doi: 10.1007/s11434-008-0219-3.

[255] R. N. Wenzel, “Resistance of solid surfaces to wetting by water,” Industrial Engineering Chemistry, vol. 28, no. 8, pp. 988–994, Aug. 1936, doi: 10.1021/IE50320A024/ASSET/IE50320A024.FP.PNG_V03.

[256] A. B. D. Cassie and S. Baxter, “Wettability of porous surfaces,” Transactions of the Faraday Society, vol. 40, no. 0, pp. 546–551, Jan. 1944, doi: 10.1039/TF9444000546.

[257] C. Neinhuis and W. Barthlott, “Characterization and Distribution of Water-repellent, Self-cleaning Plant Surfaces,” Annals of Botany, vol. 79, no. 6, pp. 667–677, Jun. 1997, doi: 10.1006/ANBO.1997.0400.

[258] B. Bhushan and Y. C. Jung, “Micro- and nanoscale characterization of hydrophobic and hydrophilic leaf surfaces,” Nanotechnology, vol. 17, no. 11, pp. 2758–2772, Jun. 2006, doi: 10.1088/0957-4484/17/11/008.

[259] D. You and P. Moin, “Effects of hydrophobic surfaces on the drag and lift of a circular cylinder,” Physics of Fluids, vol. 19, no. 8, p. 081701, Aug. 2007, doi: 10.1063/1.2756578.

[260] J. Ou, B. Perot, and J. P. Rothstein, “Laminar drag reduction in microchannels using ultrahydrophobic surfaces,” Physics of Fluids, vol. 16, no. 12, p. 4635, Nov. 2004, doi: 10.1063/1.1812011.

[261] R. Costantini, J. P. Mollicone, and F. Battista, “Drag reduction induced by superhydrophobic surfaces in turbulent pipe flow,” Physics of Fluids, vol. 30, no. 2, p. 025102, Feb. 2018, doi: 10.1063/1.5011805.

[262] E. Aljallis, M. A. Sarshar, R. Datla, V. Sikka, A. Jones, and C. H. Choi, “Experimental study of skin friction drag reduction on superhydrophobic flat plates in high Reynolds number boundary layer flow,” Physics of Fluids, vol. 25, no. 2, p. 025103, Feb. 2013, doi: 10.1063/1.4791602.

[263] D. Legendre, E. Lauga, and J. Magnaudet, “Influence of slip on the dynamics of two-dimensional wakes,” Journal of Fluid Mechanics, vol. 633, pp. 437–447, May 2009, doi: 10.1017/S0022112009008015.

[264] P. Muralidhar, N. Ferrer, R. Daniello, and J. P. Rothstein, “Influence of slip on the flow past superhydrophobic circular cylinders,” Journal of Fluid Mechanics, vol. 680, pp. 459–476, Aug. 2011, doi: 10.1017/JFM.2011.172.

[265] N. Kim, H. Kim, and H. Park, “An experimental study on the effects of rough hydrophobic surfaces on the flow around a circular cylinder,” Physics of Fluids, vol. 27, no. 8, p. 085113, Aug. 2015, doi: 10.1063/1.4929545.

[266] R. Daniello, P. Muralidhar, N. Carron, M. Greene, and J. P. Rothstein, “Influence of slip on vortex-induced motion of a superhydrophobic cylinder,” Journal of Fluids and Structure, vol. 42, pp. 358–368, Oct. 2013, doi: 10.1016/J.JFLUIDSTRUCTS.2013.04.006.

[267] J. C. Brennan, D. J. Fairhurst, R. H. Morris, G. McHale, and M. I. Newton, “Investigation of the drag reducing effect of hydrophobized sand on cylinders,” Journal of

Physics D: Applied Physics, vol. 47, no. 20, p. 205302, May 2014, doi: 10.1088/0022-3727/47/20/205302.

[268] P. Sooraj, S. Jain, and A. Agrawal, “Flow over hydrofoils with varying hydrophobicity,” Experimental Thermal and Fluid Science, vol. 102, pp. 479–492, Apr. 2019, doi: 10.1016/J.EXPTHERMFLUSCI.2018.12.021.

[269] A. Jetly, I. U. Vakarelski, and S. T. Thoroddsen, “Drag crisis moderation by thin air layers sustained on superhydrophobic spheres falling in water,” Soft Matter, vol. 14, no. 9, pp. 1608–1613, Feb. 2018, doi: 10.1039/C7SM01904A.

[270] J.-P. Mollicone, F. Battista, P. Gualtieri, and C. M. Casciola, “Superhydrophobic surfaces to reduce form drag in turbulent separated flows,” AIP Advance, vol. 12, no. 7, p. 075003, Jul. 2022, doi: 10.1063/5.0098365.

[271] F. U. Q. QURESHİ, A. MUHTAROĞLU, and K. TUNCAY, “Sensitivity analysis for piezoelectric energy harvester and bluff body design toward underwater pipeline monitoring,” Journal of Energy Systems, vol. 1, no. 1, pp. 10–20, Jan. 2017, doi: 10.30521/JES.328600.

[272] J. F. Beaudoin and J. L. Aider, “Drag and lift reduction of a 3D bluff body using flaps,” Experiment in Fluids, vol. 44, no. 4, pp. 491–501, Apr. 2008, doi: 10.1007/s00348-007-0392-1.

[273] N. A. Siddiqui and M. Agelin-Chaab, “A Simple Passive Device for the Drag Reduction of an Ahmed Body,” Journal of Applied Fluid Mechanics, vol. 14, no. 1, pp. 147–164, 2021.

[274] A. Altaf, A. A. Omar, and W. Asrar, “Review of passive drag reduction techniques for bluff road vehicles,” IIUM Engineering Journal, vol. 15, no. 1, pp. 61–69, 2014.

[275] T. Hagemeier, M. Hartmann, and D. Thévenin, “Practice of vehicle soiling investigations: A review,” International Journal of Multiphase Flow, vol. 37, no. 8. Pergamon, pp. 860–875, Oct. 01, 2011. doi: 10.1016/j.ijmultiphaseflow.2011.05.002.

[276] Lincoln P. Erm and Michael V. Ol, “An Assessment of the Usefulness of Water Tunnels for Aerodynamic Investigations ,” Dec. 2012.

[277] C. Farell, S. Carrasquel, O. Güven, and V. C. Patel, “Effect of Wind-Tunnel Walls on the Flow Past Circular Cylinders and Cooling Tower Models,” Journal of Fluids Engineering, vol. 99, no. 3, pp. 470–479, Sep. 1977, doi: 10.1115/1.3448820.

[278] M. S. H. Boutilier and S. Yarusevych, “Parametric study of separation and transition characteristics over an airfoil at low Reynolds numbers,” Experiments in Fluids 2012 52:6, vol. 52, no. 6, pp. 1491–1506, Feb. 2012, doi: 10.1007/S00348-012-1270-Z.

[279] L. Wang et al., “A study of the mechanical and chemical durability of Ultra-Ever Dry Superhydrophobic coating on low carbon steel surface,” Colloids Surf A Physicochem Eng Asp, vol. 497, pp. 16–27, May 2016, doi: 10.1016/J.COLSURFA.2016.02.022.

[280] A. Nematollahi and M. F. Tachie, “Time-resolved PIV measurement of influence of upstream roughness on separated and reattached turbulent flows over a forward-facing step,” AIP Advance, vol. 8, no. 10, p. 105110, Oct. 2018, doi: 10.1063/1.5063455.

[281] H. (Hendrik) Tennekes and J. L. (John L. Lumley, A first course in turbulence. The MIT Press, 1972.

[282] M. Samimy and S. K. Lele, “Motion of particles with inertia in a compressible free shear layer,” Physics of Fluids A: Fluid Dynamics, vol. 3, no. 8, p. 1915, Jun. 1998, doi: 10.1063/1.857921.

[283] L. Casarsa and P. Giannattasio, “Three-dimensional features of the turbulent flow through a planar sudden expansion,” Physics of Fluids, vol. 20, no. 1, p. 015103, Jan. 2008, doi: 10.1063/1.2832780.

[284] L. Xiao, Z. Xiao, Z. Duan, and S. Fu, “Improved-Delayed-Detached-Eddy Simulation of cavity-induced transition in hypersonic boundary layer,” International Journal of Heat Fluid Flow, vol. 51, pp. 138–150, Feb. 2015, doi: 10.1016/j.ijheatfluidflow.2014.10.007.

[285] K. He, G. Minelli, J. Wang, T. Dong, G. Gao, and S. Krajnović, “Numerical investigation of the wake bi-stability behind a notchback Ahmed body,” Journal of Fluid Mechanics, vol. 926, p. A36, Nov. 2021, doi: 10.1017/JFM.2021.748.

[286] G. Chen, X. B. Li, and X. F. Liang, “IDDES simulation of the performance and wake dynamics of the wind turbines under different turbulent inflow conditions,” Energy, vol. 238, p. 121772, Jan. 2022, doi: 10.1016/J.ENERGY.2021.121772.

[287] F. Bonnet et al., “Design of a modular robotic system that mimics small fish locomotion and body movements for ethological studies,” International Journal of Advanced Robotic Systems, vol. 14, no. 3, 2017, doi: 10.1177/1729881417706628.

[288] R. J. A. Howard, M. Lesieur, and U. Bieder, “Structured and Non-Structured Large Eddy Simulations of the Ahmed Reference Model,” Fluid Mechanics and its Applications, vol. 65, pp. 185–198, 2002, doi: 10.1007/0-306-48383-1_12.

[289] M. Sosnowski, “The influence of computational domain discretization on CFD results concerning aerodynamics of a vehicle,” Journal of Applied Mathematics and Computational Mechanics, vol. Vol. 17, no. nr 1, pp. 79–88, Mar. 2018, doi: 10.17512/JAMCM.2018.1.08.

[290] D. McArthur, D. Burton, M. Thompson, and J. Sheridan, “On the near wake of a simplified heavy vehicle,” Journal of Fluids and Structure, vol. 66, pp. 293–314, Oct. 2016, doi: 10.1016/J.JFLUIDSTRUCTS.2016.07.011.

[291] F. Zigunov, “Detailed flow field study of an upswept cylinder wake and experimental optimization using active flow control. Florida state university,” FLORIDA STATE UNIVERSITY, 2020.

[292] V. Uruba, O. H.-F. Dynamics, I. of T. A. CR, and undefined 2009, “On the Ahmed Body Wake,” in Colloquium fluid dynamics, Institute of Thermomechanics AS CR, 2009.

[293] J. N. Kutz, S. L. Brunton, B. W. Brunton, and J. L. Proctor, “Dynamic Mode Decomposition,” Dynamic Mode Decomposition, Nov. 2016, doi: 10.1137/1.9781611974508.

[294] S. Edwige, Y. Eulalie, P. Gilotte, and I. Mortazavi, “Wake flow analysis and control on a 47° slant angle Ahmed body,” International Journal of Numerical Methods and Heat Fluid Flow, vol. 28, no. 5, pp. 1061–1079, May 2018, doi: 10.1108/HFF-06-2017-0260/FULL/XML.

[295] M. G. Berry, M. Y. Ali, A. S. Magstadt, and M. N. Glauser, “DMD and POD of time-resolved schlieren on a multi-stream single expansion ramp nozzle,” International Journal of Heat Fluid Flow, vol. 66, pp. 60–69, Aug. 2017, doi: 10.1016/J.IJHEATFLUIDFLOW.2017.05.007.

[296] J. Jeong and F. Hussain, “On the identification of a vortex,” Journal of Fluid Mechanics, vol. 285, no. 1, p. 69, Feb. 1995, doi: 10.1017/S0022112095000462.

[297] M. Agelin-Chaab, “Structure of turbulent flows over two-dimensional bluff bodies inspired by a pickup truck geometry,” International Journal of Heat Fluid Flow, vol. 50, 2014, doi: 10.1016/j.ijheatfluidflow.2014.10.004.

[298] A. J. Smits and R. W. Smith, “Effect of Reynolds number on the large structure of turbulent boundary layers,” aiaa, vol. 29, 1991.

[299] J. Venning et al., “The effect of aspect ratio on the wake of the Ahmed body,” Experiment in Fluids, 2015, doi: 10.1007/s00348-015-1996-5.

[300] F. Zigunov, P. Sellappan, and F. Alvi, “Hysteretic flow regime switching in the wake of a cylinder with a slanted afterbody,” Experiment in Fluids, vol. 63, no. 5, pp. 1–16, May 2022, doi: 10.1007/S00348-022-03434-5/FIGURES/13.

[301] A. Wortman, “Reduction of Fuselage Form Drag by Vortex Flows,” https://doi.org/10.2514/2.2484, vol. 36, no. 3, pp. 501–506, May 2012, doi: 10.2514/2.2484.

[302] R. J. Volino, M. P. Schultz, and K. A. Flack, “Turbulence structure in rough- and smooth-wall boundary layers,” Journal of Fluid Mechanics, vol. 592, pp. 263–293, Dec. 2007, doi: 10.1017/S0022112007008518.

[303] I. J. Sobey, “Oscillatory flows at intermediate Strouhal number in asymmetric channels,” Journal of Fluid Mechanics, vol. 125, pp. 359–373, 1982, doi: 10.1017/S0022112082003371.

[304] A. Thacker, S. Aubrun, A. Leroy, and P. Devinant, “Experimental characterization of flow unsteadiness in the centerline plane of an Ahmed body rear slant,” Experiments in Fluids 2013 54:3, vol. 54, no. 3, pp. 1–16, Feb. 2013, doi: 10.1007/S00348-013-1479-5.

[305] N. D. Katopodes, Free-surface flow. Environmental fluid mechanics. 2019.

[306] A. Roshko, “Perspectives on bluff body aerodynamics,” Journal of Wind Engineering and Industrial Aerodynamics, vol. 49, no. 1–3, pp. 79–100, Dec. 1993, doi: 10.1016/0167-6105(93)90007-B.

[307] M. Minguez, R. Pasquetti, and E. Serre, “High-order large-eddy simulation of flow over the ‘Ahmed body’ car model,” Physics of Fluids, vol. 20, no. 9, p. 095101, Sep. 2008, doi: 10.1063/1.2952595.

[308] A. Thacker, “Contribution experimentale a l’ analyse stationnaire et instationnaire de l’ ecoulement a l’arriere d’ un corps de faible allongement,” 2010.

[309] H. J. Kim and P. A. Durbin, “Observations of the frequencies in a sphere wake and of drag increase by acoustic excitation,” Physics of Fluids, vol. 31, no. 11, p. 3260, Jun. 1988, doi: 10.1063/1.866937.

[310] X. Fang and M. F. Tachie, “On the unsteady characteristics of turbulent separations over a forward–backward-facing step,” Journal of Fluid Mechanics, vol. 863, pp. 994–1030, Mar. 2019, doi: 10.1017/JFM.2018.962.

[311] P. J. Schmid, “Dynamic Mode Decomposition and Its Variants,” https://doi.org/10.1146/annurev-fluid-030121-015835, vol. 54, pp. 225–254, Jan. 2022, doi: 10.1146/ANNUREV-FLUID-030121-015835.

[312] P. J. Schmid, “Dynamic Mode Decomposition and Its Variants,” https://doi.org/10.1146/annurev-fluid-030121-015835, vol. 54, pp. 225–254, Jan. 2022, doi: 10.1146/ANNUREV-FLUID-030121-015835.

[313] A. Arote, M. Bade, and J. Banerjee, “On coherent structures of spatially oscillating planar liquid jet developing in a quiescent atmosphere,” Physics of Fluids, vol. 32, no. 8, p. 082111, Aug. 2020, doi: 10.1063/5.0016480.

[314] X. Shi, M. Alam, and H. Bai, “Wakes of elliptical cylinders at low Reynolds number,” International Journal of Heat Fluid Flow, vol. 82, p. 108553, Apr. 2020, doi: 10.1016/J.IJHEATFLUIDFLOW.2020.108553.

[315] G. Pavia, M. Passmore, and M. Varney, “Low-frequency wake dynamics for a square-back vehicle with side trailing edge tapers,” Journal of Wind Engineering and Industrial Aerodynamics, vol. 184, pp. 417–435, Jan. 2019, doi: 10.1016/j.jweia.2018.12.009.

[316] D. Barros, J. Borée, B. R. Noack, A. Spohn, and T. Ruiz, “Bluff body drag manipulation using pulsed jets and Coanda effect,” Journal of Fluid Mechanics, vol. 805, pp. 422–459, 2016, doi: 10.1017/jfm.2016.508.

[317] A. Mariotti, G. Buresti, and M. V. Salvetti, “Connection between base drag, separating boundary layer characteristics and wake mean recirculation length of an

axisymmetric blunt-based body," Journal of Fluids and Structure, vol. 55, pp. 191–203, May 2015, doi: 10.1016/j.jfluidstructs.2015.02.012.

[318] N. A. Siddiqui and M. Agelin-Chaab, "Experimental investigation of the flow features around an elliptical Ahmed body," Physics of Fluids, vol. 34, no. 105119, Sep. 2022, doi: 10.1063/5.0114377.

[319] N. A. Siddiqui and M. Agelin-Chaab, "Flow features of the Ahmed body at a low Reynolds number," International Journal of Heat Fluid Flow, vol. 98, p. 109052, Dec. 2022, doi: 10.1016/J.IJHEATFLUIDFLOW.2022.109052.

[320] A. Mariotti, G. Buresti, and M. V. Salvetti, "Separation delay through contoured transverse grooves on a 2D boat-tailed bluff body: Effects on drag reduction and wake flow features," European Journal of Mechanics, B/Fluids, vol. 74, pp. 351–362, Mar. 2019, doi: 10.1016/j.euromechflu.2018.09.009.

[321] A. E. Perry and M. S. Chong, "A Description of Eddying Motions and Flow Patterns Using Critical-Point Concepts," Annual Review of Fluid Mechanics, vol. 19, no. 1, pp. 125–155, Jan. 1987, doi: 10.1146/annurev.fl.19.010187.001013.

[322] D. M. Salazar, T. Liu, and S. Woodiga, "Skin friction topology on ground vehicle models," Journal of Visualization (Tokyo), pp. 1–15, Jan. 2022, doi: 10.1007/S12650-021-00820-9/FIGURES/12.

[323] D. J. Garmann and M. R. Visbal, "High-fidelity simulations of afterbody vortex flows," AIAA Scitech 2019 Forum, 2019, doi: 10.2514/6.2019-1142.

[324] T. Morel, "Effect of Base Slant on Flow in the Near Wake of an Axisymmetric Cylinder," Aeronautical Quarterly, vol. 31, no. 2, pp. 132–147, 1980, doi: 10.1017/S0001925900010957.

[325] A. Lebedev et al., "Control of the turbulent wake flow behind a circular cylinder by asymmetric sectoral hydrophobic coatings," Physics of Fluids, vol. 33, no. 12, p. 121703, Dec. 2021, doi: 10.1063/5.0073687.

[326] H. Haibao, D. Peng, Z. Feng, S. Dong, and W. Yang, "Effect of hydrophobicity on turbulent boundary layer under water," Experimental Thermal and Fluid Science, vol. 60, pp. 148–156, Jan. 2015, doi: 10.1016/J.EXPTHERMFLUSCI.2014.08.013.

[327] Y. L. Xiong and D. Yang, "Influence of slip on the three-dimensional instability of flow past an elongated superhydrophobic bluff body," Journal of Fluid Mechanics, vol. 814, pp. 69–94, Mar. 2017, doi: 10.1017/JFM.2017.21.

[328] R. J. Daniello, "Experimental studies of superhydrophobic surfaces in flow," Doctoral Dissertations Available from Proquest, Jan. 2013.

[329] D. M. Moore and M. Amitay, "Production and migration of turbulent kinetic energy in bluff body shear layers," International Journal of Heat Fluid Flow, vol. 88, p. 108716, Apr. 2021, doi: 10.1016/J.IJHEATFLUIDFLOW.2020.108716.

[330] H. Choi, J. Lee, and H. Park, “Wake structures behind a rotor with superhydrophobic-coated blades at low Reynolds number,” Physics of Fluids, vol. 31, no. 1, p. 015102, Jan. 2019, doi: 10.1063/1.5054039.

[331] P. Sooraj, M. S. Ramagya, M. H. Khan, A. Sharma, and A. Agrawal, “Effect of superhydrophobicity on the flow past a circular cylinder in various flow regimes,” Journal of Fluid Mechanics, vol. 897, 2020, doi: 10.1017/JFM.2020.371.

[332] Y. F. Wang, X. W. Wang, X. Y. Ma, Z. Q. Tang, and N. Jiang, “Effects of the superhydrophobic surface on coherent structures in the turbulent boundary layer,” Acta Mechanica Sinica 2022 38:10, vol. 38, no. 10, pp. 1–14, May 2022, doi: 10.1007/S10409-022-22022-X.

[333] H. Ems et al., “Drag reduction in minichannel laminar flow past superhydrophobic surfaces,” Physics of Fluids, vol. 33, no. 12, p. 123608, Dec. 2021, doi: 10.1063/5.0075171.

[334] U. Modi and S. Prakash, “Wettability of 3D printed polylactic acid (PLA) parts,” AIP Conf Proc, vol. 2148, no. 1, p. 030052, Sep. 2019, doi: 10.1063/1.5123974.

[335] R. Vert, P. Carles, E. Laborde, G. Mariaux, E. Meillot, and A. Vardelle, “Adhesion of ceramic coating on thin and smooth metal substrate: A novel approach with a nanostructured ceramic interlayer,” in Journal of Thermal Spray Technology, 2012. doi: 10.1007/s11666-012-9798-2.

Appendix A

A.1 Statistical Convergence

The purpose of the convergence test was to assess whether the sample sizes used for computing the statistics were adequate. The double-frame and high-speed measurements were tested separately, and vertical profiles of different statistical quantities were extracted from various sample sizes at different locations within the recirculation bubble of the SAB.

For the double-frame measurements, Figures A.1, A.2, and A.3 in the Appendix showed the profiles of mean velocities, Reynolds stresses, and triple velocity correlations, respectively. The results showed that the mean velocities and Reynolds stresses for different sample sizes reasonably collapsed on top of each other, indicating that a sample size of $N = 1000$ was sufficient for statistical convergence. However, the profiles of triple velocity correlations showed reasonable collapse only for $N \geq 4500$, which implies that a minimum of $N = 4800$ double frame samples were needed to obtain statistical convergence for these statistics.

Similarly, for the high-speed TR-PIV measurements, four different numbers of snapshots were taken, and the profiles of mean velocities, Reynolds stresses, and triple velocity correlations were shown in Figures A.4, A.5, and A.6, respectively. The profiles of these quantities were found to collapse on each other without much deviation, indicating good convergence.

Overall, the results of the convergence test suggest that for the statistical quantities analyzed, a sample size of $N = 1000$ is sufficient for the double-frame measurements, while a minimum of $N = 4800$ double frame samples are needed for triple velocity correlations. For high-speed TR-PIV measurements, the results showed good convergence regardless of the number of snapshots taken.

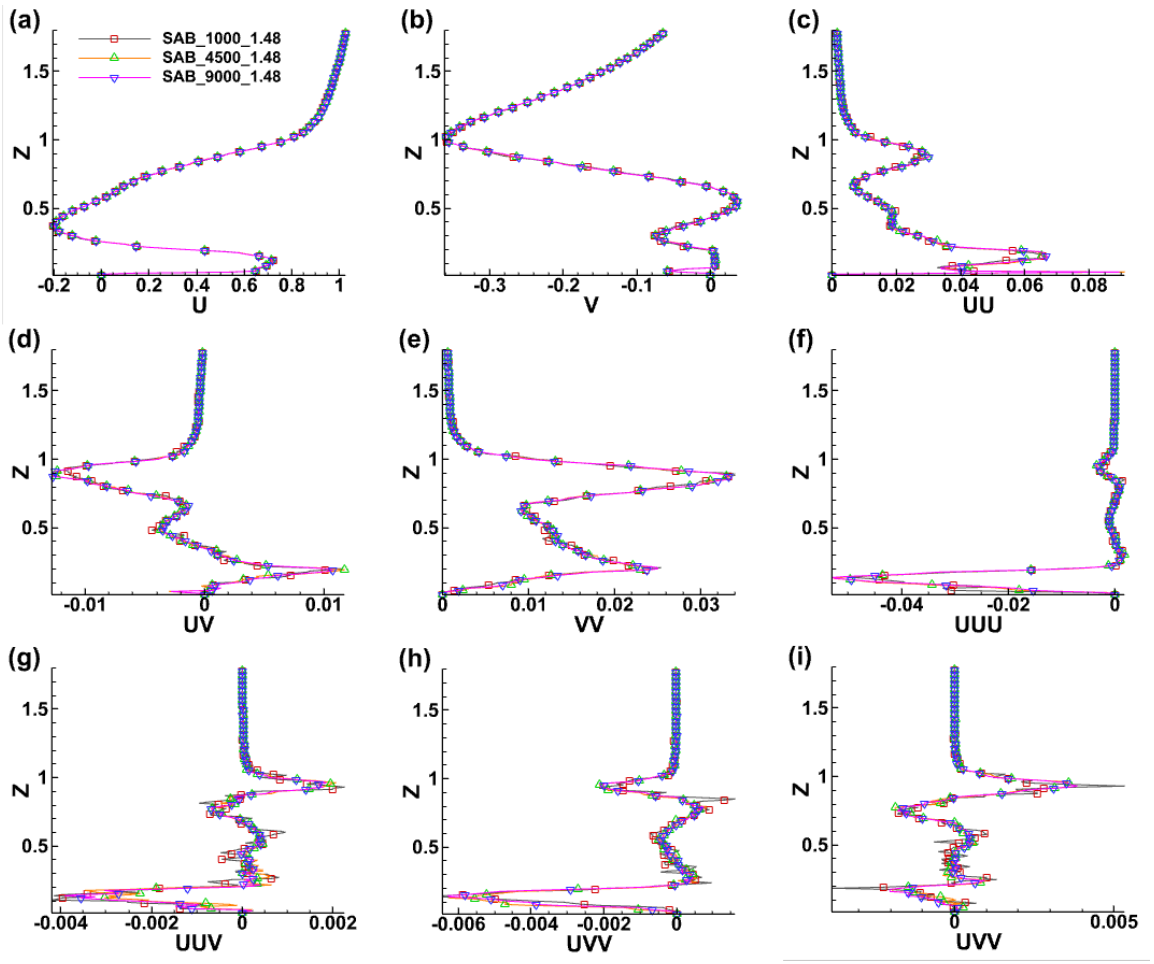

Figure A.1**:** Profiles of the normalized velocity, Reynolds stress, and triple velocity components taken at X=1.48 for DF-PIV. Three different frame sizes are N=1000,4500 and 9000.

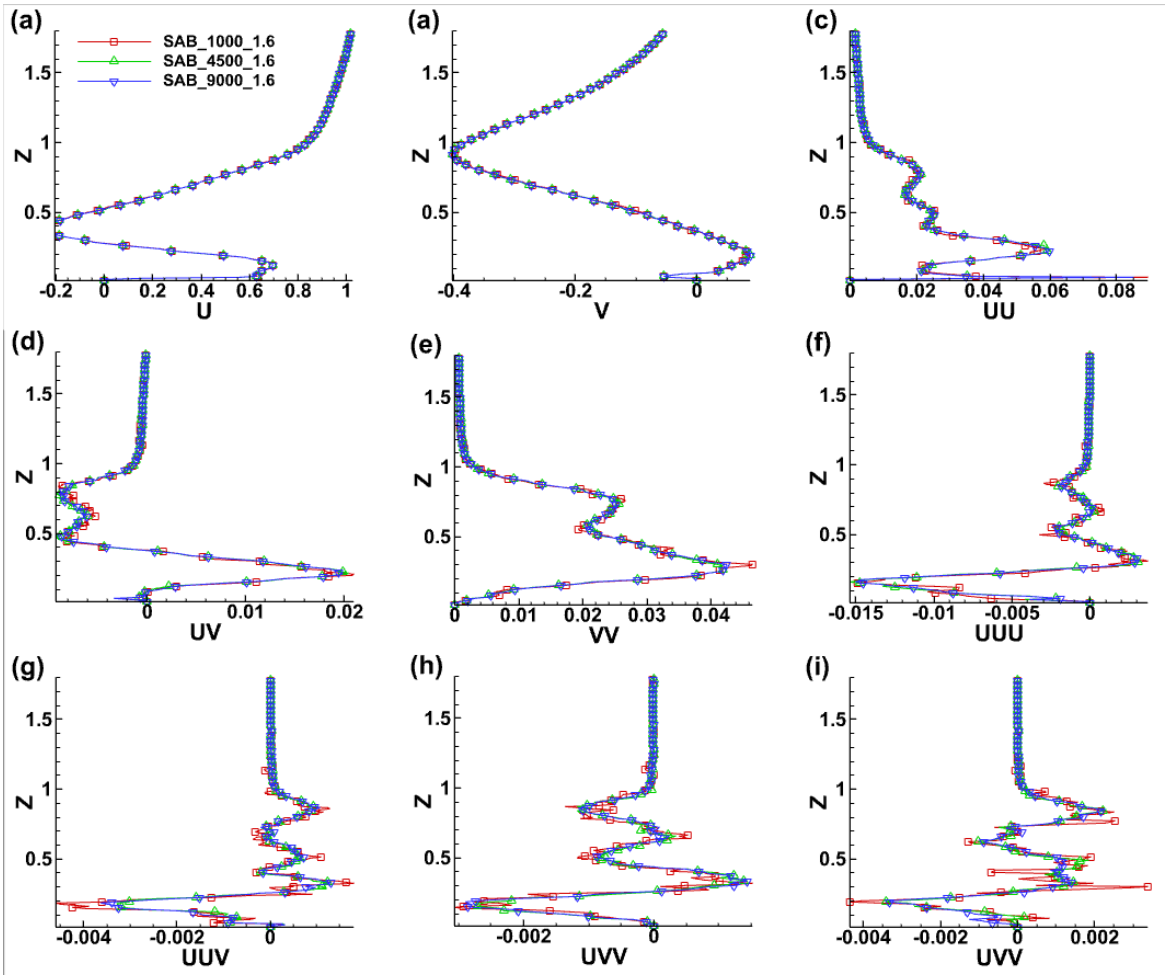

Figure A.2**:** Profiles of the normalized velocity, Reynolds stress and triple velocity components taken at X=1.6 for DF-PIV. Three different frame sizes are N=1000,4500 and 9000.

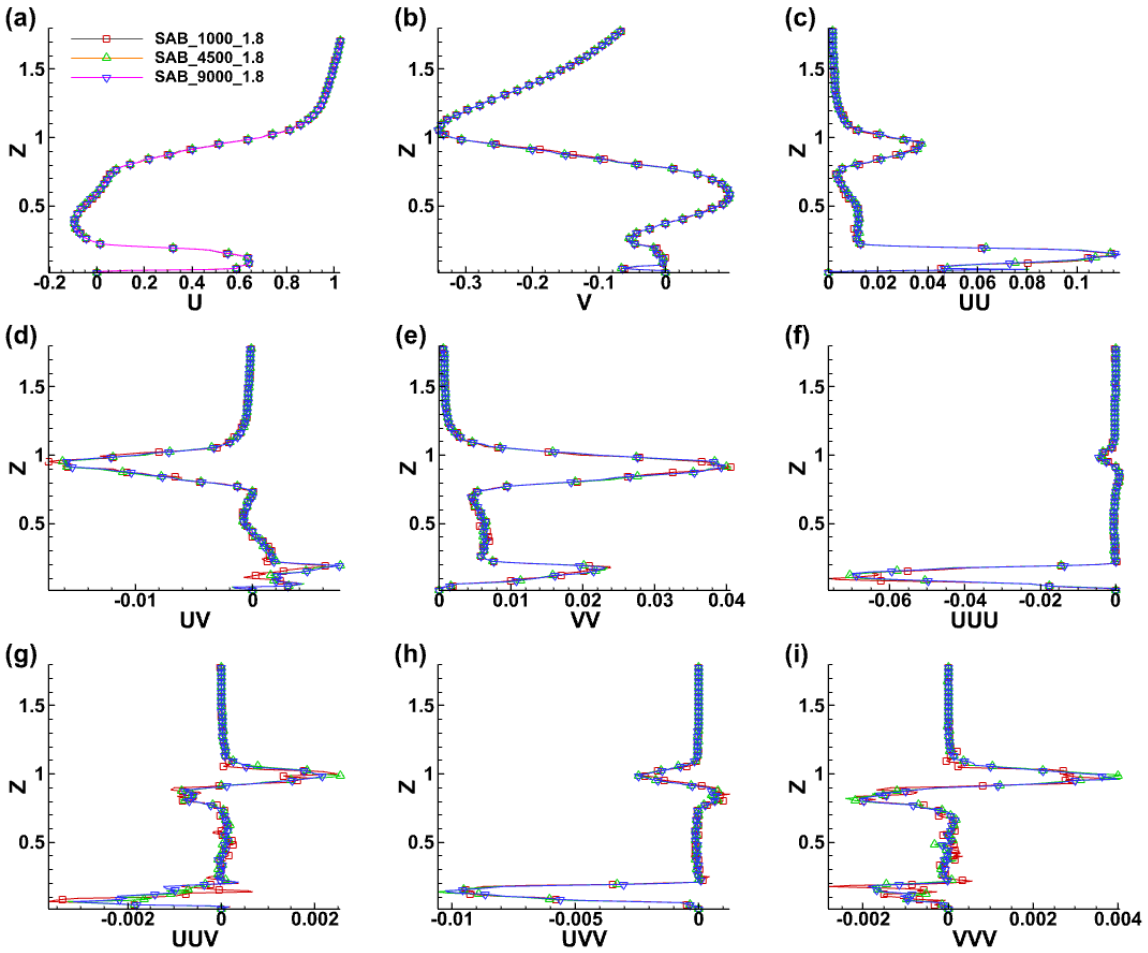

Figure A.3: Profiles of the velocity, Reynolds stress and triple velocity components taken at X=1.8 for DF-PIV. Three different frame sizes are N=1000,4500 and 9000.

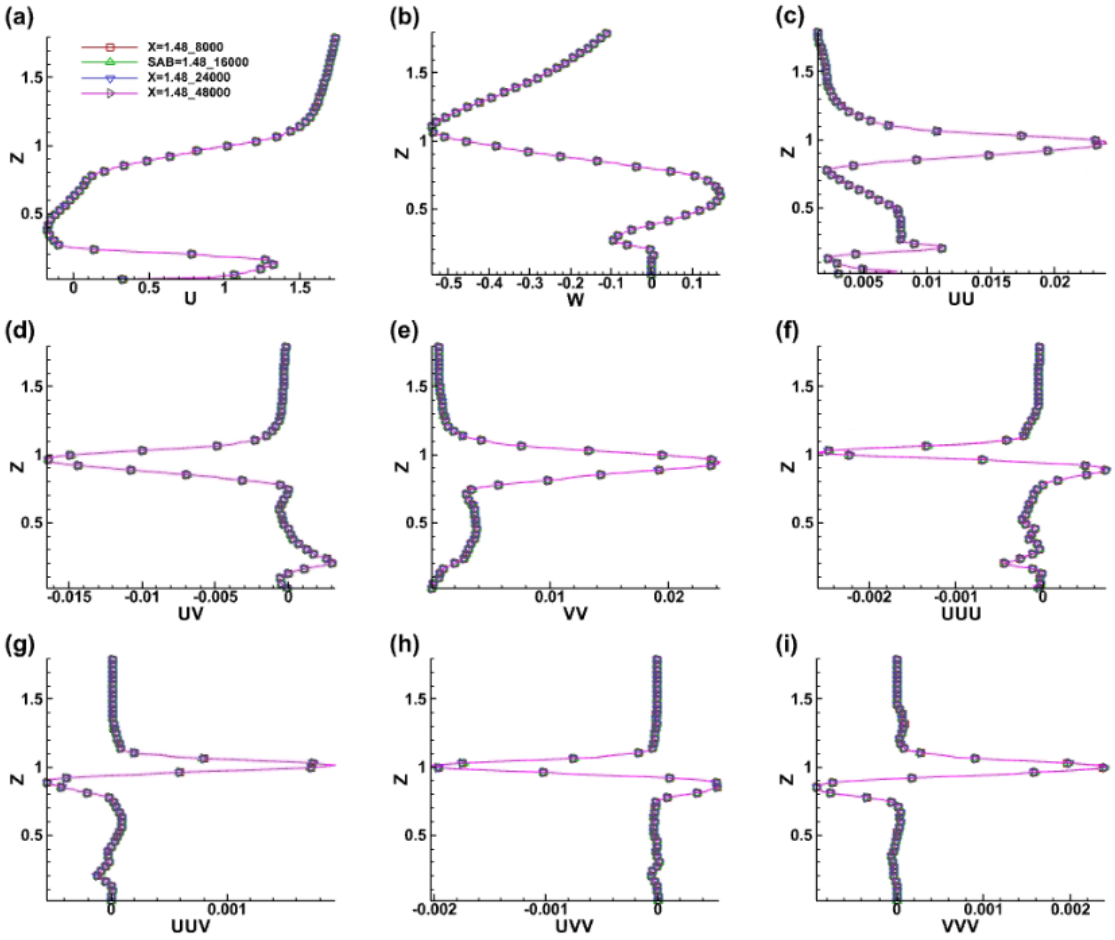

Figure A.4: Profiles of the velocity, Reynolds stress and triple velocity components taken at X=1.48 for TR-PIV. Four different frame sizes are N=8000,16000, 24000 and 48000.

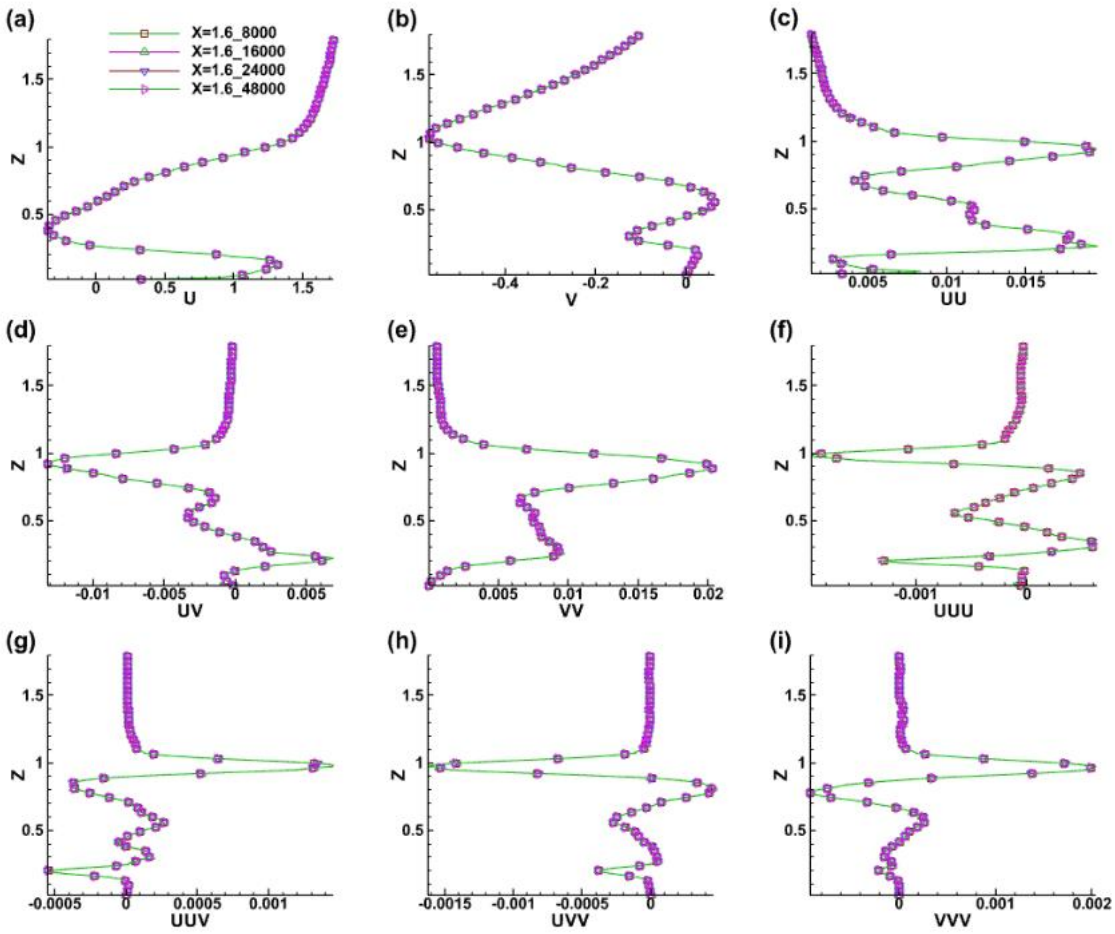

Figure A.5: Profiles of the velocity, Reynolds stress, and triple velocity components taken at X=1.6 for TR-PIV. Four different frame sizes are N=8000,16000, 24000 and 48000.

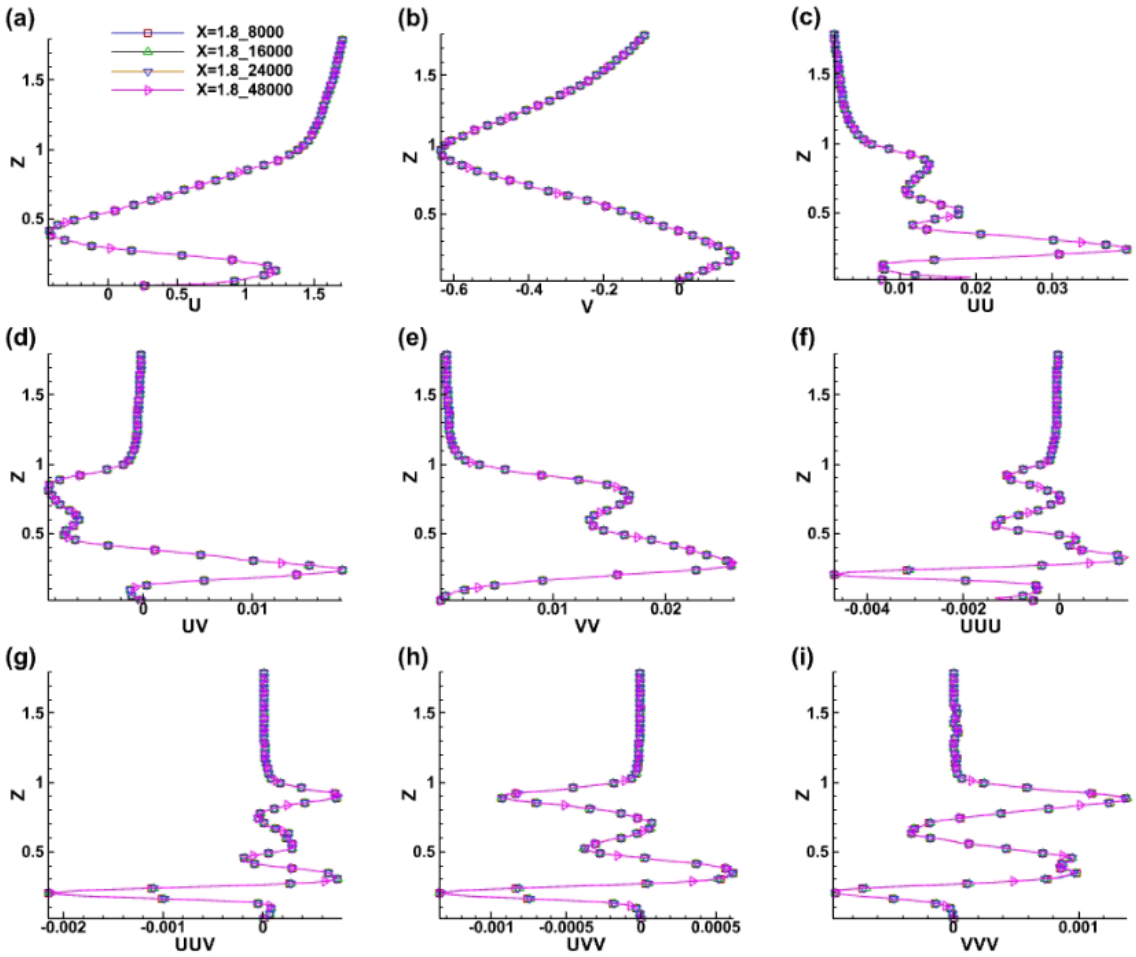

Figure A.6**:** Profiles of the velocity, Reynolds stress, and triple velocity components are taken at X=1.8 for TR-PIV. Four different frame sizes are N=8000,16000, 24000 and 48000.

A.2 PIV Uncertainty Error Analysis

In this study, the uncertainty quantification was performed on the SAB using different sample sizes, which were selected due to the relatively high Reynolds stress magnitudes in the wake of the SAB. The analysis focused on the peak locations of the streamwise Reynolds normal stress ($u'u'$) in the upper separated shear layer. To calculate the measurement uncertainties in the mean streamwise velocity (ξU), streamwise Reynolds normal stress (ξuu), and Reynolds shear stress (ξuv) for both the double frame and high-speed data, specific expressions were used.:

$$\xi_u = Z_c \, {T_u}/{\sqrt{N}} \qquad \text{(B.1)}$$

$$\xi_{uu} = Z_c\sqrt{\frac{1}{N}} \times \left(\frac{\overline{u'u'u'u'}}{\left(\overline{u'u'}\right)^2} - 1\right) \qquad \text{(B.2)}$$

$$\xi_{uv} = Z_c\sqrt{\frac{1+\rho^2{}_{uv}}{N-1}}) \qquad \text{(B.3)}$$

$$\rho_{uv} = \frac{\overline{u\prime v\prime}}{u\prime_{rms} \times v\prime_{rms}} \qquad \text{(B.4)}$$

$$N_{eff} = N\Delta t/2T_{int} \qquad \text{(B.5)}$$

From the expressions, Z_c is the confidence coefficient (value of 1.96 for 95% confidence level), ρuv represent the correlation coefficient, N is the total number of samples whereas N_{eff} is the effective sample size. The time interval between successive images and the integral time scale are, respectively, denoted by Δt and T_{int}. Similar expressions can be written for the uncertainties in the mean vertical velocity (ξ_V) and vertical Reynolds normal stress (ξ_{vv}).

Appendix B

B.1 POD Convergence Test

The convergence test about the insensitivity of the number of snapshots towards the POD analysis is performed using instantaneous snapshot numbers N=1200, 2400, 4800 and 6000. The energy contribution by the number of snapshots is shown in Figure B.1. The figure shows that the energy contribution is insensitive to the number of snapshots considered in the test. From 1200 to 6000, each provides a total amount of 31-32% energy contribution in the four modes, Furthermore, the contribution by 1-4 modes is also close to each other. Therefore, the POD analysis is carried out based on this convergence test which is well established in the literature (Arote, 2020).

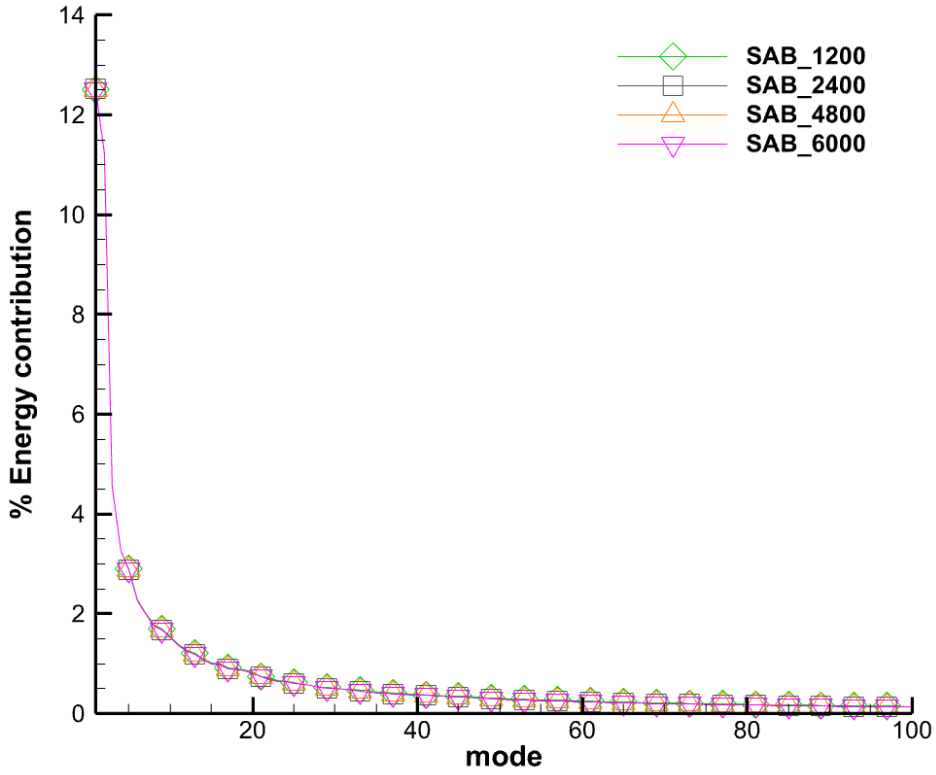

Figure B.1: POD convergence test with different numbers of snapshots.

B. 2 DMD Convergence Test

In order to accomplish the number of required instantaneous snapshots for the DMD analysis, the associated frequency has been identified, considering a different number of

snapshots. In this test, four different snapshots taken at different sampling frequencies are analyzed for the inherent Strouhal number in the SAB. Figure B.2 shows the Strouhal number against the magnitude of the DMD modes, which are sequential in the X-axis. It can be observed that snapshots N=1200, 2400,4800, and 6000 converge towards a Strouhal number of S_t=0.27, S_t=0.0.3, S_t=0.28, and S_t=0.27, respectively. These Strouhal numbers are almost similar and correspond to the Strouhal number found in the POD analysis and frequency analysis of the wake. Therefore, the number of snapshots N=1200 is selected to further reduce the time and cost involved in the analysis.

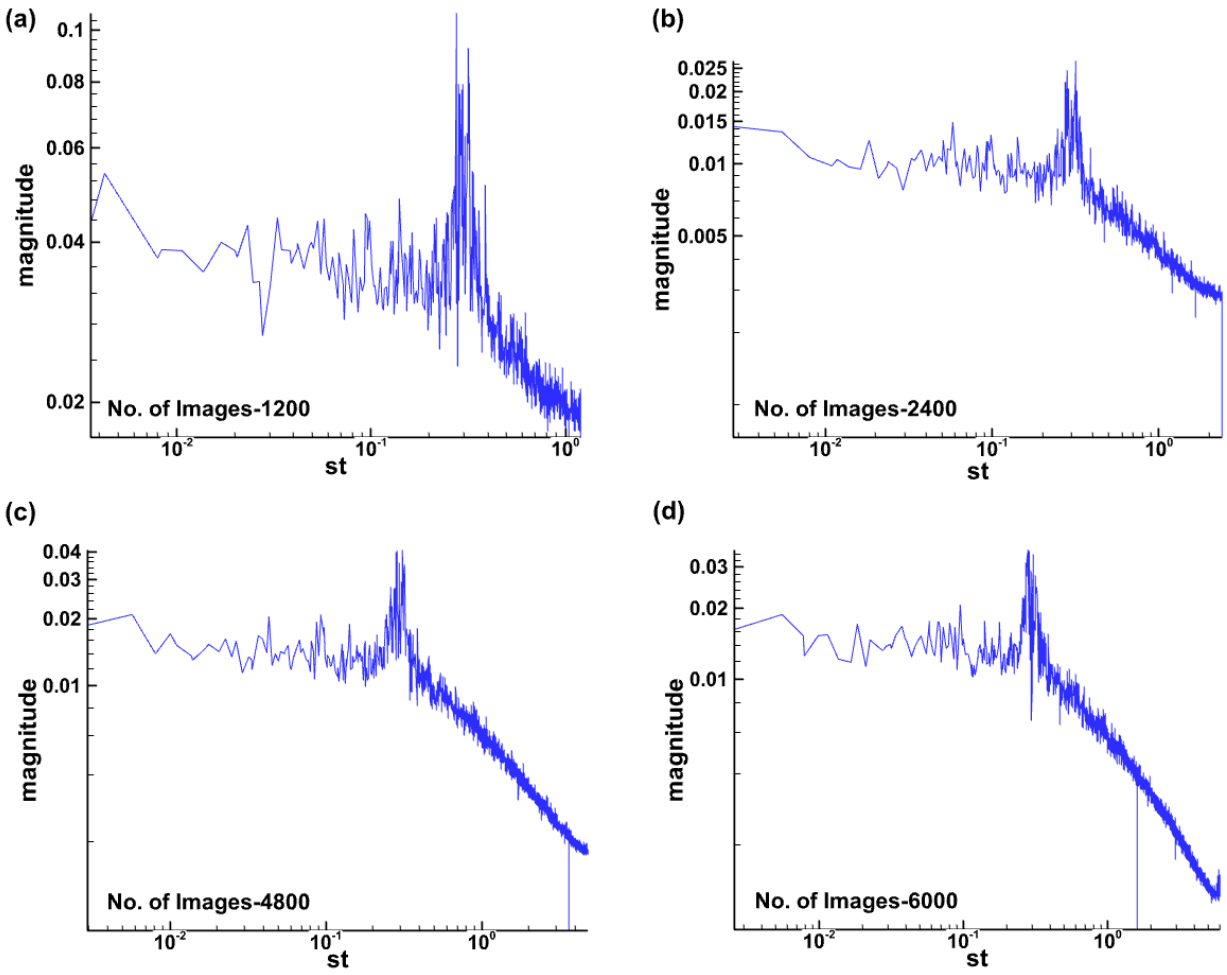

Figure B.2: Convergence test for the DMD analysis based on the number of snapshots.

B.3 Contact-Angle

Hydrophobic coatings are defined using the water contact angle, where an angle higher than 90° is classified as hydrophobic or water-repellent. However, by increasing the hydrophobicity, the contact angle higher than 150° is known as the superhydrophobic coatings [333]. The water contact angle at a 3D-printed smooth surface with Polylactic acid or polylactide (PLA) is 43.4° at a 0° raster angle, which can increase up to 65° at a raster angle of 90° [334]. The present study uses a similar method to generate test models. The Keyence digital microscope with the tangent method was employed to measure the contact angle of the droplet on these surfaces. The water contact angle of the PLA is found to be around 91°, while the angle over the spray coated ultra ever dry paint models are 133°. However, the existing studies [42], [268] reported that a contact angle near 152° can also be achieved with ultra-dry paint when applied to acrylic material. Therefore, the contact angle difference is attributed to the fabricated material, and the black paint applied over the surface in the present study. Since the present study aims to investigate the effect of hydrophobic coating over the Ahmed body, further analysis of the contact-angle difference with the existing literature is not attempted as the 133° contact-angle confirms the application of the hydrophobic coating of the surface which is higher than the required threshold of 90°.

B.4 Surface Roughness

The arithmetic mean deviation roughness (R_a) is a widely accepted parameter used to quantify the surface roughness characteristics of a material which is also used to discuss the coating used in this study in literature [42]. It represents the average magnitude of deviations between the surface profile and a reference line within a specified sampling length. By measuring R_a, valuable insights can be gained regarding the surface topography and texture. In this study, the surface roughness was evaluated using the Filmetrics Profilm 3D instrument, specifically focusing on the arithmetic mean deviation roughness (R_a). The obtained Ra values for the models without the hydrophobic coating and those with the coating were determined to be 0.18 µm and 0.35 µm, respectively. This signifies a relatively small change in roughness resulting from the application of the hydrophobic coating. Considering the obtained values, it can be inferred that both the coated and uncoated models possess surface roughness characteristics that fall within the range

commonly associated with smooth coatings [335]. This suggests that the coating does not introduce significant alterations to the overall surface roughness, and the resulting roughness values are indicative of a relatively smooth coating.

Appendix C

C.1 Numerical Simulation Error

The numerical validation used in the current study has been validated with existing literature both qualitatively and quantitatively. Qualitatively it has been validated by highlighting the mean flow features. Analytically, the dimensions of the recirculation region such as length of the slant separation bubble, wake recirculation length and aerodynamic drag coefficient has been validated. However, another analytical method is reported by calculating the biases found in the simulation compared to the experiment. The fractional bias (FB) calculated based on the Equation C.1 is within the range of -0.3>FB<0.3.

$$FB = \frac{(\overline{C_0} - \overline{C_P})}{0.5(\overline{C_0} + \overline{C_P})} \quad \text{(C.1)}$$

Where C_0 is observation and C_p is prediction.

C.2 Flow Transition

Figure C.1 shows the time-averaged contours of streamwise velocity superimposed by streamlines for EAB_40 at 26°. At first, it can be seen that at a 26° angle, the flow separates at the slant upper edge and does not reattach over the slant surface. Instead, it coalesced into the wake, forming a large recirculation region that resonated with the low-drag SAB found at a 35° providing a substantial drag reduction. Subsequently, a fully detached flow, as expected due to elliptical curvature, is achieved at 26°. Secondly, Figure C.1 (b) shows the cross-section plane at X=0 that demarcates the flow structure from the SAB_40 at 25°. In the EAB_40 at 26°, no existence of c-vortices is found. It is also clear in the Figure C.1 (c) & (d), which is shown using the Q-criterion colored by the streamwise mean velocity and the pressure, respectively. It can be seen that the slant surface is devoid of the SSB, and no side edge C-vortices are realized.

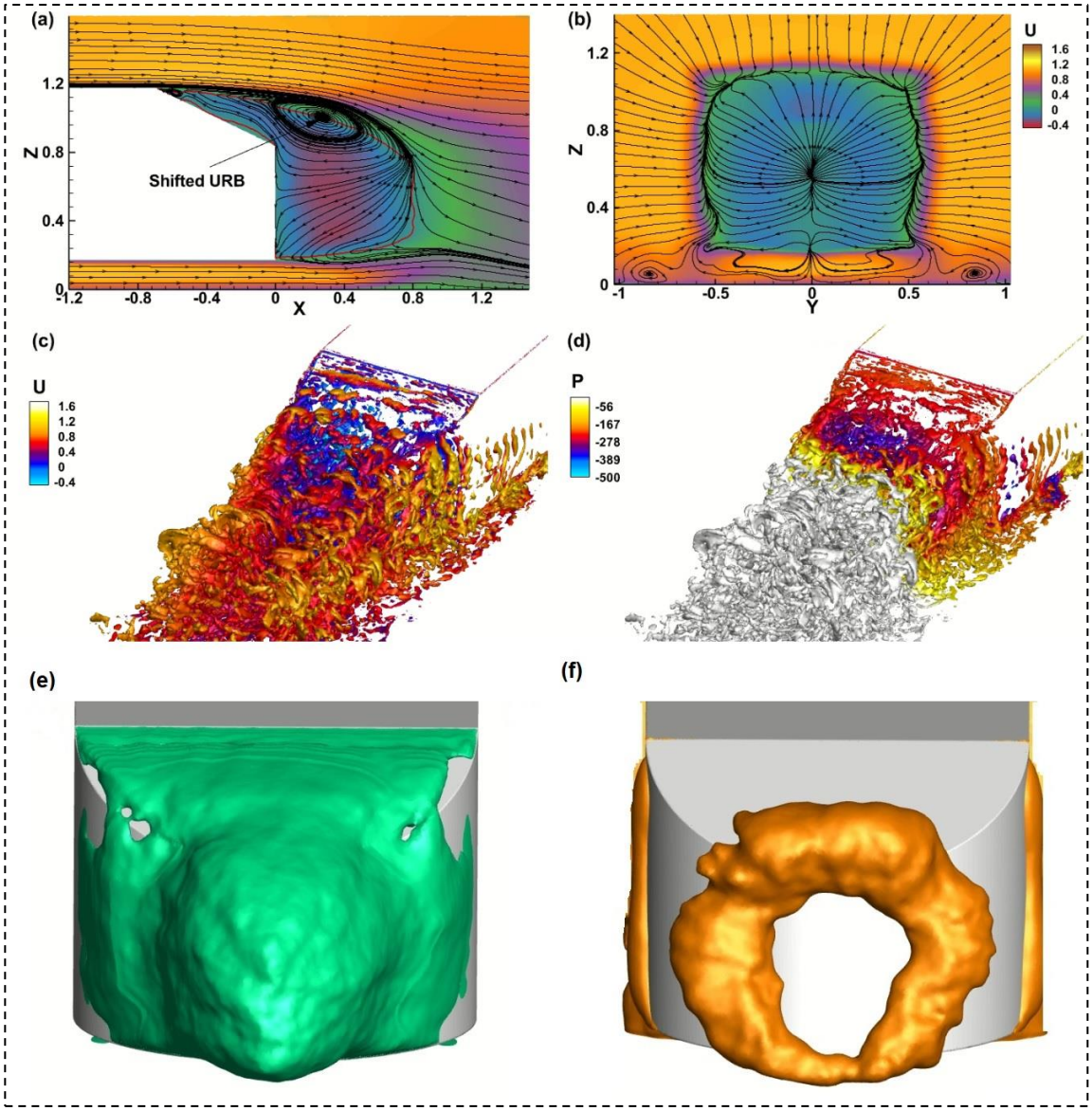

Figure C.1: Flow transition at a slant angle of 26° over the EAB_40. Where (a) Contours of streamwise velocity at the symmetry plane superimposed with streamlines, (b) contours of streamwise velocity at the cross-section plane (X=0) superimposed with streamlines, (c) iso-surface of Q-criterion at an iso-value of 500 colored by streamwise velocity, (d) iso-surface of Q-criterion at an iso-value of 10 colored by the pressure, (e) zero velocity iso-surface, and (f) pressure iso-surface at an iso value of -300.

Therefore, as expected, a fully separated flow is found in the EAB_40 at a 26º slant angle, along with the elimination of LRB and C-vortices. Such a modification provides a striking amount of drag reduction of ~18.4% compared to the 25° SAB_40 shown in Table C.1. Furthermore, it is to be noted that the SAB at a 26° slant angle has a higher value of drag coefficient. In the current simulation as well, the SAB_40 at 26° gives a higher value

of drag coefficient documented in Table C.1. Consequently, by increasing the slant angle by 1°, the drag reduction rises to ~21%. This is a significant drag reduction along with the benefits of soiling mitigation. Another question posed by the experimental study of the SAB_9_Exp. is that it provides a fully detached flow at a 25° slant angle, and therefore the possibility of accomplishing it at a high Reynolds number exists. Although the present IDDES simulation is only prone to transition at a 25°, a fully detached flow cannot be ruled out using more advanced simulation methods such as LES or DNS at a 25º angle using the EAB.

Table C.1 Drag reduction due to the elliptical curvature

	Drag coefficient					
Angle	SAB_9	EAB_9	% drag reduction	SAB_40	EAB_40	% drag reduction
25°	0.384	0.359	6.6	0.353	0.316	10.4
26°				0.365	0.288	21

Appendix D

D.1 Statement of Contribution on Similarity

It is acknowledged that the thesis, specially results and discussion in Chapter 4 have already been published in four journal papers. The author believes that altering of some crucial details, equations, and illustrations results loss of the essence of the work. Therefore, the thesis and the three papers share a considerable similarity. To ensure the work's integrity, the necessary permissions granted by the copyright owners to the thesis author are stated below:

1. AIP Publishing:

Copyright ownership and grant of rights (***Physics of Fluids***):

"*Subject to the rights herein granted to AIP Publishing, each Copyright Owner retains ownership of copyright and all other proprietary rights such as patent rights in the work. Each Copyright Owner retains the following nonexclusive rights to use the work, without obtaining permission from AIP Publishing, in keeping with professional publication ethics, and provided clear credit is given to its first publication in an AIP Publishing journal. Any reuse must include a full credit line acknowledging AIP Publishing's publication and a link to the VOR on AIP Publishing's site:*

Reprint the Version of Record (VOR) in print collections written by the Author, or in the Author's thesis or dissertation. It is understood and agreed that the thesis or dissertation may be made available electronically on the university's site or in its repository and that copies may be offered for sale on demand."

2. Elsevier Publishing:

Article: Submission declaration and verification in the Guide for authors (***International Journal of Heat and Fluid Flow***):

"Submission of an article implies that the work described has not been published previously (except in the form of an abstract, a published lecture or academic thesis, see 'Multiple, redundant or concurrent publication' for more information), that it is not under consideration for publication elsewhere, that its publication is approved by all authors and tacitly or explicitly by the responsible authorities where the work was carried out, and that,

if accepted, it will not be published elsewhere in the same form, in English or in any other language, including electronically without the written consent of the copyright-holder. To verify originality, your article may be checked by the originality detection service Crossref Similarity Check."

3. Creative Commons Attribution 4.0 Open-access (*Journal of Mechanical Engineering and Sciences*):

"The author(s) of an article published in the Journal of Mechanical Engineering and Sciences have unrestricted publication rights. The authors give the Journal of Mechanical Engineering and Sciences the right to publish the article and designate Universiti Malaysia Pahang Publishing as the original publisher of the article.

Journal of Mechanical Engineering and Sciences is an open-access journal that follows the Creative Commons Attribution 4.0 International License (CC BY-NC 4.0), which states that:

Under this license, the reusers must give appropriate credit, provide a link to the license, and indicate if changes were made. Users may do so in any reasonable manner, but not in any way that suggests the licensor endorses users or their use."

The overall percentage of similarity of the thesis, determined by Turnitin, is 57%. However, the individual percentage of similarity of the published papers to the thesis are as follows:

1. N. A. Siddiqui and M. Agelin-Chaab, "Numerical investigation of the wake flow around the elliptical Ahmed body," ***International Journal of Heat and Fluid Flow*** 101, 109125, 2023.

Similarity: 21%.

2. N. A. Siddiqui and M. Agelin-Chaab, "Experimental investigation of the elliptical Ahmed body," ***Physics of Fluids*** 34, 105119 (2022).

Similarity: 14%.

3. N. A. Siddiqui and M. Agelin-Chaab, "Flow features of the Ahmed body at low Reynolds number," ***International Journal of Heat and Fluid Flow*** 98, 109052, 2022.

Similarity: 9%.

4. N. A. Siddiqui and M. Agelin-Chaab, “Nature-inspired solutions to bluff body aerodynamic problems: A review,” ***International of Mechanical Science and Engineering*** 15(2), 8095-8140, 2021.

Similarity: 2%.

Therefore, together, these papers by the thesis’ author account for a total similarity percentage of 46%.